Measurement of the Υ meson production cross section in *ep* scattering at HERA

Dissertation
zur Erlangung des Doktorgrades
des Department Physik
der Universität Hamburg

vorgelegt von
Igor Rubinskiy
aus Moskau

Hamburg
2009

Gutachter/Gutachterin der Dissertation:	Prof. Dr. R. Klanner
	Dr. A. Geiser
Gutachter/Gutachterin der Disputation:	Prof. Dr. C. Hagner
	Prof. Dr. P. Schleper
Datum der Disputation:	16.04.2009
Vorsitzende/Vorsitzender des Prüfungsausschusses:	Prof. Dr. D. Horns
Vorsitzender des Promotionsausschusses:	Prof. Dr. R. Klanner
MIN-Dekan des Departaments Physik der Fakultät:	Prof. Dr. H. Graener

Abstract

This thesis presents a measurement of Υ meson production in ep collisions with the ZEUS detector at HERA using an integrated luminosity of 468 pb^{-1}. The Υ mesons were identified using the decay channel $\Upsilon \rightarrow \mu^+\mu^-$. The measurements were performed for exclusive diffractive production in the kinematic range $Q^2 <1$ GeV^2, $60< W <220$ GeV, and $15< Q^2 <100$ GeV^2, $60< W <220$ GeV, where Q^2 is the virtuality of the exchanged photon and W is the photon–proton centre–of–mass energy. A feasibility study for the Υ meson inelastic production has also been performed. The measured cross sections are compared to and agree well with theoretical predictions within the perturbative QCD framework such as Martin-Ryskin-Teubner two gluon exchange and NRQCD.

As the technical part of this thesis, work related to the commissioning of the Straw Tube Tracker (STT) and to the Zeus Event Visualisation (ZEVIS) software package are presented. STT developments include: the STT DSP (Digital Signal Processor) quality monitor was developed, the pattern recognition algorithm was optimised for speed, and used in the Third Level Trigger (TLT) in order to reduce the accepted event rate by rejecting non-physics background. The TLT Charge Current(CC) slot rate was reduced by an order of magnitude, offering a rate reduction for the total accepted TLT rate by $\approx 2\%$. ZEVIS developments include: the STT hit visualisation scheme in 2D, 3D and $tan(\theta) - \phi$ view, and a user-friendly interface called "EasyTool" for global ZEUS track and hit visualisation for all ZEUS components.

Kurzfassung

Diese Arbeit beschreibt eine Messung der Υ-Meson Produktion in ep-Kollisionen mit dem ZEUS-Detektor bei HERA unter Verwendung einer integrierten Luminosität von 468 pb^{-1}. Die Υ-Mesonen wurden durch den Zerfallskanal $\Upsilon \rightarrow \mu^+\mu^-$ identifiziert. Die Messung wurde durchgeführt für exklusive diffraktive Produktion im kinematischen Bereich von $Q^2 < 1$ GeV^2, $60< W <220$ GeV und $15< Q^2 < 100$ GeV^2, $60< W <220$ GeV, wobei Q^2 die Virtualität des ausgetauschten Photons und W die Photon–Proton Schwerpunktsenergie bezeichnet. Eine Machbarkeitsstudie zur inelastischen Υ-Meson Produktion wurde ebenfalls durchgeführt. Die gemessenen Wirkungsquerschnitte werden mit theoretischen Vorhersagen innerhalb der perturbativen QCD, wie z.B. Martin-Ryskin-Teubner zwei Gluonaustausch und NRQCD, verglichen und stimmen gut mit ihnen überein.

Als technischer Teil dieser Dissertation werden Arbeiten in Verbindung mit der Inbetriebnahme des Straw Tube Tracker (STT) und mit dem Zeus-Ereignisvisualisationssoftwarepaket (ZEVIS) präsentiert. Die Entwicklungen für den STT beinhalten: Die Entwicklung eines STT-Qualitätsmonitors, die Geschwindigkeitsoptimierung des Mustererkennungsalgorithmus und die Benutzung in der dritten Trigger-Stufe (TLT) zur Reduzierung der akzeptierten Ereignisrate durch Reduktion des Untergrundes, der nicht aus ep-Wechselwirkungen stammt. Die Rate des geladenen Strom-Kanals im TLT wurde um eine Größenordnung verringert, wodurch sich die totale akzeptierte TLT-Rate um $\approx 2\%$ erniedrigte. ZEVIS-Entwicklungen beinhalten: das STT-Hitvisualisierungsschema in 2D, 3D und $tan(\theta) - \phi$ Ansicht und ein benutzerfreundliches Interface, "EasyTool" genannt, für globale ZEUS Spur- und Hitvisualisierung aller ZEUS-Komponenten.

to my family

Contents

Introduction

The quest for the fundamental understanding of the laws of nature has been occupying human imagination since ages. It is still ongoing and at the present stage it has been concluded in the Standard Model (SM) [1], a theory which provides a description of the elementary structure of matter. In the SM, matter is constructed of 12 fundamental particles: quarks and leptons (Fig. 1). It describes the strong, weak, and electromagnetic interactions in terms of "gauge theories". The term ″gauge" reflects the fact that a theory describing the interaction requires it to possess a certain kind of symmetry, and the interaction laws are invariant under gauge transformations (″gauge invariance"). The interaction mediating particles are the 3 types of gauge bosons: γ (Electromagnetic force), *gluon* (Strong force), $Z^0, W^{\pm}$ (Weak force). The Electromagnetic interaction is described by the theory called Quantum Electrodynamics (QED). Both the Electromagnetic and the Weak interactions can be described within the Electroweak theory, based on QED. The Strong interactions are described by Quantum Chromodynamics (QCD).

The leptons exist as free particles, while the quarks exist only inside of hadrons, particles participating in strong interactions. This phenomenon is known as ”confinement”, and its nature is yet to be fully understood. Lepton-nucleon scattering is one of the means to investigate the way the quarks are confined in hadrons.

The HERA collider (Hadron Electron Ring Anlage) was constructed as the facility to scatter electrons[1] (leptons) off the proton (nucleon) at high energies. The electron scatters via the exchange of gauge bosons off the proton constituents. The scattered electron, as well as the hadrons produced in the hard scattering process carry the information about the internal structure of the proton. This information is contained in the so-called Parton Density Functions (PDFs). The standard way to extract the PDFs is through inclusive reactions with the virtuality of the exchanged photon $Q^2 > 1\ GeV^2$. The parton densities one can extract from such processes encode the distribution of longitudinal momentum carried by quarks, antiquarks and gluons within a fast moving proton. Exclusive reactions[2] offer information, which allows one to study more specifically the gluon content of the proton and extract the gluon PDFs in an alternative way. Moreover, the study of exclusive reactions allows one to investigate not only on the longitudinal fraction of the gluon momentum relative to the proton, which is similar to inclusive reactions, but also about its transverse component. The framework of the Generalized Parton Distributions (GPDs), which describe the $3D$-momenta distribution of the partons in the nucleon, can be applied to exclusive processes only. Exclusive production of vector mesons (ρ, ϕ, ω, J/ψ, Υ - hadrons with $J^{PC} = 1^{--}$, same quantum numbers as the photon) is an important class of exclusive reactions.

---

[1] The term electron is used further to denote both electrons and positrons, if not stressed otherwise.

[2] Reactions where both incident particles, the electron and the proton, stay intact.

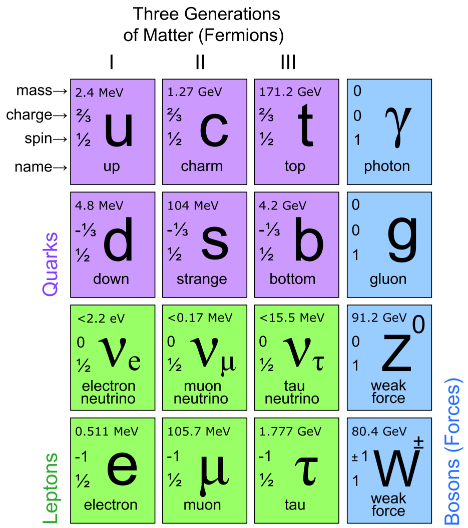

Figure 1: *The Standard Model elementary particles.*

Production of heavy vector mesons, such as $J/\psi(c\bar{c}$, *charm*-quark content) and $\Upsilon(b\bar{b}$, *beauty*-quark content) is especially valuable as it allows for perturbative QCD (pQCD) calculations to be performed, regardless of the value of Q^2. The applicability of pQCD is determined by the vector meson mass squared, M_V^2, or to be more precise, $M_V^2 + Q^2 \gg 1$ GeV^2. The calculations are expected to be more precise in case of Υ mesons, since the constituent b-quark mass is larger then the c-quark mass (Fig.1).

This thesis is devoted to the analysis of $\Upsilon(Upsilon)$ meson production in the muon decay channel in the data collected at the HERA collider by the ZEUS detector.

The structure of the thesis is presented in the following.

Chapter 1 gives a theoretical overview to physics at HERA and the importance of exclusive vector meson production for the understanding of the proton structure.

Chapter 2 gives further details on the QCD models of the Υ meson exclusive production.

Chapter 3 introduces the HERA collider and the ZEUS detector with emphasis on the detector components used in the analysis.

Chapter 4 describes the contribution of the author of the thesis to the commissioning of the Straw Tube Tracker (STT) and relevant software development.

Chapter 5 describes the contribution of the author of the thesis to the ZEUS Event Visualisation software development.

Chapter 6 introduces the issues related to the simulation of the physics processes in ZEUS.

Chapter 7 defines the event selection for the Υ meson production cross section measurement.

Chapter 8 gives further details about the physics processes simulation in ZEUS and the measurement specific corrections with special emphasis on the muon efficiency corrections.

Chapter 9 describes the processes treated as background to the Υ meson production.

Chapter 10 presents the Υ meson exclusive production cross section measurement.

Chapter 11 presents the Υ meson inelastic production cross section measurement feasibility study.

Chapter 12 gives a summary of the measurement results presented in this thesis. The measurement improvement possibilities are also discussed.

Chapter 13 presents the measurement comparison to the theoretical model predictions.

Chapter 14 concludes the Υ meson production cross section measurement and the potential physics gain from the STT detector.

Part I

Theoretical part

Chapter 1

Theory overview

1.1 The Standard Model

1.1.1 The History of the Standard Model

By the mid-1960s, physicists realised that their previous understanding, where all matter is composed of the fundamental protons, neutrons, and electrons, was insufficient to explain the myriad of new particles being discovered. Gell-Mann's and Zweig's quark theory [1, 2] solved these problems. Over the last thirty years, the theory that is now called the Standard Model of particles and interactions has gradually grown and gained increasing acceptance with new evidence from new particle accelerators. Before it obtained its present shape the Standard Model went over a long history (Fig.1.1). A few milestone events are listed below.

1964: Gell-Mann and George Zweig tentatively put forth the idea of quarks [1, 2]. They suggested that mesons and baryons are composites of three quarks or antiquarks, called up, down, or strange (u, d, s) with spin 1/2 and electric charges 2/3, -1/3, -1/3, respectively. Since such fractional charges had never been observed, the introduction of quarks was treated more as a mathematical explanation of flavor patterns of particles than as a postulate of actual physical objects. Later theoretical and experimental developments allowed one to regard the quarks as real physical objects, even though they cannot be isolated.

1964: Since leptons had a certain pattern, several papers [3] suggested a fourth quark carrying another flavor to give a similar repeated pattern for the quarks, now seen as the generations of matter. Very few physicists took this suggestion seriously at the time. Sheldon Glashow and James Bjorken coined the term "charm" for the fourth quark (the c-quark).

1965: O.W. Greenberg, M.Y. Han, and Yoichiro Nambu introduce the quark property of colour charge. All observed hadrons are colour neutral.

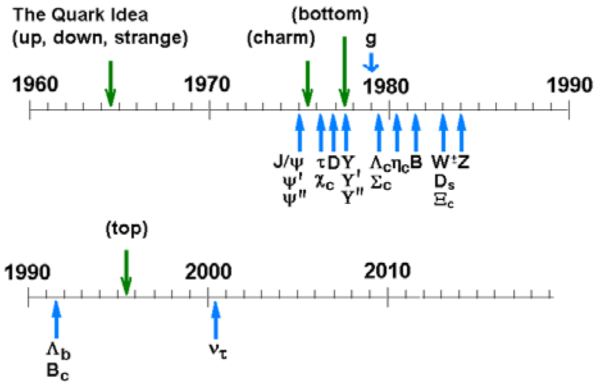

Figure 1.1: *The Standard Model development in historical perspective. The idea of quarks as the constituents of matter and their subsequent experimental confirmation are shown.*

1966: The quark model was accepted rather slowly because quarks hadn't been observed as free particles.

1967: Steven Weinberg and Abdus Salam separately proposed a theory that unifies electromagnetic and weak interactions into the electroweak interaction. Their theory requires the existence of a neutral, weakly interacting boson (now called the Z0) that mediates a weak interaction that had not been observed at that time.

1968-69: At the Stanford Linear Accelerator, in an experiment in which electrons were scattered off protons, the electrons appear to be bouncing off small hard cores inside the proton. James Bjorken and Richard Feynman analysed this data in terms of a model of constituent particles (partons) inside the proton (they didn't use the name "quark" for the constituents, even though this experiment provided evidence for quarks.)

1970: Sheldon Glashow, John Iliopoulos, and Luciano Maiani recognise [4] the critical importance of a fourth type of quark in the context of the Standard Model. A fourth quark allows a theory that has flavor-conserving Z0-mediated weak interactions but no flavor-changing ones.

1973: Andre Lagarrigue and colleagues working with the Gargamelle bubble chamber at CERN observed neutral currents (those due to a Z0 exchange) - the neutral manifestation of the weak force that had been predicted by electroweak theory [5].

1973: A quantum field theory of strong interaction was formulated. This theory of quarks and gluons (now part of the Standard Model) is similar in structure to QED, but since the strong interaction deals with colour charge this theory is called Quantum Chromodynamics. Quarks are determined to be real particles, carrying a colour charge. Gluons are massless quanta of the strong-interaction field. This strong interaction theory was first suggested by Harald Fritzsch and Murray Gell-Mann.

1973: David Politzer, David Gross, and Frank Wilczek discovered that the colour theory of the strong interaction had a special property, now called "asymptotic freedom".

1974: In a summary talk for a conference, John Iliopoulos presented, for the first time in a single report, the view of physics now called the Standard Model.

1974: (Nov.) Burton Richter and Samuel Ting, leading independent experiments, announce that they discovered the same new particle. Ting and his collaborators at Brookhaven called this particle the "J" particle, whereas Richter and his collaborators at SLAC called this particle the ψ particle. Since the discoveries are given equal weight, the particle is commonly known as the J/ψ particle. The J/ψ particle is a charm-anticharm meson. This event is recognised as the discovery of the *charm*-quark.

1975: The tau lepton was discovered by Martin Perl and collaborators at SLAC [6]. Since this lepton was the first recorded particle of the third generation, it is completely unexpected.

1977: Leon Lederman and his collaborators at Fermilab discovered yet another quark (and its antiquark). This quark was called the "bottom" quark. The $b\bar{b}$ bound state - the Υ meson production at HERA is the main subject of this thesis.

1979: Strong evidence for a gluon radiated by the initial quark or antiquark was found at PETRA, a colliding beam facility at the DESY laboratory in Hamburg,

1983: The W and Z0 intermediate bosons demanded by the electroweak theory are observed by two experiments using the CERN synchrotron using techniques developed by Carlo Rubbia and Simon Van der Meer to collide protons and antiprotons.

1989: Experiments carried out in SLAC and CERN strongly suggest that there are three and only three generations of fundamental particles. This is inferred by showing that the Z0-boson lifetime is consistent only with the existence of exactly three very light (or massless) neutrinos.

1995: After eighteen years of searching at many accelerators, the CDF and

D0 experiments at Fermilab discover the top quark at the mass of 175 GeV.

2000: The first detection of τ-neutrino interactions was announced in summer of 2000 by the DONUT collaboration at Fermilab, making it the latest particle of the Standard Model to have been directly observed [7, 8].

2008-2009: The Large Hadron Collider (LHC) at CERN is about to start, which is expected to confirm or disprove the existence of the only undetected particle in the Standard Model - the Higgs boson.

The SM incorporates the following three forces: Electromagnetic(γ), Weak(Z, $W^{\pm}$), and Strong(g). The Gravitational interaction (the 4-th force) is not a part of the Standard Model. However, work is ongoing with the goal of introducing a unified way of description of all four forces.

The SM as any theory has limitations and must be validated. The SM is being tested nowadays at the *colliders*, the facilities designed to collide particles travelling at the speed close to that of the light. The lepton-nucleon colliders play a distinct role in the present and future tests of the SM.

1.1.2 Quantum Chromodynamics

QCD is a non-Abelian gauge theory based on the $SU(3)_c$ colour symmetry. It operates with quarks(fermions, spin-$\frac{1}{2}$) and gluons(bosons, spin-1). There is one striking difference between QCD and QED. In QCD the gluons carry the strong interaction charge called *colour* (″*chromos*″ =colour (Ancient Greek), hence the term *Chromo*− in QCD), unlike QED where the photons are electrically neutral. This difference produces a dramatic effect for the interaction strength dependence on the energy scale of the interaction μ^2. The interaction strength is proportional to the coupling constant[1] α. In QED $\mu^2 = Q^2$ and the following behaviour is observed [9]:

$$\alpha(Q^2) = \frac{\alpha_0}{1 - \frac{\alpha_0}{3\pi} ln \frac{Q^2}{m_e^2}}, \tag{1.1}$$

where m_e^2 is the mass of the electron, and α_0 is the coupling constant at $Q^2 = m_e^2$. In QED the coupling constant α grows with the energy scale Q^2. In QCD the contrary behaviour of the coupling constant (α_s) is expected, allowing the explanation of two experimental phenomena: (i) the absence of free quarks in nature or the $confinement$ in hadrons and (ii) the quarks quasi-free behaviour at high energy scale, the phenomenon known as $asymptotic\ freedom$.

In QCD (as a quantum field theory) the cross sections are calculated as expansion in terms of α_s defined at the interaction vertex. The expantion

---

[1] both in QED and QCD the term ″constant″ means ″constant at given μ^2″, the dependence of the coupling constants on μ^2 produced the term ″running constants″.

converges only if α_s is small (at high energy scale). The termination of the calculation after the first or the second order terms defines the precision of the calculation as the *leading order* (LO) or the *next-to-leading order* (NLO) approximation respectively.

The dependence of the strong interaction coupling constant on the energy scale is usually expressed (at LO) as:

$$\alpha_s(\mu^2) = \frac{4\pi}{(11 - \frac{2}{3}n_f)ln(\mu^2/\Lambda^2_{QCD})}, \tag{1.2}$$

where μ^2 is the energy scale of the process, $\Lambda_{QCD} \approx 0.2$ GeV is a fundamental QCD parameter, and n_f is the number of quark flavours with the mass squared less then μ^2.

For $\mu^2 \gg \Lambda^2_{QCD}$ the QCD coupling constant is small ($\alpha_s \to 0$ for $\mu^2 \to \infty$) and the interacting quarks and gluons behave as free particles ($asymptotic\ freedom$). For $\mu^2 \lesssim \Lambda^2_{QCD}$ the coupling constant is large and quarks and gluons are bound by a strong field, forming colourless hadrons ($confinement$). The scale μ^2 introduces two different regimes. Interactions which involve large values of the scale (*hard scale*) can be calculated using perturbative QCD (pQCD) approach and are often referred to as *hard* processes. Interactions in which no hard scale is available are called $soft$ processes and require non-perturbative models.

1.2 Lepton-nucleon scattering

Over the last thirty years the Standard Model has provided a satisfactory description of the strong, weak and electromagnetic interactions of all known elementary particles. However, the QCD-part of the Standard Model can be tested with so called perturbative methods only when there is a suitable scale parameter needed to perform the series expansion. Lepton-nucleon scattering allows one to simplify the checks related to the QCD induced part of the interaction. Lepton-nucleon scattering can be used as a precision tool to study the structure of the nucleon in terms of the distribution of the partons inside of the nucleon, and eventually shed more light on the transition from the "asymptotic freedom″ of the quarks to the "confinement″ of the quarks in the nucleons. In case of HERA physics (electron-proton scattering) one can operate with ”hardness” parameters such as the incoming photon virtuality Q^2, and the quark mass[2] (m_q).

During the years of accumulating experimental data, before QCD had been accepted as theory of the strong interactions, the ”laws” of subatomic particle interactions were described phenomenologically or following a generic quantum mechanics approach derived from classical optics. The phenomenon of ”diffraction” in high-energy physics is an example where the name for the process was borrowed from its mathematical framework. Quantum mechanics required the introduction of a new mediating particle for the diffractive processes, which was done by the concept of a *Pomeron*, a particle with quantum numbers of the vacuum ($J^{PC} = 0^{++}$), and, a *Reggeon*, a particle with non-vacuum quantum numbers.

Before HERA the description of a vast amount of experimental data [10–12] on diffraction occurred within a relatively simple phenomenological model based on these newly invented particles, i.e. via a *Pomeron* (or *Reggeon*) exchange (Regge model). Once the data from HERA started arriving it became clear that about 15% of events resembles the definition of ”diffraction” and can be described with the *Pomeron* exchange model (see Chapter 1.3). However, following the Regge model phenomenology it turned out that in additiona to the ordinary diffraction there is a new class of events that was called ”hard” diffraction, and hence there was a ”*hard Pomeron*” mediating the interaction [13].

An important subset of diffractive reactions at HERA is the exclusive vector meson production. Vector mesons with heavy flavour content, charm or beauty quarks, (light flavour - up, down, strange quarks) are also called heavy (light) quarkonium states, similar to positronium (electron-positron bound state).

The terminology to distinguish different production types of quarkonium at HERA has its own specifics. Exclusive production, otherwise called ”elastic”,

---

[2] The list can be extended by e.g. the quark transverse momentum p_T, jets E_T.

belongs to the diffractive reactions domain and can be presented not only in the language of Regge phenomenology, but, in the case of heavy quarkonium[3], also in terms of gluons (simplest QCD model: two gluon exchange model) [14–16]. An alternative to the *elastic* production is the *inelastic* one, which does not belong to the domain of $diffraction$, and can be described only in pQCD (if the hard scale is present, always true for the heavy quarkonium).

1.2.1 Kinematics of lepton-nucleon scattering

The generic diagram for the lepton-nucleon scattering $e(k)p(P) \rightarrow e(k')X$ is shown in Fig.1.2.

The relevant Lorentz invariant variables are:

- $s = (k+P)^2$, the square of the centre-of-mass energy;
- $Q^2 = -q^2 = -(k-k')^2$, the negative squared four-momentum of the exchanged virtual photon;
- $y = \frac{P \cdot q}{P \cdot k}$, the fraction of the positron energy transferred to the photon in the proton rest frame.
- $x = \frac{Q^2}{2(P \cdot q)}$, the Bjorken variable, which can be interpreted as the fraction of the proton momentum carried by the struck charged parton.

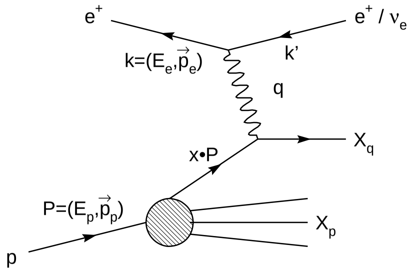

Figure 1.2: *Generic diagram for lepton-nucleon scattering. The four vectors of the particles are given in parenthesis.*

---

[3] same is true for the light quarkonium at $Q^2 > 1\ GeV^2$

Assuming that one can neglect the proton and electron masses m_p^2, m_e^2 compared to s, the x, y, s, and Q^2 can be related by the formula:

$$Q^2 \approx sxy, \tag{1.3}$$

and the interaction can be completely described by only two of them, Q^2 and x at a given s. Additional variables can be introduced to describe the kinematics:

- $\nu = \frac{P \cdot q}{m_p}$, the energy transfered by the virtual photon to the proton (in the proton rest frame)
- $W^2 = (P+q)^2 \approx sy - Q^2$, the squared centre-of-mass energy of the photon-proton system.

The following naming convention exists for splitting the phase space into two regions. The region with $Q^2 < 1\ GeV^2$ is called Photoproduction (PHP), as the interaction is induced by a $quasi-real$ photon (at $Q^2 = 0$ the photons are “real”, i.e. have zero mass and are therefore transversely polarised). The region with $Q^2 > 1\ GeV^2$ is called $Deep\ Inelastic\ Scattering$(DIS), where the photon is virtual. Sometimes the additional requirement of $W^2 \gg m_p^2$ is stressed in the definition of DIS. In the analysis presented in this thesis it is always fullfilled and therefore omitted in further references.

1.2.2 Structure functions

It has been in 1969 at SLAC [17] when the first DIS experiment took place and the first evidence on the internal structure of the proton appeared. The double differential *ep* cross section measured in DIS, as a function of x and Q^2, is given by the formula [18]:

$$\frac{d^2\sigma^{ep}(x,Q^2)}{dxdQ^2} = \frac{4\pi\alpha^2}{xQ^4}[(1-y)F_2(x,Q^2) + y^2xF_1(x,Q^2)], \tag{1.4}$$

where α is the fine structure constant and F_2, F_1 are electromagnetic structure functions describing the internal structure of the proton. These functions can not be calculated from first principles in perturbative QCD and must be determined experimentally.

We can define

$$F_L(x,Q^2) = F_2(x,Q^2) - 2xF_1(x,Q^2), \tag{1.5}$$

then the cross section 1.4 can be written as

$$\frac{d^2\sigma^{ep}(x,Q^2)}{dxdQ^2} = \frac{2\pi\alpha^2}{xQ^4}[(1+(1-y)^2)F_2(x,Q^2) - y^2F_L(x,Q^2)] \tag{1.6}$$

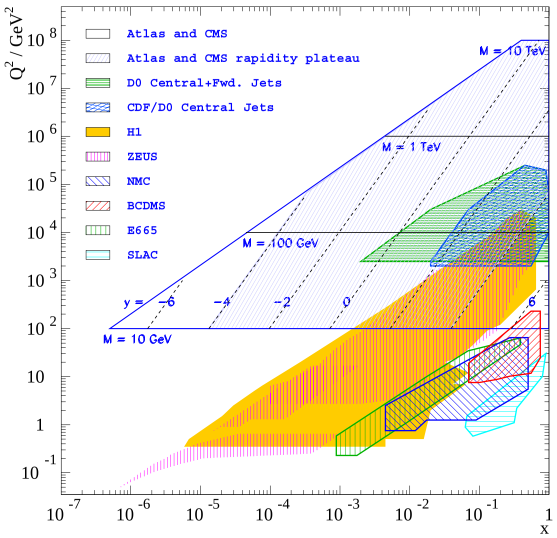

__Figure 1.3:__ The kinematic range in the $\{x, Q^2\}$ plane accessible by fixed target and the HERA experiments ZEUS and H1. The Tevatron (CDF/D0) and the LHC (Atlas/CMS) experiments coverage is given for comparison.

The structure functions measurement at HERA experiments is done in terms of a so called reduced cross section (Fig.1.4)[19]:

$$\sigma_r = F_2 - \frac{y^2}{Y_+}F_L = \frac{xQ^4}{4\pi\alpha^2 Y_+}\frac{d^2\sigma^{ep}(x,Q^2)}{dxdQ^2} \tag{1.7}$$

where $Y_+ = 1 + (1-y)^2$.

In the Quark Parton Model (QPM) [20] the proton is assumed to be constructed of pointlike objects called partons. In the infinite momentum frame of the proton, the proton and parton masses, as well as the intrinsic momenta of the partons (Fermi motion) can be neglected and the Bjorken variable x is interpreted as the fraction of the proton momentum carried by the struck parton ($0 \leq x \leq 1$).

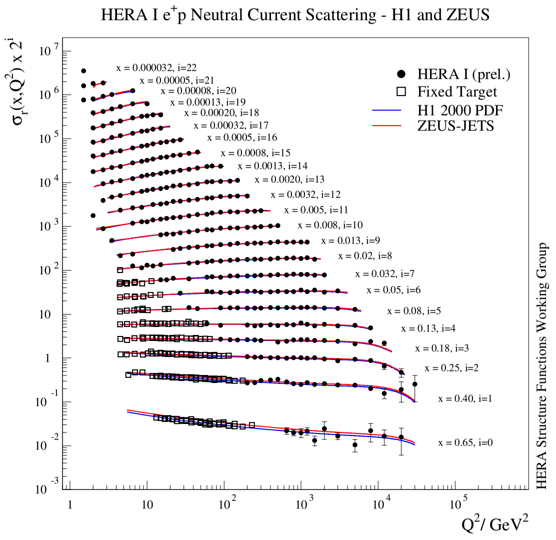

__Figure 1.4:__ The reduced cross section as a function of Q^2, the data from H1 and ZEUS experiments are combined.

The deep inelastic electron-proton scattering is regarded as an incoherent sum of elastic electron-parton scattering processes and the structure function F_2 is expressed in terms of parton density functions, $f_i(x, Q^2)$, which describe the probability of finding a parton i with the momentum fraction x in the proton at a given interaction scale Q^2:

$$F_2(x, Q^2) = \sum_i e_i^2 x f_i(x, Q^2) \tag{1.8}$$

The QPM predicts the property known as *Bjorken scaling*, describing the fact that F_2 does not depend on Q^2 at the moderately high x region measured by SLAC:

$$F_2(x, Q^2) \rightarrow F_2(x) \tag{1.9}$$

The relation between F_1 and F_2 derived for spin$-\frac{1}{2}$ partons and known as the $Callan-Gross$ relation:

$$F_1 = \frac{1}{2x}F_2 \tag{1.10}$$

was confirmed experimentally [21]. The opposite hypothesis that the partons are spin-0 particles predicted $F_1 = 0$ (apparently it was disproved). So, as it was proposed initially by Gell-Mann [22], the spin identification of the partons as fermions became another confirmation of the QPM.

However, the momentum sum rule requires the normalisation:

$$\int_0^1 \sum_i x f_i(x)dx = 1 \tag{1.11}$$

which was not fullfilled. Another issue was seen in the *scaling violation* in the structure function behaviour at low x, when Eq.1.9 is not valid any more. Bosonic neutral partons, called *gluons*, were introduced to explain both features of the data.

Direct information about the gluon distribution in the proton can be obtained from the structure function F_L:

$$F_L \sim xg(x,Q^2), \tag{1.12}$$

however F_L contributes significantly to the cross section only at high y, where the measurements are very difficult [23, 24].

The gluons introduced peculiar features that have made QCD quite a challenging field for the last decades.

1.2.3 Parton Distribution Functions

Parton distribution functions cannot be derived from first principles, but their evolution can be calculated within QCD. The QCD calculations can be done in terms of $log(Q^2)$, as it was done by Dokshitzer, Gribov, Lipatov and independently by Altarelli, Parisi (DGLAP) [25–27] (see Fig. 1.5) or in terms of $log(1/x)$ as suggested by Balitsky, Fadin, Kuraev, Lipatov (BFKL) [28, 29].

The quark and gluon PDFs, $q_i(x,Q^2)$ and $g(x,Q^2)$, can be described by coupled, integro-differential DGLAP equations:

$$\begin{aligned}\frac{dq_i(x,Q^2)}{dln(Q^2)} &= \frac{\alpha_s(Q^2)}{2\pi}\int_x^1 \frac{dy}{y}[\sum_i q_j(y,Q^2)P_{qq}(\frac{x}{y}) + g(y,Q^2)P_{qg}(\frac{x}{y})] \\ \frac{dg(x,Q^2)}{dln(Q^2)} &= \frac{\alpha_s(Q^2)}{2\pi}\int_x^1 \frac{dy}{y}[\sum_i q_j(y,Q^2)P_{gq}(\frac{x}{y}) + g(y,Q^2)P_{gg}(\frac{x}{y})]\end{aligned} \tag{1.13}$$

where $P_{ij}(z)$ are the coefficient functions, so called *splitting functions*, describing the probability of a parton j to emit a parton i with the momentum fraction $z = \frac{x}{y}$ of the parent parton.

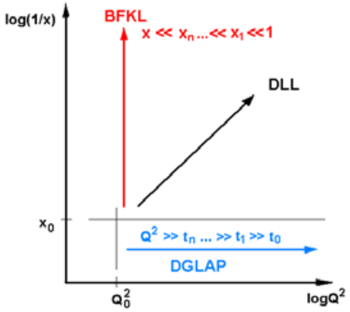

Figure 1.5: *The BFKL and DGLAP evolution sequence. The DLL approximation to DGLAP is also shown.*

The DGLAP equations explain the origin of *scaling violations* for F_2 by gluon bremsstrahlung of the initial quark and quark-antiquark pair production from the initial gluon. The DGLAP Q^2 dynamics is different for different parton contributions. The role of valence quarks is expected to vanish at small values of x, while the role of the sea quarks and gluons is expected to dominate. In QCD the gluons and quarks interact by emitting gluons, so the contribution to F_2 from the gluons is expected to exceed the contribution arising from the sea quarks at low x and high Q^2. The steep behaviour of F_2 observed by the HERA experiments and described by DGLAP evolution equations can be also given in terms of a parameter λ:

$$F_2 \sim x^{\lambda(Q^2)}, \tag{1.14}$$

where $\lambda(Q^2) \sim log(Q^2)$ for $(Q^2 > 1\ GeV^2)$ (Fig. 1.6).

The F_2 structure function gives a way to describe the gluon distribution through the following relation:

$$\frac{dF_2(x,Q^2)}{dlnQ^2} \sim xg(x,Q^2) \tag{1.15}$$

The DGLAP equations are derived in a so called leading logarithm approximation (LLA), in which terms of the form $(\alpha_s lnQ^2)^n$ are summed to all orders

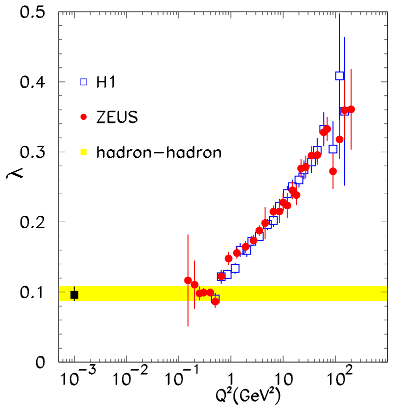

Figure 1.6: The values of λ extracted from Eq.1.14 plotted versus Q^2.

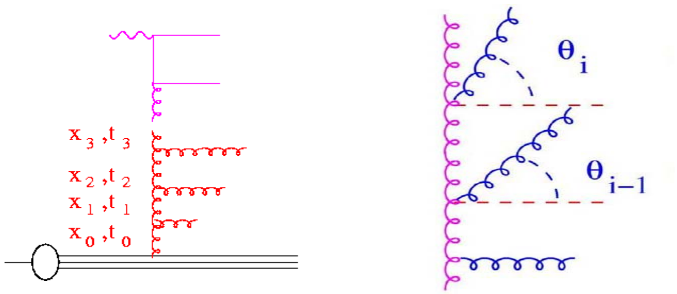

Figure 1.7: Left: DGLAP and BFKL, Right: CCFM cascade ordering.

(for finite Q^2 and x). At small values of x the DGLAP equations get the main contribution from the terms $lnQ^2 ln(1/x)$, and called Double Leading Log (DLL) approximation.

In the BFKL equation terms of $(\alpha_s ln\frac{1}{x})^n$ are summed to all orders independently of lnQ^2:

$$\frac{df(x,k_t^2)}{dln(\frac{1}{x})} = \int dk_t'^2 K(k_t^2, k_t'^2) f(x,k_t^2) = \lambda f(x,k_t^2) \tag{1.16}$$

The difference from DGLAP is that BFKL operates with the unintegrated gluon distribution, $f(x,k_t^2)$, from which the usual gluon distribution is obtained by integrating over k_t^2:

$$xg(x,Q^2) = \int_0^{Q^2} \frac{dk_t^2}{k_t^2} f(x,k_t^2). \tag{1.17}$$

The equation 1.16 predicts the steep power-law behaviour of the gluon distribution function:

$$xg(x,Q^2) \sim f(Q^2) x^{-\lambda}, \tag{1.18}$$

where $\lambda \approx 0.5$ for $\alpha_s = 0.18$.

An alternative approach developed by Ciafaloni-Catani-Fiorani-Marchesini (CCFM) [30, 31] incorporates both $ln\frac{1}{x}$ and lnQ^2 terms and unifies the DGLAP and BFKL evolution (Fig. 1.7). It is based on the idea of coherent gluon radiation corresponding to the angular ordering of gluons.

An effect of gluon recombination ($2g \rightarrow 1g$) is anticipated to become dominant in a region of small values of x and small values of Q^2. It is called "saturation" because the gluon density is expected to level off and stop growing at decreasing x at fixed low Q^2. The anticipation is motivated by the unitarity requirement (i.e. probability ≤ 1). This process was introduced as a quadratic correction to BFKL by Gribov-Levin-Ryskin (GLR) [32].

Since PDFs can not be calculated from first principles in pQCD, they are extracted from fits to the data. Parton densities are parametrised as a function of x at some starting scale Q_0^2 using a polynomial ansatz (e.g. $xg = Ax^{-\lambda}(1-x)^{-\eta}(1+\epsilon x+\gamma x)$ [33]). Their evolution to other values of Q^2 is performed using the DGLAP equations, and the free parameters of the analytic formula at Q_0^2 are determined from a global fit to F_2 and other data in the entire (x, Q^2) plane.

Parameterisations of PDFs are provided by many groups, such as CTEQ [34], MRST [35], GRV [36, 37] (see [38]). They differ in the data used in the fit and details of the analysis, such as LO and NLO approximation of DGLAP equations, the input ansatz, the Q_0^2 starting scale, the value of Λ_{QCD} etc. The H1 and ZEUS Collaborations have also performed (NLO) fits [39, 40]. The flavour decomposition of the proton structure function F_2 into valence (u and d) quarks, see quarks and gluons at $Q^2 = 10\ GeV^2$ obtained by ZEUS and H1 and fit to the combined data set is presented in Fig. 1.8, 1.9. In accordance with the expectation of a gluon-driven F_2, the gluons rise steeply at low x. When Q^2 increases, the steep rise of gluons toward low x also increases.

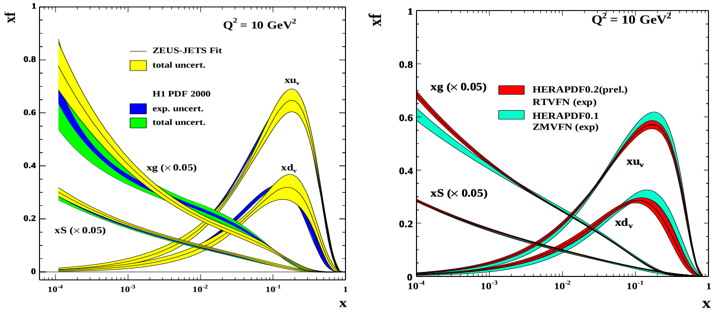

Figure 1.8: *The Parton Distribution Functions extracted from the H1 and ZEUS data at* $Q^2 = 10\,GeV^2$.

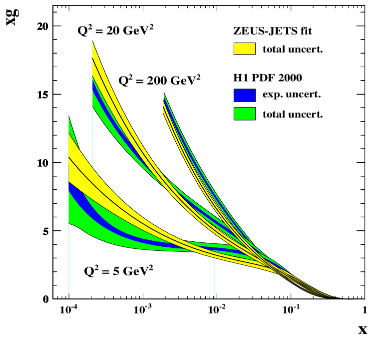

Figure 1.9: *The gluon PDFs extracted from the H1 and ZEUS data at three values of* $Q^2 = 5,\ 20,\ 200\,GeV^2$.

1.2.4 Generalized Parton Distributions

The PDFs one can extract from inclusive processes encode the distribution of the longitudinal momentum carried by quarks, antiquarks and gluons within a fast moving proton. Another important piece of information, that is missing in the picture, is how the partons are distributed in the plane transverse to the direction in which the proton is moving. In recent years it has become clear that this information can be obtained from appropriate exclusive scattering processes and encoded in the so called Generalized Parton Distributions (GPDs) [41].

The interest of a wide community in GPDs was raised in 1996, when the nonforward nature of the parton distributions entering virtual Compton scattering [41] and meson production [42, 43] was emphasized by Ji and by Radyushkin [44], and when Collins et al. [45] provided a proof of factorisation of meson electroproduction in diffractive and nondiffractive kinematics.

The potential of GPDs to study hadron structure in three dimenstions (instead of the one-dimensional projection inherent in the ordinary parton densities) has been fully recognized with the work [46] on the impact parameter representation.

The description of hard scattering processes is predominantly based on collinear factorization, the resummation of logarithms $(\alpha_s log Q^2)^n$ to all orders in n by DGLAP evolution. As it was mentioned in Section 1.2.3 in the small-x limit terms with large $log\frac{1}{x}$ appear in loops. Their perturbative treatment can be performed via schemes with different accuracy of the resulting scattering amplitudes, e.g. such as leading power in $1/Q^2$, resummed leading logarithms $(\alpha_s log\frac{1}{x})^n$, resummed leading double logarithms $(\alpha_s log\frac{1}{x} log Q^2)^n$. An important ingredient in this context are k_T dependent, or unintegrated parton distributions, where k_T denotes the transverse momentum of the partons entering the hard scattering. Simple definition of the k_T dependent gluon density is through

$$xg(x,\mu^2) = \int^{\mu^2} \frac{d\vec{k}^2}{\vec{k}^2} f(x,\vec{k}^2), \tag{1.19}$$

but there are more sophisticated versions taking into account k_T effects to different accuracy [47]. It is worth noting that the usual collinear factorisation framework also partly takes into account finite k_T of partons already in two-loop diagrams. Conversely, using only the one-loop hard scattering coefficient together with the unintegrated gluon density takes into account part of the two-loop corrections of the collinear framework.

Whether an appropriate generalization to k_T dependent GPDs as suggested in [48] or a collinear approach with GPDs provide the correct framework to describe physics in a given range of Q^2 and small x remains to be understood.

The diffractive processes (see Sect. 1.3), if pQCD can be applied, can be described via an exchange of two gluons. For simplicity both gluons are assumed to carry equal momentum $x_1 = x_2$. In general case the gluons with $x_1 \neq x_2$ are called "skewed", and the introduction of "skewed" gluons in pQCD calculations - the effect of "skewness". The GPDs present the only framework where effects of skewness are explicitely taken into account (see Chapter 2). An example of the GPDs use in exclusive vector meson production will be discussed in Sections 2.2.1, 2.2.3.

1.2.5 Relation between ep and γ^*p scattering

In the one photon exchange (Born) approximation the electron-proton scattering may be regarded as a scattering of the virtual photon off the proton. The inclusive double differential ep cross section may be described in terms of two absorption cross sections, $\sigma_T^{\gamma^*p}$ and $\sigma_L^{\gamma^*p}$, corresponding to the transverse and longitudinal polarisations of the virtual photon:

$$\frac{d^2\sigma^{ep}}{dQ^2dy} = \Gamma_T {\sigma_T}^{\gamma^*p} + \Gamma_L {\sigma_L}^{\gamma^*p} = \Gamma_T({\sigma_T}^{\gamma^*p} + \epsilon {\sigma_L}^{\gamma^*p}), \tag{1.20}$$

where Γ_L and Γ_T are the longitudinal and transverse photon fluxes [49]:

$$\begin{aligned} \Gamma_L(y,Q^2) &= \tfrac{\alpha}{2\pi Q^2}\tfrac{2(1-y)}{y}, \\ \Gamma_T(y,Q^2) &= \tfrac{\alpha}{2\pi Q^2}\left(\tfrac{1+(1-y)^2}{y} - \tfrac{2(1-y)}{y}\tfrac{Q^2_{min}}{Q^2}\right) \end{aligned} \tag{1.21}$$

where

$$Q^2_{min} = m_e^2 \frac{y^2}{1-y} \tag{1.22}$$

is the minimum of Q^2 kinematically allowed and ϵ is the ratio of the fluxes ($0 < \epsilon < 1$):

$$\epsilon = \frac{\Gamma_L}{\Gamma_T} = \frac{2(1-y)}{1+(1-y)^2} \tag{1.23}$$

The total γ^*p cross section:

$$\sigma^{\gamma^*p} = \sigma_T^{\gamma^*p} + \sigma_L^{\gamma^*p} \tag{1.24}$$

is related to the inclusive ep cross section as follows:

$$\frac{d^2\sigma^{ep}}{dQ^2dy} = \Gamma_T\left(\frac{1+\epsilon R}{1+R}\right)\sigma^{\gamma^*p}(y,Q^2) \tag{1.25}$$

where R is the ratio of cross sections for the longitudinally and transversely polarised virtual photons:

$$R = \frac{\sigma_L^{\gamma^*p}}{\sigma_T^{\gamma^*p}} \tag{1.26}$$

The proton structure functions are related to γ^*p cross sections by the following relations:

$$\begin{aligned} F_2(x,Q^2) &= \tfrac{Q^2}{4\pi^2\alpha}\sigma^{\gamma^*p}(x,Q^2), \\ F_L(x,Q^2) &= \tfrac{Q^2}{4\pi^2\alpha}\sigma_L^{\gamma^*p}(x,Q^2) \end{aligned} \tag{1.27}$$

1.3 Diffraction

There is no single precise definition of diffraction. In high energy physics the word *diffraction* is used to describe processes in which the quantum numbers of vacuum (e.g. (-1)^l) are exchanged. Many diffractive reactions in hadron-hadron and photon-hadron reactions are successfully described in terms of Regge phenomenology with the exchange of a virtual particle called *Pomeron* (P) [50]. The Regge approach proved to be a good phenomenological concept, however giving no clue to understanding neither of the nature of diffractive processes nor of the structure of the Pomeron. At HERA, Diffractive DIS and Exclusive Vector Meson production opened a possibility of studying diffraction in terms of perturbative QCD, i.e. quarks and gluons.

1.3.1 Hadron-hadron collisions

In hadron-hadron collisions diffractive reactions can be classified into three classes (Fig. 1.10) depending on the final states of the outgoing particles:

- elastic scattering ($AB \to AB$)
- single dissociation ($AB \to XB$)
- double dissociation ($AB \to XY$)

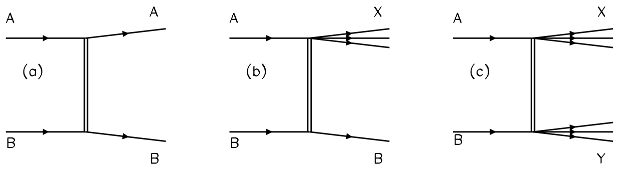

Figure 1.10: *The classification of diffractive interactions: (a) elastic, (b) single dissociation, (c) double dissociation.*

1.3.1.1 Regge Phenomenology

In 1957, starting from a simple spherically symmetric potential with discrete energy levels k and angular momentum l and then going to a complex value of l, Regge [50, 51] obtained an interpolating function $a(l, k)$, which reduced to $a_l(k)$, for $l = 0,1,2,...$. For Yukawa type potentials the singularities of $a(l, k)$ turned out to be what is called *Regge poles* [52], located at values defined by a relation of the kind $l = \alpha(k)$, where $\alpha(k)$ is a function of the energy called *Regge trajectory*. The extension of Regge's technique to high-energy particle physics began in the early 1960-s [53–55] and was followed by more than 300 articles already by 1963 [56]. Inspite of many difficulties, such as the absence of scattering amplitudes and the impossibility to study it's analytical properties, the Regge pole idea survived and kept being quite descriptive in a very simple form, where each pole contributes to the scattering amplitude a term which behaves asymptotically (i.e. for $s \to \infty$ and t fixed, where t is the 4-momentum transfer between A and B, Fig. 1.10) as

$$\lim_{s \to \inf} A(s,t) \sim s^{\alpha(t)}, \tag{1.28}$$

where $\alpha(t)$ is the Regge trajectory, assumed to be linear in t:

$$\alpha(t) = \alpha(0) + \alpha' t \tag{1.29}$$

The intercept, $\alpha(0)$, and the slope, α', of the trajectory are determined experimentally.

The forward differential cross section of the AB scattering is expressed by the following relation:

$$\left.\frac{d\sigma_{el}}{dt}\right|_{t=0} \sim \frac{|A(s,t)|^2}{s^2} \sim e^{b(s)t}\left(\frac{s}{s_0}\right)^{2(\alpha(t)-1)}, \tag{1.30}$$

where $b(s)$ is the parameter, which can be related to the transverse size of the interaction region similar to optical diffraction.

The total cross section of the process can be related to the forward ($t = 0$) elastic cross section using the optical theorem [57]:

$$\sigma_{AB \to X} \sim Im A(AB \to AB, s, t = 0), \tag{1.31}$$

hence the energy dependence of the total hadron-hadron cross sections may be derived within the Regge theory and gives:

$$\sigma_{tot} \sim s^{\alpha(0)-1}, \tag{1.32}$$

It has been an exciting step forward of Donnachie and Landshoff [10–12], when they did their work on bringing together various publications on hadron-hadron interactions and unifying the style of the parameterisation of the cross sections.

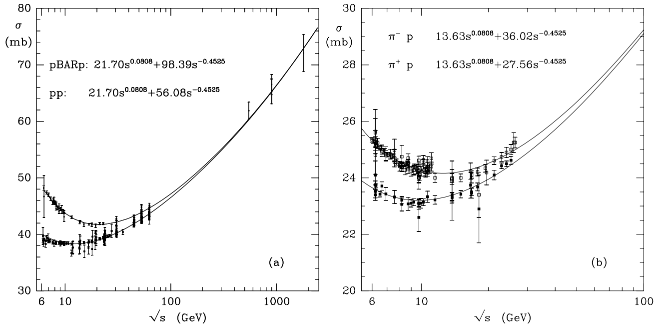

Figure 1.11: *Total cross section for scattering as a function of centre of mass energy. Lines present the results of the fits performed by DL .*

Donnachie and Landshoff analysed available hadron-hadron collisions data and performed a global fit of the form:

$$\sigma_{tot} = Xs^{\alpha_{R(0)}-1} + Ys^{\alpha_{P(0)}-1}, \tag{1.33}$$

where the first term corresponds to the exchange of all Reggeons dominating at low energies and the second term accounts for the Pomeron exchange at higher energies. The results of the fit are shown in Figure 1.11. DL have also performed fits to the $|t|$ dependence of pp and $p\bar{p}$ cross sections following the parametrisation (1.30). The result of the fits is given by the following trajectory:

$$\alpha_P(t) = 1.08 + 0.25t, \tag{1.34}$$

where t is given in GeV^2, is often referred to as $soft$ Pomeron.

1.3.2 Photon-proton collisions

A typical signature for a diffractive event at high energies is a *Large Rapidity Gap* (LRG). Schematically it is shown in Fig. 1.12.

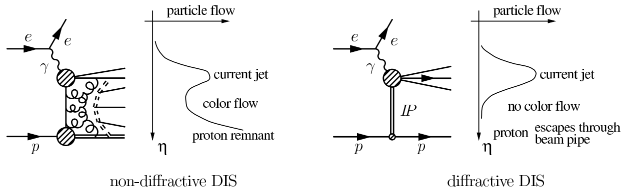

Figure 1.12: *Schematic presentation of the energy(particle) flow for a non-diffractive DIS event and(left) and for a diffractive DIS event with LRG (right).*

1.3.2.1 Vector Dominance Model

The measurements of photon-hadron and hadron-hadron collisions turned out to be similar in the total cross section energy dependence [58]. This similarity was interpreted as a manifestation of a hadronic structure of the photon and gave rise to the Vector Dominance Model (VDM), which states that a photon is a superposition of a QED photon and a hadronic component. The hadronic component arises due to quantum fluctuations ruled by the uncertainty principle. It should be mentioned here that in the original VDM the hadronic component is assumed to be a superposition of light vector mesons ($V = \rho, \omega, \phi$). In the Generalised VDM (GVDM) [59], when $Q^2 \gg M_V^2$, higher mass states are included as well.

If the fluctuation time is large compared to the interaction time, then the photon fluctuates into the vector meson long before it hits the proton and the hadron-hadron type of interaction occurs between the vector meson and the proton. Hence, a combination of the VDM and Reggy phenomenology can be applied to describe physics processes at HERA.

Photon-proton interactions can be classified into four processes:

- elastic scattering ($\gamma^* p \rightarrow Vp$) - the photon fluctuates into a vector meson, which scatters quasi-elastically off the proton
- photon dissociation ($\gamma^* p \rightarrow Xp$) - the photon fluctuates into a vector meson, which dissociates into a higher mass state, X, while the proton stays intact (Fig.1.13)
- proton dissociation ($\gamma^* p \rightarrow VY$) - the photon fluctuates into a vector meson, which remains intact, while the proton dissociates into a higher mass state, Y

- double dissociation ($\gamma^* p \rightarrow XY$) - the photon fluctuates into a vector meson, which dissociates into a higher mass state, X, and the proton dissociates into a higher mass state, Y

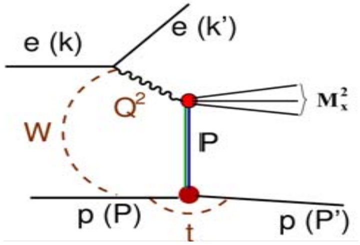

Figure 1.13: Kinematics of diffractive $\gamma p \rightarrow Xp$ reaction.

1.3.3 Soft and hard Pomeron

One of the discoveries made at HERA is the change in the character of the inclusive cross section rise at higher values of the Q^2. The photon-proton scattering cross section, $\sigma_{tot}^{\gamma p}$ at $Q^2 = 0$, was found to follow a power law dependence on the centre of mass energy squared, W^2, in good agreement with Regge theory (Eq. 1.32):

$$\sigma_{tot}^{\gamma p} \sim (W^2)^{\alpha_P(0)-1}, \tag{1.35}$$

with the intercept of the soft Pomeron, $\alpha_P(0) = 1.0808$.

The total photon-proton cross section for virtual photons, $\sigma_{tot}^{\gamma^* p}$, measured at HERA for $Q^2 \geq 1\ GeV^2$ exhibits a steeper rise with energy at higher energies, as shown in Fig. 1.14. Such a behaviour needs an effective Pomeron intercept higher than that of the soft Pomeron (Fig. 1.14(right)). In addition, it also provides an indication for the perturbative nature of the Pomeron. The high energy behaviour of total cross sections is related to the low x behaviour of gluon densities in the proton. From Eq. 1.27 and for $x \sim W^{-2}$, the relation $F_2 \sim x^{-\lambda}$ implies $\sigma_{tot}^{\gamma^* p} \sim W^{2\lambda}$, where $\lambda = \alpha(0) - 1$. In particular, the solution of the BFKL equation yields the slope $\lambda \approx 0.5$, which in the Regge formalism may be translated into the intercept, $\alpha_P(0) = 1 + \lambda \approx 1.5$. The corresponding Pomeron trajectory is often referred to as *hard* or $BFKL$ Pomeron.

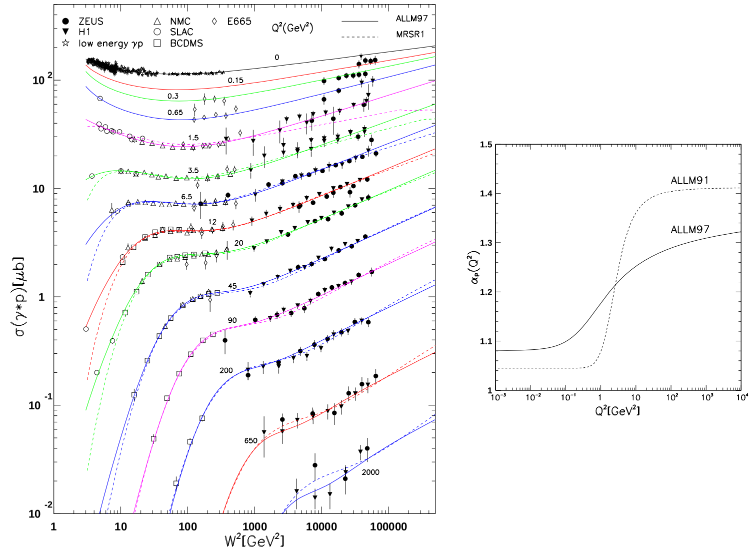

Figure 1.14: (left)Total γp and $\gamma^* p$ cross sections as a function of the centre of mass energy squared, W^2, for different values of Q^2, and (right) the Pomeron intercept, $\alpha_P(0)$, as a function of Q^2, obtained from ALLM fits.

1.3.4 Vector Meson production

Exclusive Vector Meson production belongs to a realm of diffractive processes. The HERA experiments showed that just as in inclusive diffraction there is a soft-to-hard transition in exclusive processes.

Exclusive diffractive reactions are also called elastic (see Eq. 1.36). This terminology is due to the underlying two-body scattering process $\gamma^{(*)}p \rightarrow Vp$, in which the proton stays intact and the vector meson holds the quantum numbers of the incident $\gamma^{(*)}$.

$$e(k)p(P) \rightarrow e(k)V(v)p(P), \tag{1.36}$$

here $V = \{\rho, \omega, \eta, J\psi, \psi', \Upsilon\}$ and k, k', P, P', and v are the four-momenta of the incident lepton (positron or electron), scattered lepton, incident proton, scattered proton and vector meson, respectively. The new kinematic variable is $t = (P - P')^2$, the squared four-momentum transfer at the proton vertex (see Fig. 1.15).

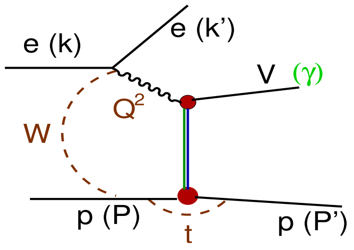

Figure 1.15: Kinematics of elastic Vector Meson production.

The variable $|t|$ can be defined for diffractive processes and requires a specific detector design in order to be measured directly. A good approximation to $|t|$ is the vector meson transverse momentum squared p_T^2.

The photoproduction (Fig. 1.16) of light vector mesons (ρ, ω, ϕ) is well described by the Regge theory with the soft Pomeron exchange: the cross section rises slowly with energy: W^δ with $\delta \approx 0.2 - 0.3$.

The t-dependence of the cross sections exhibits an exponential behaviour: $e^{-b|t|}$ with $b \approx 10\ GeV^{-2}$. The observed $b(W)$ dependence known as *shrinkage* is described with the Pomeron intercept $\alpha' = 0.25\ GeV^{-2}$:

$$b = b_0 + \alpha' ln\frac{W}{W_0}, \tag{1.37}$$

where b_0 is the t-slope at the energy W_0.

In [60] the t-slope b has been related to the transverse size of the target. In the case considered in this thesis (exclusive Υ meson production) and in a more general case for the vector meson production at high $Q^2 + M_V^2$, the target content is dominated by the gluons, hence the "transverse size of the traget" obtains the meaning of the distance from the $q\bar{q}$ pair coupling to gluon measured to the geometrical center of the target (in the transverse plain). The size of the target can be also estimated via a naive relation based on the uncertainty principle:

$$b \approx (\frac{r}{\hbar c})^2. \tag{1.38}$$

The b value measured in experiment opens an interplay of transverse scales. The first one coming from the transverse size of the vector meson, the second one coming from the transverse size of the target.

$$b_{meas} = b_V + b_{target}. \tag{1.39}$$

At high values of $Q^2 + M_V^2$, when the vector meson transverse size b_V becomes small, and $b_V \ll b_{target}$, one should expect the "scaling" behaviour of the b_{meas}:

$$b_{meas} = b_{target} \neq f(Q^2 + M_V^2). \tag{1.40}$$

For the heavier vector mesons ($J/\psi, \psi'$) in PHP and DIS and for the light vector mesons in DIS the cross section exhibits a steeper rise with energy: W^δ with $\delta \approx 0.7 - 1.1$, consistent with expectations from pQCD. The slope (Fig. 1.17(left)) of the exponential t dependence is of the order $b \approx 5\ GeV^{-2}$ and the shrinkage, $b(W)$, is described with the Pomeron α-slope $\alpha' \approx 0.1\ GeV^{-2}$.

The ratio of the cross sections for the longitudinally and transversely polarised photons (Fig. 1.17(right)), $R = \frac{\sigma_L}{\sigma_T}$, rises with Q^2.

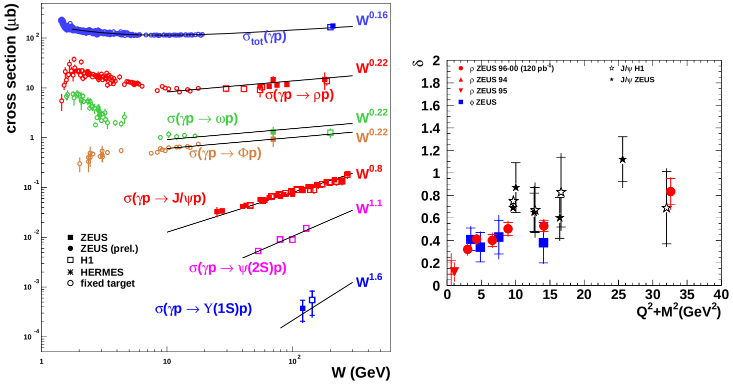

Figure 1.16: Vector meson production at HERA: (left) γp cross section photoproduction, (right) extracted energy slope δ in photo- and electroproduction.

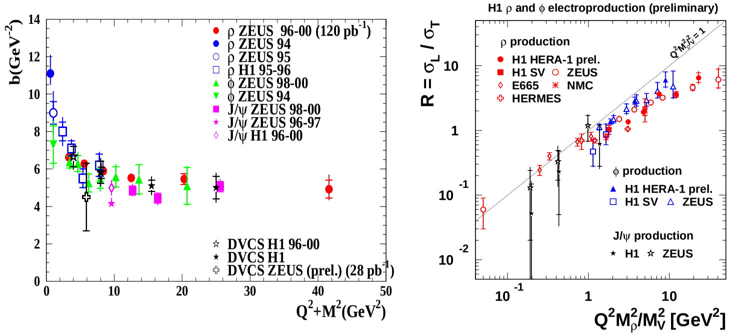

Figure 1.17: (left) t-slope dependence on the scale, (right) ratio of the cross section obtained for longitudinal and transversely polarised photons.

Chapter 2

Theory of Υ meson production

In this chapter production mechanisms are being discussed for the mesons consisting of heavy quarks. The models described in this chapter will be used for comparison with the measured Υ meson cross section in Chapter 13. More detailed information on the Heavy Vector Meson production and relevant QCD models can be found in [61].

2.1 Rigorous QCD calculations

The open production of heavy quarks at HERA can be described in LO QCD in terms of the boson-gluon fusion process (BGF) which is depicted in Fig. 2.1. Theory calculations based on pQCD use a factorisation ansatz in order to extract cross section predictions which can be compared with experimental data. In these factorisation approaches, the cross section is composed of a non-perturbative part, which is given by the parton distributions of the initial state particles f_j^p, the perturbative evolution according to the evolution equation and a perturbative hard scattering process, i.e. the photon-parton cross section $\hat{\sigma}^j$, which is calculable in perturbative QCD:

In addition, to predict production cross sections for heavy hadrons and/or other exclusive final states, the fragmentation of the heavy quark into a hadron and additional final state particles must be considered. Based on the assumption of universality, the non-calculable non-perturbative parts, i.e. usually the parton distributions and fragmentation functions are taken from measurements of other processes at HERA or other experiments.

For heavy quark processes the calculation of the "hard" matrix element using perturbative QCD is possible due to the high mass of the quarks. Already the charm quark mass provides an energy scale, which allows perturbative expansion. Other possible scales are the photon virtuality Q^2 (for DIS) or the transverse

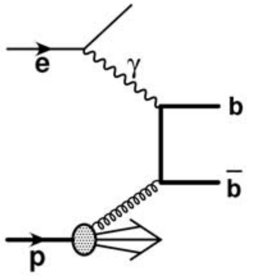

Figure 2.1: Diagram of the process of Boson-Gluon Fusion in ep-scattering.

momentum p_T of the final state particles (or jets).

It is not crucial for the calculations whether the $q\bar{q}$ forms a bound state or not. Hence, the same theoretical approach can be applied both to *open* and to *closed* heavy flavour quark production.

Moreover, the difference in the description of the elastic and inelastic production mechanisms almost vanishes in the case of heavy vector meson production (Fig. 2.2). An approach of non-Relativistic QCD calculations has been developed primarily for "inelastic" processes, but also can be applied to the exclusive Υ production at HERA [62].

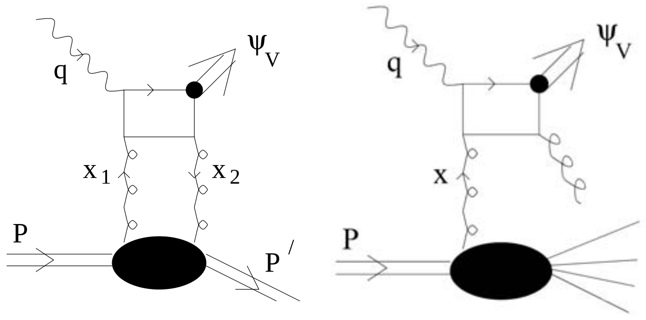

Figure 2.2: QCD representation of elastic (left) and inelastic (right) production of a vector meson V.

2.1.1 Non-Relativistic QCD

In order to make use of perturbative methods, one must first separate the short-distance/high-momentum, perturbative effects from the long-distance/low-momentum, nonperturbative effects, a procedure, which is known as "factorisation". One convenient way to carry out this separation is through the use of the effective field theory non-Relativistic QCD (NRQCD) [63]. NRQCD is expected to reproduce full QCD accurately at momentum scales of order mv and smaller, where v is the typical heavy-quark velocity in the bound state in the centre-of-the-mass (CM) frame. ($v^2 \approx 0.3$ for charmonium, and $v^2 \approx 0.1$ for bottomonium).

The inclusive cross section for the production of the quarkonium H can be written as a sum of products of NRQCD matrix elements and short-distance coefficients:

$$\sigma[H] = \sum_n \sigma_n(\Lambda)(O_n^H(\Lambda)) \tag{2.1}$$

Here, Λ is the ultraviolet cutoff of the effective theory, the σ_n are short-distance coefficients, and the $< O_n^H >$ are vacuum-expectation values of four-fermion operators in NRQCD. The size of the σ_n coefficient depends on its order in α_s, colour factors, and dimensionless kinematic factors, such as m^2/p_T^2.

The short-distance coefficients $\sigma_n(\Lambda)$ in Eq. 2.1 are essentially the process-dependent partonic cross sections to make a $q\bar{q}$ pair, convoluted with parton distributions if there are hadrons in the initial state. The $q\bar{q}$ pair can be produced in a *colour-singlet* state or in a *colour-octet* state. Its spin state can be singlet or triplet, and it also can have orbital angular momentum. The short-distance coefficients are determined by matching the square of the production amplitude in NRQCD to full QCD. Because the scale of the $q\bar{q}$ production is of order m^2 or greater, this matching can be carried out in perturbation theory.

The NRQCD factorisation approach is also called the "colour-octet model“, because colour-octet terms are expected to dominate in some situations, such as J/ψ production at large p_T in hadron colliders. However, there are also situations in which colour-singlet terms are expected to dominate, such as J/ψ production in continuum e^+e^- annihilation at the B factories. It should be noted that the NRQCD factorisation is not a model, but a rigorous consequence of QCD in the limit $\Lambda_{QCD}^2/m^2 \to 0$.

2.1.2 Colour Singlet Model (CSM)

The colour-singlet model (CSM) was first proposed shortly after the discovery of the J/ψ. The initial applications were to η_c and χ_c production through two-gluon fusion [64]. Somewhat later, the CSM was applied to the production of J/ψ and η_c in B-meson decays [65–67] and to the production of J/ψ plus a gluon [68] through two-gluon fusion and photon-gluon fusion. The CSM was taken seriously until around 1995, when experiments at the Tevatron showed that it underestimates the cross section for prompt charmonium production in $p\bar{p}$ collisions by more than one order of magnitude. An extensive review of the colour-singlet model can be found in [61].

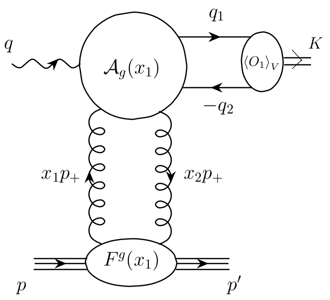

Figure 2.3: *NRQCD description of elastic vector meson production. The amplitude $A_g(x_1)$ can be calculated within pQCD, the matrix element $< O >_V$ is a scalar factor derived from vector meson decay width (in this specific case the colour singlet matrix only counts and is proportional to the vector meson decay width Γ_{ee}), $F^g(x_1)$ is the gluon density function and is also taken from experiment.*

The colour-singlet model can be obtained from the NRQCD factorisation formula in Eq. 2.1 by dropping all of the colour-octet terms and all but one of the colour-singlet terms. The term that is retained is the one in which the quantum numbers of the $q\bar{q}$ pair are the same as those of the quarkonium. The CSM production matrix elements are related to the corresponding decay matrix elements by the vacuum saturation approximation, and, so, they can be determined from annihilation decay rates. Thus, the CSM gives absolutely normalised predictions for production cross-sections. However, for the states with nonzero orbital angular momentum the CSM leads to infrared divergences that cancel only when one includes colour-octet terms whose matrix elements are of the same order in v. Thus, the CSM is theoretically inconsistent and the term is disfavoured in publications.

2.1.3 IKS calculations

A combined approach of nonrelativistic QCD with the collinear factorisation is developed by Ivanov, Krasnikov, Szymanowski (IKS) [62]. The physics behind collinear factorisation is the separation of scales. The mass of the heavy quark, m, provides a hard scale. A photon fluctuates into the heavy quark pair at small transverse distances $\sim 1/m$, which are much smaller than the ones $\sim 1/\Lambda$ related to any nonperturbative hadronic scale Λ. It was shown by IKS, that it is possible to construct a model free description of heavy meson photoproduction which is free of any high energy approximation. The calculations have been performed at next-to-leading order, reducing this way the scale dependence of the calculations. The latter is especially important at high energies, since in this case (small x region) the dependence of the gluon distribution on the scale is very strong.

The IKS cross section calculations for $\gamma p \rightarrow \Upsilon(1S)p$ will be discussed in comparison with the measurement in Chapter 13.

2.2 Colour Dipole Approach

A $q\bar{q}$ pair can be viewed as a dipole with colour charges at the poles. This representation served as the basis to a so called Colour Dipole Approach (CDA). The CDA is based on the factorisation of the interaction process description into three steps (see Fig. 2.4):

- the photon fluctuates into a $q\bar{q}$ colour dipole ($\gamma^* \rightarrow q\bar{q}$),
- the $q\bar{q}$ pair scatters off the proton,
- after the interaction the $q\bar{q}$ pair forms a vector meson bound state ($q\bar{q} \rightarrow V$).

The amplitude for the $\gamma^* p \rightarrow Vp$ process can be written as:

$$A(\gamma^* p \rightarrow Vp) = \psi_{q\bar{q}}^{\gamma^*} \otimes \sigma_{(q\bar{q})p} \otimes \psi_{q\bar{q}}^{V}, \qquad (2.2)$$

where $\psi_{q\bar{q}}^{\gamma^*}$ and $\psi_{q\bar{q}}^{V}$ are the photon and the vector meson wave-function, $\sigma_{(q\bar{q})p}$ is the dipole-proton cross section and $\otimes$ stands for the convolution. Since the $(q\bar{q})p$ scattering proceeds by an exchange of a two-gluon state, the process is sensitive to the square of the gluon density $xg(x,\bar{q}^2)$ in the proton. Writing it explicitly, the leading order formula is [69] :

$$\frac{d\sigma}{dt}(\gamma^* p \rightarrow Vp)|_{t=0} \sim A_V \alpha_s^2(\bar{q}^2) \frac{|xg(x,\bar{q}^2)|^2}{Q^6}, \qquad (2.3)$$

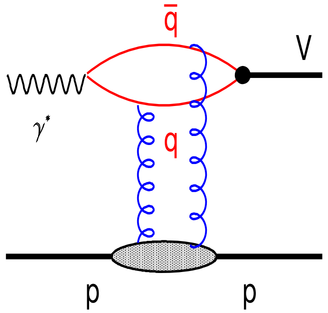

Figure 2.4: *Vector Meson production via colour dipole interaction with the proton. In the proton rest frame the time of the $q\bar{q}$ fluctuation $\tau_{q\bar{q}} \sim \frac{2E_\gamma}{Q^2+M_v^2}$ is bigger than the time of the γp interaction, which is of the order $\tau \sim R_{proton}$, where R_{proton} is radius of the proton.*

where $xg(x,\bar{q}^2)$ is the gluon PDF and $\bar{q}^2$ is the scale at which the gluon densities and α_s are probed. The scale choice varies in different CDA models. In the Ryskin model [70] the scale for the exclusive vector meson production is given by:

$$\bar{q}^2 = \frac{Q^2 + M_V^2 + |t|}{4} \qquad (2.4)$$

The Q^2 and W dependence of the cross section can be derived from Eq. 2.3. The $|t|$ dependence is assumed to follow an exponential form, $e^{-b|t|}$, at small values of $|t|$ ($|t| \lesssim 1\ GeV^2$).

In this framework the following characteristics of the vector meson production can be expected:

- The cross section rises with W:

$$\sigma(W) \approx |xg(x,Q^2)|^2 \approx |x^{-\lambda}|^2 \approx (\frac{1}{W^2})^{-2\lambda} = W^{4\lambda}, \qquad (2.5)$$

  which gives $W^{0.8}$ for $\lambda = 0.2$ (for J/ψ, $Q^2 + M_V^2 \approx 10\ GeV^2$), and $W^{1.2}$ for $\lambda = 0.3$ (for $\Upsilon(1S)$, $Q^2 + M_V^2 \approx 90\ GeV^2$),

- The Q^2 dependence for the longitudinal cross section is of the form: $\sim (Q^2)^{-3}$. Due to contributions from α_s, gluon distributions, and the vector meson wave function this dependence can be reduced to $(Q^2)^{-2.5}$

- $b \approx 4 - 5GeV^{-2}$. For high values of the scale, the exponential dependence of the cross section, $e^{-b|t|}$, is described with a universal b slope, for all vector mesons. Since the transverse size of the $q\bar{q}$ dipole is expected to be small, the dominant contribution to the slope originates from the transverse distribution of gluons in the proton.

- $b(W) = const$, no or little shrinkage (dependence of the t-slope on W). In pQCD the dependence of the cross section on W and t factorises with no dependence of the t-slope on energy, $b(W)$. However, little dependence arises from NLO effects [71]

- At higher values of the scale, all vector mesons should be described by a common wave-function [18]. Hence, in the limit $Q^2 \gg M^2$ a flavour independent production mechanism is expected. The production rates for different vector mesons are expected to obey the flavour symmetry (Table 2.1). From wave-function and charge considerations the cross section ratios can be written as:

$$\sigma_\rho : \sigma_\omega : \sigma_\phi : \sigma_{J/\psi} : \sigma_\Upsilon = 9 : 1 : 2 : 8 : 2. \tag{2.6}$$

V	$\lvert V >= \lvert q\bar{q} >$	$\lvert e_q\rvert^2$	e_V^2	$\epsilon_V = e_V^2/e_\rho^2$
ρ	$1/\sqrt{2}(\lvert u\bar{u} > -\lvert d\bar{d} >)$	$[1/\sqrt{2}(2/3 - (-1/3))]^2$	1/2	1
ω	$1/\sqrt{2}(\lvert u\bar{u} > +\lvert d\bar{d} >)$	$[1/\sqrt{2}(2/3 + (-1/3))]^2$	1/18	1/9
ϕ	$\lvert s\bar{s} >$	$[-1/3]^2$	1/9	2/9
J/ψ	$\lvert c\bar{c} >$	$[2/3]^2$	4/9	8/9
Υ	$\lvert b\bar{b} >$	$[-1/3]^2$	1/9	2/9

Table 2.1: *The linear combinations of the quark components for different vector meson wave-functions, the squared sum of their charges and the relative ratio w.r.t the ρ meson.*

In the CDA the $q\bar{q}$ cross section is stated to be proportional to the transverse size of the dipole $\sigma \sim r$. In the infinitely small limit of $r \rightarrow 0$, the QCD cross section is zero due to effective screening of the colour field of the quarks. The latter is known as colour transparency [72, 73]. The photon-proton total cross section $\sigma_{tot}^{\gamma^* p \rightarrow X}(x, Q^2)$ obeys a scaling in the single variable $Q^2/Q_s^2(x)$, where Q^2 is the virtuality of the photon and Q_s^2 - the saturation scale. This momentum scale increases with x according to $Q_S^2(x) = Q_0^2 x^{-\lambda}$ with $\lambda \approx 0.3$ and $Q_0 \approx 0.1$ GeV (giving a saturation scale of order 1 GeV for $x \approx 10^{-4}$).

Several models based on the CDA are briefly discussed.

2.2.1 MNRT model

The calculations of Martin, Ryskin, and Teubner (MRT) [15, 69] are performed in the leading $\alpha_s ln(\frac{1}{x})$ approximation. The cross section of the process $\gamma^* p \rightarrow Vp$ is calculated as a diffractive open $q\bar{q}$ production, $\gamma^* p \rightarrow q\bar{q}p$, and the $q\bar{q}$ state formation into the vector meson ($J^{PC} = 1^{--}$) is treated using a parton-hadron duality hypothesis. The cross section calculation takes into account the skewness of the gluons via the GPDs (Sect. 1.2.4). GPDs are estimated from conventional NLO gluon PDFs, $xg(x, Q^2)$. The real part of the amplitude is taken into account. The distinguishing feature of the MRT model is the scale of the interaction selection:

$$\bar{Q}^2 = z(1-z)(Q^2 + M_V^2 + |t|) \tag{2.7}$$

which reduces in case of no-skewness to Eq. 2.4 ($z = 1/2$).

The forward cross section is given by:

$$\frac{d\sigma}{dt}(\gamma^* p \rightarrow Vp)\bigg|_{t=0} = \frac{\Gamma_{\mu\mu} M_V^3 * \pi^3}{48\alpha}[\frac{\alpha_s(\bar{Q}^2)}{\bar{Q}^4} xg(\bar{x}, \bar{Q}^2)]^2 (1 + \frac{Q^2}{M_V^2}). \tag{2.8}$$

The cross section of polarised photons is calculated directly, leading to the prediction of the ratio of the σ_L and σ_T cross sections:

$$R = \frac{\sigma_L}{\sigma_T} = \frac{Q^2}{M^2}(\frac{\gamma}{\gamma + 1})^2 \tag{2.9}$$

where γ is the effective anomalous dimension of gluons: $xg(x, Q^2) \sim x^{-\lambda}(\bar{q}^2)^\gamma$. By involving GPDs in calculations the MRT model is sensitive to the gluon density at lower values of x, unlike the calculations which use conventional PDFs.

The Martin-Nockles-Ryskin-Teubner (MNRT) [74] is one of the striking recent publications in the field, where perhaps the first ever extraction of gluon densities is performed from an exclusive process. The uncertainties on $xg(x, Q^2)$ at low values of x and moderate values of Q^2 are significantly reduced compared to the standard PDF uncertainties as it is claimed by the authors and seen from Fig. 2.5.

The MNRT cross section calculations for $\gamma p \rightarrow \Upsilon(1S)p$ will be discussed in comparison with the measurement in Chapter 13.

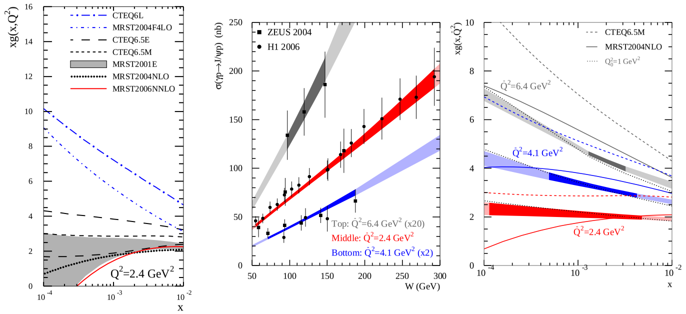

Figure 2.5: *(left) The gluon density extracted from global fits (grey band is the uncertainty for the central value obtained in MRST2004NLO). (middle) The J/ψ cross section measurement by ZEUS and the MNRT fits at $Q^2 = 2.4, 4.1, 6.4\ GeV^2$. (right) The gluon density extracted from the J/ψ cross section fit, the size of the lower band ($Q^2 = 2.4\ GeV^2$) to be compared to the grey band on the left-hand plot. The MNRT calculations are depicted as grey bands in the $middle$ and $right$-hand plots.*

2.2.2 FMS model

Another QCD approach is presented by Frankfurt, McDermont, and Strikman (FMS) [75] and is a continuation of the work published by Frankfurt, Koepf, Strikman (FKS) [76]. In FMS the calculations are performed in the leading $\alpha_s lnQ^2$ approximation, using gluon distributions from LO PDFs (CTEQ). The effect of skewness and the real part of the amplitude are taken into account. The scale at which α_s and gluon densities are calculated is related to the transverse size of the dipole and is obtained by the so called *rescaling of the hard process*:

$$\bar{Q}^2 = Q^2 \frac{< b^2_{\gamma L} >}{< b^2_V >}, \tag{2.10}$$

where $< b^2_{\gamma L} >$ and $< b^2_V >$ are the effective sizes of the $q\bar{q}$ pair for the longitudinal photon and the vector meson, calculated from the Fourier transform of the amplitude into the impact parameter space. The resulting scale is higher than that suggested by Ryskin.

The vector meson wave function is based on the non-relativistic potential and accounts for the Fermi motion of quarks in the vector meson. The cross section for transversely polarised photons, σ_T, is equivalent in terms of the longitudinal cross section, σ_L, and the QCD inspired parametrisation of $R = \frac{\sigma_L}{\sigma_T}$.

The FMS cross section calculations for $\gamma p \rightarrow \Upsilon(1S)p$ will be discussed in comparison with the measurement in Chapter 13.

2.2.3 RSS model

In [77] by Rybarska-Shäfer-Szczurek (RSS) a pQCD k_T-factorisation approach was applied to describe Υ photoproduction. The approach uses an unintegrated gluon distribution constrained by inclusive deep-inelastic structure functions, and the light-cone wave function of the vector meson. The real part of the amplitude is taken into account. The cross section is given by:

$$\sigma_{tot} = \frac{1+\rho^2}{16\pi B(W)} |Im \frac{M(W,\Delta^2)}{W^2}|^2, \tag{2.11}$$

where ρ corrects for the real part of the amplitude:

$$\rho = \frac{ReM}{ImM} = tan(\frac{\pi}{2}\Delta_P), \tag{2.12}$$

$B(W)$ gives proper normalisation to the cross section:

$$B(W) = B_0 + 2\alpha' log(\frac{W^2}{W_0^2}), \tag{2.13}$$

and the amplitude

$$ImM(W,Q^2) \sim W^2 \int \frac{d^2\mathbf{k}}{k^4} \alpha_s(q^2) F(x_1, x_2, \mathbf{k}_1, \mathbf{k}_2), \tag{2.14}$$

is related to the off diagonal unintegrated gluon distribution $F(x_1, x_2, \mathbf{k}_1, \mathbf{k}_2)$, x_1, x_2 are the longitudinal and $\mathbf{k}_1, \mathbf{k}_2$ - transverse momenta of gluons coupled to the $q\bar{q}$ pair, fullfilling the relation:

$$\mathbf{k}_1 = \mathbf{k} + \frac{|\mathbf{t}|}{2}, \mathbf{k}_2 = -\mathbf{k} + \frac{|\mathbf{t}|}{2} \tag{2.15}$$

The unintegrated gluon distribution $F(x, k^2)$ is normalised such that for a large scale $\bar{Q}^2$ it will be related to the integrated gluon distribution $g(x, \bar{Q}^2)$ through:

$$xg(x, \bar{Q}^2) = \int^{\bar{Q}^2} \frac{dk^2}{k^2} F(x, k^2). \tag{2.16}$$

The running coupling α_s enters at the largest relevant virtuality:

$$q^2 = max\{k^2, k_t^2 + m_b^2\}, \tag{2.17}$$

where k_t is the relative transverse momentum of the quark (anti-quark) in the bound state.

Due to the finite mass of the final state vector meson, the longitudinal momentum transfer is nonvanishing, and, as indicated above, a more precise treatment would require the use of skewed/off-diagonal gluon distributions. The effect of skewness can be taken into account by an appropriate rescaling of the diagonal gluon distribution [78]. In [77] the effect is emulated by taking the ordinary gluon distribution at [79]:

$$x_{eff} = C_{skewed} \frac{M_V^2}{W^2} \sim 0.41 \frac{M_V^2}{W^2}. \tag{2.18}$$

Further details on the k_T-factorisation approach and it's implementation to diffractive vector meson production can be found in [80].

The RSS cross section calculations for $\gamma p \rightarrow \Upsilon(1S)p$ will be discussed in comparison with the measurement in Chapter 13.

Part II

Instrumental part

Chapter 3

Experimental setup

This chapter describes the Storage Ring HERA and the ZEUS experiment at HERA. Details of the most relevant ZEUS detector components for this analysis are given.

3.1 HERA collider

HERA [81] is the only high energy elementary particle accelerator in the world which collided electrons and protons. It was located at the DESY (Deutsches Electronen SYnchrotron) laboratory, in Hamburg, Germany, and operated since autumn 1991 till 30 June 2007 (Fig. 3.1).

The storage ring with a circumference of 6.3 km was separated into two rings mounted on top of each other, one for the electrons, the other one for the protons. The electron ring consisted of normal-conducting dipole-magnets at 0.3 T and super-conducting cavities to accelerate the electron beam up to an energy of 27.5 GeV.

The proton machine consisted of super-conducting magnets with a magnetic field of 4.7 T and normal-conducting cavities, delivering a beam with the energy of 920 GeV (820 GeV until 1997). For colliding beams this results in a centre-of-mass energy of 300 GeV until 1997 and 318 GeV after increasing the proton energy. There were four interaction regions at HERA, shown in Fig. 3.2. At two of them, *ep* collisions are delivered for the detectors H1 and ZEUS. The HERMES detector used only the polarised electron beam with a fixed polarised or unpolarised gas target to investigate the spin structure of electron-proton or electron-deuteron interactions. Until the end of 2000 HERA-B was using the proton beam together with a fixed wire target. HERA-B was designed to investigate CP violation in the $B^0\bar{B}^0$ -system.

The proton acceleration chain started with negative hydrogen ions (H^-) accelerated in a LINAC to 50 MeV. The electrons were then stripped off the H^- ions to obtain protons, which were injected into the proton synchrotron DESY III, accelerated up to 7.5 GeV, and then transferred to PETRA, where they were accelerated to 40 GeV. Finally they were injected into the HERA proton storage ring, where they reached the nominal beam energy of 920 GeV (see Fig. 3.2).

Figure 3.1: *An aerial view of DESY and HERA. Four interaction points are marked with open circles.*

The electron (positron) pre-acceleration chain started in a linear accelerator, LINAC I (LINAC II), where the leptons were accelerated up to 450 MeV. The leptons were then injected into DESY II, accelerated to 7 GeV and then transferred to PETRA II, where they reached an energy of 14 GeV. They were then injected into HERA where they reached the nominal lepton beam energy of 27.5 GeV. HERA could be filled with a maximum of 210 bunches each of leptons and protons spaced by 96 ns. Some of these bunches were kept empty (pilot bunches) in order to study the background conditions. When either the lepton or the proton bunch was empty, the beam-related background, originating from the interaction of the lepton or the proton beam with the residual gas in the beam pipe, could be studied, whereas when both bunches were empty the non-beam-related background was estimated, e.g. the rates of cosmic rays. In Fig. 3.3 the performance of HERA is shown.

The running operations began in 1992 with an electron beam period, alternating with periods with positron beam. In 1998 the energy of the proton

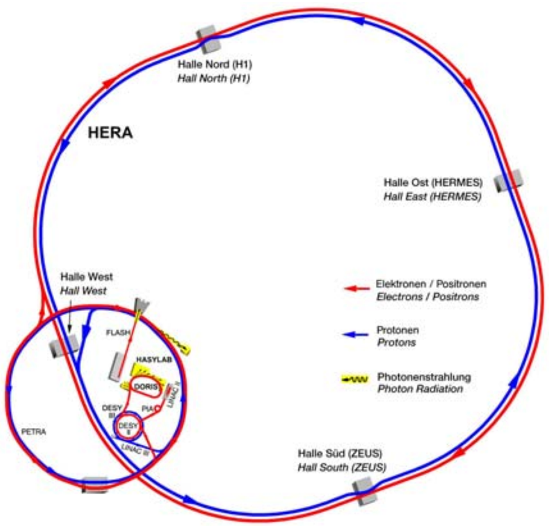

Figure 3.2: HERA and its pre-accelerators. At each straight section detectors are located.

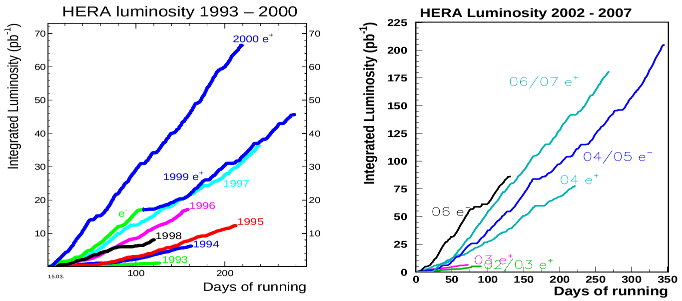

Figure 3.3: *The integrated luminosity as delivered by HERA in each operating year as a function of running days.*

---

beam was raised from 820 to 920 GeV.

The HERA I data-taking ended in the year 2000. During the shutdown 2000/2001 HERA was upgraded to deliver longitudinally polarised lepton beams at all interaction regions and to achieve an increased specific luminosity [82–84]. Until the mid of 2003 HERA and the experiments had to cope with severe background problems [85]. Since October 2003 stable beam operation has been achieved again. The period from October 2003 to June 2007 is usually refered to as HERA II.

3.1.1 Polarimeters

Due to an effect of natural polarisation of the beams (Sokolov-Ternov effect [86]) the electron beam was always (transversely) polarised. Its polarisation is given by:

$$P_T(t) = P_\infty(1 - e^{\frac{t}{\tau}}) \tag{3.1}$$

where t is the time of the electron beam circulation in the beampipe counting from the injection, $\tau = 37$ min for HERA. Due to the beam depolarisation effect P_T can not exceed $\approx 50 - 60\%$.

Additional *Spin Rotators* were installed in 2000/2001 to produce longitudinally polarised electron beams (see Fig. 3.4).

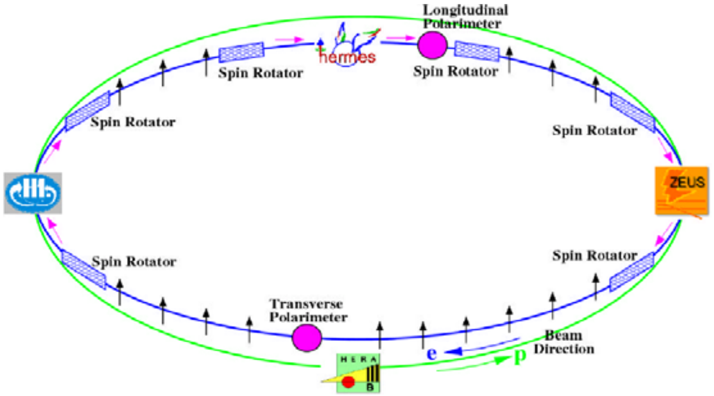

Figure 3.4: Spin rotators convert polarisation to longitudinal at HERMES, ZEUS and H1.

In addition to the existing Longitudinal Polarimeter (LPOL) [87, 88] operated by the HERMES collaboration a Transverse Polarimeter (TPOL) [89, 90] was installed in the area of the HERA-B experiment and was maintained by the H1 and ZEUS DESY groups. Both polarimeters used Compton scattering of laser light on polarised electron beam. Both alternated left-and right-handed circularly polarised laser light. The spin-dependent cross section allows one to measure the polarisation of the electrons in the beam. The TPOL measured a vertical spatial asymmetry. LPOL measured an asymmetry in the energy spectra. It worked in multi-photon mode with $\sim$ 1000 Compton photons per laser pulse on a lepton bunch.

3.2 ZEUS detector

The ZEUS detector [91] is a general purpose detector designed to study various aspects of lepton-proton scattering at HERA. It is a quasi hermetic detector since it covers most of the 4π solid angle with the exception of small regions around the beam pipe (see Fig. 3.5). Most of the final state particles were boosted to the forward direction because of the large momentum imbalance between the lepton and the proton beam. The layout of the detector was dictated by the topology of the processes to be studied at HERA. The energies measured by the detector range from few tens of MeV to hundreds of GeV in the forward region.

The ZEUS coordinate system is shown in Fig. 3.6. It is a right-handed, orthogonal system with the origin at the nominal interaction point (IP), the z axis pointing in the proton direction (also referred to as the forward direction), the x axis pointing toward the centre of HERA and the y axis pointing upwards. The polar angle ϕ and the azimuth angle θ are measured relative to the z and x axes respectively. The pseudorapidity, which is defined as $\eta = -ln(tan\frac{\theta}{2})$ is often used instead of θ.

The ZEUS sub-detectors were arranged coaxially (see Fig. 3.7) but asymmetrically around the interaction point to accommodate the boost of the centre-of-mass system in the proton beam direction with respect to the laboratory frame due to the large energy asymmetry between the lepton and the proton beams. A cross section of the detector layout along the beam axis is shown in Fig. 3.8. The main detector was approximately 20 m long, 12 m wide and 11 m high and weighed around 3.6 kt. A short description of the main components of the detector used in the analysis is given. Some detectors will be discussed in more detail in Chapters 4, 5.

During 1996-2000 data-taking the detector closest to the interaction point was the Central Tracking Detector (CTD, [92–94]) which is a cylindrical drift chamber. It is enclosed by a superconducting solenoid providing a magnetic field of 1.43 T for the determination of charge and momentum of charged particles.

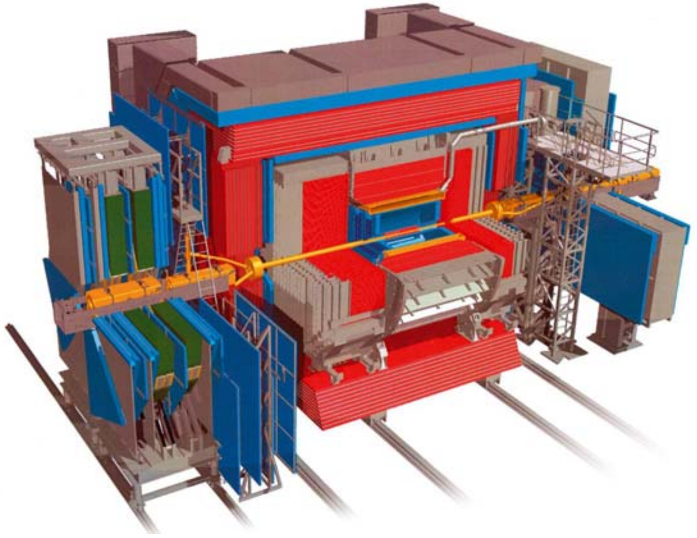

Figure 3.5: ZEUS 3D view showing the main components.

The CTD was supplemented in the forward direction by the Forward Detector (FDET) [91]. The Straw Tube Tracker (STT, [95–98]) was added (2002-2007)[1] to the FDET to improve the tracking performance in the forward area. The Micro Vertex Detector (MVD, [99]) was inserted (2002-2007) inside of the CTD area to improve the primary/secondary vertex separation for the purpose of better beauty and charm meson tagging. The rear direction was supplemented by the Rear Tracking Detector (RTD) [91]. The tracking system is surrounded by a compensating high resolution uranium-scintillator calorimeter (CAL, [100–103]) which is used as the main device for energy measurements. It is divided into forward, barrel and rear sections (respectively FCAL, BCAL and RCAL) with different thicknesses.

The calorimeter was enclosed by an iron yoke that provided the return path

---

[1] In 2005 the detector was excluded from the DAQ chain.

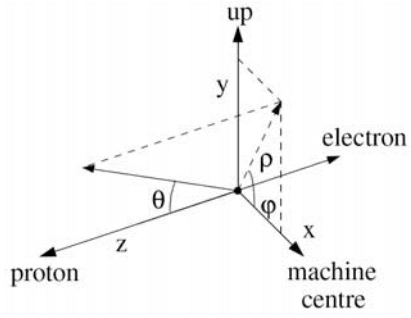

Figure 3.6: *ZEUS coordinate system.*

for the solenoidal magnetic field flux, and served as absorber for the Backing Calorimeter (BAC, [104, 105]), which measures energy that escapes detection from the main calorimeter. Due to muon high penetration power BAC contributes also to the muon identification and reconstruction. Dedicated muon identification detectors were located inside (FMUI, BMUI and RMUI) and outside (FMUO, BMUO and RMUO) the iron yoke [91].

The VETO wall [91] was located in the rear direction at about z = -7.5 m from the interaction point. It consisted of an iron wall supporting scintillator hodoscopes and is used to reject background from beam gas interactions. The luminosity measurement detector (LUMI) [91] was made of a small lead-scintillator calorimeter (HERA I) at z = -107 m and detected photons from bremsstrahlung events for the luminosity measurement. In HERA II the system was complemented with a spectrometer system to cope with the increased instantainious collider luminosity (see Sect. 3.2.4).

3.2.1 Tracking detectors

The tracking system of ZEUS consists of the Central Tracking Detector (from begining of ZEUS in 1991 to the end of HERA in 2007) covering the central pseudorapidity range from -1.75 to +1.75. This is the major device for track reconstruction in all running periods. During HERA II the Micro Vertex Detector was installed for precision vertex position measurement. The forward region of the ZEUS detector required enhanced tracking and particle identification capabilities due to the asymmetric beam energies [106] . It consisted of the

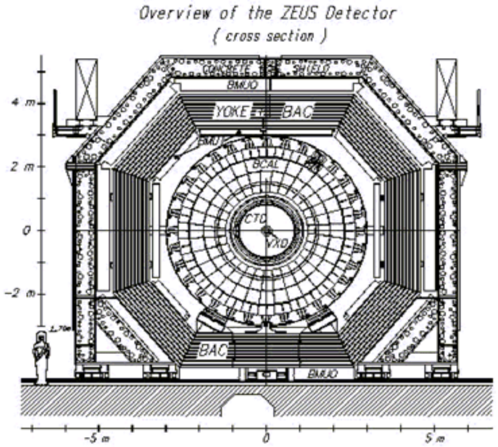

Figure 3.7: *Cross section of the ZEUS detector in $X - Y$ plane.*

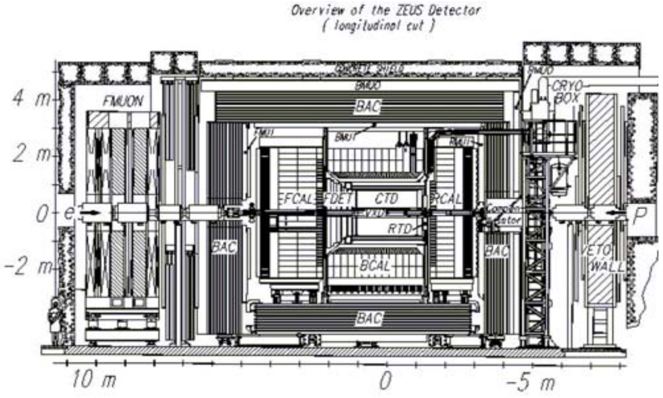

Figure 3.8: *Cross section of the ZEUS detector in $Z - Y$ plane.*

Forward Tracking Device (FTD) and in 1992-2000 of the Transition Radiation Detector (TRD). The purpose of the FTD was to reconstruct low angle tracks of ionising particles whereas the TRD separated electrons from hadrons. For the HERA II upgrade programme the TRD was replaced in 2000-2001 by the STT. The STT was specifically designed to improve the tracking purity in events with high multiplicities. Forward tracking extends the accessible kinematic range to lower hadronic energies, W.

The basic performance idea of the tracking detectors will be discussed below.

3.2.1.1 Central Tracking Detector (CTD)

The CTD [92–94] is a cylindrical wire drift chamber used to measure the directions and momenta of the charged particles and to estimate the energy loss dE/dx to provide information for particle identification. The inner radius of the chamber is 18.2 cm, the outer is 79.4 cm, and its active region covered the longitudinal interval from $z = -100$ cm to $z = 104$ cm, resulting in a polar angle coverage of $15^o < \theta < 164^o$. The CTD was filled with a mixture of argon (Ar), carbon dioxide (CO_2) and ethane (C_2H_6) in the proportion $85 : 5 : 1$. The CTD consisted of 72 radial layers of sense wires, divided into groups of eight to nine superlayers (SL). A group of eight radial sense wires with associated field wires in one superlayer make up a cell. The drift cells in each superlayer were similar. The sense wires were 30 μm thick while the field wires had different diameters. A total of 4608 sense wires and 19584 field wires was contained in the CTD. The CTD was designed to operate in a magnetic field. The 8 sense wires were in a plane, at 45^o to the radial line from the chamber axis. The drift field was at a Lorentz angle of 45^o to the radial axis, which helped in left - right ambiguity breaking. One octant of the CTD is shown in Fig. 3.9. A charged particle crossing the CTD produced ionisation of the gas in the chamber. The electrons from the ionisation drifted towards the sense wires (positive), whereas the positively charged ions drifted towards the negative field wires.

The superlayers (SL) were numbered so that the number 1 is the innermost SL, whereas the outermost is number 9. For the trigger purposes, the three inner axial superlayers (SL1, SL3, SL5) were equipped with a system that determines the z positions using the time difference between the arrival times of the signal from the opposite ends of the CTD ($z - by - timing$ system).

The resolution achieved on the z coordinate with this system was 4 cm. Odd numbered SLs had wires parallel to the z direction (axial superlayers), while wires in even numbered SLs were at a small stereo angle of 5^o (stereo superlayers) to achieve a better resolution in z.

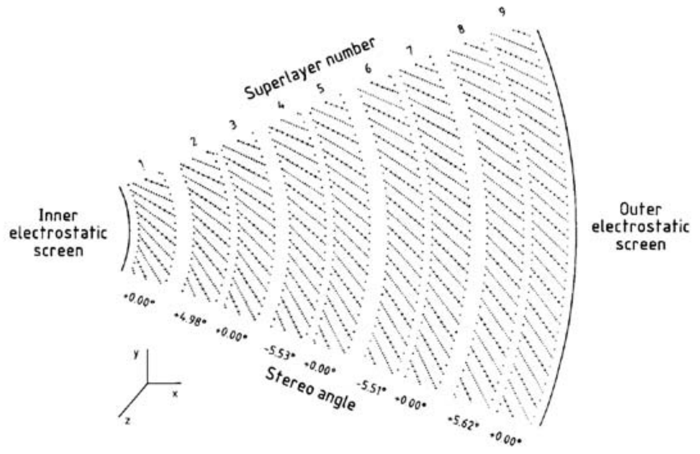

Figure 3.9: *Layout of a CTD octant. The superlayers are numbered and the stereo angles of their sense wires are shown.*

HERA I performance In HERA I the achieved CTD hit resolution was 200 μm in the $r-\phi$ plane and 2 mm in the z coordinate. The resolution on p_T, for tracks fitted to the interaction vertex and passing at least three CTD superlayers and with $p_T > 150$ MeV, is given by:

$$\frac{\Delta p_T}{p_T} = 0.0058 \cdot p_T \oplus 0.0065 \oplus \frac{0.0014}{p_T} \qquad (3.2)$$

where p_T is given in GeV and the symbol $\oplus$ indicates the quadratic sum. The first term is the hit position resolution, while the second and the third depend on the multiple scattering inside and before the volume of the chamber, respectively.

HERA II performance In the HERA II data taking period the conditions at which the CTD operated changed. The high voltage was lowered which led to a slightly worse hit resolution. The overall track transverse momentum and vertex resolution improved by adding the information from the MVD. The tracking angular coverage was extended due to the forward MVD (Section 3.2.1.2) and the STT (Section 3.2.1.4).

3.2.1.2 Micro Vertex Detector (MVD)

The silicon-strip micro vertex detector (MVD) [99] was installed in 2001. It aimed at a significant improvement of the tracking capabilities to permit the reconstruction of impact parameters and secondary vertices. Figure 3.10 displays the layout of the MVD, which is split into a barrel and a forward region. The sensitive areas are called ladders and contain two layers of orthogonally oriented silicon strips.

The MVD measured the charge-deposit on its strips. In combination with the known geometry of the detector and the orientation of the tracks this was used to measure the ionisation rate. It is possible to use the MVD for particle identification in a similar way as the CTD. As one can observe in Fig. 3.10 a typical track passes 3 ladders, i.e. at most 6 silicon strips. This number is small compared to the number of hits for a typical track in the CTD.

Performance comparison of the tracking used for HERA I data samples (CTD only) to the tracking used for the HERA II data (MVD-CTD:2003-2007, and MVD-CTD-STT:2003-2007 excluding 2005) is not a trivial task. Since the HERA II tracking used in the analysis presented in Part III of this thesis was not yet in its final shape, only qualitative remarks can be given.

The track transverse momentum resolution improved by $\approx 50\%$. The vertex position in X-Y plane improved changing from ~ 0.1 cm (HERA I) to better than 0.01 cm (HERA II). The z-coordinate of the vertex position also improved

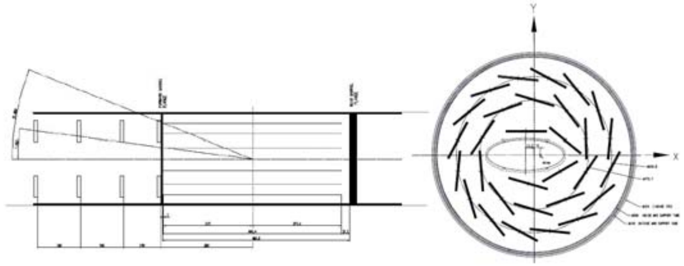

Figure 3.10: *Cross sections of the MVD along the beam pipe (left) and in the X-Y plane (right).*

due to a few extra hits located closer to the interaction point, however having no consequences for the analysis. The cuts defining the vertex position in X, Y, Z coordinates were conservative remaining identical to the ones used in the analyses of HERA I data samples only (see Chapter 7).

3.2.1.3 Forward and Rear Tracking Detectors (FTD, RTD)

The FTD measured the tracks of charged particles in planar drift chambers (see Fig. 3.11) located at the ends of the central tracking detector in forward (proton) and rear (electron) directions (see Fig. 3.12).

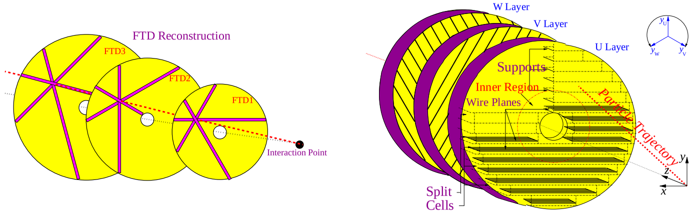

Figure 3.11: *The Layout of the FDET drift chambers in (left) overall view and (right) view of the 3 layers inside of one of the chambers.*

A charged particle passed in the FTD through 3 chambers (RTD - 1 chamber).

Each chamber contained 3 layers with a total of 18 wire planes. The layers consisted of drift cells which were rotated by 60 degrees with respect to each other. The FTD cells are rectangular with six signal wires strung perpendicular to the beam axis.

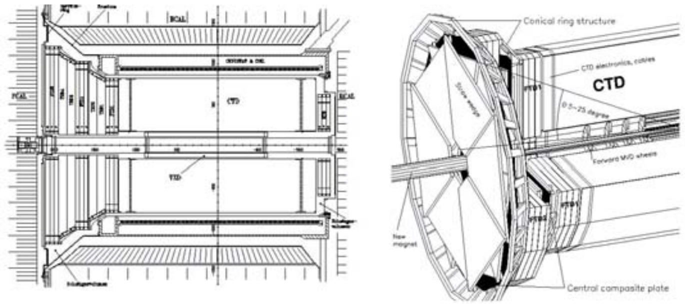

Figure 3.12: *(left) a ZR view of the tracking detectors, in the forward area the four TRD planes are shown, which were replaced with two STT wheels, (right) the angular coverage of the STT compared to the CTD and forward MVD wheels.*

3.2.1.4 Straw-Tube Tracker (STT)

The Straw-Tube Tracker (STT) was designed to significantly improve the pattern finding and track reconstruction in the forward region of the ZEUS detector. It was installed during the HERA shutdown in 2001. After some problems in the beginning the detector was repaired during the shutdown in 2002. At the end of 2003 the first physics data with the STT were taken. The component was switched off in 2005 due to the unbalanced heating between the STT and the Solenoid. After additional cooling has been installed during the shutdown in the end of 2005 the STT has rejoined the DAQ chain. The integrated luminosity of the data sample with working STT equals $\sim 220\ pb^{-1}$.

STT used most of the former TRD infrastructure: mechanical support, high voltage (HV), low voltage (LV), gas system. The geometric layout of the STT sectors and their position along the z-axis is presented in Fig. 3.13. The STT angular coverage $5^o < \theta < 25^o$. It overlaps with the forward MVD wheels and part of the CTD (Fig. 3.12(right)).

The STT overall specifications are given in Table 3.1. Some of the STT commissioning details implemented as part of the technical work for this thesis are discussed in Chapter 4.

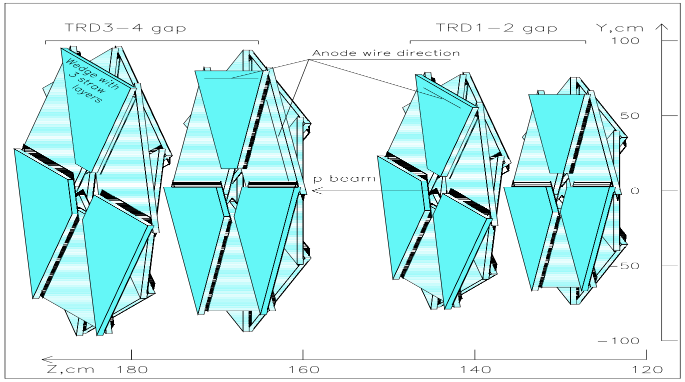

Figure 3.13: *The layout of the STT sectors, and their location along the z-axis.*

Angular acceptance	$5^o - 25^o$
Number of straw tubes	11616
Straw tube outward diameter	8 mm
Straw tube wall thickness	$\sim 120\mu m$
Straw tube length	15-83 cm
Wire thickness	50 μm
Wire material	Cu-Be
Number of straw layers in	24 z
Max drift time	80 ns
Radiation thickness	$\leq$ 15% X
Weight	$\sim$ 80 kg
Gas mixture $Ar - CO_2$	80:20
Straw occupancy	
average	$\leq 2\%$
local in DIS jet	$\sim 15\%$
Single wire spatial resolution	$\sim 140\mu m$
Efficiency per straw	96%
Radiation hardness	$\geq 2C/cm$
Number of readout channels	2112

Table 3.1: *Straw Tube Tracker specifications.*

3.2.2 Calorimeter detectors

3.2.2.1 Uranium Calorimeter (CAL)

The ZEUS calorimeter (CAL) [100–103] is a high-resolution compensating calorimeter. It completely surrounds the tracking devices and the solenoid, and covers 99.7% of the 4-π solid angle. It consists of 3.3 mm thick depleted uranium plates (98.1% U^{238}, 1.7% Nb, 0.2% U^{235}) as absorber alternated with 2.6 mm thick organic scintillators (SCSN-38 polystyrene) as active material. The thickness of the absorber and of the active material have been chosen in order to have the same response for an electron or a hadron of the same energy passing through the detector ($e/h = 1.00 \pm 0.05$). This mechanism is called compensation, and allows to achieve good resolution in the determination of both the electromagnetic and the hadronic energy.

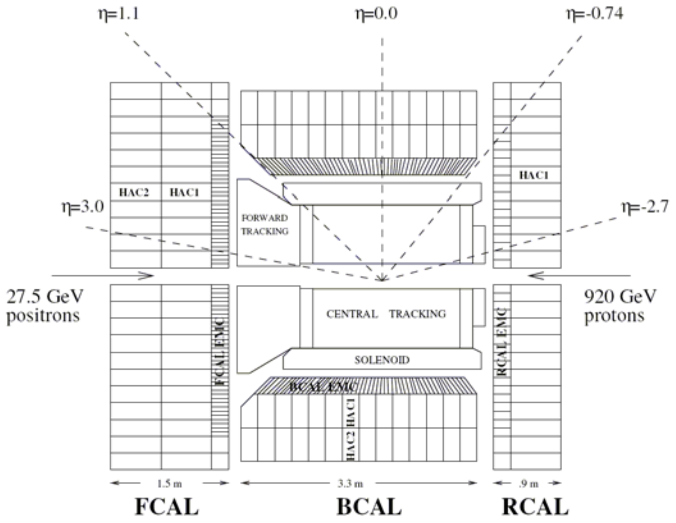

Figure 3.14: *Cross section of the ZEUS CAL in the Y-Z plane.*

The achieved hadronic resolution is

$$\frac{\Delta E}{E} = \frac{35\%}{\sqrt{E}} \oplus 1\% \tag{3.3}$$

while the electromagnetic resolution is

$$\frac{\Delta E}{E} = \frac{18\%}{\sqrt{E}} \oplus 2\% \tag{3.4}$$

where E is the particle energy, measured in GeV. The CAL is divided into three parts: the forward (FCAL), barrel (BCAL) and rear (RCAL) calorimeter (Fig. 3.14).

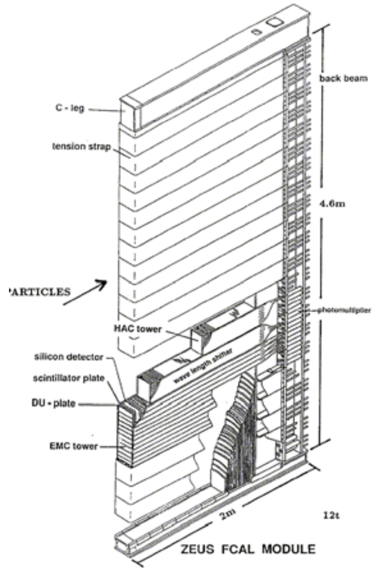

Figure 3.15: View of an FCAL module. The towers containing the EMC and HAC sections are shown.

The three parts are of different thickness, the thickest one being the FCAL ($\sim 7\lambda$), then the BCAL ($\sim 5\lambda$) and finally the RCAL ($\sim 4\lambda$), where λ is the

interaction length[2]. Each part of the calorimeter is divided into modules, and each module is divided into one electromagnetic (EMC) and two (one in RCAL) hadronic (HAC) sections. These sections are made up of cells, whose sizes depend on the type (EMC or HAC) and position (in FCAL, BCAL or RCAL) of the cell.

The FCAL consists of one EMC (first 25 uranium-scintillator layers) and two HAC (remaining 160 uranium-scintillator layers) sections. The electromagnetic section has a depth of $\approx 26\ X_0$, while each hadronic section is 3.1 λ deep. The EMC and HAC cells are superimposed to form a rectangular module, one of which is shown in Fig. 3.15, 23 of these modules make up the FCAL.

The BCAL consists of one EMC and two HAC sections, the EMC being made of the first 21 uranium-scintillator layers, the two HACs of the remaining 98 layers. The resulting depth is 21 X_0 for the electromagnetic section, and 2 λ for each hadronic section. The cells are organised in 32 wedge-shaped modules, each covering 11.25^o in azimuth.

The RCAL is made up of 23 modules similar to those in the FCAL, but it consists of one EMC and only one HAC section. Therefore its depth is 26 X_0 for the EMC part and 3.1 λ for the HAC part.

The light produced in the scintillators is read by 2 mm thick wavelength shifter (WLS) bars at both sides of the module, and brought to one of the 11386 photomultiplier tubes (PMT) where it is converted into an electrical signal. This information is used for energy and time measurements. The CAL provides accurate timing information, with a resolution of the order of 1 ns for tracks with an energy deposit greater than 1 GeV. This information can be used to determine the timing of the particle with respect to the bunch-crossing time, and it is very useful for trigger purposes in order to reject background events, as it will be illustrated later, in the trigger section. The stability of the PMTs and of the electronics is monitored with lasers and charge pulses. In addition, the small signal coming from the natural radioactivity of the depleted uranium gives a very stable signal, also used for the calibration. The achieved accuracy is better than 1%.

3.2.2.2 Small Angle Rear Tracking Detector (SRTD)

The Small Angle Rear Tracking Detector [107] is formally not related to energy measurement, however it plays an important role in the measurement of the

---

[2] The interaction length $\lambda = A/(N\sigma\rho)$ is the average distance a strongly interacting particle travels in material, N is Avogadro's number, A is the atomic mass of the medium, ρ is the density and σ is the absorption cross section.

The radiation length X_0 is the characteristic amount of matter traversed by high-energy electrons or photons. One radiation length X_0 gives the mean distance over which an electron remains 1/e of its energy, and 7/9 of the free mean path for pair production by a photon.

DIS electron position in the trigger and it is used in the offline reconstruction for the electron energy corrections. The SRTD consists of two layers of plastic scintillators. It has spatial and timing resolutions of < 5 mm and < 1 ns, respectively, and full coverage between $167^o < \theta < 174.5^o$.

3.2.2.3 Hadron-Electron Separator (HES)

The Hadron-Electron Separator [108] consists of 20000 3x3 cm silicon pads found in the electromagnetic sections of the rear- and forward-CAL at a depth of 3 radiation lengths. The spatial resolution of the HES is about 5 mm. It is also used for electron reconstruction.

3.2.2.4 Backing Calorimeter (BAC)

The Backing Calorimeter (BAC) [104, 105], fulfils the following requirements:

- The gas mixture is $Ar : CO_2$,
- By vetoing late showers it allows the selection of an event sample, where energy is measured with a resolution corresponding to that of an infinitely deep uranium-scintillator calorimeter (CAL).
- It distinguishes between muons and hadron showers,
- It provides a muon trigger with all detector coverage, e.g. also in the bottom yoke, where no muon chambers are present. This was fully implemented from 2006 onwards.

The implementation of the BAC has been changed relative to the Technical Proposal [91, 109, 110]. Instead of plastic limited streamer tubes, aluminium proportional tubes filled with $Ar : CO_2$ have been used. The BAC is composed of modules assembled by 7 or 8 cells with cross section 11x15 mm and a length of 1.8-7.3 m. Gold plated tungsten wires with diameter of 50 μm are stretched in the cell centres and supported every 50 cm in the longitudinal direction. Flat aluminium cathodes of length 50 cm are mounted on top of the modules. The wires are read out on one side and provide both analog and digital signals. The pads have only an analog readout. Energy is measured by summing up the analog signals from the wires grouped in addition into towers of a width of 25-50 cm (2-4 modules) over the full depth of the BAC. The pads of 2-4 neighbouring modules are added to pad towers with an area of 50x50 cm^2 (4 modules) similar to the wire towers. They provide a measurement of the location of the energy deposit along the wires. The signals from the wires provide patterns of hit positions in the BAC to reconstruct muon trajectories.

The BAC can recognise events with showers leaking out of the CAL (e.g. high energy jets penetrating the CAL) to veto or to correct them later. It can distinguish between hadron and muon showers and provides muon identification and trigger capabilities in the bottom yoke and other areas poorly covered by the muon chambers.

3.2.3 Muon detectors

Muons can traverse large amounts of material without being absorbed since they lose energy mainly by ionisation. The muon detectors have to measure tracks produced in the interaction region which cross the whole calorimeter thickness and the iron yoke. The momenta of the muons can be very different depending on their polar angle due to the boosted system to the forward region. Muons with 10 GeV momentum are frequently produced into the forward region. In the barrel and rear regions the average momentum of the muons is expected to be much smaller. Therefore the muon detection system is split into two sub-detectors, the forward muon detector (FMUON, see Sect. 3.2.3.1) and the barrel and rear muon detector (BMUON and RMUON respectively, see Sect. 3.2.3.2).

3.2.3.1 Forward Muon Spectrometer (FMUON)

The forward muon detector is divided into two regions (see Fig.3.16). The inner region is located between the FCAL and the BAC (FMUI), the other is positioned outside the BAC (FMUO).

The FMUON detector consists of a system of:

- four planes of limited streamer tubes (LST) trigger planes (LST1-LST4) with digital radial ρ and azimuthal ϕ readout.
- two larger planes of the LSTs with digital (ρ, ϕ) and analog (ρ) readout in the large polar angle region (LW1, LW2);
- four planes of drift chambers (DC1 - DC4);
- two large toroidal iron magnets providing a magnetic field of 1.7 T for the momentum separation and measurement in the angular region $5^o < \theta < 16^o$.

The first streamer plane (LST1) and drift chambers (DC1) make up the FMUI detector, placed inside the iron yoke while the rest of the system is located on the outside. The individual components of the FMUON detector are described in the following.

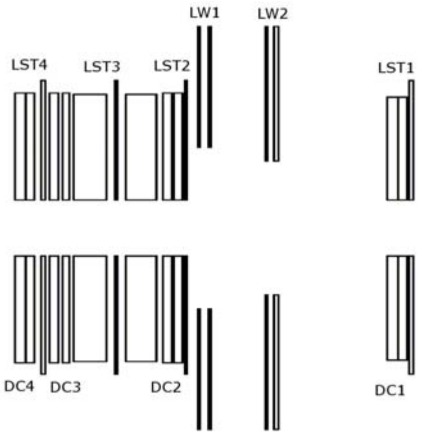

Figure 3.16: *Schematic layout of the FMUON detector. The inner FMUON (FMUI) components are LST1 and DC1. The outer FMUON (FMUO) components are LST2,3,4, DC2,3,4 and LW1, LW2.*

The limited streamer tube planes: A trigger plane is made of four LST chambers grouped in two half-planes. A quadrant consists of two layers of LST positioned horizontally inside a plastic sheet. The tubes of the two planes are slightly displaced (0.5 cm) in order to achieve a complete geometrical acceptance. Each quadrant is contained in an air tight aluminium box. On the outer side, copper strips are glued in polar geometry. The LSTs induce a signal in the copper strips if a particle crosses the plane. The number of radial strips is 132 while each strip is 1.9 cm wide. They are divided along the bisector of the quadrant so that the simplest unit of the trigger plane to be read out is the octant. The number of strips is 32 per octant. Each strip covers an interval of 1.4 in the azimuthal angle. The aim of the limited streamer tube (LST) planes is to trigger on muon candidates and to reconstruct their position in terms of the azimuthal and radial coordinates of the track.

The drift chambers: The drift chambers are needed in order to obtain a good momentum resolution. Each plane consists of four chambers grouped two by two in two half planes fixed on a support panel. The basic element of the chamber is the cell made of four sense wires and of the layers needed to generate the appropriate electric field. The four sense wires measure the radial coordinate. The information gathered by the wires are sent to a TDC which converts them into a time interval related to the drift distance by a known relation.

The large angle coverage planes: The two large angle coverage planes (LW) are needed in order to achieve the desired geometrical acceptance also in the region left uncovered by the toroids ($16^o < \theta < 32^o$). Each plane consists of eight air tight aluminium wrappings that contain a LST layer. The LST signal is induced on copper strips with radial geometry spaced of 0.7^o in the ϕ coordinate and of 1.8 cm in the ρ coordinate. There are 64 ϕ strips and 192 ρ strips per octant. The achieved resolution in the coordinate, using a centre of gravity algorithm, is ≈ 1 mm.

3.2.3.2 Barrel(BMUON) and Rear(RMUON) Muon Chambers

The barrel and rear muon detector [111] covers a very large area (~ 2000 m^2) and consists of LST chambers as the basic structure. The chambers covering the inner barrel part between the CAL and the iron yoke are called BMUI while the chambers situated outside the yoke are denoted as BMUO. The rear region is divided into RMUI and RMUO chambers in a similar way (see Fig. 3.17).

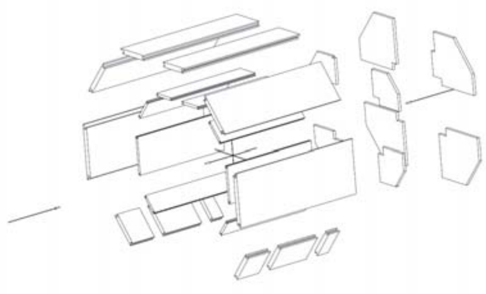

Figure 3.17: *Layout of the BMUON and RMUON detectors.*

The chambers have different shapes and dimensions depending on their location, but their internal structure is always the same. The supporting structure of each chamber is an aluminium honeycomb frame 20 cm thick in the rear chambers and 40 cm in the barrel ones. Two planes of LST are placed on both sides of the honeycomb. The two layers on the same side of the chamber are displaced by 8.3 mm in order to minimise dead areas for particles traversing at 90^o with respect to the wire plane. Each LST is made of a plastic profile with eight cells. In each cell a copper-beryllium wire of 100 μm diameter is located. The distance between two sense wires is 1 cm. Each LST plane is equipped on one side by 13 mm wide readout strips with 15 mm pitch that run orthogonal to the wires. In the BMUI and BMUO chambers the LSTs are parallel to the beam direction while in RMUI and RMUO they are horizontal (parallel to the ZEUS x direction). With the analog strip readout the achievable spatial resolution on the coordinate orthogonal to the wires is 200 μm while it is 700 μm for the coordinate parallel to the wires.

3.2.4 Luminosity measurement

The luminosity measurement at ZEUS (for 1992-2000 data see [112–114], for 2003-2007 see [115]) is made using a Bethe-Heitler[3] QED bremsstrahlung process:

$$ep \rightarrow e'p\gamma, \tag{3.5}$$

where the lepton and the photon are scattered at very small angles. This process has a large cross section ($\sigma_{BH} \approx 20$ mb) yielding sufficient statistics. The differential cross section as function of the photon energy of this process is described by Eq. 3.6 and is known with an accuracy of $\sim 0.5\%$:

$$\frac{d\sigma_{BH}}{dk} = 4\alpha r_e^2 \frac{E'}{kE}\left(\frac{E}{E'} + \frac{E'}{E} - \frac{2}{3}\right)\left(ln\frac{eE_pEE'}{m_em_pk} - \frac{1}{2}\right) \tag{3.6}$$

where α is the fine structure constant, r_e the classical electron radius, k, E and E$'$ the energies of the photon, the incoming and outgoing electron, respectively. Bremsstrahlung photons emitted at an angle $\theta_\gamma < 0.5$ mrad with respect to the beam axis leave the beampipe through a Cu-Be window of a thickness of 0.095 X_0 at $z =$ -92.5 m.

With a well known cross section σ_{BH} and N_{BH}, the corresponding number of events observed over a period of time:

$$L = \frac{N_{BH}}{\sigma_{BH}}. \tag{3.7}$$

---

[3] The term Bethe-Heitler is also used alternatively to denote lepton pair QED production as described in Section 9.1.2

3.2.4.1 Photon calorimeter

The photons produced in the reaction (Eq 3.5) are detected by a lead/scintillator sampling calorimeter (LUMIG) at $z =$ -107 m (see Fig. 3.18).

The detector is shielded from synchrotron radiation by a graphite block with a thickness of 2 X_0 resulting in an energy resolution of $\delta E/E = 23\%/E$ (E measured in GeV). The impact position of the photons can be reconstructed with a resolution of 3 mm making use of the embedded layers of scintillator fingers. The bremsstrahlung event rate is determined by counting the number of photons above a fixed energy threshold. The luminosity is then calculated by dividing the evaluated rate by the bremsstrahlung cross section corrected for the detector acceptance. The main contribution to the background is given by the bremsstrahlung of leptons on the residual gas in the beam pipe. This can be measured using pilot bunches, i.e. lepton bunches with no associated proton bunch, evaluating for these the rate of bremsstrahlung events. The statistical uncertainties are negligible due to the sufficiently large recorded Bethe-Heitler rates. The systematic uncertainty of the luminosity measurement originates mainly from the background subtraction, pile-up effects and the energy calibration, linearity and acceptance of the photon calorimeter. The achieved precision is of the order of $1.5 \div 2\%$ for 1996-2000.

3.2.4.2 Spectrometer system

The upgrade of the HERA accelerator has provided an increase of instantanious collider luminosity. The ZEUS HERA-I technique, with a calorimeter to directly measure all bremsstrahlung photons faced new difficulties at HERA-II, including the following:

- A significant increase in the direct synchrotron radiation (SR) flux from the electron beam occurs due to the higher beam currents and to a new beam focusing scheme to optimise high luminosity near the interaction region.
- Much larger numbers of overlaid bremsstrahlung events (pile-up) occur. Colliding bunches producing more than one photon are not separated in the calorimeter technique. HERA-II luminosity implies a significant probability (approaching unity) for several final state photons with $E_\gamma > 0.5$ GeV in each bunch-crossing.
- There are additional requirements for accurate cross sections using polarised beam electrons (or positrons).

In order to suppress the increased rate of the photons the absorber thickness has been increased and a spectrometer system [116] has been installed to trace the electrons produced from the photon to electron-positron pair conversion. The layout of the system is presented in Figures 3.19, 3.20. The main systematic uncertainty to the luminosity measurement with the spectrometer system coming from the aperture and detector alignment (1%), window conversion (2%), rate (0.6%), and X-position of the conversion point (1.1%). The overall uncertainty being 2.6%.

3.2.5 Trigger and Data Acquisition (DAQ)

The HERA beam bunch structure leads to a beam crossing every 96 ns corresponding to a rate of potentially interesting events of 10.4 MHz. The rate of *ep* events ranges from less than 0.1 Hz (for NC DIS events with $Q^2 > 100$ GeV^2) to 250 Hz (for soft photoproduction).

The actual event rate exceeds the rate of *ep* physics events by several orders of magnitude. The non *ep*-physics events are coming mainly from interactions of protons with the residual gas nuclei or elements of the beamline (beam gas events). The other sources of the non *ep*-physics background consist of cosmic muons, cosmic showers, and "halo muons", the muons accompanying the proton beam and parallel to the z-axis with highest rate close to the beam pipe.

The total data size per event is 150 kB and the writing speed to the permanent storage facility is limited to 1.5 MB/s. Hence a significant reduction of the data rate and size is required.

The goal of the trigger is to distinguish the physics events from the non-physics background. A three level trigger system (Fig.3.21) with increasing complexity of the decision making algorithm and decreasing throughput rate is used to select events online.

3.2.5.1 Global First Level Trigger (GFLT)

The First Level Trigger has to strongly suppress the following background events, in order to pass a cleaner sample to the other trigger components:

- events coming from interactions of leptons or protons with the residual gas in the beam pipe, near the interaction point. The estimated rate of this kind of events, assuming a sensitive region of 100 cm before and after the interaction point, with the nominal beam currents and with a vacuum of 10 Torr, is 50 kHz;

- events coming from interactions of the protons in the beam halo with the collimators, that can produce secondary hadrons decaying into high energy muons, crossing all the detector; these events, however, have a typical

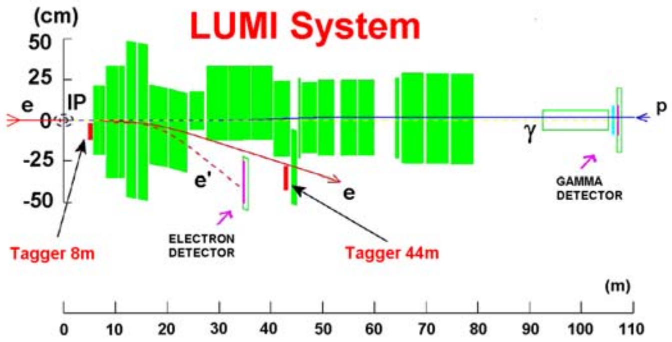

Figure 3.18: *The ZEUS luminosity monitoring system with the photon LUMIG and electron LUMIE detectors is shown (HERA I).*

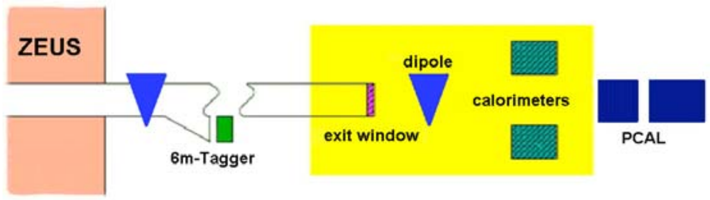

Figure 3.19: *The ZEUS luminosity monitoring system with the photon calorimeter and the spectrometer (HERA II).*

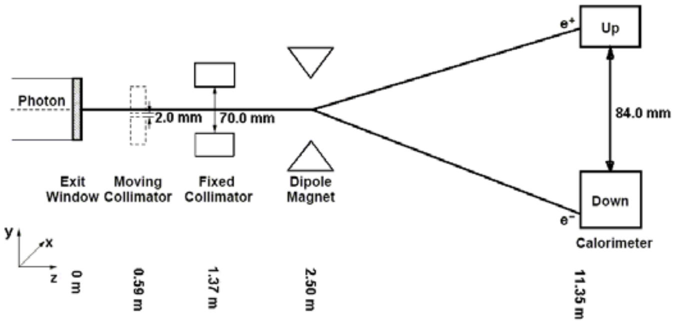

Figure 3.20: Schematic showing major elements of the luminosity spectrometer (HERA II).

topology (the muons are typically parallel to the proton beam direction) and usually can easily be distinguished from *ep* events;

- cosmic ray muons, with a rate of the order of 1 kHz.

The First Level Trigger has to be synchronized with the HERA bunch crossing so it has to handle events at a rate of 10 MHz, giving as output events at a rate of the order of 1 kHz, the design rate of the Second Level Trigger. The FLT is a hardware trigger, designed to analyse every bunch crossing. The data of each bunch crossing are stored into pipelines, that are 46 bunch crossings deep and allows the FLT a time of 4.4 μs to accept or discard an event. The FLT operates on a subset of the full data coming from an event, based essentially on the calculation of crude event observables (e.g. regional energy sums, number of tracks, timing information). Each detector component has its own first level trigger processor, and the 4.4 μs interval has to be shared between the component trigger and the Global First Level Trigger (GFLT). After 26 bunch crossing times (2.5 μs) every component send its FLT signal to the GFLT, which uses the remaining 20 crossing times (1.9 μs) to take the final decision. The component data are processed and combined in parallel in eight Trigger Logic Modules of the GFLT, and 64 individual subtriggers (slots) are generated. The GFLT accepts or rejects the event looking at the OR of these 64 sub-triggers. If the event is accepted, all the components have to digitise their data in order to send them to a system of digital CPUs for the next analyses. This operation takes 10 μs after the GFLT

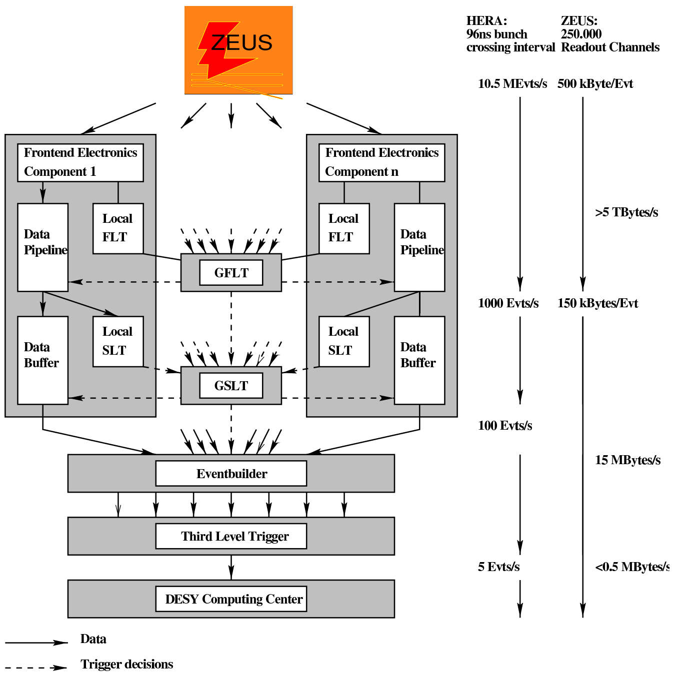

Figure 3.21: Diagram of the ZEUS trigger and data acquisition chain in HERA I. The effect of trigger selection on lowering the rate (in events per second and in data size) is shown in the right hand side of the diagram.

decision, and during this time no event acquisition is possible. This is the only deadtime of the GFLT chain, and is of the order of 1%.

3.2.5.2 Global Second Level Trigger (GSLT)

The Second Level Trigger (SLT) further reduces the background events with respect to the *ep* events. The SLT, which receives events from the FLT with a rate of 1000 Hz, has an output rate of 100 Hz. The SLT is software based and runs on a network of transputers. The analysis of the events is done in parallel so that the available processing time is much larger than at the FLT, of the order of some milliseconds. As in the FLT, each detector component has its own SLT processor, and all the information from the single components is sent to the Global Second Level Trigger (GSLT) after the processing. The information the GSLT uses to distinguish between *ep* and background events is based mainly on the time of arrival of the particles at the calorimeter.

As it was shown in Section 3.2.2 the CAL can give timing information with a resolution of the order of 1 ns. The time is calibrated so that physics events originating from the interaction point have zero time in the whole calorimeter. A proton-gas event, originating upstream of the detector, produces particles reaching the RCAL before the FCAL, with a time difference of 10 ns. In the same way, events coming from lepton-gas interactions downstream the detector will produce particles arriving at the FCAL before the RCAL, with a time difference larger than the CAL timing resolution. Also cosmic events and electronic noise will appear asynchronous to the HERA time and would therefore be suppressed.

The selective physics logic has been implemented in the form of the software code which had harsh CPU speed performance requirements. In HERA II the information from the MVD and STT has been processed in the so called Global Track Trigger (GTT) (Fig. 3.22).

In most of the cases, when a tracking or vertex precision information was not required, the Second Level Trigger repeated the FLT selective logic with better precision, and more sophisticated algorithms were ran only at the Third Level Trigger.

3.2.5.3 Third Level Trigger (TLT)

If the event is accepted by the GSLT, all the components send their information to the event builder (EVB), which combines their data, writes them in a standard format, and makes them accessible to the Third Level Trigger (TLT). The input rate to the TLT is ∼100 Hz, while the output rate is 3 - 5 Hz (up to 20 Hz at the late HERA II). Therefore the aim of the TLT is not only to reject background events but also to select the particular classes of *ep* interactions under investigation. The TLT consists of a series of algorithms written in a mixture of C and FORTRAN code, running on a dedicated farm (SGI, and later PC based), where a full event reconstruction is done. In addition to the reconstruction program, also some selection programs are run on the data, in order to select good *ep* events. The main information that the reconstruction program sends to the selection algorithms are the addresses and the energies of the calorimeter cells above threshold, and the parameters (momentum and position) of the tracks reconstructed by the tracking detectors. The resolution on the energy and on the track parameters is lower than that obtained with the final reconstruction program. After having accepted an event, the TLT sends the data via an optical link to the DESY computing centre, where the events are written to disk to be available for further offline reconstruction and data analysis.

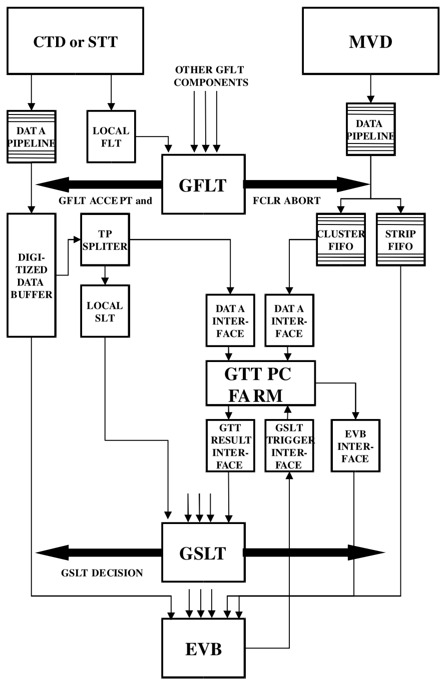

Figure 3.22: Schematic way the GTT was implemented in the ZEUS GSLT logic.

Chapter 4

Straw Tube Tracker

The Straw Tube Tracker (see Section 3.2.1.4) was introduced to ZEUS during the HERA upgrade in 2001 to extend the kinematic coverage and improve both the purity and efficiency of the particle track reconstruction and identification in the ZEUS forward region. The STT documentation can be found in [95–98, 117–122]. Chapter 4 and Section 5.2 in this thesis are introduced to extend the STT documentation.

Beyond the design, assembly and setup within the ZEUS detector, the STT operation splits in two parts:

- the data taking part includes the following regular checks:
  - dead straw list update,
  - gas mixture circulation,
  - voltage for the front end and remote electronics,
  - the signal from the straws readout and transfer,
  - the signal coding in the defined format,
  - storage in a global ZEUS event record.
- the operations which are not directly associated to the data taking:
  - STT geometry in terms of the straws position and rotation angles defined in the GAFs[1]
  - the STT alignment relative to other components,
  - the STT internal sectors alignment,

---

[1] GAF - Generic Adamo File. ADAMO is a system for scientific programming in FORTRAN and other languages, based on the Entity- Relationship (ER) model [123].

  - the straws response calibration,
  - the pattern recognition, which already partially accomplishes the STT purpose,
  - participation in the DAQ system, to reduce the non-physics background (see Sections 3.2.5, 4.2),
  - the combined track fit, which uses the output of the pattern recognition from the STT, MVD, CTD, and provides the final result for physics analysis,
  - visualisation of the STT elements in the ZEUS event visualisation software (Section 5.2).

This chapter describes several steps of the STT commissioning to which the author contributed. Some aspects of the STT commissioning can be found in [118–122].

Section 4.1 discusses the STT Signal Processing.

Section 4.2 discusses the STT Third Level Trigger software and its direct application.

Section 4.3 outlines the possibilities for physics analysis with the STT.

4.1 Digital Signal Processing

The sequence of the STT signal processing is shown on the Fig. 4.1. As it was mentioned in Section 3.2.1.4 the TRD infrastructure was used, therefore at the initial stage of the processing the STT straws were grouped by 6 straws per readout channel, one signal packet including 6 pulses. The signal in analogue form is sent then from the front-end board located on the STT sectors via a twisted pair cable for further processing to the crates located in a hut called Rucksack. The signal processing in the crates started with Flash Analog-Digital-Converters (FADC). The FADC output was the pulse train shown in Fig.4.2. The pulse train was truncated by the Digital-Signal-Processor (DSP) which ran dedicated software code, then the signal was passed to a Transputer based Read-Out Controller (ROC) and then on a positive trigger decision was transmitted to the Event-Builder (Fig. 3.21).

The FADC boards operated at 100 MHz which allowed one to make the time binning for the digitisation of the signal at 9.6 ns per bin[2]. The profile of the digital signal is given at Fig.4.2. For the purpose of increasing the information density of the transfered data the signal was truncated by the DSP according to

---

[2] The drift time information precision is determined by the frequency of 100 MHz.

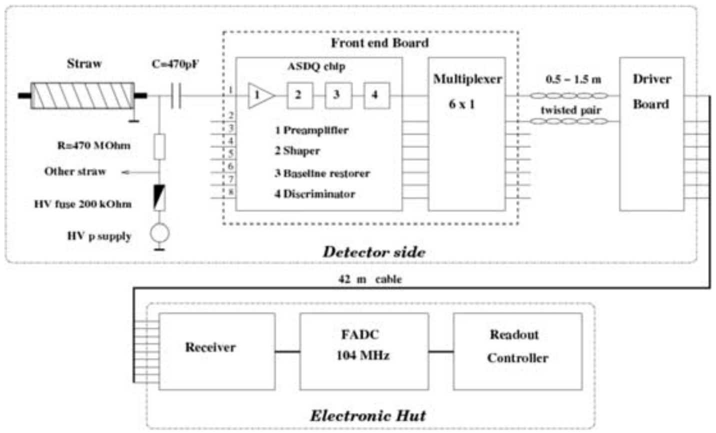

Figure 4.1: STT signal processing scheme.

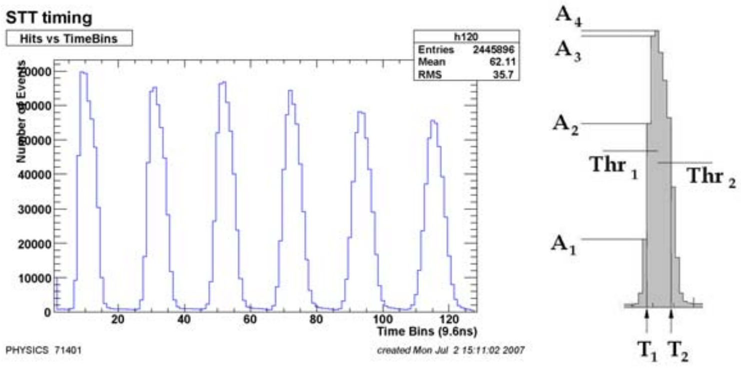

Figure 4.2: (left) The STT FADC pulse-train example for data taken in early 2004. Pulse-train contains drift time spectra of 6 straws combined in one readout channel. (right) The DSP coding-decoding definition of the signal coming from a straw.

the following logic. One packet could occupy 128 bins, which translates into ≈ 20 bins per one straw. Furthermore, one straw pulse could be packed without

losing the drift time information into 6 8-bit words[3]:

- T_1 - the time of the rise of the pulse,
- T_2 - the time of the drop of the pulse,
- A_1, A_2, A_3, A_4 - 4 values of the Amplitude of the pulse near T_1.

Hence, the data volume is reduced by factor ≈ 3.5. The DSP logic requires the following ratios to be valid:

- $A_1 < THR_1 < A_2$,
- $A_3 > THR_2$,

where the values of the threshold can be different for the rising part of the signal and for the falling part of the signal. They were set to be THR_1=60.0, THR_2=50.0.

As part of the Data Quality Monitoring a set of checks was developed by the author to ensure the correct performance of the DSP. The result of the checks was taken as the motivation for the next version of the DSP code release at the beginning of 2003.

4.2 Participation in the Trigger

This section describes the contribution of the author of the thesis to the non *ep*-physics background reduction at the TLT level (Sect. 3.2.5.3) by using the vertex information, reconstructed with the STT pattern recognition software.

4.2.1 Third Level Trigger

The increased luminosity at HERA II and beam related radiation of the vacuum produced high rates of background, and the logic of several trigger slots needed to be reconsidered, even at the cost of losing physics events. The STT positioned in the forward region of the detector was providing additional information about isolated tracks and the *ep* vertex position.

A version of the TLT STRECON with the vertex finding efficiency similar to the corresponding offline version was implemented at the TLT to reduce the rate of the TLT EXO 6 slot (aiming to select Charge Current (CC) events). The

---

[3] The 8 bits is actually the FADC precision.

CC TLT EXO 6 logic was designed to keep all possible CC events going in the forward region defined by low values of γ_{had} of the hadronic system:

$$\gamma_{had} = \frac{p_T^2 - (E - P_z)^2}{p_T^2 + (E - P_z)^2} \tag{4.1}$$

where $p_T,\ E,\ P_z$ are measured by the CAL, so that low values of γ_{had} correspond to the energy flow in the forward direction. In the offline analysis one of the standard cuts is $\gamma_{had} < 0.4$. This cut defines the region outside of the CTD acceptance and requires another approach for the background rejection with a tedious event-by-event eye-scanning.

The standard STT reconstruction software (STRECON) has been optimised for speed to fit the tight requirements of the TLT (TLT STRECON). The optimisation was done at the cost of the STT track efficiency. The vertex finding efficiency was kept at the same level (close to 100%). The slowest part of STRECON has been identified in the jet-like “busy regions″ with high occupancy, which were found to be of no importance at the trigger level. One “busy region″ was treated in TLT STRECON as a single track. The time reduction depending on the topology of an event was about a factor 20. On a data sample of TLT input events[4] the following numbers in the CPU time per event were obtained: for the standard offline STRECON $\sim$ 600 ms, TLT-STRECON $\sim$40 ms, to be compared to TLT-VCRECON (TLT-CTD) $\sim$30 ms. The reduced CPU time consumption by the TLT-STRECON allowed for its smooth running in sequence with the TLT-VCRECON. The occupancy sharing between the STT and the CTD make the CPU time consumption not an additive value, i.e. the average CPU time for the TLT code increased by a factor $\approx$ 1.3, comparing to the runs where the TLT-STRECON was switched off (or, equally, when the STT was excluded from the DAQ chain).

For the purpose of the purity increase of the TLT EXO 6 selection the new information from the STT has been considered. The logic of the TLT EXO 6 with an additional requirement on the STT vertex was coded in a new trigger slot, TLT EXO 20:

$$EXO20 = EXO6.and.((STT_{z-vertex}.or.CTD_{z-vertex}).or.(P_T^{CAL} > 30\ GeV)) \tag{4.2}$$

or in other words if the event has a $P_T > 30$ GeV, then the old EXO 6 logic is used.

First tests on a CC MC sample ($Q^2 > 100\ GeV^2$) gave an encouraging estimation of the possible inefficiency at the level of 0.7% (72/9873 events)(Fig.4.3). The tests on the MC sample of the final EXO20 configuration with 8575 events (taken by EXO6 in the range $8 < P_T < 30$ GeV) rejected only 2 events (inefficiency $\approx 0.03\%$).

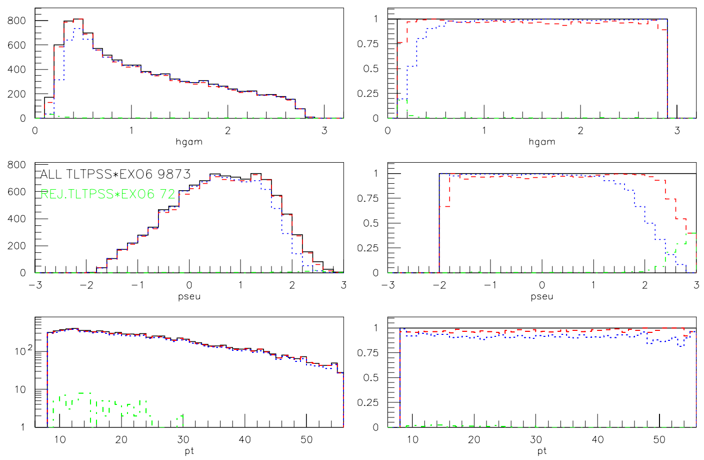

Figure 4.3: *The MC CC sample with $Q^2 > 100\ GeV^2$. Top: hadronic system γ_{had} distribution (left), and the efficiency of the STT and CTD vertex finding (right). Middle: same as in the Top, but the hadronic system γ_{had} is translated into the pseudorapidity of the hadronic system. Bottom: the event transverse momentum measured by CAL. Legend: solid line histograms - EXO 6 selection, taken as 100% for the right-hand plots, dotted line - EXO 6 with CTD vertex found in the range $\pm 100cm$, dashed line - EXO 6 with CTD or STT vertex found in the range $\pm 100cm$, dash-dotted line - EXO 6 with no STT and no CTD vertex found in the range $\pm 100cm$.*

Further tests have been performed on real data on a sample with 357 events selected by the standard offline cuts for the Charge Current selection[5] (13.9 pb^{-1}). In the sample 5 events have been rejected by the EXO20 logic, while 4 of them would have been removed by eye scanning in the event display. The remaining one event had an unclear signature favoring a CC physics event.

The conclusions from the tests were an increase in the purity of the selection by 1.1% (5/357 events) at the cost of $0.03 \div 0.70\%$(MC)/0.3%(data) inefficiency (Fig.4.3,4.4). The introduced inefficiency is located in the range 8 GeV$< P_T <$30 GeV.

---

[4] They are so called TLT passthrough events.

[5] The tests have been done by Catherine Fry, Imperial College London

The rate of the TLT EXO 20 was factor 10 smaller then the former EXO 6 (Fig. 4.5), yielding a 2% overall TLT rate reduction, which is the main achievement of the new trigger logic.

The CPU time of the TLT STRECON was at the level of the CPU time of the CTD tracking reconstruction by the VCRECON package.

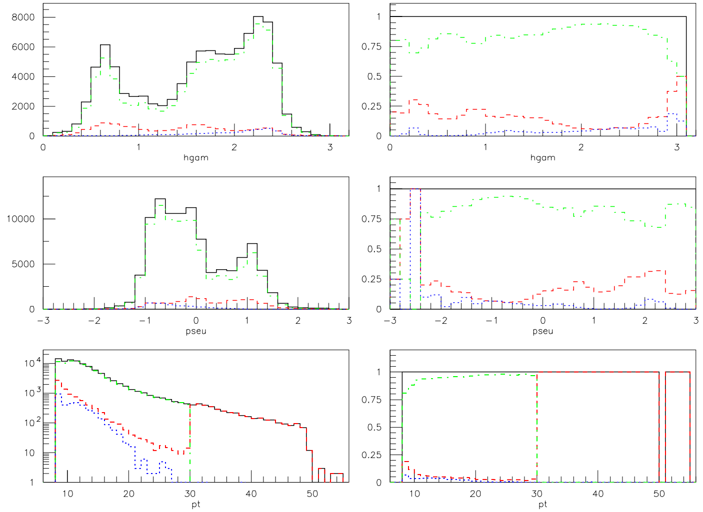

Figure 4.4: *The data sample preselected with TLT EXO 6. The plots description and the legend identical to Fig.4.3. The event rate with no vertex exceeds 75% at all values of γ_{had}.*

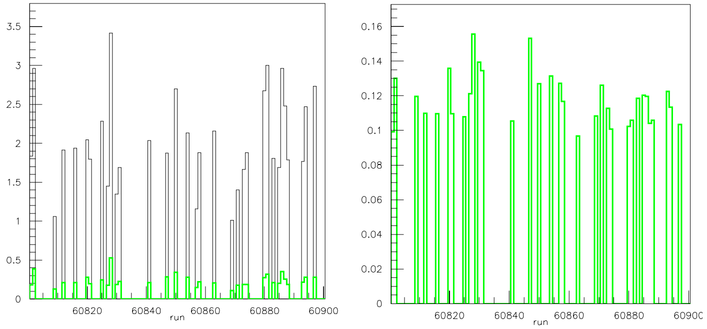

Figure 4.5: *The accepted event rates are presented for a range of runs from 60800 to 60900. (left) The slots EXO20 (grey) and EXO6 (black) are compared, the number of events is normalised to the luminosity in the run, (right) The relative fraction of the events triggered by EXO20 in the sample triggered by EXO6.*

4.3 Physics gain

The STT as a complementary tracking device extends the range of the available kinematic region for the measurement. Other physics tasks, which potentially benefit from the STT:

- Forward open charm production: D^*, D^{0+-}, and related to it,
- Open beauty production with a D^* tag,
- Strange hadrons production: K^0, Λ^0,
- Vector meson production at low W (both the electron and the muon decay channels),
- CC for low $\gamma_{had} < 0.4\ radians$,
- Lepton flavor violation ($\mu^+\mu^-/e\mu$),
- Exotics search: Penta- and tetraquark states, leptoquarks in NC$\rightarrow e + jet$.

So far the STT has been applied successfully to the CC studies, both the trigger and the offline analysis [124]. Other implementations are strongly dependent on the tracking issues, and will resume after the Grand Reprocessing of the HERA II data has been completed.

Chapter 5

ZEUS Event Visualisation - ZEVIS

ZEVIS (ZEUS Event Visualisation) - is the event visualisation tool for the HERA II phase of the ZEUS experiment, which provides the functionality required by the new detector components implemented during the HERA luminosity upgrade, in particular the silicon micro-vertex detector (MVD) and the forward straw tube tracker (STT). The basic concept and motivation has been described in detail in [125]. The design is centred around a client-server concept, which allowed to obtain random access to the ZEUS central event storage as well as to the events taken online via the HTTP protocol, even from remote locations. The client is a lightweight C++ application, and the ROOT system is used as underlying toolkit. Particular attention has been given to a smooth integration of 3-dimensional and layered 2-dimensional visualisations.

In the ZEUS experiment, new requirements have emerged with the installation of new detector components. In particular the silicon micro-vertex detector (MVD) and the forward straw tube tracker (STT) required more thoughtful $3D$ and $2D$ visualisation than the previous tool could have provided.

Sections 5.2-5.6 in this chapter describe the contribution of the author of this thesis to the ZEVIS software development.

5.1 Basic concept

The design of the event display is governed by two criteria described in the following (see also [125]).

The system should consist of a highly portable lightweight client, capable of running on many different platforms with the host possibly residing off-site, and a server application on a stationary host in direct contact with the event

store (on the DESY site). The term “light-weight″ implies that the client should be independent of the huge legacy libraries making up the main reconstruction and analysis code. The server application, on the other hand, should incorporate standard analysis tools. The connection protocol between client and server should be standardised and likely not to be stopped by firewalls.

Perspective $3D$ views with hidden lines and hidden surface removal proved to be very helpful to understand detector geometry. Standard projections in the straight-forward sense, e.g. along the beam line or transverse to it, present detector and event in such a way that coordinates can be measured, and every item is in principle visible. However, straight-forward projections can get too complicated in a multi-component detector, and do not fulfil their role in the cylinder symmetry geometry of the colliding-beam experiments. Layered projections are a good alternative to simple straight-forward ones. They use filled areas to show the geometry and the event but arrange them in layers such that all relevant information is visible.

The ROOT framework was chosen to moderate the graphics implementation of the application, since it provides drawing capabilities both for 2-dimensional graphics primitives as well as 3-dimensional graphics in wireframe mode and with hidden lines and surface removal. The ZeVis package is structured such that the client application depends only on one dynamically linked library, which contains the geometry and event classes. The server application uses several libraries which contain the classes to build the geometry and event in ROOT format from the ZEUS internal data model.

The data structures are designed using the built-in ROOT containers, in particular the TClonesArray. The geometry, which is loaded only once per session, is designed such that it can be drawn quickly without further modification, hence the data structures are all directly derived from ROOT geometry classes which are able to draw themselves. The present size of the geometry file is about 450 kB. The data event file should be compact in size since a typical event display session operates with many events. The data content is reflecting the event information in the official ZEUS mini-DST format, which is about 30 kB/evt. In layered projections, each geometry object acquires a 2-dimensional shape which can be different in each projection, e.g. the drift chamber outline is a circle in the XY view while it becomes two rectangles in a ZR view. The parallel implementation of $3D$ and $2D$ representations is achieved by *overloading* the Paint() *member function* in the derived geometry classes. A fish-eye view introduces a nonlinear transformation of radius and Z coordinate in the layered XY and ZR projections, with the aim to enable simultaneous inspection of inner (e.g. MVD) and outer tracking components (F/BRMUON) within the same picture. It is implemented by *overloading* the TView::WCtoNDC()

member function of ROOT.

5.2 STT elements visualisation

The STT is a complementary forward tracking detector with complicated geometry (Fig. 3.13). The hits are implemented by introducing a new class ZSTTRAWHit which *inherits* from TObject, a basic *abstract* class in ROOT. The STT straws are tubes with radius $\approx 8mm$, which is not very important for the visualisation, and due to the large number of straws they are visualised by simple straight lines (TPolyline3D objects). The $3D$ map of the STT straws is read from the geometry GAF files and referenced to when the information about the STT hits is converted into their $3D$ coordinates. The XY and $3D$ views implementation is straightforward as seen from Fig. 5.1, 5.2 . The ZR projection (Fig. 5.1, right-hand pad) requires a non-linear transformation of the lines (STT straws) from kartesian coordinates to its cylindrical representation. The solution is simplified by the requirement to draw only the projection of a curved straw, i.e. to translate only two distances and connect them with a line segment.

To be more precise, one ought to calculate the minimal and maximal distance from the straw to the z-axis in the straw plane perpendicular to the z-axis. Therefore, the ZR projection of a straw is linear and its length l_{ZR} is given by:

$$l_{ZR} = R_2 - R_1 \tag{5.1}$$

where R_1 and R_2 are the minimal and the maximal distance from the straw to the z-axis, R_1 is equal to the straw r coordinate, given for the straw centre in cylindrical coordinates of $ZEUS$, R_2 is the distance from the straw end-point to the z-axis, and it is related to both r and the straw length l:

$$R_2 = \sqrt{r^2 + (l/2)^2} \tag{5.2}$$

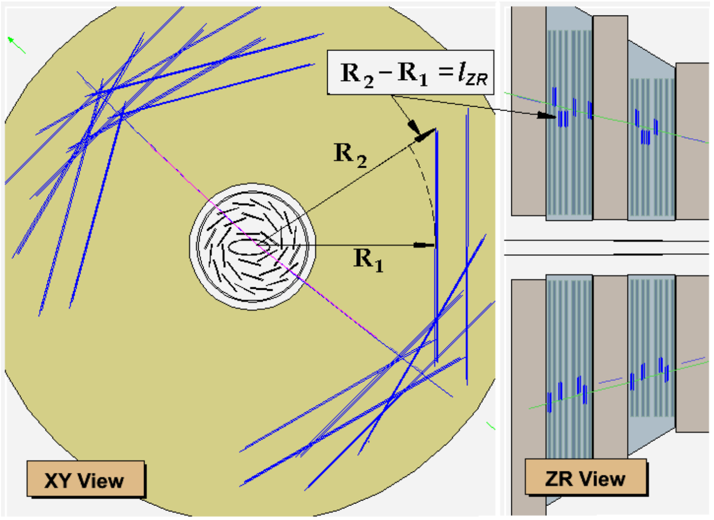

Figure 5.1: *A two muon event from an $\Upsilon(1S)$ meson decay is presented in the XY and ZR views. (left) XY projection of the STT straws geometry is identical to the orthogonal xyz geometry of the STT detector, (right) ZR projection shows the "transformed" side projection of the STT straws. The definition of the coordinates R_1 and R_2 of the ZR straw projection end-points is given in the text.*

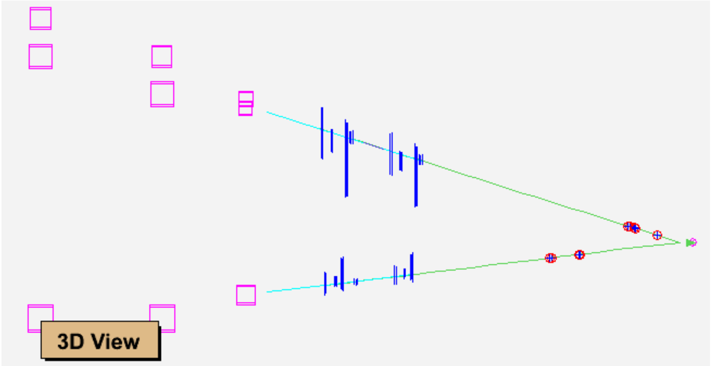

Figure 5.2: *An event example with STT hits seen in the $3D$ view. A two muon event from an $\Upsilon(1S)$ meson decay is presented in the transverse detector plane (ZY). The open (pink) boxes represent FCAL cells (EMC, HAC1, HAC2) with energy deposits in them, The vertical lines represent the STT straws hit by a muon, the circles with the crosses on the inside indicate the forward MVD silicon strips hit by the muon. The reconstructed tracks are drawn as helix curves (green) (the helix curvature is too weak to be seen on the plot) in the region from the vertex to the first STT straws and continued as straight lines (light blue) in the region throughout the STT volume up to the EMC FCAL cells.*

5.3 Hot keys

In order to facilitate the use of the $3D$ view a set of keyboard buttons, called ”hot keys”, has been associated with $3D$-space rotations. Below a short description of the keyboard buttons and corresponding actions are given. The ”hot keys”, which define the shifts along the axes set by the screening projections are given for completeness:

- ”q”,(”w”) - rotate by 5 degrees in Z-Y plane (counter-) clockwise,
- ”e”,(”r”) - rotate by 5 degrees in Z-X plane (counter-) clockwise,
- ”t”,(”y”) - rotate by 5 degrees in X-Y plane (counter-) clockwise,
- ”j”,(”k”) - shift the view along the axis perpendicular to the screen keeping the view perspective (zoom out (in)),
- ”h”,(”l”) - shift the view to the left (to the right),
- ”u”,(”i”) - shift the view upwards (downwards).

5.4 Special View, ZEUS forward display

An interactive tool ″Special View :: ZEUS Forward Display″ (Fig.5.3) is a visual representation of the Hough transform used in the STT track reconstruction algorithm implemented in the standard ZEUS reconstruction library. The ″Special View″ allows one to see the hits in the same way the reconstruction algorithm ″sees″ them. The ″Special View″ is a 2-dimensional ($tan(\theta)$, ϕ) histogram with fixed binning in both axes. The angles θ and ϕ are the angles at which the centre of the straw is seen from the assumed vertex position. The angle θ can be varied by a hypothesis on the vertex position (0,0,z). Each hit is seen as a symmetric parabola segment in the $tan(\theta) - \phi$ plane. The intersection of several hits plotted this way produces, as it can be seen from the figures, a peaking structure with the height giving the number of hits a real or a ”ghost” particle must have passed travelling at a straight line from the vertex. Typical values of a peak height are of the order of 20 hits. The tool allows one to see the algorithm and the detector component performance for the particles passing through the STT. The users can ″simulate″ the reconstruction algorithm logic by setting different threshold values above which the ″Special View″ peaks are taken as the seed areas to reconstruct the track candidate parameters, the z-vertex position can be changed as well to emulate ”ghost” tracks and vertices.

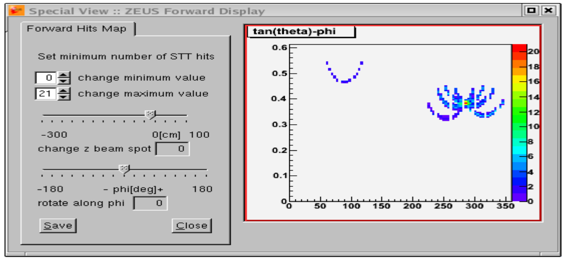

Set minimum number of STT hits
0 change minimum value
21 change maximum value
change z beam spot 0
rotate along phi 0

Figure 5.3: *STT hits depicted on the 2D histogram of the Special View. The horizontal axis is the ϕ angle in the ZEUS frame and the vertical axis is the $tan(\theta)$, where θ is reconstructed assuming an interaction point at $(Z = z, X = 0, Y = 0)$ cm in the ZEUS frame, z and ϕ are tunable via the slidebars on the left-hand side of the Special View window. The axises' have 100 bins each. The parabolas are the STT hits, which are the STT straws hit by the charged particle. The standalone hit in this figure is obviously located at the STT acceptance edge and is discarded in the reconstruction. In this figure the histogram is filled as if the hits are viewed from the nominal (z=0 cm, true position) vertex position. The height of the peak, 18 hits, can be treated as the probability measure of the reconstructed track to be a true track. If the peak height is close to the maximum number of the hits (24 hits) the hits have a high probability to be produced by a real charged particle. The hits in the peak are used to build the track seed. If a track seed has less than 8 hits the seed is discarded.*

An example of z-vertex position variation depicted in the Figures 5.4, 5.5 shows that the probability of a given 1-track event to originate from the vertex at $z = 50$ cm or $z = -300$ cm are significantly lower as seen from the "track" peak height, which is a factor 2 lower than in the original (true) hypothesis $z = 0$ cm (Fig. 5.3). The threshold variation option (Fig. 5.6) allows to see the area where the hits intersection gives the signature, corresponding to the most probable direction of the track. The tool has a ϕ-rotation feature, that allows the user to shift the whole $(tan(\theta), \phi)$ histogram leftwards (clockwise) or rightwards (counter-clockwise) (Fig. 5.7, 5.8) in case the region of interest is at the edge of the histogram.

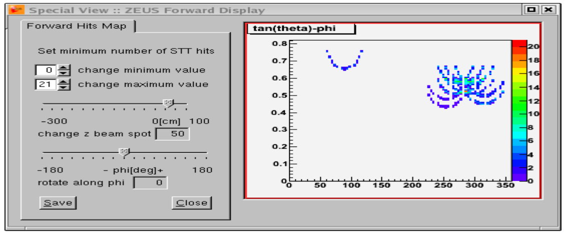

Set minimum number of STT hits
0 change minimum value
21 change maximum value
change z beam spot 50
rotate along phi 0

Figure 5.4: *STT hits viewed on the Special View. The histogram is filled as if the hits are viewed from the shifted (z=50 cm) vertex position.*

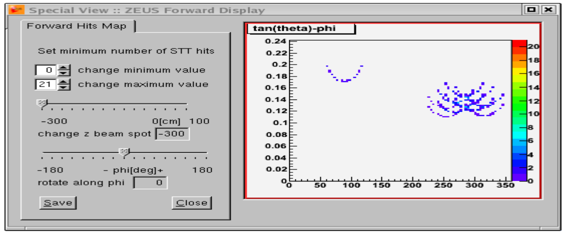

Set minimum number of STT hits
0 change minimum value
21 change maximum value
change z beam spot -300
rotate along phi 0

Figure 5.5: *STT hits viewed on the Special View. The histogram is filled as if the hits are viewed from the shifted (z=-300 cm) vertex position.*

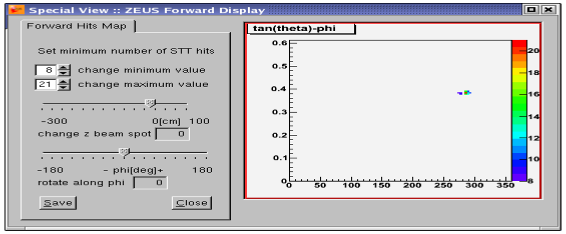

Set minimum number of STT hits
8 change minimum value
21 change maximum value
change z beam spot 0
rotate along phi 0

Figure 5.6: *STT hits viewed on the Special View. The histogram is filled as if the hits are viewed from the nominal vertex position. The threshold is set to be at least 8 hits.*

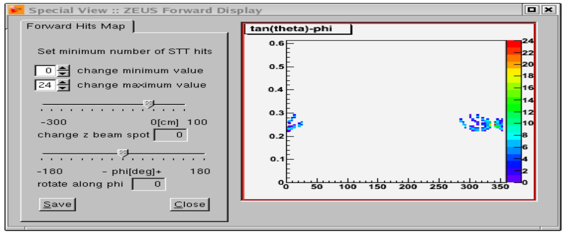

Set minimum number of STT hits
0 change minimum value
24 change maximum value
change z beam spot 0
rotate along phi 0

Figure 5.7: *STT hits viewed on the Special View. An event with a "badly" positioned peak is shown.*

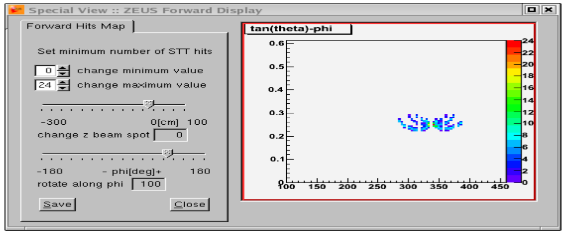

Set minimum number of STT hits
0 change minimum value
24 change maximum value
change z beam spot 0
rotate along phi 100

Figure 5.8: *STT hits viewed on the Special View. The same event (Fig.5.7) is shown with the shifted ϕ-axis edges.*

5.5 Easytool - user friendly navigation

The ZEUS detector upgrade for HERA II introduced not only two new components (the STT and the MVD) but also produced two extra types of tracks with respect to HERA I. The two new track types come from the tracking package which includes the hits from the MVD and the STT but treats the track candidates differently at the later stages of a full MVD-CTD-STT hit chain track fit. The former approach of switching ON/OFF the track types and detector component projections via a drop-down cascade menu is shown on Fig. 5.9.

This cascade type menu has accumulated a certain inefficiency.

A new approach with improved navigation has been implemented in a control panel called Easytool. The Easytool design and development was performed by the author of this thesis. It has a simple one-window layout split into three tabs. In its essence it is a new way to access the same visibility flags, which were available in the cascade menu (and still are for backward compatibility). The Easytool offers a user-friendly control over the system with a minimal number of mouse clicks. The window layout allows to add further functionality on top in a resource safe way. Extra useful features added to the Easytool track navigation tab include the control over the visibility of tracks via a set of logic conditions. The logic selection for the CTD superlayers and track transverse momentum were implemented in a form of number fields setting the minimum and the maximum allowed values for the track to keep its visibility. The conditional settings for the number of the STT and the MVD hits are kept in the code for test purposes, but hidden from the end user.

The Easytool consists of three tabs. The first tab "Tracks and Vertices" (Fig. 5.10) brings together all possible visualisation options for the event tracks and vertices. The second tab "Hits, cells, segments, etc." (Fig. 5.11) gives a good overview of the ZEUS detector components implemented (shaded with grey if the implementation is not complete) with possible splitting into the forward, barrel or rear parts of the detector. The third tab "Extra options" (Fig. 5.12) stores all the options used by the tracking experts or when a specific level of detail is required for a given event.

All the implementations described in this chapter have become default parts of the ZEVIS tool used by the whole ZEUS collaboration.

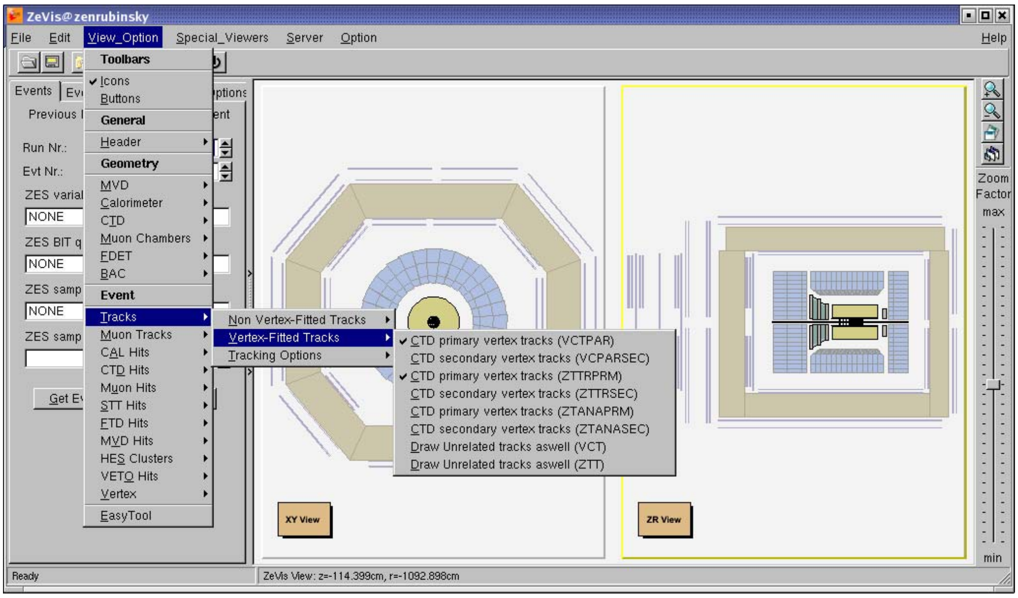

Figure 5.9: *The old navigation style, that controls the visibility of the track types and detector components. It requires 4 operations of mouse pointer navigation and it must be repeated every time for a single option to be changed.*

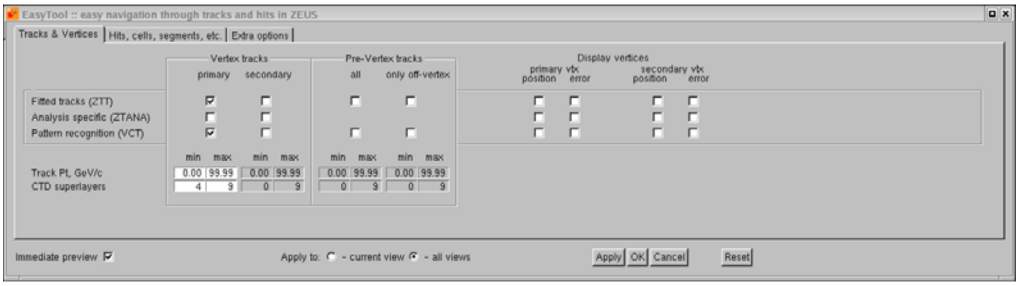

	Vertex tracks primary	Vertex tracks secondary	Pre-Vertex tracks all	Pre-Vertex tracks only off-vertex	Display vertices primary vtx position	Display vertices primary vtx error	Display vertices secondary vtx position	Display vertices secondary vtx error
Fitted tracks (ZTT)	☑	☐	☐	☐	☐	☐	☐	☐
Analysis specific (ZTANA)	☐	☐			☐	☐	☐	☐
Pattern recognition (VCT)	☑	☐	☐	☐	☐	☐	☐	☐

	Vertex primary min	Vertex primary max	Vertex secondary min	Vertex secondary max	Pre-Vertex all min	Pre-Vertex all max	Pre-Vertex only off-vertex min	Pre-Vertex only off-vertex max
Track Pt, GeV/c	0.00	99.99	0.00	99.99	0.00	99.99	0.00	99.99
CTD superlayers	4	9	0	9	0	9	0	9

Immediate preview ☑

Apply to: ○ - current view ● - all views

Figure 5.10: *The Easytool track and vertex tab.*

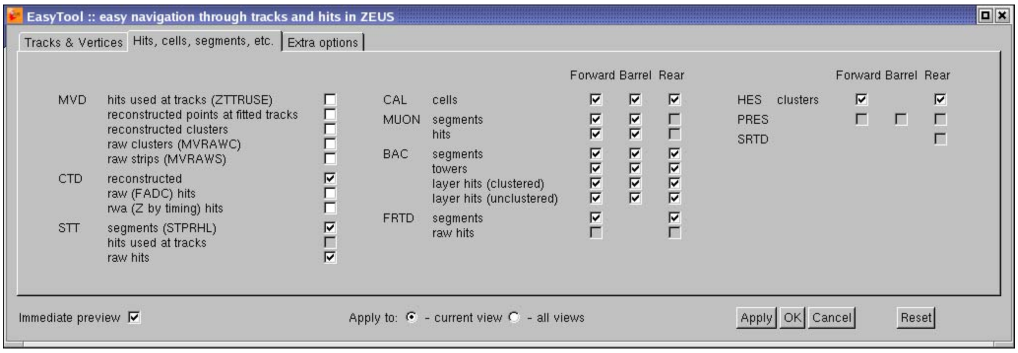

MVD	hits used at tracks (ZTTRUSE)	☐
	reconstructed points at fitted tracks	☐
	reconstructed clusters	☐
	raw clusters (MVRAWC)	☐
	raw strips (MVRAWS)	☐
CTD	reconstructed	☑
	raw (FADC) hits	☐
	rwa (Z by timing) hits	☐
STT	segments (STPRHL)	☑
	hits used at tracks	☐
	raw hits	☑

		Forward	Barrel	Rear
CAL	cells	☑	☑	☑
MUON	segments	☑	☑	☐
	hits	☑	☑	☐
BAC	segments	☑	☑	☑
	towers	☑	☑	☑
	layer hits (clustered)	☑	☑	☑
	layer hits (unclustered)	☑	☑	☑
FRTD	segments	☑		☑
	raw hits	☐		☐

		Forward	Barrel	Rear
HES	clusters	☑		☑
PRES		☐	☐	☐
SRTD				☐

Immediate preview ☑

Apply to: ● - current view ○ - all views

Figure 5.11: *The Easytool hits and track segments tab.*

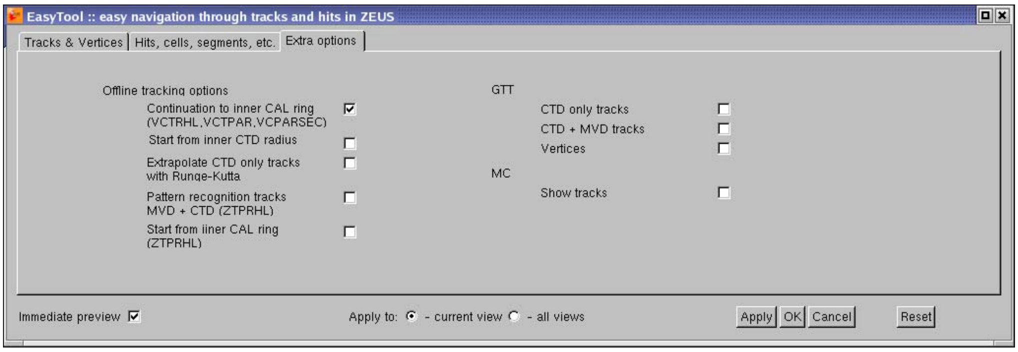

Offline tracking options

Continuation to inner CAL ring (VCTRHL,VCTPAR,VCPARSEC)	☑
Start from inner CTD radius	☐
Extrapolate CTD only tracks with Runge-Kutta	☐
Pattern recognition tracks MVD + CTD (ZTPRHL)	☐
Start from iiner CAL ring (ZTPRHL)	☐

GTT

CTD only tracks	☐
CTD + MVD tracks	☐
Vertices	☐

MC

Show tracks	☐

Immediate preview ☑

Apply to: ● - current view ○ - all views

Figure 5.12: *The Easytool extra options tab.*

5.6 Icon based menubar

An old Toolbar used to switch between the four running modes of the Event Display (Fig. 5.13) is described below.

- Request Event from Server - gives an opportunity to access an event (DATA only) by its Run and Event number and/or view all subsequent events which satisfy certain selection logic criteria,
- Download File from Server - allows to access a file (DATA or MC) located in the ZEUS storage system,
- Local File - allows to access a locally stored file (DATA or MC) produced with a specifically developed software program, which is also a part of the ZEUS Event Display software tools,
- Online Mode - allowed (during the data taking periods) to view the last event being registered by the ZEUS detector and written to the ZEUS offline storage system.

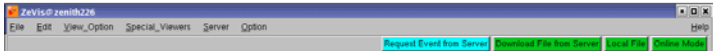

Figure 5.13: An old Toolbar to access the four running modes of the Event Display (see text).

A new Iconbar, depicted in Fig. 5.13, has been implemented in order to improve the face layout of the ZEUS Event Display giving it a more professional look. The new iconbar keeps all the necessary functionality from the old Toolbar and presents some actions from the main Menubar "*File*" section such as "*Open*" root file, "*Save*" an event display image, "*Exit*" the program, and from the "View_Option", newly developed "*EasyTool*".

Figure 5.14: A new Iconbar, which presents the necessary functionality from the old Toolbar and some actions from the main Menubar "$File$" section such as "$Open$" root file, "$Save$" an event display image, "$Exit$" the program, and from the "View_Option", "$EasyTool$".

Chapter 6

ZEUS detector simulation

This chapter gives some details of the ZEUS detector computer simulation. The measurements discussed in Chapters 9, 10 are done with muons, therefore special attention is given to proper simulation of the response of the detectors used for muon identification.

6.1 MOZART

The physics processes in terms of charged and neutral particle propagation in the media are simulated in the computer model of the ZEUS detector called MOZART based on GEANT (versions - 3.13 for HERA I and 3.21 for HERA II). GEANT follows the nested volumes concept. A detailed description of MOZART can be found in [91].

6.2 Muon detector response correction

Minimum ionising particles (mips) are the charged particles with $\beta\gamma \approx 3$ (see Fig. 6.1 taken from [126]). Muons in the energy range of relevance to the analysis presented in this thesis, $p_\mu \sim 1 \div 10$ GeV, while crossing material in ZEUS, lose energy through ionisation only and thus behave almost perfectly like mips. Their average energy loss in a calorimetric detector is often referred to as a ”mip”, which leave a characteristic signature in different detectors, ranging from the tracking system via calorimetry to the external muon systems. Consequently, there are several ways to identify muons, depending on the processes considered and the subdetectors used for the analysis. The corresponding software is called muon finders and includes the following packages: BREMAT and GLOMU (based on the information from BRMUON chambers), MPMATCH, MUFO, MAMMA

(FMUON), MUBAC (BAC). The logic of the muon finders will be discussed in Chapter 7. The MC simulation of the detector does not always reproduce the real life detector behaviour. The motivation for the corrections applied to the detector simulation and some implementation details, which are specific for this thesis, will be discussed in Chapter 8.

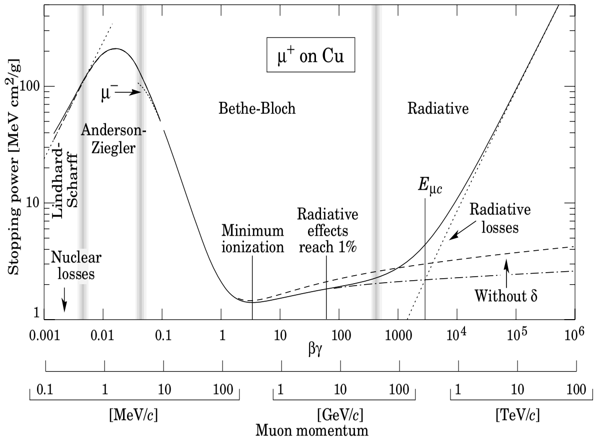

Figure 6.1: *Stopping power (dE/dx) for positive muons in copper as a function of $\beta\gamma = p/Mc$ over nine orders of magnitude in momentum. Solid curves indicate the total stopping power.*

Part III

Analysis part

Chapter 7

Signal definition and event selection

This thesis is devoted to the experimental study of Υ meson production at HERA with the ZEUS detector.

In Chapter 7 the experimental signature of the signal, exclusive Υ meson production decaying into muons, is defined. In Chapter 9 the backgrounds to the signal are discussed. In Chapter 8 the computer simulation of the relevant physics processes and the ZEUS detector response is discussed. The Υ cross section measurement in elastic Photoproduction (PHP, $Q^2 < 1$ GeV^2) and Deep Inelastic Scattering (DIS, $Q^2 > 1$ GeV^2) is discussed in Chapter 10.

7.1 Dataset

The results presented in this thesis are based on the data collected by ZEUS from 1996 to the end of running of HERA in June, 2007.

The PHP and DIS measurements require slightly different selections. In photoproduction the analysis is largely dependent on the BRMUON chamber efficiency due to the trigger selection, therefore the runs with reliable performance of the chambers are used (the runs are tagged with an MBTAKE flag) in addition to standard requirement of valid tracking (CTD), Solenoid, and CAL (EVTAKE flag). The cross section measurement in DIS depends on the CAL based trigger and muon finders (mainly CAL based), therefore the BRMUON chamber validity is not critical. The luminosity values for the runs used in the analysis are listed in Table 7.1.

The separation of the data by periods is motivated by:

- 96p-97p - proton beam energy still $E_p = 820$ GeV, in the following years raised to $E_p = 920$ GeV,

data period	Luminosity, pb^{-1} (EVTAKE)	Luminosity, pb^{-1} (EVTAKE & MBTAKE)
96p-97p	38.62	38.02
98e-99e	16.68	15.89
99p-00p	65.87	60.17
03p-04p	40.76	36.88
05e	134.61	126.90
06e	54.98	53.52
06p-07p	142.18	136.88
total	493.7	468.3

Table 7.1: *Luminosity measured in different data taking periods. The values are given for the runs with an EVTAKE flag and the runs where both EVTAKE and MBTAKE flags were ON.*

- 98e-99e, 99p-00p - electron/positron beams in HERA I detector setup, differences in the trigger configurations,
- 03p-04p, 05e, 06e, 06p-07p - HERA II detector setup, differences in the trigger configurations, muon chamber performance, tracking software versions, in 05e STT has been excluded from the DAQ.

7.2 Reconstruction of kinematic variables

The single particle kinematic variables, defined below, were reconstructed from the track momenta and their resolution is limited by the resolution of the tracking detectors (in HERA I - CTD only, HERA II - MVD+CTD(+STT)). The tracks are treated within a muon hypothesis based on the muon identification discussed in Section 7.4. The basic variables are:

- P - muon 4-momenta,
- p_x, p_y, p_z - x, y, z components of the muon momentum reconstructed by the tracking system,
- $p_T = \sqrt{p_x^2 + p_y^2}$ - transverse muon momentum,
- E - energy of the muon, reconstructed from the track full momentum and mass of the particle from the muon hypothesis, based on muon identification.

- $\eta = -ln(tan\frac{\theta}{2})$, muon pseudorapidity,
- θ - muon polar angle in the ZEUS coordinate system,
- ϕ - muon azimuth angle in the ZEUS coordinate system.

The following variables were used to define the dimuon system:

- $M_{\mu\mu} = |P_1 + P_2|$, effective mass of a dimuon system,
- $W = \sqrt{2E_p \sum_{1,2}(E - p_z)_\mu}$, the energy of the γp system in the elastic PHP case, where only two muons are produced in the reaction; the virtuality of the photon, Q^2, and the proton mass, m_p, are negligible, and E_p=920[1] GeV - proton beam energy,
- $\Delta\theta^{2D} = |\pi - (\theta_1 + \theta_2)|$,
- $\Delta\Omega = \Delta\theta^{3D} = |\pi - \theta^{3D}|$, where θ^{3D} (see Eq. 7.1) is the 3D openning angle between the two tracks,

$$cos\theta^{3D} = \frac{\vec{p_1}\vec{p_2}}{|p_1||p_2|}, \tag{7.1}$$

The $\Delta\theta^{2D}$ and $\Delta\theta^{3D}$ are defined in order to reject cosmic muons. In practice only one of the two variables is used to reject the events with two tracks forming a straight line in the detector frame system.

The momentum transfer $t = |P_p - P_{p'}|^2$ is measured only if the scattered proton stays intact and is detected by dedicated hardware, which is not the case in this analysis. In elastic PHP, i.e. for[2] $Q^2 \lesssim 1$ GeV^2, a good approximation to the $|t|$ measurement is $|t| \approx p_T^2$, where p_T is the transverse momentum of the dimuon system.

In the DIS case, the scattered electron is detected and the $|t|$ value can be determined with better accuracy, than in PHP, due to an additional constraint from the electron p_{Te}:

- $|t| = (\sum_{1,2} p_{x\mu} + p_{xe})^2 + (\sum_{1,2} p_{y\mu} + p_{ye})^2$.

In DIS the so called constrained method was used in order to improve the resolution of DIS specific variables:

---

[1] $E_p = 820$ GeV for 1996-1997 data and MC samples.

[2] In the elastic case a more precise requirement is $p_T^{\mu\mu} \gg p_T^e$, the transverse momentum of the dimuon system should be much greater than the transverse momentum of the scattered DIS electron.

- E'_e (see Eq. 7.2), the energy of the DIS electron calculated from the polar angle, θ_e, of the scattered electron, known with good precision, $E_e = 27.5\ GeV$, the energy of the incoming electron, and $(E - P_z)$ of the produced muons,

$$E'_e = \frac{2E_e - \sum_{1,2}(E - p_z)_\mu}{1 - cos(\theta_e)}, \tag{7.2}$$

- $Q'^2 = 2E_e E'_e(1 + cos(\theta_e))$, the event Q^2,
- $W' = \sqrt{-Q'^2 + m_p^2 + 2E_p \sum_{1,2}(E - p_z)_\mu}$, the event W,

7.3 Trigger

The trigger selection of the events is limited in PHP to the trigger bits with the logic based on the information from the Barrel, Rear, and Forward Muon Chambers, and in DIS to the trigger bits based on the reconstruction of the scattered DIS electron (see Appendix A).

7.4 Muon identification

As it was mentioned earlier the information from CAL, BRMUON, FMUON, and BAC was used to identify muons. The relevant software algorithms are collected in a so called GMUON package, which includes 8 separate muon finders: MIP, MV finders (CAL)[127], GLOMU, BREMAT (BRMUON)[128], MPMATCH, MAMMA, MUFO (FMUON)[129, 130], and MUBAC (BAC)[131]. Detailed information on GMUON can be found in [85, 132].

Main features of the finders are:

- MIP - the most straightforward algorithm. It performs a simple matching of CTD tracks with a CAL island consistent with a mip signature. Main features:
  - angular coverage - CTD acceptance limited,
  - high efficiency for muons with $p_T > 2$ GeV,
  - it can be applied only to isolated muons.
- MV - a multidimensional polynomial function that gives a probability of a CAL cluster to be a mip (muon). It uses both the CAL cluster shape and energy to match with the CTD track momentum, when the latter is avilable. Main features:

  - angular coverage - CAL geometry limited,
  - its efficiency is similar to the MIP finder in the CTD acceptance region,
  - high efficiency for muons with $p > 1$ GeV,
  - it can be applied only to isolated muons,
  - capable to identify muons with no-CTD track match,
  - a version of the MV finder has been implemented at TLT level.

- GLOMU - a Distance of Closest Approach (DCA) type match of a CTD track to an inner, outer, or inner+outer BRMUON track segment. A match to a mip cluster is also required. Main features:
  - angular coverage - BRMUON chamber geometry limited,
  - muon p_T range compatible with that of a MIP finder, but with lower threshold $p_T \approx 1.5$ GeV,
  - it can be applied mostly to well isolated muons,
  - in the MC the muon chamber response requires corrections,
  - a TLT version of this algorithm implemented in TLT MUO 3 is mostly identical to the described (offline) version, but its preupgrade version (year$\leq$2000) does not perform a match to the outer BRMUON chambers only,
  - a TLT version of this algorithm implemented in TLT EXO 11,12 does not require a mip coincidence.

- BREMAT - a more sophisticated matching algorithm than in GLOMU. It is based on GEANE [133] for a full CTD track extrapolation to the muon chambers using the full error matrix. It also calculates the χ^2 from the full error matrix to quantify the matching probability. The matching is performed to either inner BRMUON chambers only (4 degrees of freedom (dof)) or to outer or inner+outer chambers (5 dof). In the latter case, momentum consistency (magnetic field + multiple scattering in the BAC) provides an additional degree of freedom to the fit. The BREMAT documentation is well maintained [134]. Main features:
  - angular coverage - BRMUON chamber geometry limited,
  - muon p_T range is limited by the lower threshold $p_T \approx 1.5$ GeV,
  - it can be applied regardless of muon isolation,
  - in the MC the muon chamber response requires corrections,

  - appropriate GEANE settings must be chosen by the user, as they are not included by default.

- MAMMA - an FMUON chamber track segment or FMUI hits match to a CAL mip and/or CTD track. Main features:
  - angular coverage - FMUON chamber geometry limited,
  - muon p rangeout threshold is above ≈ 2 GeV,
  - it can be applied only to isolated muons,
  - in the MC the muon chamber response requires corrections,
  - mainly designed for TLT.

- MPMATCH - a combined Kalman filter fit of an FMUON track segment to a CTD track. The fit is based on track extrapolation using GEANE and on a combined momentum requirement. Main features:
  - angular coverage - limited by the FMUON chamber geometry and CTD acceptance,
  - muon p rangeout threshold is above ≈ 2 GeV,
  - a CTD track is required to originate at the primary vertex,
  - it can be applied regardless of muon isolation,
  - in MC the muon chambers response requires corrections,
  - appropriate GEANE settings must be taken by the user, as they are not included by default.

- MUFO - an algorithm similar to MPMATCH. A Kalman filter fit is performed from an FMUON track segment towards the primary vertex. The CTD track is not required, but is used when available. Main features:
  - angular coverage - FMUON chamber geometry limited,
  - muon p rangeout threshold is above ≈ 2 GeV,
  - a primary vertex must exist,
  - it can be applied regardless of muon isolation,
  - in the MC the muon chamber response requires corrections,
  - appropriate GEANE settings must be chosen by the user, as they are not included by default.

- MUBAC - strictly speaking the MUBAC algorithm reconstructs the BAC standalone track segments based on its pad and strip information. In the following the term is applied to a simple DCA match between a CTD track and such a BAC track segment. Main features:
    - – angular coverage - BAC geometry limited,
    - – muon p_T rangeout threshold is higher than the one for the BRMUON inner chambers (4dof BREMAT), but lower than that for the outer chambers (5dof BREMAT),
    - – it can be applied regardless of muon isolation,
    - – in the MC the BAC response requires corrections.

A coherent use of all 8 finders in a so called GMUON approach covers the maximum possible phase space and reduces the systematic uncertainties for muon identification making an analysis robust and the result more stable. A natural extension of the GMUON logic is in the assignment of a quality flag. In general the quality of a muon increases if it is identified by a larger number of finders, but in practice the logic is more complicated and is defined in Tables 7.2, 7.3.

The "quality" of muons defined this way allows fast preselection of the events with good signal/background ratio and tighter muon identification cuts can be developed later fitting the purposes of the analysis. Reasonable starting values for most of the inclusive analyses (original goal of GMUON) are muons with quality ≥ 4. For the analyses with well isolated muons this cut should be lowered, and could in principle start e.g. with ≥ 0.

The GMUON approach is derived to use in a consistent way the information from different and in most cases independent detector components. An ideal solution would be to perform a closed-cycle fit including the information about hits and full error matrices in all detector components in the same framework simultaneously in a similar manner in which the combined MVD+CTD+STT track fit has been performed. This has however not been implemented so far.

7.5 Tracking and Vertex Reconstruction

From the tracking point of view the selection is quite straightforward. In HERA I the tracking is based on CTD-only, and in HERA II on the combination of the CTD and MVD+STT hits. The charged track transverse momentum resolution for HERA I data (MC) is described by the formula [135]:

$$\sigma(p_T)/p_T = 0.0058 p_T \oplus 0.0065 \oplus 0.0014/p_T \tag{7.3}$$

quality	finder combination	CTD	match prob. /DCA	vtx ass	mip prob.	range
6	BREMAT 5dof	yes	>0.01	yes	-	-
	MPMATCH or MUFO	yes	>0.05	-	-	-
	MPMATCH/MUFO + MV	yes	>0.01,<0.05	-	>0.6	p>1
5	BREMAT 4dof + MV	yes	>0.01	yes	>0.6	$\lvert\eta\rvert > 0.6$
	MUBAC+MV	yes	-	yes	>0.6	$\lvert\eta\rvert > 0.6$
	MUBAC+BERMAT 4dof+MV	yes	>0.01	yes	>0.6	$\lvert\eta\rvert < 0.6$
	MUBAC+BERMAT 5dof+MV	yes	>0.01	no	>0.6	-
	MPMATCH or MUFO	yes	>0.01,<0.05	-	-	-
	MUFO good vtx	no	-	yes	-	-
	MAMMA+CTD	yes	-	-	impl.	-
4	BREMAT 4dof	yes	>0.01	yes	-	-
	MUBAC	yes	50 cm	yes	-	-
	MUBAC + MV	yes	120 cm	yes	>0.6	$\lvert\eta\rvert < 0.6$
	MUBAC + MIP	yes	120 cm	-	impl.	$p_T > 2$
	MUFO other vtx	no	-	yes	-	-
	MAMMA + vtx	no	-	-	impl.	-
3	MV	yes	-	yes	>0.95	$p > 1$
	BREMAT 5dof	yes	>0.01	no	-	-
	GLOMU + MV	yes	implicit	-	>0.6	-
	MUBAC + MV	yes	120 cm	-	>0.4	$p > 1$
	MUBAC + GLOMU	yes	implicit	-	-	-
	MAMMA	no	-	-	impl.	-
2	MV	yes	-	yes	>0.8	$p > 1$
	MUBAC	yes	120 cm	yes	-	-
	BREMAT 4dof	yes	>0.01	no	-	-
	GLOMU	yes	implicit	-	-	-
1	MV	yes	-	yes	>0.6	$p > 1$
0	MV CAL only	-	-	-	>0.4	$p > 1$
	MIP	yes	-	-	impl.	$p_T > 2$
-1	BREMAT 5dof	yes	<0.01	-	-	-
-2	BREMAT 4dof	yes	<0.01	-	-	-
-3	any finder. same CTD track	yes	-	-	-	-
-999	MC μ not reconstructed	-	-	-	-	-
-1000	MC π, K decay not reconstructed	-	-	-	-	-

Table 7.2: *Default muon quality assignments. CTD - yes/no, for a match with the tracking system (CTD for HERA I, MVD/CTD/STT - HERA II); mip prob, probability for the CAL island to be a mip (quantitative only for MV finder, other finders based on CAL use it implicitly).*

Finder combination	relevant property	value	quality change
MPMATCH or MUFO	Number of d.o.f.	3	-2
MPMATCH or MUFO	Number of d.o.f.	1	-3
MPMATCH or MUFO	start at inner plane (FMUi)	no	-1
MPMATCH or MUFO	match to MUBAC	yes	+1
MPMATCH or MUFO	MV match: MV prob.>0	yes	+2
MUBAC	not (MPMATCH or MUFO) and $\eta^{\mu} > 1.2$	yes	-1

Table 7.3: Quality values for forward muons redefined at ntuple(analysis) level. The quality values were corrected by the "quality change" numbers.

in principle, the same kind of parametrisation can be produced for the HERA II combined MVD+CTD tracking [136]:

$$\sigma(p_T)/p_T = 0.0026 p_T \oplus 0.00104 \oplus 0.0019/p_T \tag{7.4}$$

However, the HERA II tracking used in this analysis is not final and slightly different in different HERA II years due to the reconstruction software versions, therefore there is no final parameterisation beyond the one given in Equation 7.4.

The resolution both for the CTD-only and for MVD+CTD tracks is dependent on the number of CTD superlayers a particle passed. The resolution for the effective mass of two tracks is dominated by the track with the worst resolution. For the analysis with two muons with average $p_T \approx 4.5 - 5$ GeV the number of CTD superlayers for each track was selected to be ≥ 5.

- two tracks of opposite charge originating from the event vertex were required,
- the vertex position was,
  - in $|Z|_{vtx} < 50$ cm,
  - in XY plane the deviation from the nominal beam spot position[3] < 0.5 cm,
- each of the track transverse momenta $p_T > 1.5$ GeV,
- each of the tracks passing at least 5 superlayers in CTD,
- the effective mass of the two tracks must be in the range $[5:15]$ GeV.

---

[3] HERA I - {0,0}, HERA II electron beam - {1.33 cm, 0.20 cm}, positron beam - {1.92 cm, 0.17 cm}

7.6 Elasticity

Event elasticity for an exclusive event can be defined from the CAL island energy distribution being consistent with the detector noise. This requirement rejects neutral particles in the detector, suppresses the proton dissociative event background, seen by the non-zero energy in the FCAL. The CAL island energy noise level was quantified by means of events taken with a so called random trigger (FLT 16), which takes events based on the HERA clock only. The fraction of physics events in the random trigger selection is negligible. The CAL island energy noise level was defined by the combined EMC+HAC islands (after the energy corrections for the dead material in the detector) < 0.5 GeV and by its contributions in the EMC and in HAC separately (before the corrections have been applied) < 0.4 GeV each. The difference between these two methods of defining the elasticity threshold is taken into account as one of the systematic errors (Sect. 10.6).

7.7 DIS electron selection

The events for the DIS cross section measurement were selected by requiring one candidate found by a so called Sinistra electron finder. The Sinistra finder is a neural network based algorithm comparing the EMC-HAC energy deposits. In order for a candidate to be treated as an electron it must have a probability > 0.9 at the Sinistra output.

In case a Sinistra candidate had a CTD track match, the track multiplicity requirement was raised to 3 tracks per event.

In order to identify reliably a DIS electron it must have deposited its energy in the CAL leaving a characteristic electromagnetic shower shape with Moliere radius ≈ 5 cm (transverse to the shower growth direction). Therefore a set of (period dependent) cuts was implemented.

The offline selections were:

- In HERA I the X-Y position of a Sinistra candidate was restricted such that a symmetric box-like area around the RCAL beam pipe would be excluded:

  $|X_{electron}| < 13$ cm, $|Y_{electron}| < 8$ cm.
- In HERA II the RCAL towers were shifted in the direction opposite to the direction of the shift of the nominal beam spot. For these reasons the box cut is shifted in X and increased in Y:

  $-14\ cm < X_{electron} < 12$ cm, $|Y_{electron}| < 14$ cm.

The Sinistra electron candidate must have an energy > 10 GeV.

7.8 Event selection for the Υ PHP cross section measurement

The final event selection for the cross section measurement (see Chapter 10) is:

- Trigger selection: a logical OR of BRMUON and FMUON trigger bit chains (Appendix A),
- CAL global timing $|t^{CAL}_{global}| < 10$ ns (Sect. 9.1.1), applied to the data only since it is not simulated in MC; the resolution of t^{CAL}_{global} is ~ 1 ns, therefore the limit value of 10 ns is extremely safe,
- only two tracks in CTD (in HERA II CTD+MVD+STT) fitted to same (primary) vertex,
- each track passes at least 5 superlayers in CTD,
- primary vertex position (Sect. 9.1.1):
  - Z coordinate: -50 $< Z <$ 50 cm,
  - XY plane: $\sqrt{(X_{vtx} - X_{nominal\ b.spot})^2 + (Y_{vtx} - Y_{nominal\ b.spot})^2} < 0.5$ cm,
- each track $p_T > 1.5$ GeV,
- anticosmic rejection: $|\pi - \theta_1 - \theta_2| > 0.1$, where θ_1 and θ_2 are the tracks polar angles in the ZEUS coordinate system (Sect. 9.1.1),
- muon identification is partially based on GMUON quality requirement and is a logical OR of:
  - both tracks are identified as muons in GMUON block with quality ≥ 4,
  - only one track is identified as a muon in GMUON block with quality ≥ 4, the second one has quality < 4, but is found by MIP or MV finders with probability > 0.4,
- invariant mass of two muons is in the range $5 < M_{\mu\mu} < 15$ GeV,
- pseudorapidity distance between two muons $|\eta_{\mu_1} - \eta_{\mu_2}| < 1.5$ (Sect. 9.1.2),
- event elasticity:
  - sum of energy in FCAL inner ring (40 cm around the beam pipe) $\sum_{i=1}^{N} E_i^{zufo} < 1$ GeV,

  - CAL islands outside of the FCAL inner ring and not associated to muons are allowed to have energy $E^{zufo} < 0.5$ GeV, consistent with the detector noise,

A typical event, which qualifies the selection criteria, is presented in Fig. 7.1.

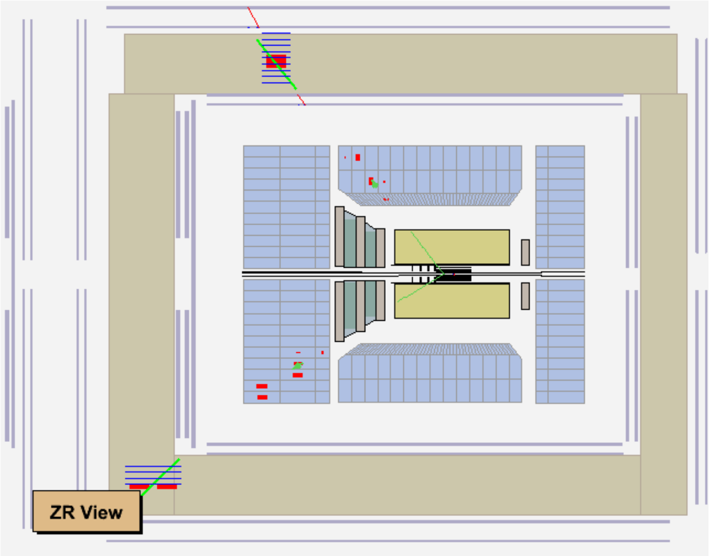

Figure 7.1: A typical elastic photoproduction event, which qualifies the selection criteria. An event from elastic MC Υ sample.

7.9 Event selection for the Υ DIS cross section measurement

The final event selection for the cross section measurement (see Chapter 10) is:

- Trigger selection: a logical OR of DIS, BRMUON and FMUON trigger bit chains (Appendix A),

- CAL global timing $|t^{CAL}_{global}| < 10\ ns$ (Sect. 9.1.1), applied to the data only,
- one Sinistra candidate with energy $E_e > 10$ GeV,
- the probability > 0.9 for the CAL island to be an electron is required by the Sinistra algorithm,
- the X, Y position of the Sinistra candidate is set by the period dependent selection:
  - In HERA I the X-Y position of a Sinistra candidate was restricted such that a symmetric box-like area around the RCAL beam pipe would be excluded:
    $|X_{electron}| < 13$ cm, $|Y_{electron}| < 8$ cm.
  - In HERA II the selection along the X axis is asymmetric and increased in Y:
    $-14\ cm < X_{electron} < 12$ cm, $|Y_{electron}| < 14$ cm.
- if a Sinistra candidate has no CTD track match: two CTD[4] tracks fitted to same (primary) vertex,
- if a Sinistra candidate has a CTD track match: three CTD[4] tracks fitted to same (primary) vertex,
- muon identification is partially based on GMUON quality requirement and is a logical OR of:
  - both tracks are identified as muons in GMUON block with quality ≥ 4,
  - only one track is identified as a muon in GMUON block with quality ≥ 4, the second one has quality < 4, but is found by MIP or MV finders with probability > 0.4,
  - if both muons have quality < 4 they are required to be found by MIP or MV finders with probability > 0.4,
- primary vertex position (Sect. 9.1.1):
  - Z coordinate: -50 $< Z <$ 50 cm,
  - XY plane: $\sqrt{(X_{vtx} - X_{nominal\ b.spot})^2 + (Y_{vtx} - Y_{nominal\ b.spot})^2} < 0.5$ cm,
- each muon track passes at least 5 superlayers in CTD,

---

[4] in HERA II - combined CTD+MVD+STT tracks.

- each muon track $p_T > 1.5$ GeV,
- anticosmic rejection: $|\pi - \theta_1 - \theta_2| > 0.1$, where θ_1 and θ_2 are the muon tracks polar angles in the ZEUS coordinate system (Sect. 9.1.1),
- invariant mass of two muons is in the range $5 < M_{\mu\mu} < 15$ GeV,
- event elasticity:
  - sum of energy in FCAL inner ring (40 cm around the beam pipe) $\sum\limits_{i=1}^{N} E_i^{zufo} < 1$ GeV,
  - CAL islands outside of the FCAL inner ring and not associated to muons or to a Sinistra candidate are allowed to have energy $E^{zufo} < 0.5$ GeV, consistent with the detector noise.

A typical event, which qualifies the selection criteria, is presented in Fig. 7.2.

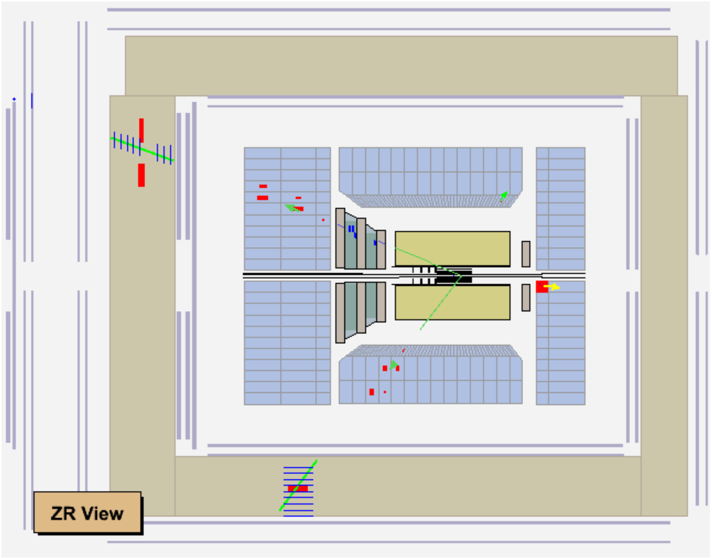

Figure 7.2: *A typical elastic DIS event, which qualifies the selection criteria. An event from elastic MC Υ sample.*

Chapter 8

Monte Carlo

This chapter describes the physics process simulation in ZEUS. The first level is the simulation of the physics processes in electron-proton collision and described in Section 8.1. In Sect. 8.2 details of the MC samples are presented. The particles produced in the simulated *ep* collisions are further propagated through the ZEUS detector components. Issues related to the details of the detector components simulation and muon identification are discussed in Section 8.3.

8.1 Generators

8.1.1 DIFFVM

The simulation of the vector meson production and decay is implemented in the ***Diffvm*** 2.0 software package [49]. The software program implements Regge phenomenology and the Vector Dominance Model (see Chapter 1.3) with a set of parameters, which can be set via the control cards. S-Channel Helicity Conservation (SCHC) [49] is assumed in the generation of the angular distribution of the decay products. The program is primarily used to generate samples of elastic production of the following vector mesons ρ^0, ω, ϕ, $\rho(1450)$, $\rho(1700)$, $\phi(1680)$, J/ψ, $\psi^{'}$, Υ, $\Upsilon^{'}$, $\Upsilon^{''}$.

Processes with dissociation of the proton can be generated as well. For the generation of the proton remnant M_Y spectrum ***Diffvm*** uses a parametrisation of the experimental data of the mass spectra of excited states of hadrons. This spectrum consists of some resonances-like structures superimposed on the diffraction dissociation continuum. The inclusive cross section for diffractive processes, at fixed t, can be parametrised as follows:

$$\frac{d\sigma}{dM_Y^2} \sim \frac{f(M_Y^2)}{M_Y^{2(1+\epsilon)}}, \tag{8.1}$$

where $f(M_Y^2)$ is a function of the diffractive mass at the proton vertex accounting for the low mass behaviour, including the resonance states.

Diffvm uses the following parametrisation for this function:

- in the continuum region ($M_Y^2 \geq 3.6\,GeV^2$), $f(M_Y^2) = 1$; this reproduces the behaviour $\sim \frac{1}{M_Y^{2(1+\epsilon)}}$ of diffractive dissociation,
- in the "resonance region" ($M_Y^2 < 3.6\ GeV^2$), $f(M_Y^2)$ is the result of a fit of the measured differential cross section, at fixed t, for proton diffractive dissociation on deuterium $pD \rightarrow YD$ [137];

The continuum state may dissociate into a quark-diquark system (simulated via ***Jetset*** [138]) or decay isotropically.

The t-distribution b parameter is set:

$$b(W, M_Y) = b(W_0, M_0) + 4\alpha_P^{\prime}(ln\frac{W}{W_0} - ln\frac{M_Y}{M_0}) \tag{8.2}$$

and is assumed to hold at all values of Q^2.

The W and Q^2 dependence of the cross section is given by:

$$\sigma^{\gamma^* p}(Q^2, W) \sim \frac{W^\delta}{(Q^2 + M_V^2)^n}, \tag{8.3}$$

where n ≈ 2.5 is an empirical parameter, $\delta = 4(\alpha_P(0) - 1)$ and M_V mass of the vector meson.

The ratio of the cross sections of the photons with transverse and longitudinal polarisation is given by:

$$R(Q^2) = \frac{\xi\frac{Q^2}{\Lambda^2}}{1 + \chi\xi\frac{Q^2}{\Lambda^2}}, \tag{8.4}$$

where Λ, χ, ξ are free parameters. The recommended values are $\Lambda = M_V$, $\chi = 0.66$, $\xi = 0.33$ [49].

8.1.2 GRAPE

The simulation of the QED lepton pair production (Bethe-Heitler) is implemented in the **Grape** 1.1k software package [139]. The QED processes are considered to be well known, however for the HERA physics some uncertainty is left due to determination of the electro-magnetic form factor of the proton, and the parton density functions. Moreover, different requirements to the accuracy of the calculations which include assumptions for the set of Feynman diagrams to be used can produce an effective difference on the cross section of the order of a few percent.

The **Grape** generator settings are read from the control cards. The QED lepton pair production off the proton can not be described in a homogeneous way. There are three kinematic regions defined with a different approach to calculations in each of them (Fig. 8.1). The three regions are:

- ELA - elastic production (the proton stays intact), calculation using proton electric and magnetic form-factors.
- QEL - quasi-elastic (the proton dissociates), calculation based on the electromagnetic proton structure functions, which are parameterised with [140] for $M_Y < 2$ GeV and with [141] for $M_Y > 2$ GeV, the exclusive hadronic final state is generated using the MC event generator **Sophia** [142].
- DIS - deep-inelastic scattering. The scattering occurs on a quark in the proton. The calculations are based on parton density functions (PDFLIB [143]) interfaced to **Pythia** [144] to get complete hadronic final states. Unlike the standard HERA terminology this "DIS" is defined with the virtuality Q_p^2 of the photon off the quark.

The **Grape** recommendations on the Q_p^2 and M_{had} values to divide the phase space into three complementary regions are given in Fig. 8.2.

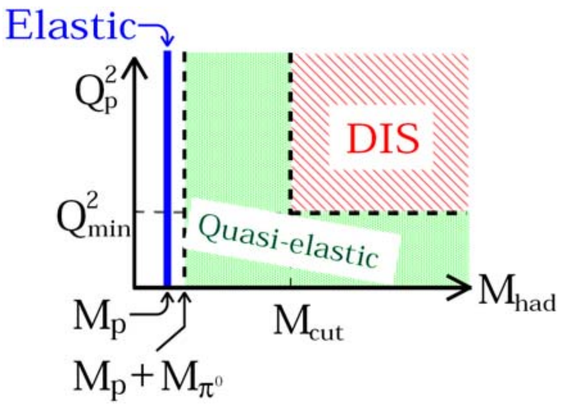

Figure 8.1: *The phase space divided by* **Grape** *. The term DIS corresponds to the $inelastic$ process definition at HERA. The Q_p^2 is the photon virtuality at the proton interaction vertex, and M_{had} is the mass of the proton remnant system (defined as M_Y in* **Diffvm** *).*

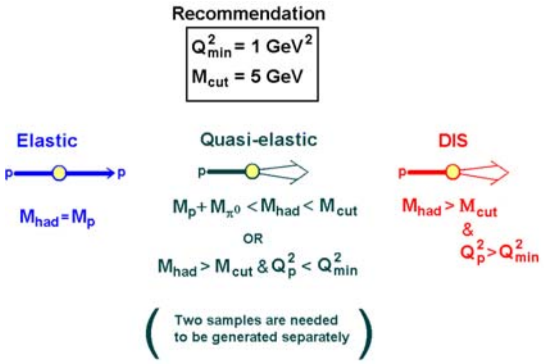

Figure 8.2: *The* **Grape** *recommendations on the boundary values to generate the QED dimuons and cover the whole phase space.*

8.2 MC samples

In order to produce an adequate simulation to the data sample used for the analysis (Ch. 10) the MC samples were generated in proportion to the luminosity of each data taking period (Sect. 7.1), and to the trigger subperiods accordingly[1]. A detailed list of the trigger subperiods and of the MC samples can be found in Appendix B.

The Υ meson elastic production in the three lower states (1S, 2S, 3S) decaying into muons have been simulated with **DIFFVM** . The Pomeron trajectory parameters were set:

- $\alpha_0 = 0.4$,
- $\alpha^{'} = 0$.

The t-slope parameter was set to $b = 4.0$ GeV^{-2} with no dependence on W as it follows from the $\alpha^{'}$ value. Further in the analysis the MC samples were reweighted to reproduce the value $b = 4.5$ GeV^{-2} (the weighted average of the J/ψ values measured in PHP and DIS). The parameter n=2.5 (Eq. 8.3). The parameters in Eq. 8.4 were set according to the recommendations.

Elastic J/ψ samples were generated for muon efficiency correction purposes (Section 8.3) and for the proton dissociation studies (Chapter 9.2.1). The Pomeron trajectory parameters were set:

- $\alpha_0 = 0.22$,
- $\alpha^{'} = 0$.

The t-slope parameter was set to $b = 4.0$ GeV^{-2}.

For the QED lepton pair production the samples were generated with **GRAPE** . As it follows from Figure 8.2 effectively there are 4 different samples to be generated. The Quasi-elastic sample can be split into QEL_1 and QEL_2, where:

- QEL_1: $1.08 < M_{had} < 5.0\ GeV$, $0 < Q_p^2 < 1000\ GeV^2$,
- QEL_2: $5.0 < M_{had} < 10^{20}\ GeV$, $0 < Q_p^2 < 1\ GeV^2$.

The DIS subprocess simulation steering allows to trace the contribution of γ-$quark$ interaction diagrams for different quarks (u, d, s, c, b, t) separately, as well as their antiquarks and quarks (antiquarks) different combinations. For simplicity the DIS samples were generated for an electron scattering off the u-quark only. An empirical[2] factor 1.8 was applied in order to correct the normalisation of the "DIS"(**GRAPE**) sample for the missing contributions from the scattering on other quarks.

The cross section of the four subprocesses defined above is given in Table 8.1.

Subprocess	cross section, pb
ELA	2052 ± 2
QEL$_1$	442.5 ± 0.4
QEL$_2$	85.7 ± 0.1
DIS (γ-u)	94.0 ± 0.1

Table 8.1: *The cross section of the four subprocesses of QED lepton pair production. The values were obtained for $E_{electron}$ = 27.5 GeV, E_{proton} = 920 GeV, muon pair production with $p_T > 0.5$ GeV for each muon. The errors for the cross section values are defined by the fine sampling of the phase space in the numeric method used in the calculations.*

8.3 Analysis specific corrections to MC

8.3.1 Muon related corrections

This section gives an introduction to the logic of the muon efficiency corrections. More information on the muon efficiency corrections can be found in [85, 145].

In particular, corrections for the BREMAT/GLOMU, MPMATCH/MUFO and MUBAC finders were calculated, supplemented by information from the MV finder. All corrections are designed to be applied exclusively to MC events, i.e. the real data events are taken as the reference and their efficiency is never modified. These corrections use some of the basic ideas that have been used in previous determinations of the muon efficiency corrections [146, 147].

8.3.1.1 Motivation for the corrections

The efficiency of the used subdetectors is not always well implemented in the MOZART simulations. The muon range (energy loss) and multiple scattering are not always perfectly simulated either. Therefore, the muon reconstruction

---

[1] In HERA I each data period included only one trigger subperiod, HERA II includes more subperiods due to low/high luminosity rates and developments in the early HERA II years: 03p-04p includes 5 subperiods, 05e - 4, 06e - 2, 06p-07p - 2 subperiods. Overall in HERA I - 3 trigger subperiods, in HERA II - 13.

[2] The FCAL energy and $|t|$ distributions were used to determine the missing part of the BH MC contribution.

efficiencies obtained from the MC, and used for the analysed physics process acceptance calculation, should be corrected in order to correspond to the real detector response.

There are two ways to develop and apply these corrections. The first approach (offered by the BRMUON experts from the Padova University group) is considering only corrections for the Barrel and Rear Muon Chamber. In this approach the corrections for the offline reconstruction and the FLT bits simulation are taken into account. It works well for the analyses using finders based only on the information from BRMUON chambers [148]. The second approach (followed in the analyses based on GMUON finders: in this thesis and [85, 121, 149, 150]) relies largely on the fact that a muon is usually identified by a combination of muon finders. This approach of the muon efficiency corrections can be called the "GMUON efficiency corrections".

8.3.1.2 Basic idea

There are several possibilities to correct the muon reconstruction efficiency at various stages of the muon simulation and reconstruction chain. The best option is to achieve a perfect description of all detector effects at the level of the detector simulation in Mozart.

This involves several ingredients.

- The simulation of muon propagation in the central tracking detectors.

  In these detectors, muons behave essentially like pions, i.e. the majority of the tracks in an event. Since tracking is one of the core parts of almost any analysis, considerable effort has been invested by the ZEUS collaboration to obtain a very precise simulation already at the Mozart level. Therefore, the efficiency of the tracking is assumed to be perfectly simulated. It has been thoroughly checked for the HERA I simulations. For the HERA II simulations, not all possible corrections have been implemented yet (e.g. MVD hit efficiencies), but can be expected to factorise and be applied independently of and in addition to the corrections discussed in this section.

- The simulation of muon propagation in material.

  The material of the central tracking detectors is almost negligible for muons. However, on their way through the ZEUS detector, muons need to cross i) the magnet coil, ii) the calorimeter, iii) the return yoke (BAC detector) and iv) potentially the magnets of the forward muon system. Muon detectors are placed in between the calorimeter and the yoke (inner BRMUON and FMUON chambers), inside the yoke (BAC), outside the yoke (outer BRMUON and FMUON chambers), and within the forward toroid system (toroid part of FMUON system) (see Chapter 3.2). While passing the ZEUS detector the muons may lose all their energy in the material due to ionisation and stop in the respective detector component, therefore not reaching muon chambers which are located further outside. Moreover, muons will be subjected to multiple scattering in this material. Together with a changing curvature in the magnetic field due to their energy loss, this will influence the position and angle at which muons will reach the muon detectors. This can have major consequences. If the muon energy loss is not simulated fully correctly, the probability for the muons to reach the muon chambers, and therefore to be detected there, is somewhat incorrect. In the ZEUS simulation, GEANT seems to be slightly underestimating the muon energy loss. Therefore, the probability to reach the muon chambers has a tendency to be too large. Indirectly, this also affects the position and angle simulation, since the muon tracks will be slightly less curved in the magnetic field, e.g. inside the yoke, than they should be. Furthermore, also the multiple scattering might be slightly less in the simulation than in reality. Both muon energy loss and multiple scattering also need to be accounted for in the reconstruction, i.e. for the extrapolation of the expected position and angle in the muon chambers, needed in the procedure of matching muon track candidates in the central detector to muon chamber hits and tracks. Since a self-consistent GEANT package is used for both simulation and extrapolation, the matching simulation for MC events will appear to be very good. However, since there is less bending and multiple scattering in the data than the MC assumes, the matching χ^2 will be slightly worse in the data than in the MC. Therefore, the efficiency for a cut on this χ^2 (or its probability) will not be fully correctly reproduced, and the matching efficiency will usually be slightly overestimated by the MC.

- For active material such as the calorimeter, the energy lost must be converted into a measured energy. Depending on the calibrations used, this can deviate significantly from the energy actually lost. Furthermore, the simulated detector response can differ from the actual one. In ZEUS, the reconstructed MIP energy has a tendency to be slightly larger than the one in real data. As long as the exact value of this energy is not used (but e.g. only a lower or upper limit), this does not have significant consequences for the muon reconstruction efficiency.

- Finally, for muons reaching the muon chambers, the muon detector hit and track reconstruction efficiency might not be correctly simulated. For example, the hit efficiency of the BRMUON and BAC detectors is 100% in the simulation, such that effectively only the geometric acceptance is taken into account. In reality the efficiency is significantly less than 100%. This is the single largest effect to be corrected for, and can lead to correction factors in the range 0.6-0.9. In contrast, the FMUON hit efficiency is simulated already at the Mozart level, such that for high momentum tracks (not suffering strongly from the imperfect rangeout and multiple scattering simulation) the further corrections needed are expected to be small.

The inefficiencies mentioned above will usually affect both the online muon trigger simulation and the offline reconstruction of simulated muons in a different but correlated way.

To compensate for incomplete simulations at the Mozart/GEANT level, corrections can be applied at the level of the muon reconstruction software. For example, a muon hit efficiency correction package for the BRMUON system [147] has been implemented in the ZEUS software package ORANGE. This package reevaluates the efficiency for each muon hit, and removes it if appropriate. The resulting modified efficiencies are propagated to the first level trigger simulation, and to the muon chamber track reconstruction, and therefore implicitly to all muon finders based on BRMUON information. They are unfortunately not (yet) propagated to the 2nd and third level trigger decisions. The advantage of this scheme is that local inefficiencies of the chambers are properly accounted for, including the correlations for several muons within the same event. Furthermore, a coherent treatment of (first level) trigger and reconstruction is possible. However, the simulation of the energy loss and multiple scattering inefficiencies is not yet corrected within this scheme, such that further corrections are needed at the final analysis level. Including such corrections, this scheme is very appropriate for analyses using the BRMUON chamber information only. Unfortunately, if information from other detectors with overlapping acceptance, e.g. BAC, is also included in the muon reconstruction, this scheme can lead to conceptual difficulties.

A similar scheme is under development for the correction of the BAC detector response [104, 105].

Finally, corrections can be applied at ntuple analysis level. In practice, whatever variant of Mozart simulations and reconstruction level corrections is used, some residual corrections will always be needed for the muon reconstruction in ZEUS. These corrections often dominate the systematic error of muon based analyses, and therefore are treated with highest attention. This is the type of the corrections implemented in the ″GMUON efficiency corrections″ approach and is therefore discussed further in detail.

The GMUON corrections are derived in such a way that they are applied to the result of the muon finding algorithms. This is usually done by selecting a clean reference sample in the data, for example a sample of elastic J/ψ and Bethe-Heitler events, and comparing the performance of the various muon finders on this sample (after all previous corrections, if applicable) to a corresponding sample in the MC. The ratio of the efficiencies found from data and MC is then the correction factor F to be applied to the MC for the efficiency of this finder:

$$F_{finder} = \frac{\epsilon_{finder}^{DATA}}{\epsilon_{finder}^{MC}}, \tag{8.5}$$

where the finder efficiency is idefined as the ratio of $N_{MV\&finder}$, the number of muons found by at least two finders, the MV finder and the $finder$ under study, and N_{MV}, the number of muons identified by at least only the MV finder:

$$\epsilon_{finder} = \frac{N_{MV\&finder}}{N_{MV}}, \tag{8.6}$$

Biases from the trigger and selection procedure can be eliminated as described below. This procedure has the advantage that it simultaneously corrects for all potential sources of inefficiency at once, whatever their origin is. Hence, it will account for muon chamber inefficiencies, rangeout probabilities, and matching inefficiencies at the same time in a single step. It has the disadvantage that the correction depends on the momentum and angle of the muon, and on the quality cuts applied, but this is an unavoidable problem in the last step of any muon correction procedure in the ZEUS data analysis.

The correction procedure is set for each finder for each muon candidate. This is achieved by treating the single muon finder correction factor as a survival probability rather than an event weight, i.e. by generating a random number and eliminating the finder entry if that random number is above the value of the correction factor. This procedure has the advantage that it does not depend on which finder combination is eventually used to identify the muon, that it does not depend on the number of muon candidates per event, and that it should automatically yield the correct fraction of any particular finder combination, even for multiple muons. The resulting finder combinations can be directly compared to the data. This procedure can hence be applied as a universal algorithm to many different analyses. It has the disadvantage that it relies on random numbers, which will lead to differing results from the same MC sample if care is not taken to treat the events always in the same order and with the same random number starting seed (of course, on average the results will stay the same). Furthermore, the procedure fails in case the correction factors are larger than 1, since it only allows a decrease, but not an increase of the detection efficiency[3]. To avoid

---

[3] It can happen if some kind of "averaged″ corrections have been already applied, and over

this problem as much as possible, it is preferable in some cases not to apply intermediate reconstruction level corrections, even if available, and to correct for all effects at once at analysis level, with correction factors which are usually sufficiently far below 1 in order not to cause problems.

In order to apply the Formula 8.5 the efficiencies for the Data and MC must be derived in an unbiased way. The MC samples contain all events, but the Data samples are strongly biased by the event preselection at the trigger level (the majority of the events is saved on tapes only if there is a BRMUON chamber signal, the efficiency of which is exactly being attempted to determine).

The condition is fulfiled in the dimuon event selection and the following trigger bias unfolding, a strategy to accept both or only one of the two muons to calculate the efficiencies.

8.3.1.3 Event selection for efficiency correction samples

The event selection must be such that it takes the maximum of the events with muons, at the same time the events should contain only physics events for which the physics process is well known.

At HERA the following processes are most suitable: elastic J/ψ and Bethe-Heitler (QED lepton pair production)[4]. The list of the MC samples is given in Appendix B.

The following cuts were applied to Data and MC:

- EVTAKE = 1, require only events with reliable CTD, CAL, Solenoid. MBTAKE ON, only allow events with working BRMUON chambers. FMUON chambers flag FMUTAKE - not required (part of efficiency correction). (applied to DATA only)
- exclude shifted vertex runs (run range: 37588-37639) (applied to DATA only)
- global CAL timing $|t^{CAL}_{global\ timing}| < 10$ ns. This rejects cosmic ray candidates. (applied to DATA only)
- at least two muon candidates from GMUON with Quality ≥ 1 and found at least by MV finder and with momentum taken from the CTD reconstruction package.
- at most 2 tracks fitted to the primary vertex.

---

corrected regions emerged. It can also be a result of a statistical fluctuation in the procedure of the determination of the correction factors.

[4] Reminder: both processes have exactly two muons in the final state.

- any number of total tracks in the events.
- $|Z_{vertex}| < 50$ cm, identical to the vertex cut in the physics analyses. This rejects comics and other non-ep background.
- $X^2_{vertex}+Y^2_{vertex} < 3$ cm^2, identical to the vertex cut in the HERA I analyses. This rejects comics and other non-ep background.
- the two muon candidates are required to have opposite sign.
- angular cuts: $|\pi - (\theta_1 + \theta_2)| < 0.0157$ and $|\pi - |\phi_1 - \phi_2|| < 0.0157$. The two tracks are required to be not back-to-back in θ and ϕ ZEUS system angles. This almost completely eliminates remaining cosmics.
- $(\eta_1 - \eta_2)^2 + (\phi_1 - \phi_2)^2 > 0.5$, require the two muons not to be collinear, this one and the selection in the next bullet protect against fake muon pairs constructed by assigning two different central detector tracks to the same muon chamber information.
- dimuon mass $M_{\mu\mu} > 2$ GeV,
- no explicit trigger requirement

8.3.1.4 Trigger bias unfolding

The MC samples used here are completely unbiased in the sense that all events are available for analysis, independent of whether the muons are identified or not. In the data, only events which have passed the three trigger levels are available. Since part of the triggers require signals in the muon chambers, this introduces a bias in the efficiency determination which needs to be unfolded. The data events are therefore subdivided into three classes.

- Events which satisfy a non-muon trigger chain, e.g. DIS trigger chain listed in Appendix A. Only triggers which do not require any muon chamber information at any of the three trigger levels fall into this class. These events are completely unbiased by the muon chamber efficiency, and both muon candidates of each event can thus be used without any restriction.
- Events which satisfy a BRMUON TLT trigger (Appendix A). The BRMUON TLT uses several slightly differing variants of the GLOMU algorithm to identify muon candidates. The very similar offline version of the GLOMU algorithm is therefore used to verify which of the two muon candidates actually fired the trigger (the more detailed raw trigger

information is not available any more at ntuple level). It has been checked that this is a very good approximation.

  - if only one of the two muon candidates fires the trigger, this candidate is discarded from the efficiency evaluation, since it is biased, and only the other one is used.
  - if both muon candidates fire the trigger, each of them is unbiased, since, if it would not have triggered, the other one would. Both are thus used for the efficiency determination.
  - if none of the two satisfy the offline GLOMU algorithm, which can rarely happen due to small differences between the online and offline GLOMU algorithms, the event is discarded.

- Events which satisfy other triggers involving muon information, e.g. forward muon triggers, are not used, since their rate in HERA I is small, and they would unnecessarily complicate the analysis. For HERA II the procedure is kept for simplicity. The addition of forward muon and BAC triggers for HERA II should be reconsidered for the final version of the GMUON efficiency corrections production[5].

It has been checked both mathematically and on MC events that this procedure reliably eliminates the muon trigger bias.

8.3.1.5 Muon efficiency corrections

The muon reconstruction efficiency to be corrected depends on the detector geometry, the material distribution, the local efficiency of the different muon chambers, and the quality cuts used in the muon identification procedure. The corrections are thus different for each muon finder, and depend on all three momentum components, or alternatively, on p_T (or p), η, and ϕ of the muon. Ideally, a triple differential correction table should thus be generated for each muon finder. In practice, this is difficult due to the limited statistics of the reference sample in the data. On the other hand, the physics processes to which the efficiency corrections are to be applied are usually not ϕ-dependent. A correction averaged in ϕ is thus an acceptable compromise for most applications. In the barrel region, especially at medium to high p_T, the muon efficiency corrections are expected to depend only on p_T to first order. In the forward and rear regions, a strong dependence on η is expected.

---

[5] The HERA I efficiency corrections are already final and will not be redone.

In general, there must be a compromise between the available statistics and the size of the bins used for the correction. If the bin size is very small, the statistical fluctuations of the correction might be very large. On the other hand, if the bin size is large, variations of the efficiency correction within the bin will take away the universal meaning of the corrections. For example, if the bin size of the corrections, say in η, is bigger than the bin size of the cross sections to be measured, these cross sections will get distorted by the average correction, unless the correction does not depend on η within this bin.

So, an approach has been followed to make the binning as small as reasonably possible, such that the variation of the correction within a bin is minimised, and the correction becomes universally applicable[6].

A 2D $[p_T;\eta]$ grid has been defined with the following bin boundaries:

- p_T: 0.75; 1.0; 1.1; 1.2; 1.3; 1.4; 1.5; 1.6; 1.7; 1.8; 1.9; 2.0; 2.2; 2.4; 2.8; 5.0;
- η: -4.0; -1.7; -1.2; -0.9; -0.4; 0.0; 0.4; 0.8; 1.2; 1.5; 1.9; 2.5; 4.0;

The bins were chosen in such a way that the events number in each 2D cell would lead to similar statistical uncertainty.

An example of BRMUON chamber efficiency as function of muon pseudorapidity in the range of $2.8 < p_T < 5.0$ GeV is depicted in Fig. 8.3. The ratio of the efficiencies gives the corrections needed to be applied to the MC in order to adjust it to the data. The resulting correction factors are stored in the form of 2D histograms in the $ROOT(HBOOK)$ format, therefore easily accessible at the analysis level. The correction factors were defined for HERA I and HERA II data taking periods separately (Fig. 8.4, 8.5, 8.6, 8.7, 8.8). The corrections factors are presented in the levels of grey color and range from 0.0 to 1.0 (see the plots grey color band). The subsequent application of the correction factors is determined by the values stored in (η, p_T) bins, which have the meaning of probability for a MC muon to keep its identification flag by the corresponding finder.

The correction factors application at the analysis level can be given on a simplified example of a muon identified by BREMAT finder in the HERA I MC sample. First of all, a muon is identified by BREMAT muon finder and a correction factor $\epsilon_{BREMAT}(\eta, p_T)$ located in the 2D BREMAT correction table (see Fig. 8.4) according to the (η, p_T) values of the muon. A random number γ, uniformly distributed from 0.0 to 1.0, is generated and compared to the previously determined $\epsilon_{BREMAT}(\eta, p_T)$ value. If $\gamma < \epsilon_{BREMAT}(\eta, p_T)$ the MC muon is marked as being NOT found by the BREMAT finder any longer. If $\gamma > \epsilon_{BREMAT}(\eta, p_T)$ the MC muon keeps its BREMAT identification flag. The

---

[6] An efficiency correction in small bins is particularly important if muons close to rangeout threshold are to be included into the analysis.

correction factors are applied on the muon-by-muon basis, which means that the random number γ is generated for every muon independently.

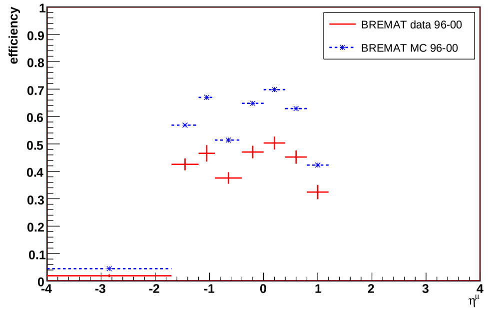

Figure 8.3: *An example of BRMUON chamber efficiency compared for data (cross) and MC (star) as function of muon pseudorapidity in the range of $2.8 < p_T < 5.0$ GeV. The data and MC samples comparison is done for 1996-2000.*

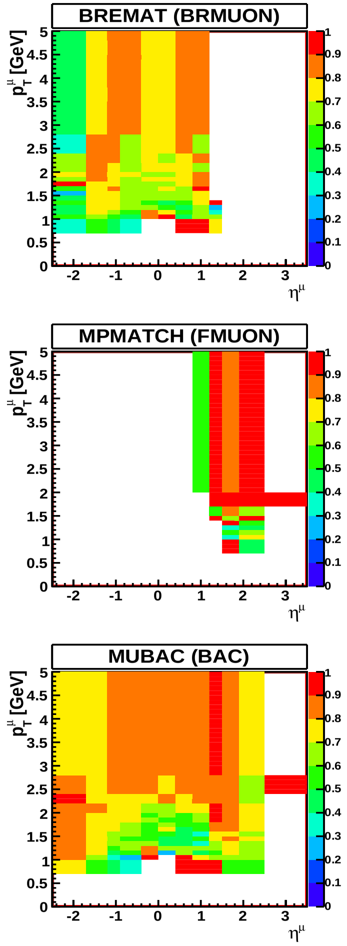

Figure 8.4: *The correction factors for BRMUON(BREMAT), FMUON(MPMATCH), BAC(MUBAC) defined for the years 1996-2000.*

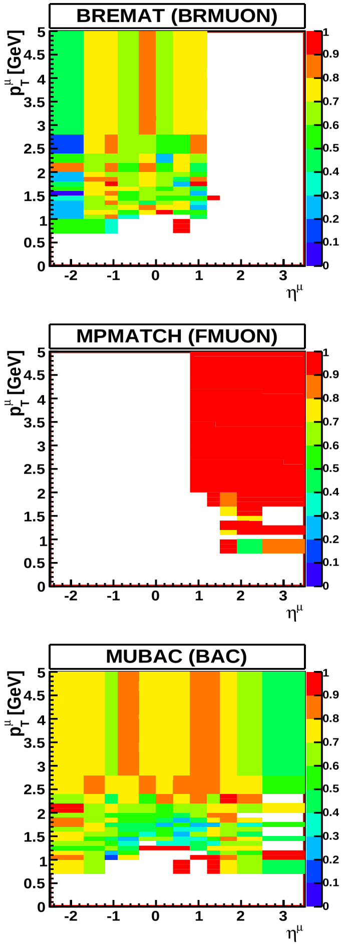

Figure 8.5: *The correction factors for BRMUON(BREMAT), FMUON(MPMATCH), BAC(MUBAC) defined for the years 2003-2004.*

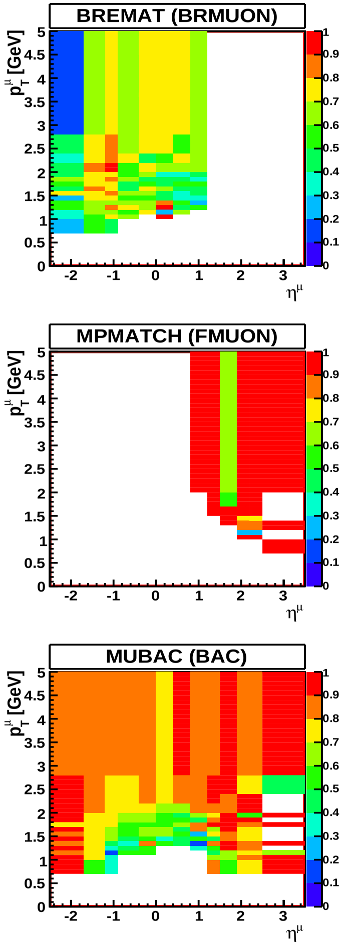

Figure 8.6: *The correction factors for BRMUON(BREMAT), FMUON(MPMATCH), BAC(MUBAC) defined for the years 2005.*

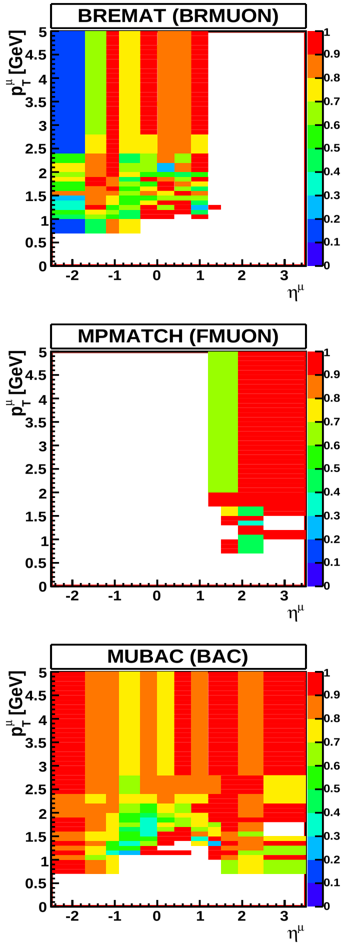

Figure 8.7: *The correction factors for BRMUON(BREMAT), FMUON(MPMATCH), BAC(MUBAC) defined for 2006 (electron).*

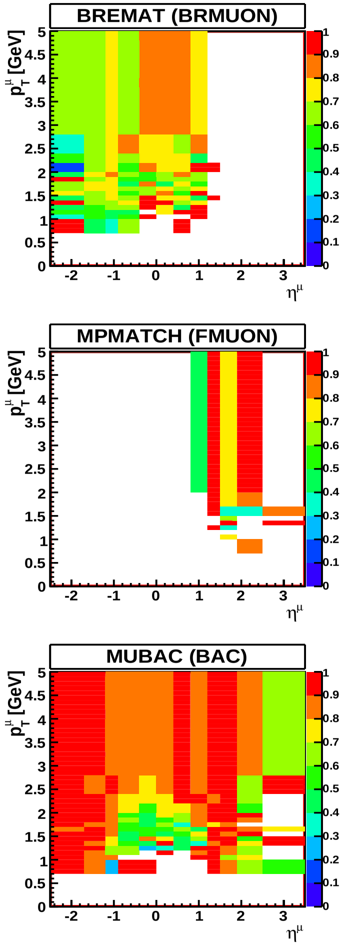

Figure 8.8: *The correction factors for BRMUON(BREMAT), FMUON(MPMATCH), BAC(MUBAC) defined for 2006-2007 (positron).*

8.3.2 Non-muon related corrections

Another set of corrections to be applied to the MC samples are the trigger related corrections and incomplete tracking detector hit efficiency information. The trigger issues are well documented and can be found in [151].

The HERA II MVD hit inefficiencies were implemented recently in the latest versions of the ZEUS MC simulation, but not yet in the MC samples used in this analysis. A separate set of corrections for HERA II was developed by the author of this thesis. The way the corrections are developed allows one to consider all MC imperfections as having been taken into account. The logic to obtain the corrections is:

- assume that the Bethe-Heitler (BH) process cross section does not change with data taking period (true for any physics process),
- the HERA I MC corrections are final and can be taken as the reference to calculate the expected HERA II global corrections,
- compare the BH number of the events in HERA I from the data and to the events number in the MC (MC/Data=0.98 ±0.05(stat)),
- the HERA II data.vs.MC should follow the same ratio as in HERA I.

This can be summarized in:

$$\tau^{MC}_{HERA\ I} = \frac{N^{MC}_{HERA\ I}}{N^{data}_{HERA\ I}} = \frac{N^{MC}_{x}}{N^{data}_{x}}, \tag{8.7}$$

where x is the index of the period under study ($x = 03p04p, 05e, 06e, 06p07p$), $\tau^{MC}_{HERA\ I}$ is the ratio of the MC events over the data events in HERA I, $N^{MC}_{HERA\ I}$, $N^{data}_{HERA\ I}$, N^{data}_{x} are known, and N^{MC}_{x} is unknown and is related to $N^{MC}_{x,observed}$, the number[7] of events in the x-period MC:

$$N^{MC}_{x} = \epsilon N^{MC}_{x,observed}, \tag{8.8}$$

where ϵ is the global correction factor to be determined.

This approach corrects for all possible efficiency discrepancies between MC and Data[8]. However, the numbers are ″global″ and must be recalculated if the analysis splits the phase space into subregions. The correction values are listed in Table 8.2 for the selection given in Section 7.8 and in Table 8.3 for the selection described in Section 7.9.

---

[7] This is the number to be corrected for the missing detector inefficiency. $N^{MC}_{x,observed}$ already includes corrections for muon detectors inefficiency described in Section 8.3.1.

[8] E.g. FastClear bug, CTD FLT track inefficiency, MVD hit inefficiency.

W range	03p04p	05e	06e	06p07p
60 ÷ 220	0.97	0.83	0.79	0.73
60 ÷ 130	1.17	0.89	0.84	0.70
130 ÷ 220	0.65	0.72	0.70	0.78

Table 8.2: *The effective global corrections, ϵ, for HERA II MC samples. The numbers are valid for event selection given in Section 7.8. The values given in the table have an uncertainty of $\approx 5\,\%$, which is the statistical uncertainty of the HERA I data sample. For the 60$< W <$220 GeV range the ratio $\tau^{MC}_{HERA\ I}$=0.98 ±0.05.*

W range	03p04p	05e	06e	06p07p
60 ÷ 220	0.58	0.95	0.56	0.60

Table 8.3: *The effective global corrections, ϵ, for HERA II MC samples. The numbers are valid for event selection given in Section 7.9. The ratio $\tau^{MC}_{HERA\ I}$=1.02 ±0.19.*

8.3.3 Control plots

An important part of the analysis are the cross checks proving that the MC simulations are correct and reproduce specific behavoiur of the detector. As it will be shown in Chapter 10 the Υ meson signal is sparce, so the control distributions are shown for the QED muon pair production in PHP and DIS. The PHP and DIS event selection and the corresponding simulations include the corrections discussed in Sections 8.3.1, 8.3.2.

8.3.3.1 QED muon pair photoproduction

The relative efficiency of the muon finders in the data and MC is presented in Figure 8.9, 8.10. The control plots can be found in Section 9.1.2 and demonstrate the muon related quantities distributions. The selection from Sec. 7.8 has been applied.

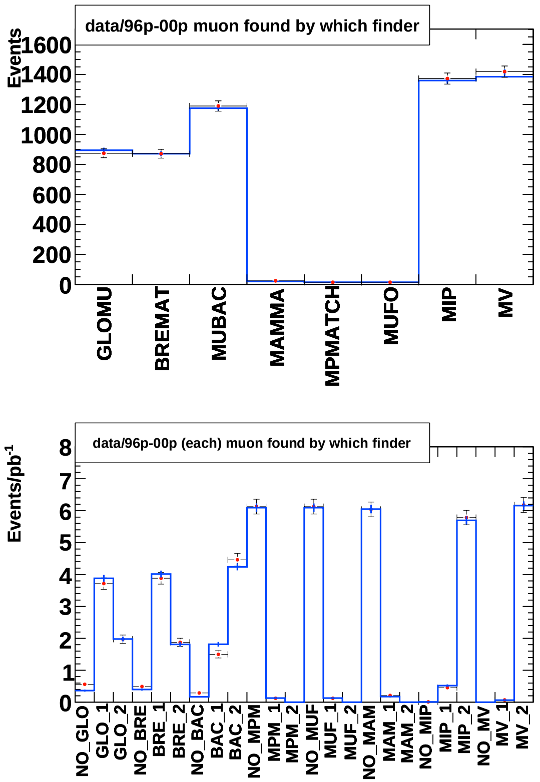

Figure 8.9: *(top) HERA I event distribution by muon finders, which identified at least one muon, (bottom) HERA I event distribution by finders, given for each muon finder separately, which identified both muons, just one muon, or did not identify the muons. The bottom plots show the event distribution by the number of muons identified in the event, e.g. NO_GLO - no muons were identified by the GLOMU finder, GLO_1 - exactly one muon was identified by the GLOMU finder, GLO_2 - exactly two muons were identified by the GLOMU finder. The labels were also shortened for the BREMAT (NO_BRE, BRE_1, BRE_2), MUBAC (NO_BAC, BAC_1, BAC_2), MPMATCH (NO_MPM, MPM_1, MPM_2), MUFO (NO_MUF, MUF_1, MUF_2), MAMMA (NO_MAM, MAM_1, MAM_2), MIP (NO_MIP, MIP_1, MIP_2), MV (NO_MV, MV_1, MV_2) finders. The points are the data, the histograms - BH MC.*

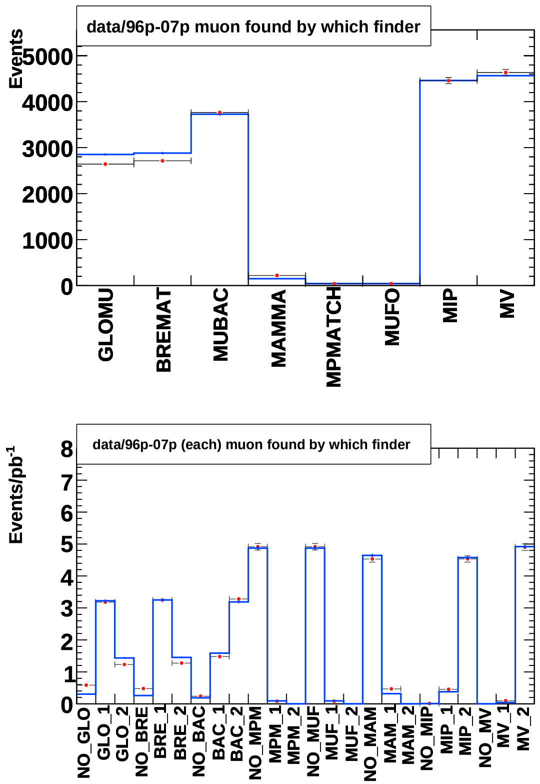

Figure 8.10: *The event distribution by finders as in Fig. 8.9 is plotted for the combined HERA I and HERA II data sets.*

8.3.3.2 QED muon pair production in DIS

The relative efficiency of the muon finders in the data and MC is presented in Figure 8.11, 8.12. The control plots presented in Fig. 8.13 demonstrate the DIS electron related quantities distributions. The selection from Sec. 7.9 has been applied.

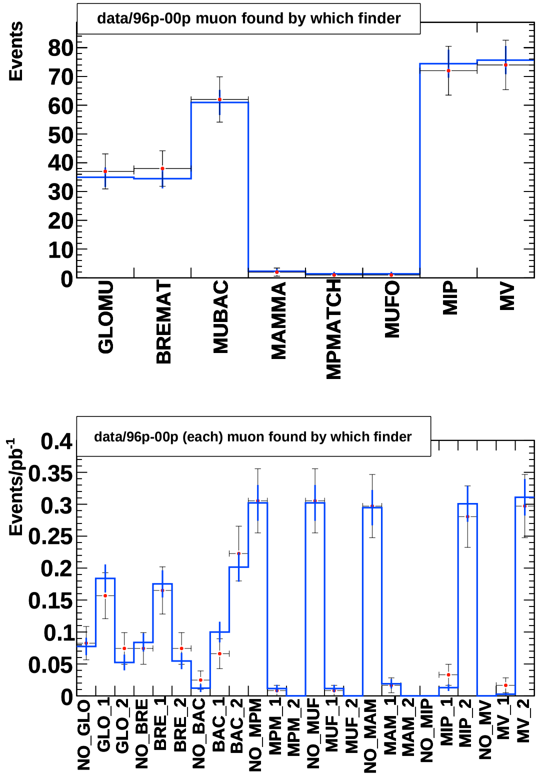

Figure 8.11: *(top) HERA I event distribution by muon finders, which identified at least one muon, (bottom) HERA I event distribution by finders, given for each muon finder separately, which identified both muons, just one muon, or did not identify the muons. The labels as in Fig. 8.9*

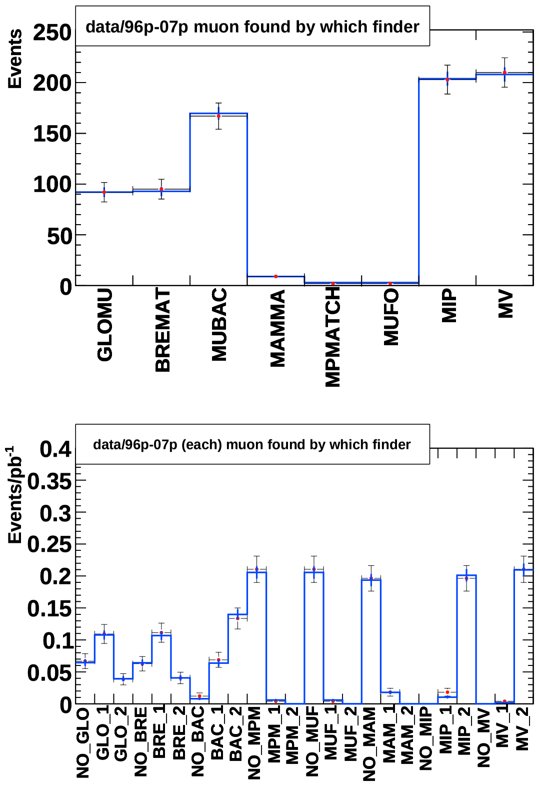

Figure 8.12: *The event distribution by finders as in Fig. 8.11 is plotted for the combined HERA I and HERA II data sets.*

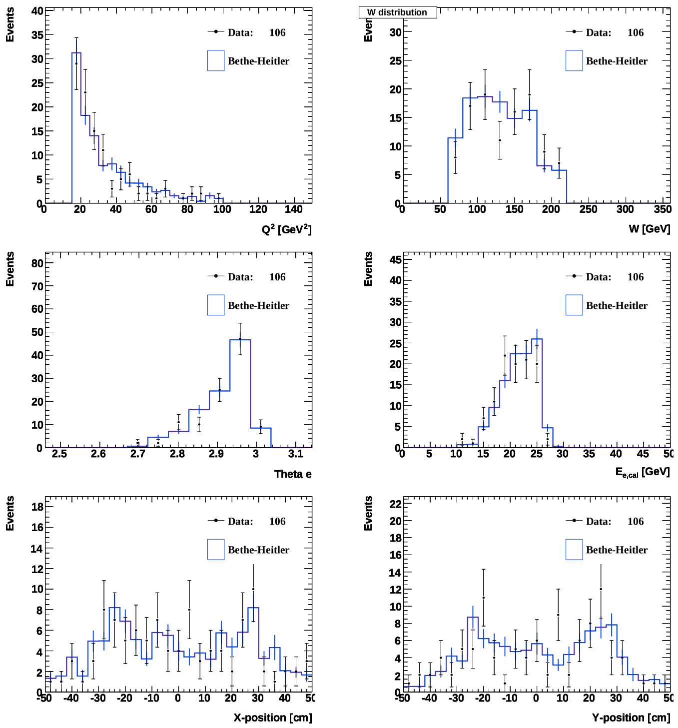

Figure 8.13: *(top,left) Corrected Q'^2 distribution, (top,right) corrected W' distribution, (middle,left) scattered electron polar angle θ_e distribution. (middle,right) corrected scattered electron energy E'_e distribution, (bottom) X and Y position of the scattered DIS electron reconstructed for $z = -143\,cm$ (RCAL surface).*

8.3.4 Summary

As it can be seen in the history of many MC simulation packages there is always a need for a certain amount of extra work at the analysis level to be done in order to correct for the features missed when the detector MC simulation was developed (sometimes due to objective and indisputable reasons).

The GMUON efficiency correction approach allows a consistent use of the same set of corrections to be implemented in different physics processes, be it a beauty quark cross section measurement with muons [85, 150] or exclusive Υ meson production (Chapter 10). The HERA I corrections are final and the HERA II corrections are newly developed and will be finalised with the Grand-Reprocessed data. GMUON efficiency corrections do not correct any muon trigger bits, which makes the trigger selection hard to handle. An ideal efficiency correction approach should foresee a way to correct simultaneously both the muon finder and the related FLT-SLT-TLT trigger bits. Factorisation of the corrections into a purely muon detector related part and non-muon related issues allows an introduction of global correction factors.

Chapter 9

Background studies

Elastic vector meson production and decay to a muon pair is treated as the signal and must satisfy the selection criteria (see Sec. 7.8, 7.9). There are other physics processes with identical experimental signature, which can not be excluded from the final sample by further optimisation of the selection. They are called the background and are discussed in this chapter. The background study is done with the aid of the Monte Carlo simulation of the signal and background processes. The details of the Monte Carlo simulation are discussed in Chapter 8.

9.1 Non-resonant background

9.1.1 Cosmics

The cosmic muons passing through the interaction region can mimic the dimuon production in *ep* scattering. They are not simulated with MC and must be removed first of all. In the ZEUS magnetic field a charged particle travelling from the outside of the detector through the CTD volume and again to the outside looks like a valid oppositely-charged dimuon event.

The rejection of this kind of events is threefold:

- The CAL timing system allows to measure an event relative to the HERA *ep* collision clock with good precision. The value $|t^{CAL}_{timing}| < 10$ ns can be used and is considered to be a conservative one (see Sect. 7.8).

- The tracking system allows one to reconstruct the "presumed" vertex in the dimuon event. The resolution of the vertex position in the XY plane is dominated by HERA I (CTD-only), therefore a typical cut on the vertex distance to the nominal *ep* interaction position < 0.5 cm is used (see below).

- The *straightness* of the "dimuons" with cosmic origin allows one to apply a so called back-to-back cut, which can be implemented in 3D and calculated from the scalar product of the muon 3-vectors, or in 2D simply from the θ polar angles of the muons measured in the ZEUS frame (see Sect. 7.2).

In the following discussion the selection from Sect. 7.8 is assumed, the "vertex distance to the nominal beam spot cut" and the "back-to-back anti-cosmic" cut not applied. The effective rejection power for the latter two is demonstrated in the comparison of the MC (BH only) versus the data sample, which contains both, the BH and cosmic muons, and presented in Fig. 9.1, before the cuts were applied, and after both cuts have been applied in Fig. 9.2. As it is seen from the figures comparison, the cosmic muons are reconstructed as muon pairs with the openning angle $\pi - 0.1 < \theta_1 + \theta_2 < \pi + 0.1$ consistent with a straight line expectation. The "presumed" vertex position is distributed uniformly in the XY plane and the muon pairs with cosmic origin can be effectively removed by requiring the vertex position to be within 5 *mm* from the nominal beam spot position.

The difference between the rejection power and introduced inefficiency for the 3D and 2D back-to-back angular cuts is shown in Figure 9.3. The CAL global timing (for the data only) and the "vertex distance to the nominal beam spot" cuts have been applied. The comparison is made only for the remaining third type of the anti-cosmic rejection cut. The BH MC distributions are normalised to luminosity, Υ MC histograms are normalised to the number of events extracted within a procedure described in Sect. 10.5 (Fit B). The cut value on the measured entity $\Delta\theta$ ($\Delta\theta = \pi - (\theta_1 + \theta_2)$ for 2D case, and $\Delta\theta = \pi - \Omega_{12}$ - in 3D) can be set at $log10(\Delta\theta) > -1$, which is translated into $|\Delta\theta| > 0.1$, and introduces an inefficiency for the signal $5.3 \pm 2.4\%$ and $3.5 \pm 2.9\%$ for the $2D$ and $3D$ cases respectively. The comparison shows that the two variable distributions differ slightly in the shape, with (obviously) weaker sensibility to cosmic "dimuons" (the tail towards the negative values) in the $3D$ (no entries in $log_{10}(|\pi - \Omega_{12}|) < -2.2$). The two variables are identical in terms of the introduced inefficiency in respect to the Υ signal. The $2D$ back-to-back cut was selected for the analysis (Sect. 7.8).

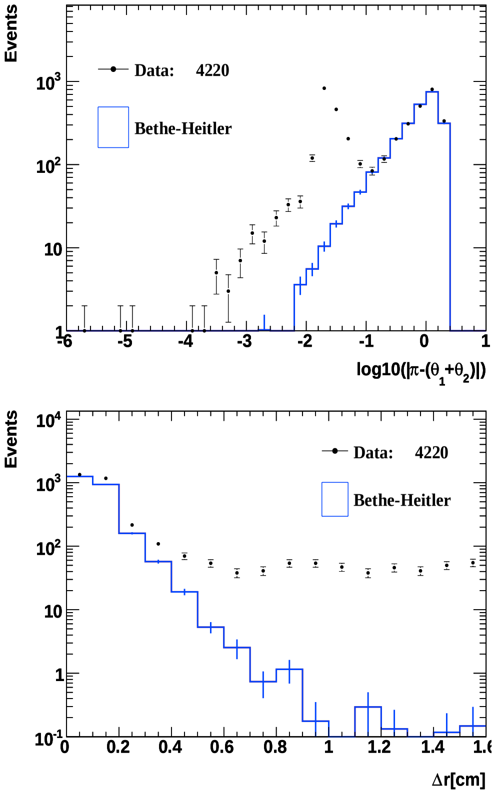

Figure 9.1: *(top) Distribution of events as function of log10(pi-th1-th2). (bottom) Distribution of events as function of* $|BeamSpot_{nominal}\text{-}Vertex|$ *in XY plane.*

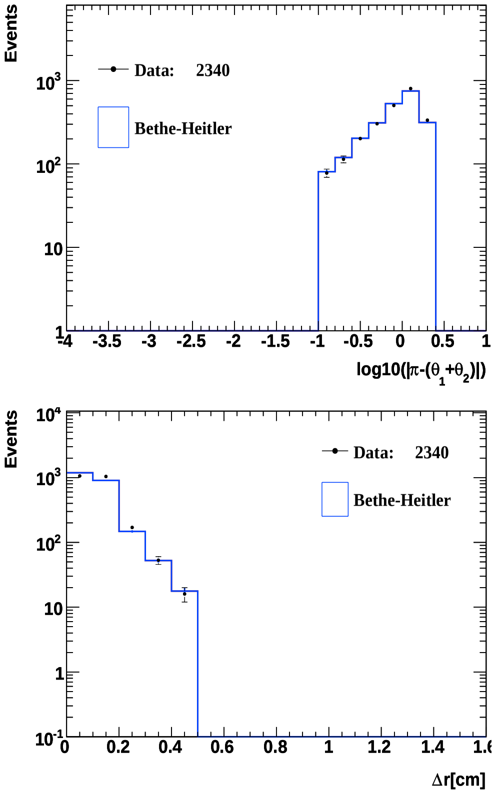

Figure 9.2: *(top) Distribution of events as function of log10(pi-th1-th2). (bottom) Distribution of events as function of* $|BeamSpot_{nominal}\text{-}Vertex|$ *in XY plane.*

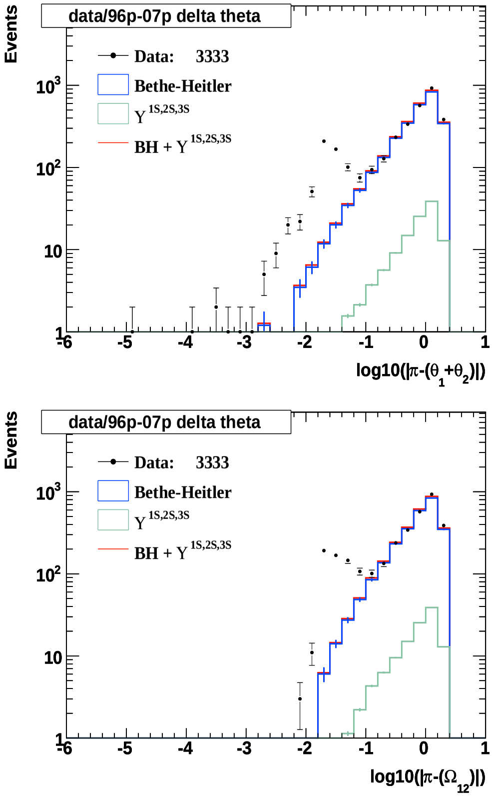

Figure 9.3: *(top) Distribution of events as function of* $log10(|\pi-(\theta_1+\theta_2)|)$. *(bottom) Distribution of events as function of* $log10(|\pi-\Omega_{12}|)$.

9.1.2 QED lepton pair production (Bethe-Heitler)

The QED lepton pair production is the only source of the non-resonant background after cosmic rejection. The details on the physics of the process and MC simulation are given in Chapter 8.1.2. The Bethe-Heitler background in terms of statistics substantially exceeds the amount of the Υ mesons observed in the full data sample (Sect. 7)). The main features of the BH process in comparison with the MC are presented in this section.

For the plots presented in this section the selection criteria from Sect. 7.8 has been applied. In addition, the events with the dimuon invariant mass in the Υ meson mass window $[9 \div 11]$ GeV have been excluded to obtain signal-free distributions. The dimuon invariant mass distribution presented in the Fig. 9.4 demonstrates the mass range selected for the comparison. The main variable to distinguish between the BH process and the Υ signal is the invariant mass of the two muons. For the BH process the invariant mass distribution is smooth and falling steeply with the mass of the dimuon system. The BH process is taken as the reference to check the detector performance in the kinematic region of interest. In the following plots the BH distributions are normalised to the luminosity in the data[1].

The control plots in the mass range $M_{\mu\mu} \in (5 \div 9) \cup (11 \div 15)$ GeV are presented in the Fig. 9.5, 9.6, 9.7. The agreement in the shape description is clearly seen. This also allows one to make a positive statement on the quality of the ZEUS detector simulation[2] in the given kinematic range and proceed with the measurement in the mass range 5< $M_{\mu\mu} < 9$ GeV, where the Υ signal is located.

---

[1] To be precise the HERA I MC samples are normalised to the luminosity. The HERA II MC samples make use of the global correction factors, which were calculated based on the MC to the data ratios between HERA I and HERA II (see Sect. 8.3.2). All corrections discussed in Sect. 8.3 were applied.

[2] All corrections discussed in Sect. 8.3 have been applied.

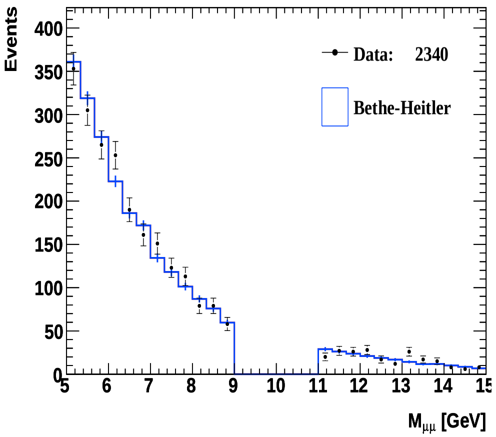

Figure 9.4: *Event distribution as a function of the invariant mass of the two muons.*

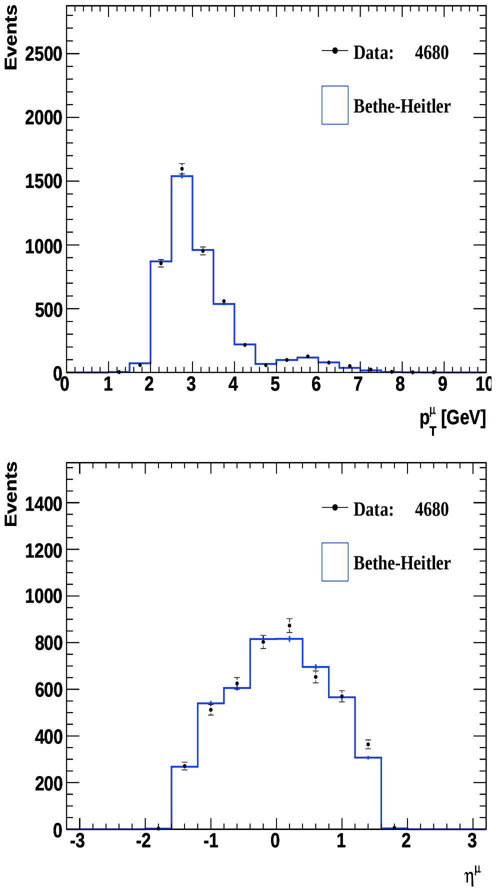

Figure 9.5: *(top) Distribution of the muon p_T. (bottom) Distribution of the muon η.*

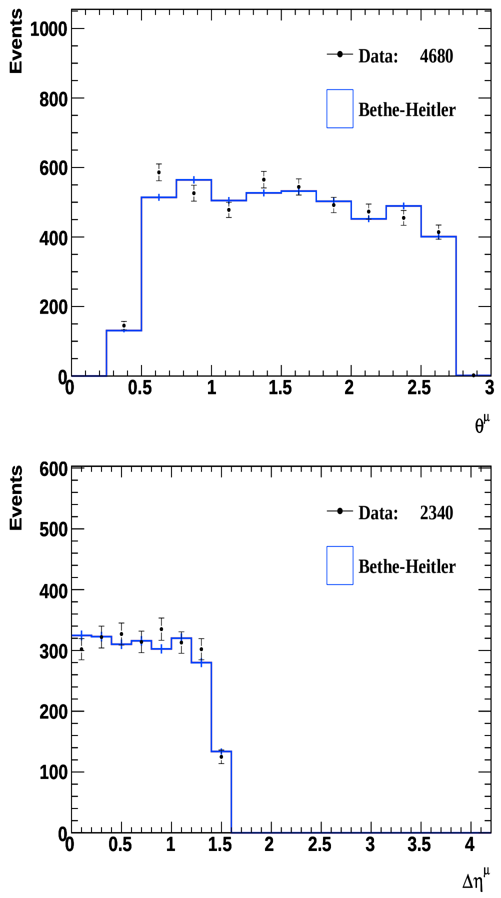

Figure 9.6: *(top) Distribution of the muon θ. (bottom) Event distribution of the difference between the pseudorapidity η of the two muons.*

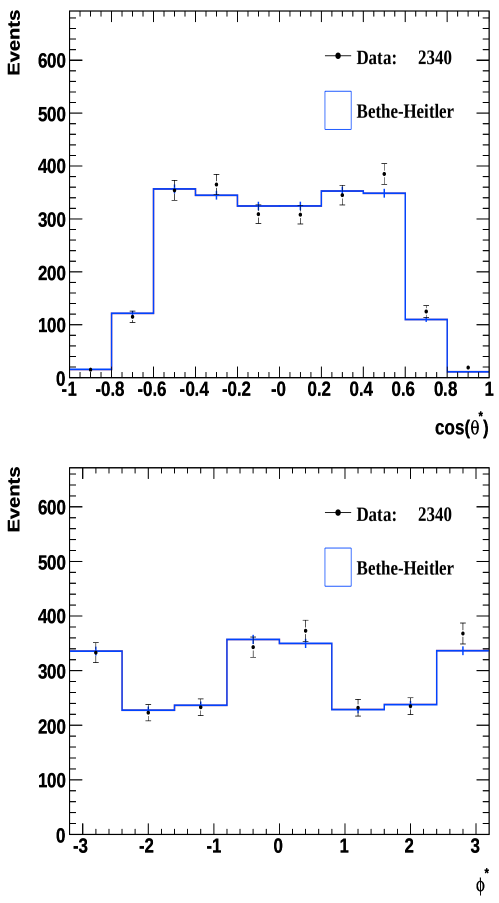

Figure 9.7: *(top) Distribution of the positive muon angle θ (in the dimuon rest frame) relative to the direction of the $dimuon$ production in the lab frame. (bottom) Distribution of the positive muon angle ϕ (in the dimuon rest frame) relative to the $dimuon\text{-}ep$ production plane in the lab frame.*

9.2 Resonant background

9.2.1 Υ meson production with dissociation of the proton

The Υ meson production with the dissociation of the proton is the only significant resonant type background to the elastic production process. The fraction of the events, which qualify the selection (Sect. 7.8) but which were produced in the reaction with the dissociation of the proton, f_{pdiss}, is expected to be similar in all vector meson diffractive processes [152]. Therefore, the f_{pdiss} estimation methods can be applied to the J/ψ meson diffractive production and the resulting f_{pdiss} value used to measure the elastic Υ meson production cross section (see Chapter 10).

The f_{pdiss} can be estimated in two ways.

The first way relies on the assumption of the full knowledge of the dead material distribution in the FCAL area around the beam pipe, and operates with the parameters in the physics model of proton dissociation. Formerly MC generators such as **PYTHIA** , **EPSOFT** , and **DIFFVM** were considered with their models of the proton dissociation. The results of the proton dissociation studies can be found in [153, 154].

An alternative way[3], developed in this analysis, is based on the *t-dependence* study and its features comparison in the elastic and proton dissociation production processes. It relies on the consistent tracking performance between data and MC, and assumes negligible correlation[4] of the proton remnant mass, M_Y, distribution and the t-slope value, b. This assumption is reasonable taking into account the $b(W)$ parameterisation (Eq. 8.2) and the low value of the Pomeron intercept, $\alpha'_P \lesssim 0.1$. Further details of the method and final estimation of the proton dissociation contamination, f_{pdiss}, are given below.

The elastic photoproduction selection cuts (Sec. 7.8) with one modification has been applied. The only modification which was involved lowered the muon transverse momentum requirement to $p_T > 1.0$ GeV cut in order to increase the rate of the muon pairs from the J/ψ decay. The data sample contains both the J/ψ and the QED muon pairs (BH, see Sec. 9.1.2), so it is necessary to correct the data by subtracting the BH background in the following way. The data in the mass window from 2 to 3.5 GeV was selected and fitted against the MC BH and J/ψ histograms following the Barlow templates method [156](implemented in TFractionFitter in ROOT) in order to estimate the BH and the J/ψ fractions contributing to the data mass distribution. The BH MC $|t|$-*distribution*, estimated to contribute $15.8 \pm 0.3\%$ to the data, was subtracted from the corresponding data $|t|$-*distribution*, producing, thus, a "pure" J/ψ data $|t|$-*distribution*.

The resulting J/ψ data $|t|$-distribution histogram was fitted against the elastic and proton dissociation J/ψ MC distributions in order to build a grid of the χ^2 values depending on the t-slope values used in the MC samples. The elastic and proton dissociation J/ψ MC samples were generated only one time with the t-slope values $b = 4$ and $b = 1$ GeV^{-2} respectively, and were reweighted before each time a fit was to be performed. An example of the t-distribution for the J/ψ data and MC is given at the Figure 9.8(top). At each fit iteration the χ^2 of the fit was put into the 2-dimensional histogram (see Fig. 9.8(bottom-left)) and the fraction of the MC template corresponding to proton dissociation to another 2D histogram (see Fig. 9.8(bottom-right)).

The result of the procedure is the global minimum showing the values preferred by the data b_{el}, b_{pd} and f_{pdiss} (Tab. 9.1). The values agree with the published $f_{pdiss} = 0.22 \pm 0.02 \pm 0.02$ extracted for 96p-97p data period [153], no numbers are available for comparison with the remaining data subsamples. The systematic uncertainty takes into account only[5] the BH contribution uncertainty.

data taking period	b_{pd}, GeV^{-2}	b_{el}, GeV^{-2}	f_{pdiss}, %
96p97p	$0.94 \pm 0.06 \pm 0.02$	$4.70 \pm 0.10 \pm 0.10$	$22.4 \pm 1.3\ ^{+0.2}_{-0.3}$
98e00p	$0.90 \pm 0.01 \pm 0.02$	$4.40 \pm 0.05 \pm 0.10$	$14.6 \pm 0.8\ ^{+0.0}_{-0.3}$
03p07p	$0.90 \pm 0.01 \pm 0.00$	$4.80 \pm 0.05 \pm 0.10$	$22.0 \pm 1.0\ ^{+0.0}_{-0.3}$
96p07p	$0.88 \pm 0.01 \pm 0.02$	$4.60 \pm 0.05 \pm 0.10$	$20.4 \pm 0.4\ ^{+0.0}_{-1.2}$

Table 9.1: *The proton dissociation fraction extracted from the t-distributions fit, performed for the J/ψ data and MC samples. The BH background relative contribution $15.8 \pm 0.3\%$ is known from the mass distribution fit and was subtracted from the data t-distribution respectively. The first error is the one from the fit procedure and mostly dominated by the bin size of the axes. The second error is a part of systematic uncertainty obtained by variation of the subtracted amount of the BH component in the sample. The variation was performed within the errors of the BH background determination.*

As it is seen from the table the detector configuration in terms of position and acceptance of the FCAL is very similar in 96p97p and 03p07p data periods. The drop down of the value obtained for 98e00p can be explained by the energy

---

[3] The method is based on the idea from [155].

[4] The elasticity and the FCAL inner ring energy cuts select $M_Y \lesssim 4$ GeV. These cuts reduce the statistics, but should be used as a precaution, since **DIFFVM** is known to fail in the forward energy flow description. Other models, namely **EPSOFT** or **PYTHIA** , describe the forward energy flow better, but their application to HERA II is yet constrained by the forward material simulation in the MC.

[5] Full understanding of the systematics requires a homogenious HERA II track reconstruction software, which involves the alignment, calibration, reconstruction and fitting packages versions.

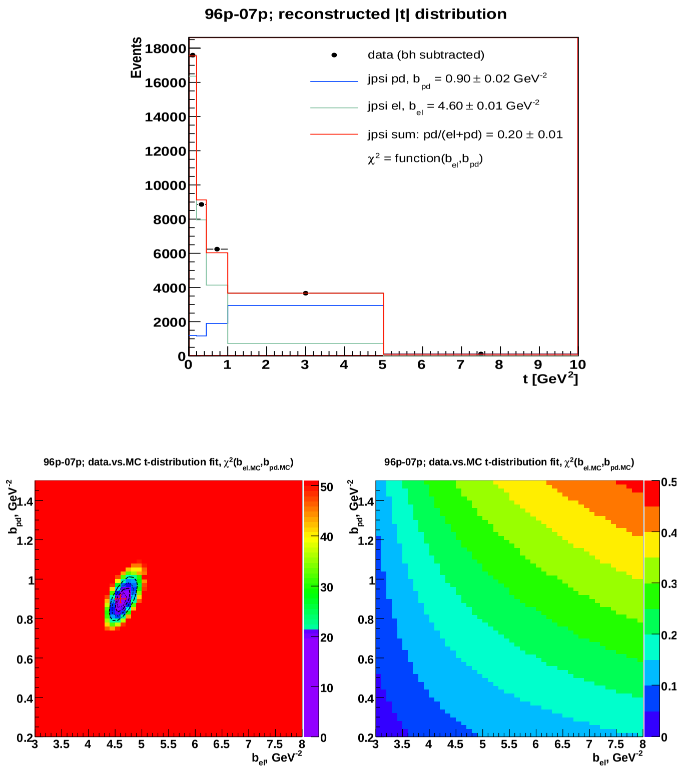

Figure 9.8: *(top) Distribution of events as function of $|t|$. The points represent the data corresponding to J/ψ signal after the estimated BH background was subtracted. The histograms - J/ψ MC simulation, b_{el} - elastic production, b_{pd} - production with dissociation of the proton. The b values implemented in the $elastic$ and $protondissociation$ MC samples are given in the legend, the errors to the b values were estimated from the $\chi^2(b_{el}, b_{pd})$ plot (see bottom-left). The proton dissociation fraction value $pd/(pd + el)$ and its error were estimated from the $f_{pdiss}(b_{el}, b_{pd})$ plot (see bottom-right). (bottom-left) 2D distribution of χ^2 value as function of the t-slope parameters b used in the elastic and pdiss J/ψ MC simulation, (bottom-right) 2D distribution of the f_{pdiss} ratio as function of t-slope parameters b for elastic and proton dissociative production.*

leakage effect into the FCAL from the FPC, which was installed right inside of the FCAL inner ring.

The proton dissociation fraction value obtained for the combined 96p07p data period with symmetrised statistical and partial systematic uncertainties added in quadrature:

$$f_{pdiss} = 20 \pm 2\% \tag{9.1}$$

is used in Chapter 10 for the elastic cross section calculation.

9.2.2 Decays from higher excitation states

The contributions to the observed peak in the invariant mass distribution for the process $\gamma p \to \Upsilon(1S)p, \Upsilon(1S) \to \mu\mu$ from the cascade decays from the reactions like $\gamma p \to \Upsilon(XS)p, \Upsilon(XS) \to \Upsilon(1S)\pi\pi, \Upsilon(1S) \to \mu\mu$ were estimated with **DIFFVM** to be at the level of 0.1% and ignored in the following.

Chapter 10

Elastic Υ production

This chapter presents the PHP and DIS Υ production cross section measurement. Possibilities to extend the measurement to the inelastic production channel will be addressed in Chapter 11.

Photoproduction events are usually recognised by the absence of a scattered energetic electron and by the event being well balanced in transverse energy. In the untagged PHP the scattered electron escapes into the beampipe being undetected and therefore the information about it is lost. In tagged PHP the scattered electron is detected at very small angles and requires dedicated equipment. In general inclusive case an event $E - p_Z$ balance is used to separate PHP and DIS.

This analysis follows the untagged PHP method and for simplicity is referred to as PHP in the following discussion. For the photoproduction events, the Q^2 ranges from the kinematic minimum, $Q^2_{min} = m_e^2 \frac{y^2}{(1-y)}$, where m_e is the electron mass, up to $Q^2_{max} \approx 1$ GeV^2, the value at which the scattered electron starts to be visible in the calorimeter.

Events with a scattered electron seen in the ZEUS detector cover $Q^2 \gtrsim 1$ GeV^2 and are called DIS events. The Q^2 threshold value at which the electron energy can be reliably measured in ZEUS is close to Q$^2 \approx 1$ GeV^2 for the HERA I detector configuration and Q$^2 \approx 4$ GeV^2 for HERA II. In order to simplify the analysis the kinematic region for the measurement with the lower boundary of the region was selected to be above the HERA II threshold.

This chapter presents only the measurement of the elastic Υ(1S) meson cross section in photoproduction with the kinematic region defined $Q^2 < 1$ GeV^2 and $60 < W < 220$ GeV and production in DIS in the kinematic region $15 < Q^2 < 100$ GeV^2 and $60 < W < 220$ GeV. Possibilities to extend the measurement to inelastic production channel are addressed in Chapter 11. The measurement summary and outlook is given in Chapter 12. The discussion of the measurement in the context of the theory predictions (Section 2) is given in Chapter 13.

10.1 ep cross section

The Υ_i, where $i = 1S, 2S, 3S$, ep cross section in the $\Upsilon_i \rightarrow \mu\mu$ channel is calculated from the observed number of the events via:

$$\sum_{i=1,2,3} \sigma^{ep\rightarrow\Upsilon_i ep} Br_i = \frac{N_{sig}}{LA}(1 - f_{pdiss}), \tag{10.1}$$

where N_{sig} is the number of the signal events in the sample, L - luminosity of the sample, A - acceptance, Br_i - branching fraction $\Upsilon_i \rightarrow \mu\mu$, f_{pdiss} - fraction of proton dissociative events in the sample, which needs to be applied to measure pure elastic cross section of the process.

10.2 γp cross section

The total γp cross section[1] at a certain value of Q^2_0 and W_0 can be obtained from the ep cross section measured in a certain range $[W_{lower} \div W_{upper},\ Q^2_{lower} \div Q^2_{upper}]$ range using the formula:

$$\sigma^{\gamma p}(Q^2_0, W_0) = \frac{\sigma^{ep}}{\Phi}, \tag{10.2}$$

where Φ is the effective photon flux, which accounts for the translation of the ep cross section measured in the bin range (W, Q^2) to the value at given W_0 and Q^2_0 for the γp cross section[2]. The effective photon flux was evaluated according to the formula (see [154]):

$$\Phi = \frac{\int_{\Delta Q^2}\int_{\Delta W} dQ^2 dW (\frac{2W}{s})\Gamma_T(\frac{1+\epsilon R}{1+R})\sigma^{\gamma p}(Q^2, W)}{\sigma^{\gamma p}(Q^2_0, W_0)}, \tag{10.3}$$

where Γ_T is defined in Eq. 1.21 and the integration is performed over the differential cross section given in Eq. 1.25 in the kinematic region of the

---

[1] The same formulas are applied to $\gamma^* p$ [154], where γ^* stands to distinguish virtual photons from the real ones - γ in PHP

[2] In PHP $Q^2_0 = 0$ by definition, however for plotting at logarithmic scale another convenient value is chosen $Q^2_0 = 10^{-3}\ GeV^2$. In practice the cross sections obtained at both values of the Q^2_0 are identical to a high level of precision. The choice of W_0 and Q^2_0 is arbitrary, since it leads to values which can be calculated from the parameterisation of $\sigma^{\gamma p}(Q^2, W)$ used in Eq. 10.3 and given in Eq. 8.3

measurement $[Q^2_{lower} : Q^2_{upper}]$, $[W_{lower} : W_{upper}]$. In PHP the lower boundary of the Q^2 range is defined by the kinematic limit of the *ep* scattering process and given by Eq. 1.22. For the purpose of integration a certain functional form for $\sigma^{\gamma p}(Q^2, W)$ and $R = \sigma_L/\sigma_T$ was assumed following Eq. 8.3, 8.4.

10.3 Kinematic region

The kinematic region for the cross section measurement was defined as

- for PHP: $60 < W < 220$ GeV and $\mathrm{Q}^2 < 1$ GeV^2, with further splitting of the W range to $60 < W < 130$ GeV and $130 < W < 220$ GeV.
- for DIS: $60 < W < 220$ GeV and $15 < Q^2 < 100$ GeV^2.

As it can bee seen from the Figure 10.1 the bulk of the data is located in $60 < W < 220$ GeV, the efficiency of the detector reconstruction vanishes fast outside of the region (See Fig. 10.2). The Q^2 range for the DIS measurement was chosen based on the comparison of a BH and $\Upsilon(1S)$ Q^2 dependence distributions. The BH MC Q^2-distribution was found to be falling faster[3] than the one of the $\Upsilon(1S)$ meson, therefore the lower range boundary was chosen, $Q^2 > 15$ GeV^2. The upper range boundary, $Q^2 < 100$ GeV^2, is determined by statistics in the data.

10.4 Acceptance calculation

The acceptance calculation has been performed on a MC sample for the elastic Υ(1S) state production in the muon decay channel according to the formula:

$$Acceptance = \frac{N_{taken}}{N_{generated}}, \tag{10.4}$$

where N_{taken} - is the number of events reconstructed after the selection criteria (Sections 7.8, 7.9) and efficiency corrections (Sect. 8.3.1, 8.3.2) have been applied, $N_{generated}$ - is the number of events generated in the kinematic region of the measurement (Section 10.3). Both numbers, $N_{generated}$ and N_{taken}, are normalised to the luminosity in the corresponding data period.

---

[3] The comparison was made for the dimuon invariant mass range $5 < M_{\mu\mu} < 15$ GeV, where the MC BH Q^2-distribution is, actually, dominated with the contribution from the muon pairs with low invariant mass, so, effectively the lower boundary cutting value, $Q^2 \gtrsim 15$ GeV^2, suppresses the lower mass part of the sample.

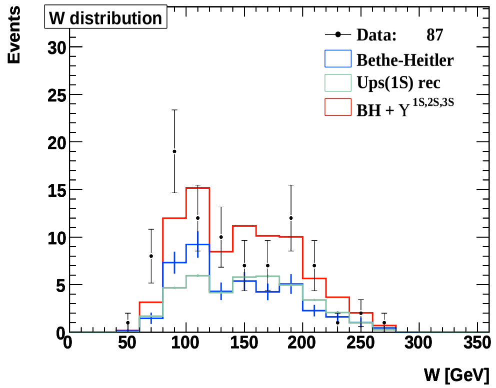

Figure 10.1: *The W distribution for the data and MC dimuon samples, the bulk of the data is concentrated in the range W=[60:220] GeV. The events are selected in the dimuon mass range [9.33:9.66] GeV.*

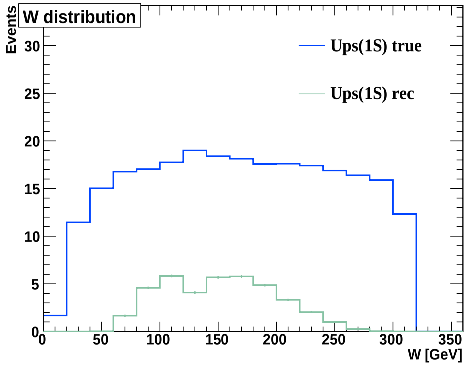

Figure 10.2: *The W distribution for the $\Upsilon(1S)$ MC dimuon samples, the acceptance falls rapidly beyond the range W=[60:220] GeV.*

A set of two histograms with W distributions of N_{taken} and $N_{generated}$ was produced for each trigger period. After reweighting of the histograms to keep the luminosity proportions between separate trigger periods the histograms have been summed up. The numbers corresponding to each trigger period are presented in the Tables 10.1, 10.2, 10.3, 10.4, where the number of "generated" and "taken" events is normalised to luminosity in each period respectively. The overall acceptance values are presented in the most-right column of the tables.

	$96p00p$	$03p04p$	$05e$	$06e$	$06p07p$	$96p07p$
$N_{generated}$	33.00	10.27	40.38	17.14	45.20	146.98
N_{taken}	9.96	2.44	8.50	3.72	8.41	33.02
$Acceptance$	0.302	0.237	0.210	0.217	0.186	0.226

Table 10.1: *Number of generated events and events taken after all reconstruction cuts have been applied in the kinematic region $Q^2 < 1$ GeV^2, $60 < W < 220$ GeV.*

	$96p00p$	$03p04p$	$05e$	$06e$	$06p07p$	$96p07p$
$N_{generated}$	16.61	5.26	19.71	8.65	22.80	73.02
N_{taken}	4.73	1.28	4.19	1.81	3.78	15.79
$Acceptance$	0.285	0.243	0.213	0.209	0.166	0.216

Table 10.2: *Number of generated events and events taken after all reconstruction cuts have been applied in the kinematic region $Q^2 < 1$ GeV^2, $60 < W < 130$ GeV.*

	$96p00p$	$03p04p$	$05e$	$06e$	$06p07p$	$96p07p$
$N_{generated}$	16.40	4.78	20.35	8.37	22.55	72.45
N_{taken}	5.22	0.93	3.98	1.79	4.77	16.69
$Acceptance$	0.318	0.194	0.196	0.213	0.212	0.230

Table 10.3: *Number of generated events and events taken after all reconstruction cuts have been applied in the kinematic region $Q^2 < 1$ GeV^2, $130 < W < 220$ GeV.*

	$96p00p$	$03p04p$	$05e$	$06e$	$06p07p$	$96p07p$
$N_{generated}$	2.329	0.634	2.964	1.082	2.762	9.771
N_{taken}	1.224	0.146	1.124	0.294	0.811	3.598
$Acceptance$	0.525	0.230	0.379	0.271	0.294	0.368

Table 10.4: *Number of generated events and events taken after all reconstruction cuts have been applied in the kinematic region $15 < Q^2 < 100$ GeV^2, $60 < W < 220$ GeV.*

10.5 Signal extraction

There are several methods to extract the signal in the situation where the signal-to-background ratio is not high and rather close to ≈ 1. All methods are based on assumptions for the background and the signal distribution shapes.

1. Smooth background subtraction - the background is assumed to follow a smooth analytic function (e.g. $e^{p_0+p_1x+p_2x^2}$):
    - the muon pair invariant mass distribution in the data is being fit by a function, for which the form and number of parameters are defined by the user,
    - a so called signal window must be defined, outside of the signal window region the contribution from the background process(-es) is assumed to be close to 100%,
    - the method is sensitive to assumption about the signal distribution in its tails and, therefore, the signal window range can be different for different signal distribution shape hypotheses,
    - the events in the signal mass window are excluded from the fit procedure,
    - the method is sensitive to assumptions about the background shape, i.e. the type of the analytic function,
2. MC simulated background subtraction - similar to pp.1, but the background shape is taken from MC simulation:
    - the MC simulation of the background is assumed to reproduce the background in the data,
    - no further assumptions on the background behaviour are made,
    - the MC statistics must be several times as much as in the data,
    - the method is less sensitive to statistical fluctuations than pp.1, since the shape of the background is fixed by the MC,
    - the method should be preferred when the background shape can not be easily parameterised with a smooth function (a la pp.1),
3. MC histogram templates for signal and background shape simultaneous fit to the data histogram:
    - this is one of the basic methods, when both the signal and the background can not be reproduced in simple analytic form,

- the method implemented in the TFractionFitter in ROOT follows [156],
- Poissonic character of the data and MC is taken into account,
- this method should be prefered in all cases, if the MC simulation is perfect.

The signal extraction method listed in pp.1 was followed in [157], but in recent studies, which showed significant sensitivity to background fluctuations, the method was disfavoured. In the following discussion the results obtained with the latter two methods are discussed.

The signal extraction methods were applied to the histograms containing the invariant mass distributions.

The methods listed in pp.2 and pp.3 are referred to as Fit A and Fit B respectively in the following discussion. The ZEUS tracking resolution does not allow to resolve the $\Upsilon(1S)$, $\Upsilon(2S)$, $\Upsilon(3S)$ states. Moreover the mass peak resolution is different in HERA I ($\sigma \approx 0.3\ GeV$) and HERA II ($\sigma \approx 0.15\ GeV$) periods, giving in average $\sigma \approx 0.2\ GeV$. The bin width 0.333 GeV^{-1} (Fig. 10.3, 10.4) has been selected to be $\approx 1.5 \div 2$ times the $\Upsilon(1S)$ mass peak width.

Fit A requires the signal region to be defined. The dimuon mass window $9.0 \div 10.7$ GeV was selected based on the estimated resolution of the mass peak. The window covers the $\pm 2\sigma$ region from around the $\Upsilon(1S)$ state (9.46 GeV) to the $\Upsilon(3S)$ state (10.36 GeV). The number of the signal events was estimated as the excess above the background:

$$N_{signal} = N_{DATA} - N_{MC\ background}, \qquad (10.5)$$

where the number of background events, $N_{MC\ background}$, was calculated as the number MC BH events in the signal window. The statistical uncertainty of the signal, N_{signal}, was calculated from the number of the data events in the signal window:

$$\Delta N_{signal} = \sqrt{N_{DATA}}. \qquad (10.6)$$

Fit B gives the fractions (in %) of the data events corresponding to the signal and background according to the shapes of the invariant mass distributions simulated in the MC, from which the signal events number N_{signal} can be easily calculated. The error on N_{signal} is determined from the fit procedure.

Both methods give an estimatation of the integral of the three states. In order to extract the $\Upsilon(1S)$ state contribution from the sum of $\Upsilon(1S)$, $\Upsilon(2S)$ and $\Upsilon(3S)$ the CDF measurements [158] have been used under the assumption that the cross section ratio is the same at HERA and Tevatron. The ratio of the three states of the Υ meson has been calculated from the cross section values, σBr, given in Table 1 in [158] for the lowest Υ p_T range ($1 \div 2$ GeV): $89.6 \pm 9.3 : 22.6 \pm 3.3 : 10.3 \pm 2.7$, which leads to:

$$1S : 2S : 3S = 0.73 : 0.19 : 0.08 \qquad (10.7)$$

and the fraction of the 1S state

$$f_{1S} = 73^{+5}_{-6}\ \% \qquad (10.8)$$

in the sum of the three states, where the error was calculated by $\pm 1\sigma$ variation of the cross section values to maximize (minimize) the $1S$ state relative contribution to the sum of the three states cross section values.

In both methods the background MC template is a luminosity normalized BH dimuon mass distribution (see Sect. 8.2). In Fit B in order to construct the signal MC template the invariant mass distribution histograms for 1S, 2S, 3S states were summed up according to the ratio given in Eq. 10.7.

The dimuon invariant mass distributions for the kinematic regions listed in Section 10.3 with the result of Fit B signal extraction method applied are presented in Fig. 10.3 ($60 < W < 220$ GeV, $Q^2 < 1\ GeV^2$ and $15 < Q^2 < 100\ GeV^2$) and Fig. 10.4 ($Q^2 < 1\ GeV^2$, $60 < W < 130$ GeV and $130 < W < 220$ GeV).

The signal values extracted with Fit A and Fit B are compared in Tables 10.5, 10.6. The 1S state fraction contribution to the integral signal (Eq. 10.8) should be applied to the numbers given in the tables in order to extract the number of 1S state candidates.

W range GeV	$N\ events$ Fit A	$N\ events$ Fit B
60 – 130	41 ± 13	48 ± 12
130 – 220	44 ± 12	40 ± 12
60 – 220	85 ± 17	87 ± 17

Table 10.5: *Number of events extracted with two methods for the PHP selection. The number of extracted events includes a significant fraction of events coming from the process with proton dissociation and is an integral over the three (1S,2S,3S) Υ states.*

The elastic contribution to the numbers of candidates given in Tables 10.5,10.6 is known[4] to be 80±2% (see Chapter 9.2.1). The absolute value of the proton dissociation fraction is related to the general detector acceptance and holds no dependence to the type of the vector meson produced (see Eq. 8.2, [161]).

---

[4] In [159] a value (1-f_{pdiss}) $= 75 \pm 5\%$ based on a J/ψ meson analysis [153, 157, 160] is used.

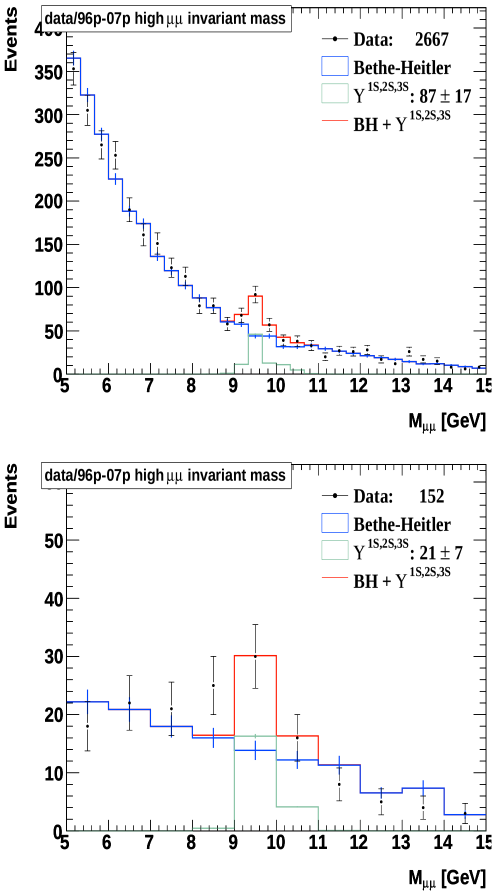

Figure 10.3: *(top) Effective mass distribution of two muons in the range 60<W<220 GeV, Q^2 <1 GeV^2. (bottom) Effective mass distribution of two muons in the range 60<W<220 GeV, 15<Q^2 <100 GeV^2. The number of signal events estimated with Fit B is given in the legend.*

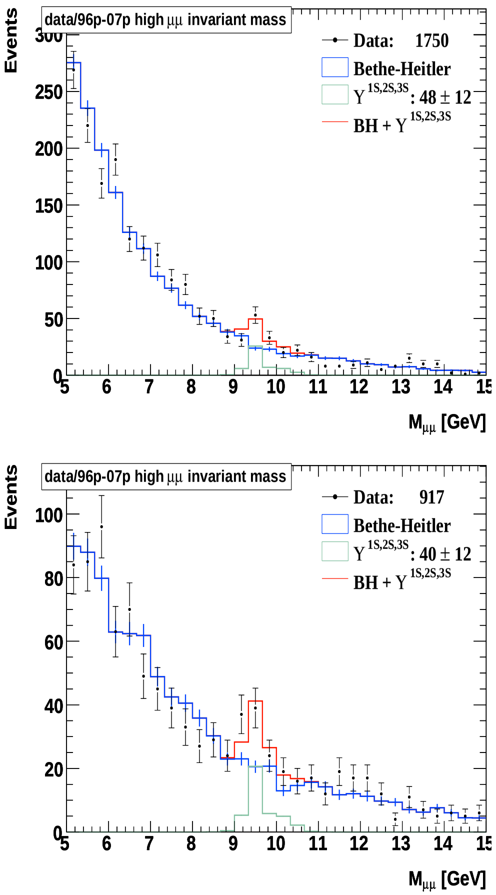

Figure 10.4: *(top) Effective mass distribution of two muons in the range 60<W<130 GeV, $Q^2 < 1$ GeV^2. (bottom) Effective mass distribution of two muons in the range 130<W<220 GeV, $Q^2 < 1$ GeV^2. The number of the signal events estimated with Fit B is given in the legend.*

Q^2 range GeV^2	*N events* Fit A	*N events* Fit B
15 – 100	21 ± 7	21 ± 7

Table 10.6: *Number of events extracted with two methods for the DIS selection. The number of extracted events includes a significant fraction of events coming from the process with proton dissociation and is an integral over the three (1S,2S,3S) Υ states.*

10.6 Cross section and sources of systematic uncertainty

The *ep* cross section for Υ(1S) production was evaluated according to:

$$\sigma^{ep\to\Upsilon(1S)p} = \frac{N_{\Upsilon(1S)}(1-f_{pdiss})}{\mathcal{ABL}}, \tag{10.9}$$

where $N_{\Upsilon(1S)}$ is the number of signal events (calculated from Tables 10.5, 10.6 and Eq. 10.8), $\mathcal{A}$ is the overall acceptance (Tables 10.1, 10.2, 10.3, 10.4), $\mathcal{B}$ = 2.48 ± 0.06% is the 1S state decay branching ratio into $\mu^+\mu^-$, and $\mathcal{L}$ is the corresponding integrated luminosity (Table 7.1).

The γp cross section for exclusive Υ production was obtained through

$$\sigma^{\gamma p\to\Upsilon(1S)p} = \frac{1}{\Phi}\sigma^{ep\to\Upsilon(1S)p}, \tag{10.10}$$

where Φ is the effective photon flux (Eq. 10.3).

The cross section was extracted with the selection described in Sections 7.8, 7.9. The sources of systematic uncertainty for the cross section measurement in PHP are listed in Table 10.7 and depicted in Fig. 10.5, 10.6. The total systematic uncertainty was determined by adding the individual contributions in quadrature. The values for the different W ranges are given.

The numbers for the full W range cross section measurement in PHP are commented below:

- signal extraction method: the normalisation of the background was varied to match either the left (5.0< $M_{\mu\mu}$ <9.0 GeV) or the right (10.7< $M_{\mu\mu}$ <15.0 GeV) sides of the mass spectra outside of the signal region: +1%, −9%.

- the uncertainty of the CTD track and muon chamber performance in the trigger, and the subsequent muon reconstruction in the offline analysis: ±9%.

  – This uncertainty splits into several period dependent components:
    - offline identification and reconstruction: the uncertainty was estimated from the control plot finder distributions (Fig. 8.9), the systematic uncertainty is smaller than the statistical one, so the statistical uncertainty is taken as an upper limit $\leq 5\%$ (Section 9.1.2),
    - trigger corrections for HERA I (CTD FLT, GLOMU): 5% (see [162]) this does not include an uncertainty on offline corrections already included in the above,
    - the uncertainty for the GMUON corrections application via random seed generation, upper limit 3% [149],
    - corrections for HERA II (354 pb^{-1}) have larger uncertainty due to the effects not yet perfectly reproduced in MC (e.g. CTD FLT, Fast Clear, different reconstruction versions with varying calibrations, MVD hits). An upper limit on this value is obtained from the statistical comparison of HERA II BH with HERA I BH (data.vs.MC) the uncertainty incorporates the statistical error for HERA I data = 5%, and sums up at $\sqrt{5^2+7^2} = 7.7\%$.

    The total HERA I and II uncertainty is calculated as a positively correlated linear sum of the weighted HERA I and HERA II uncertainties.

- the uncertainty for the proton dissociation fraction value $f_{pdiss} = 80 \pm 2\%$ (Sec. 9.2.1) resulted in an uncertainty for the cross section: ±2.5%;

- the event elasticity can be defined by the combined EMC+HAC energy in the relevant EFO after the corrections for the dead material in the detector have been applied (the cut value is 500 MeV). Another way to define the elasticity is by the EMC and HAC energies measured and stored separately before the energy corrections have been applied. The threshold value is 400 MeV for each section (EMC and HAC) determined in the same procedure (by the random trigger runs). The uncertainty to the *ep* cross section due to different ways of defining the event elasticity: −3.8%;

- the variation of $\delta = 1.2 \pm 0.5$ results in an uncertainty of $+3.2, -2.2\%$ on the *ep* cross section and $-3.9\%, +1.6\%$ on the γp cross section;

- variation of the slope parameter $b = 4.5 \pm 0.5$ GeV^{-2} gives a negligible effect on the acceptance.

The total systematic uncertainty, added in quadrature, was $^{+10}_{-14}\%$. In addition, the following uncertainties were also considered:

- $\Upsilon(1S)$ fraction variation: the proportions of $\Upsilon(1S)$, $\Upsilon(2S)$, $\Upsilon(3S)$ were varied within the quoted total uncertainties in the CDF paper [158] (Eq. 10.8): $+6.8\%, -8, 2\%$;
- $\Upsilon(1S)$ decay branching ratio: $\pm 2.4\%$ [126].

Taking into account the latter two, added in quadrature, gives: $^{+12}_{-17}\%$.

The uncertainty related to the luminosity measurement is different over the years: 1.8% in 1996-1999(e), 2.25% in 1999(p)-2000, and 2.6% in 2003-2007 [163]. The weighted average the uncertainty is ±2.6% and is not included into the final total systematic uncertainty.

	$60 < W < 130$ [GeV], %	$130 < W < 220$ [GeV], %	$60 < W < 220$ [GeV], %
signal extr.; norm. to right	-2.4	-31.8	-9.4
signal extr.; norm. to left	26.8	6.8	1.2
trigger & muon efficiency -9%	-9.0	-9.0	-9.0
trigger & muon efficiency +9%	9.0	9.0	9.0
proton diss. 20-2%	-2.5	-2.5	-2.5
proton diss. 20+2%	2.5	2.5	2.5
$E_{ZUFO} \rightarrow E_{EMC} : E_{HAC}$	1.9	-8.6	-3.8
$SL5 \rightarrow SL7$	1.4	0.0	0.4
$acc; W^{\delta}; \delta = 0.7$	3.3	0.4	3.2
$acc; W^{\delta}; \delta = 1.7$	-3.1	-0.4	-2.2
$acc + flux; W^{\delta}; \delta = 0.7$	-1.4	-2.4	-3.9
$acc + flux; W^{\delta}; \delta = 1.7$	0.5	2.1	1.6
1s state frac. -6%	-8.2	-8.2	-8.2
1s state frac. $+5\%$	6.8	6.8	6.8
$\mu\mu$ branching -2.4%	-2.4	-2.4	-2.4
$\mu\mu$ branching +2.4%	2.4	2.4	2.4

Table 10.7: *Sources of systematic uncertainty in exclusive PHP, $60 < W < 220$ GeV. The numbers reflect the amount (in %) and the direction of the cross section deviation from the central value (see text).*

The uncertainties for the cross section measurement in DIS are the same as in PHP except the uncertainty related to the trigger and muon acceptance, the upper value for which was estimated to be $\approx 5\%$, and can be neglected compared to the uncertainty related to the signal extraction: $+29, -14\%$.

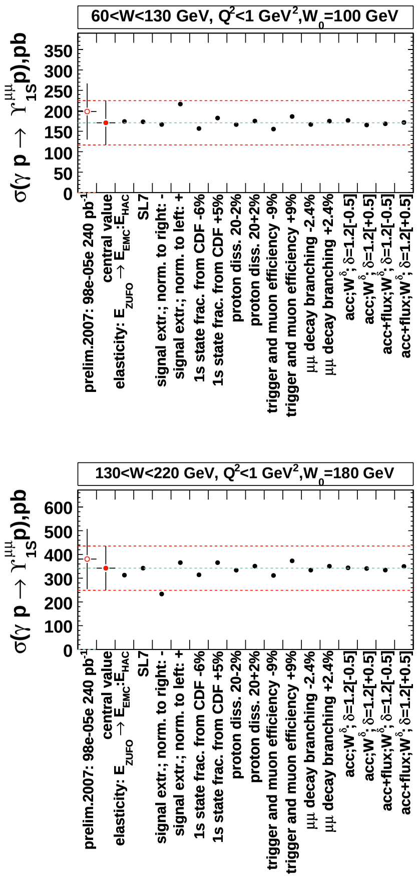

Figure 10.5: *(top) Systematics for the lower W range ($60 < W < 130$ GeV), (bottom) Systematics for the higher W range ($130 < W < 220$ GeV). The dashed lines indicate the statistical uncertainty of the "central value".*

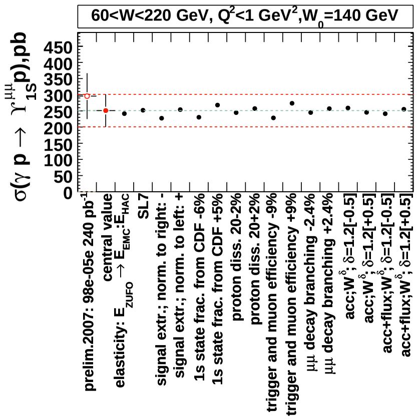

Figure 10.6: Systematics for the full W range. The dashed lines indicate the statistical uncertainty of the "central value".

10.7 W dependence of the cross section

The ep and γp cross section for $\Upsilon(1S)$ production was evaluated according to the Eq. 10.9, 10.10.

The following results were obtained for PHP (Q_0^2=0 GeV^2):

$$\sigma^{\gamma p\to\Upsilon(1S)p} = 171 \pm 54^{+50}_{-21} \text{ pb}, \quad 60 < W < 130 \text{ GeV} \tag{10.11}$$

$$\sigma^{\gamma p\to\Upsilon(1S)p} = 342 \pm 93^{+44}_{-119} \text{ pb}, \quad 130 < W < 220 \text{ GeV} \tag{10.12}$$

$$\sigma^{\gamma p\to\Upsilon(1S)p} = 251 \pm 50^{+29}_{-38} \text{ pb}, \quad 60 < W < 220 \text{ GeV} \tag{10.13}$$

The number of events, the acceptance, the flux and the cross sections in the different W intervals are given in Tables 10.8, 10.9.

W range $[GeV]$	N_{obs}	$N_{\Upsilon(1S)}$	$\mathcal{A}$	Cross section $\sigma^{ep\to\Upsilon(1S,2S,3S)p}Br[pb]$	Cross section $\sigma^{ep\to\Upsilon(1S)p}[pb]$
60 - 130	$41 \pm 13^{+11}_{-1}$	$30 \pm 9^{+8}_{-2}$	0.216	$0.32 \pm 0.10^{+0.09}_{-0.04}$	$9.5 \pm 3.0^{+2.8}_{-1.1}$
130 - 220	$44 \pm 12^{+3}_{-14}$	$32 \pm 9^{+4}_{-10}$	0.230	$0.33 \pm 0.09^{+0.04}_{-0.11}$	$9.5 \pm 2.6^{+1.2}_{-3.3}$
60 - 220	$85 \pm 17^{+1}_{-8}$	$62 \pm 12^{+6}_{-7}$	0.226	$0.64 \pm 0.13^{+0.07}_{-0.10}$	$18.8 \pm 3.8^{+2.1}_{-2.9}$

Table 10.8: Measurements of the Υ production cross section for $Q^2 < 1$ GeV^2. The first uncertainty is statistical, the second systematical. N_{obs} is the uncorrected number of events in the signal mass region, $N_{\Upsilon(1S)}$ is the determined number of signal events, $\mathcal{A}$ is the acceptance,

W range (GeV)	Φ (GeV)	$< W_0 >$	Cross section $\sigma^{\gamma p\to\Upsilon(1S,2S,3S)p}Br(pb)$	Cross section $\sigma^{\gamma p\to\Upsilon(1S)p}(pb)$
60 - 130	0.055	100	$5.9 \pm 1.9^{+1.7}_{-0.7}$	$171 \pm 54^{+50}_{-21}$
130 - 220	0.028	180	$11.7 \pm 3.2^{+1.5}_{-4.1}$	$342 \pm 93^{+44}_{-119}$
60 - 220	0.075	140	$8.7 \pm 1.7^{+1.0}_{-1.3}$	$251 \pm 50^{+29}_{-38}$

Table 10.9: Measurements of the Υ production cross section for $Q^2 < 1$ GeV^2. The first uncertainty is statistical, the second systematical. Φ is the effective photon flux used to compute the γp cross section from the ep cross section (Tab. 10.8) at $< W_0 >$ and $< Q_0^2 >= 10^{-3}GeV^2$.

The data are compared in Fig. 10.7, 10.8 to several theoretical calculations. Frankfurt, McDermott and Strikman (FMS) [75] based their calculation on a two-gluon exchange between the interacting $q\bar{q}$ dipoles and the proton, using CTEQ4L parton density functions (pdfs) [164]. Ivanov, Krasnikov and Szymanowski (IKS)

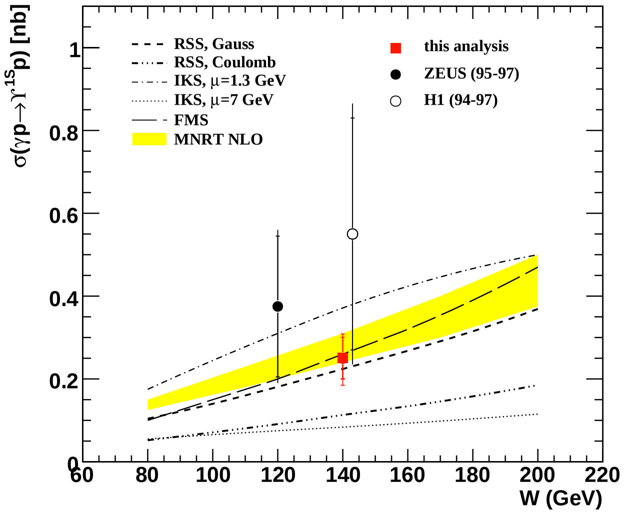

Figure 10.7: *The $\gamma p \rightarrow \Upsilon(1S)p$ cross section as function of W over the whole W range 60<W<220 GeV. Theory curves described in the text.*

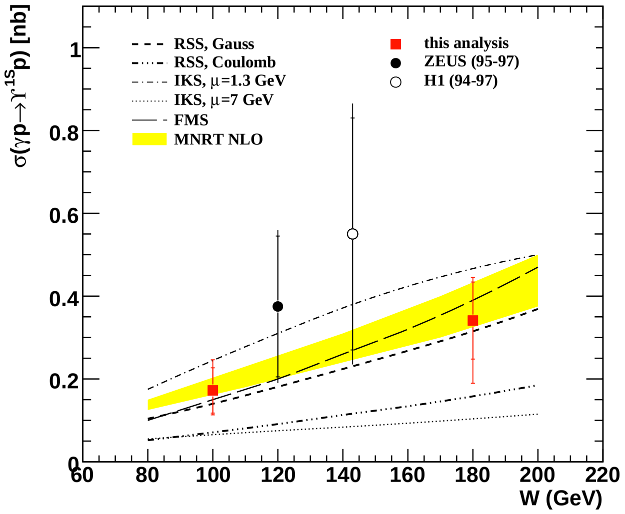

Figure 10.8: *The $\gamma p \rightarrow \Upsilon(1S)p$ cross section as function of W over the two W subranges 60<W<130 GeV and 130<W<220 GeV. Theory curves described in the text.*

[62] use a calculation in which the prediction for the W dependence of the cross section depends on the scale adopted for the hard scattering (presented here for $\mu = 1.3$ GeV and $\mu = 7$ GeV). Martin, Nockles, Ryskin and Teubner (MNRT) [74] have both a leading-order (LO) and a next-to-leading-order (NLO) calculation using the gluon PDFs extracted from J/ψ data fits [165]. Rybarska, Schäfer and Szczurek (RSS) [77] use a k_T-factorisation approach trying a Gaussian-like and a Coulomb-like light-cone wave-function for the vector meson. All the calculations are consistent with the data.

Also shown are a previous ZEUS result [157] based on a partially overlapping data set and a H1 result [166]. The presently measured two cross section values were used to calculate δ, resulting in $\delta = 1.2 \pm 0.8$, a value consistent with the theoretical expectation $\delta_{FMS} = 1.7$ [167].

10.8 $|t|$ dependence of the cross section

For the $d\sigma/dt$ measurement the number of bins to extract the t-slope is strongly limited by the resolution of $|t| \approx p^2_{T\mu\mu}$. The dimuon mass was limited to be within the range $9.33 \div 9.66$ GeV in order to reject poorly reconstructed muon tracks from the beginning of the study. The resolution of the variable $|t|$ defined as the RMS of the distribution of the difference between the MC generated level $|t|_{gen}$ and the reconstructed level $|t|_{rec}$:

$$Resolution_{|t|} = RMS(|t|_{rec} - |t|_{gen}) = f(|t|_{rec}) \tag{10.14}$$

is presented on the Figure 10.9 for all periods taken for the analysis. The binning was selected such that the bin width along the $|t|_{rec}$ axis would be about 2 times as much as the resolution value, as taken from the "all periods" plot on the Fig. 10.9(bottom,right).

The acceptance defined for each $|t|^i_{rec}$ bin as the ratio of the number of the events

$$Acceptance^i_{|t|} = \frac{N^i_{rec}}{N^i_{gen}}, \tag{10.15}$$

where N^i_{rec} is the number of the events with $|t|^i_{rec}$ in the range of the $i-bin$, and N^i_{gen} is the number of the events with $|t|^i_{gen}$ in the range of the $i-bin$. The ratio shows the fraction of the events reconstructed in the $|t|$ range (see Fig. 10.10).

The purity defined for each $|t|^i_{rec}$ bin as the ratio of the number of the events

$$Purity^i_{|t|} = \frac{N^i_{rec}\&\&N^i_{gen}}{N^i_{rec}}, \tag{10.16}$$

where the operation && requires that both $|t|^i_{rec}$ and $|t|^i_{gen}$ belong to the same $i-bin$. The ratio shows the fraction of the events reconstructed in the "correct" $|t|$ range (see Fig. 10.11).

The loss of the Purity and worsening of the Resolution with the rising $|t|_{rec}$ is explained by event migration from lower $|t|_{rec}$ values to the higher ones due to an unidentified DIS electron. Since the electron in the untagged PHP is not detected, the transverse momentum of the electron can not be taken into account for the correct measurement of the $|t|_{rec}$ (see Section 7.2).

An exercise technically identical to the one performed with the J/ψ samples and described in Sect. 9.2.1, has been repeated with the Υ samples. The fraction of the $Upsilon$ proton dissociation sample was fixed at the value obtained in Sect. 9.2.1. The event t-distribution and the $\chi^2 = \chi^2(b_{el}, b_{pd})$ plots are presented (Fig. 10.12). The contour lines are the χ^2_{min}+1, +2, and +3 isolines given to guide the eye. The 1-, 2-, and 3-sigma contours, which correspond to the axis parameter uncertainties, are given by the formula:

$$1 - Prob(\chi^2, n) = \{0.68, 0.95, 0.99\}. \tag{10.17}$$

In case one of the parameters can be treated as being fixed (b_{pd}, proton dissociative t-$slope$) the number of parameters is $n = 1$ and the χ^2 values are calculated as:

$$\chi^2 = \chi^2_{min} + \{1, 4, 9\}. \tag{10.18}$$

The result of the exercise is expressed in:

$$b_{el} = 4.7^{+1.7}_{-0.8}\ GeV^{-2}, \tag{10.19}$$

where b_{el} is the t-slope value for the elastic $\Upsilon(1S)$ photoproduction process.

A more conventional way to extract the elastic t-slope is to perform a simple exponential fit to the dN/dt distribution unfolded with the $|t|$ dependent acceptance dA/dt. The results of the fit using three points in the range $|t| < 1\ GeV^2$ and two points in the range $|t| < 0.45\ GeV^2$ are presented on Figures 10.13 and 10.14. Both results agree with value quoted in Eq. 10.19.

The sources of systematic uncertainty for the measurement are:

- BH background subtraction, variation of the background fraction within the uncertainties of the estimation $16 \pm 1\%$ gives: $\pm 0.1\ GeV^{-2}$,
- proton dissociation fraction variation $20 \pm 2\%$ gives: $\pm 0.3\ GeV^{-2}$,
- systematics related to the $|t|$ resolution: can not be fully quantitatively estimated, but is not expected to give an effect larger then $\pm 1.0\ GeV^{-2}$, based on the J/ψ study (Sec 9.2.1), and disagreement with the previous J/ψ measurments.

The measured b slope value for the t-dependence of the exclusive $\Upsilon(1S)$ cross section agrees with the one measured in the J/ψ production, which is consistent with expectations.

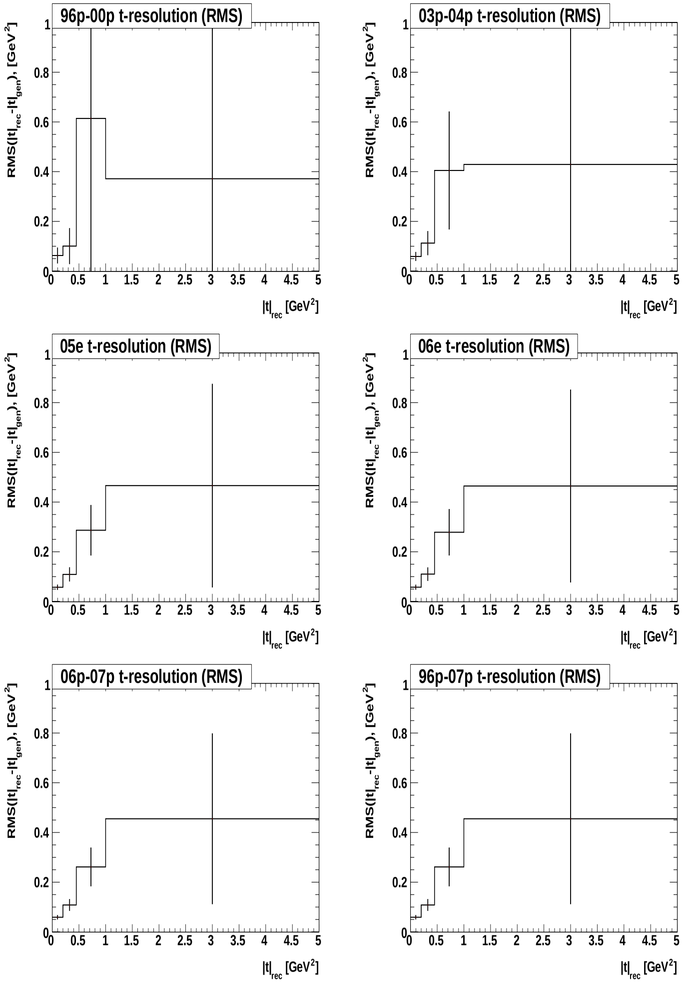

Figure 10.9: The resolution as function of $|t|$ given for HERA I(96p00p), for HERA II(03p-04p,05e,06e,06p-07p), and for all periods (96p-07p). The error bars denote the statistical significance of the RMS($|t|_{rec} - |t|_{gen}$).

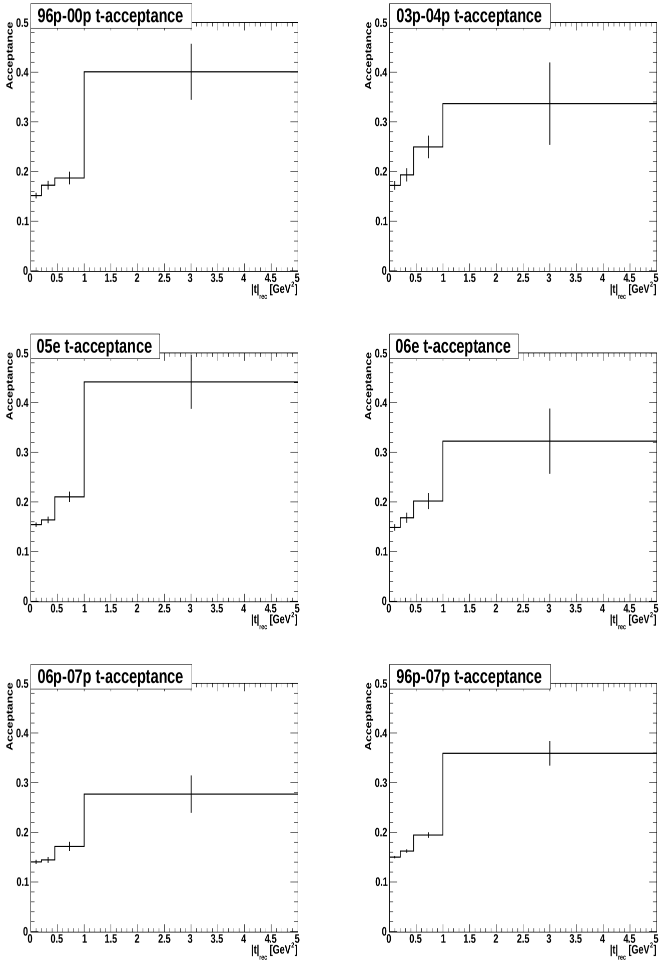

Figure 10.10: The acceptance as a function of $|t|$ given for HERA I(96p00p), for HERA II(03p-04p,05e,06e,06p-07p), and for all periods (96p-07p).

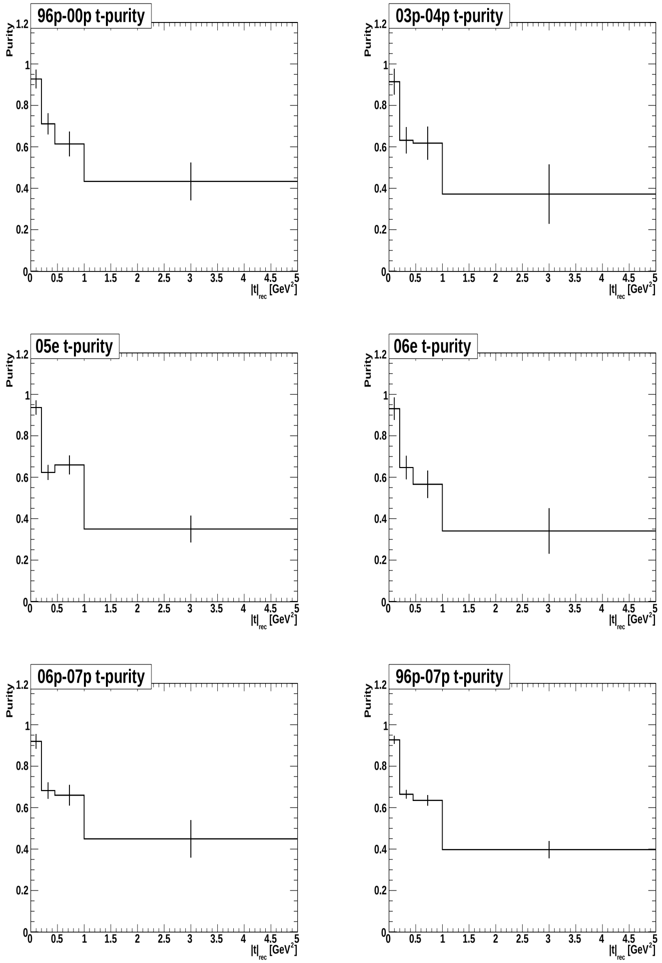

Figure 10.11: The purity as a function of $|t|$ given for HERA I(96p00p), for HERA II(03p-04p,05e,06e,06p-07p), and for all periods (96p-07p).

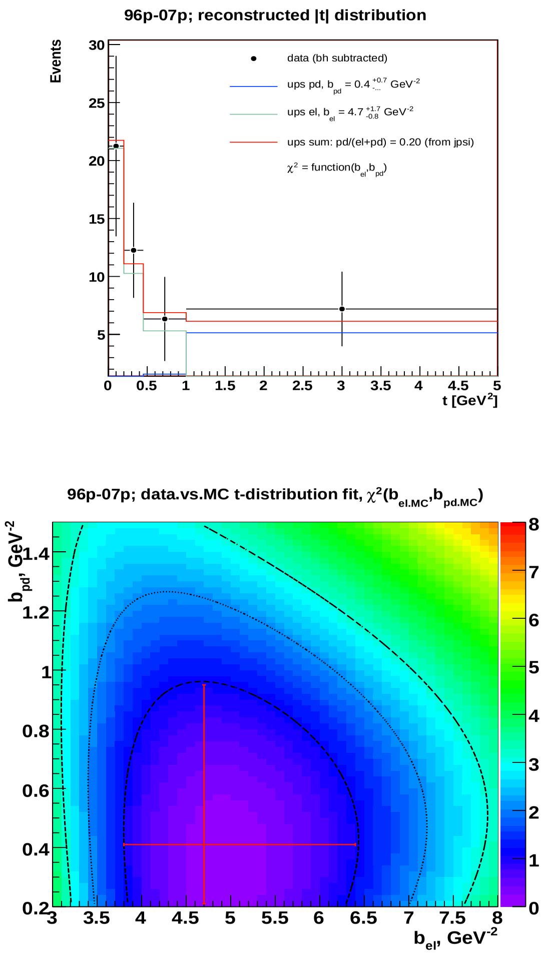

Figure 10.12: *(top) Distribution of events as function of $|t|$. (bottom) 2D distribution of χ^2 as function of t-slope parameters b for elastic and p.dissociative production processes. The contour lines are the χ^2_{min}+1, +2, and +3 isolines given to guide the eye.*

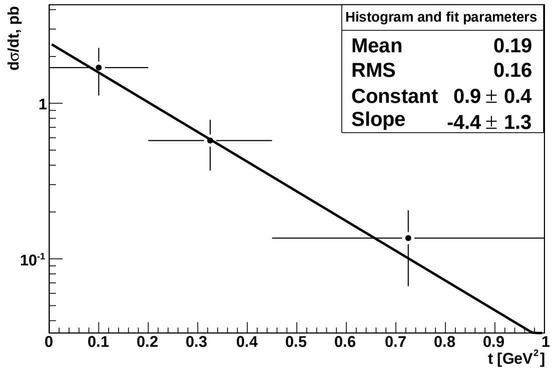

Figure 10.13: *Differential cross section distribution of the $\Upsilon(1S)$ meson. The fit is performed using the weighted center of the bins.*

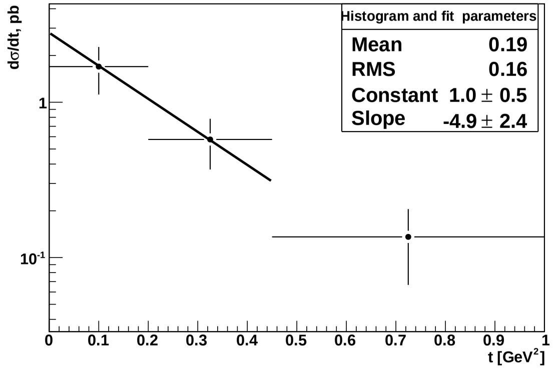

Figure 10.14: *Differential cross section distribution of the $\Upsilon(1S)$ meson. The fit is performed using the weighted center of the bins.*

10.9 Q^2 dependence of the cross section

The cross section value for the Υ production in $15 < Q^2 < 100$ GeV^2 and $60 < W < 220$ GeV was measured in similar manner to the cross section measurement in PHP (Sect. 10.7). The values of the extracted signal (Tab. 10.6, Fig. 10.3(bottom)), acceptance (Tab. 10.4), elastic production fraction (same as in PHP, Eq. 9.1) and the ep cross section values are presented in Table 10.10.

The combination of the cross section measurement in PHP and DIS allows to study the Q^2 dependence of the exclusive production cross section (see Table 10.11).

Figure 10.15 presents a comparison of the Q^2 dependence of the cross section for ρ [168] and J/ψ [154] mesons with the $\Upsilon(1S)$ obtained in this thesis. A parametrisation of the cross sections was made with the function $\frac{1}{(Q^2+M_V^2)^n}$, and the plotted curves are given to guide the eye. In the case of the ρ meson the $n = n(Q^2)$ and in the case of J/ψ and Υ value $n = 2.5$ is used.

W range GeV	Q^2 range GeV^2	N(1S,2S,3S) events	Acc.	Elastic fraction	Cross section, (pb) $\sum\limits_{i=1,2,3} \sigma(ep \to \Upsilon_i ep)Br_i$
60 – 220	15 – 100	21±7	0.37	0.80±0.02	0.092 ± 0.031

Table 10.10: *Cross section of the integral signal seen in the muon decay channel of the Υ(1S,2S,3S) states in the $ep \to \Upsilon_i ep$. The signal is observed in the sample of 493 pb^{-1}.*

W_0	Q_0^2	Effective Flux	$\sigma(\gamma^* p \to \Upsilon(1S)p)$ (pb)
90	0.001	$0.127^{+0.025}_{-0.018}$	0.144±0.029
90	30	$0.011^{+0.002}_{-0.002}$	0.244±0.080

Table 10.11: *Cross section $\sigma(\gamma^* p \to \Upsilon(1S)p)$ calculated for the measured $\sum\limits_{i=1,2,3} \sigma(ep \to \Upsilon_i ep)Br_i$ in the range 60< W <220 GeV listed in the Tables 10.8, 10.10. The 1S state fraction (Eq.10.8) and the muon branching Br=2.48±0.06% have been taken into account. The value Q_0^2 = 30 GeV^2 is chosen to be close to the centre of weight of the Υ meson distribution in the range $15 < Q^2 <$ 100 GeV^2.*

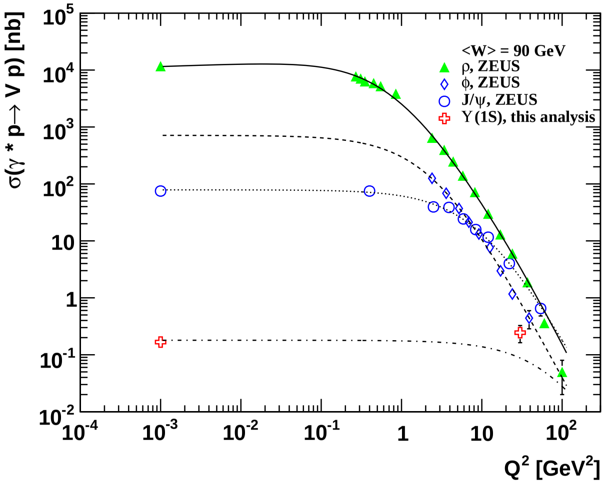

Figure 10.15: *The $\Upsilon(1S)$ meson cross section as function of Q^2 presented in comparison with the ρ and J/ψ mesons. The implemented fit function is of the order $\frac{1}{(Q^2+M^2)^n}$, where n is known to vary with Q^2 for ρ meson production, and to be constant $n = 2.5$ for the J/ψ production. The suggested form of $n = n(Q^2)$ as $n = a + b \cdot log(Q^2 + M^2)$ is implemented for the full range of the ρ measurements and is drawn in dots. The fit of the J/ψ cross section gives $n = 2.5$. The Υ cross section measurement does not allow to perform a fit to extract the value of n. A curve with fixed $n = 2.5$ is applied.*

Chapter 11

Inelastic Υ production

This Chapter presents a possibility of an extension of the elastic Υ production measurement to the inelastic channel as function of the event inelasticity z.

11.1 Kinematics

The inelastic production determines the production with accompaning energy flow seen in the detector. The transition from elastic to inelastic can be defined in terms of the energy flow not related to the Υ meson decay products and expressed in terms of the variable:

$$z = \frac{(E-p_z)_\Upsilon}{(E-p_z)_{had} + (E-p_z)_\Upsilon} \tag{11.1}$$

where $(E-p_z)_{had}$ is calculated by the hadronic activity in the tracking system and calorimeter and excludes the Υ decay products and DIS electron by definition. There are three regions of z:

- z=1, elastic production,
- $0.95 < z < 1$, production with dissociation of the proton,
- $z < 0.95$, inelastic production.

The boundary value $z_0 = 0.95$ is arbitrary and is defined by convention. In a more general sense the proton dissociation is an inelastic process. However, for some features it is considered together with the elastic production in terms of Pomeron exchange. The dissociation of the proton is described in phenomenological models (e.g. **Sophia** [142]) due to the low mass excitations of the proton following the interaction and abundance of the baryonic resonances in

the mass range $m_p < M_Y < 4$ GeV, where m_p is the mass of the proton, and M_Y is the mass of the proton remnant system. Nevertheless, conseptually it might be reasonable to include the diffractive processes with the proton dissociation into the domain of inelastic processes with $z < 1$, i.e. not *elastic* ($z = 1$) processes.

Another variable is the muon isolation which is defined in terms of the sum of the energy in the cone ΔR around a muon:

$$\Delta R = \sqrt{\Delta\phi^2 + \Delta\eta^2} < 1. \tag{11.2}$$

The single muon isolation variable:

$$I^{\mu j} = \sum_{i=1}^{N_{EFO}} p_T^{EFO_i}|_{EFO_i \neq muon_j}, \tag{11.3}$$

can also be used to define the isolation for two muons as:

$$I^{\mu\mu} = \sqrt{I_{\mu 1}^2 + I_{\mu 2}^2}. \tag{11.4}$$

Dimuons from semileptonic decays of charm and beauty quarks are accompanied by hadronic activity. Dimuons from quarkonia decays lead to very isolated dimuons in the detector (see Fig. 11.1 taken from [85]). A good value to suppress the open charm and beauty decay dimuons is to select $I^{\mu\mu} < 1$ GeV (or $I^{\mu} < 1$ GeV).

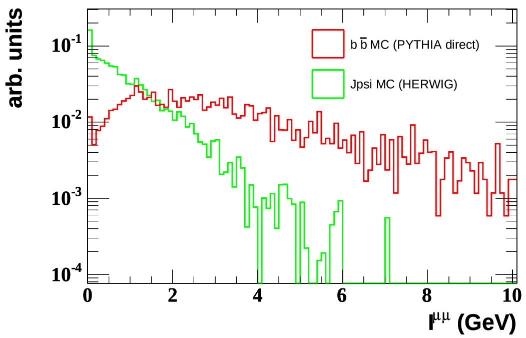

Figure 11.1: *Dimuon isolation distribution for J/ψ and open beauty MC.*

11.2 Signal extraction

The signal extraction partially followed the selection of the open beauty production with dimuon tag [85]. The event selection for the inelastic Υ production and decay into muons was:

- data events from 1996 to 2007 corresponding to 473 pb^{-1},
- global CAL timing $<$ 10 ns,
- vertex position $z_{vtx} < 50\ cm$,
- transverse CAL energy excluding the FCAL inner ring, $E_T^{CAL} - E_{innerring}^{FCAL} >$ 8 GeV, legacy cut [85],
- quality of each of the two muons ≥ 4, typical selection for muon identification in inelastic processes [85],
- both muons are required to match a CTD track originating from the primary vertex to suppress dimuons from secondary vertices,
- transverse momentum of each muon $>$ 2.5 GeV to suppress dimuons from charm decay,
- dimuon isolation $I_{\mu\mu} < 1$ GeV to suppress dimuons from open heavy quark production [85],
- the DIS contribution was suppressed by an explicit requirement of no Sinistra candidates to be found in the sample to suppress elastic DIS contribution.

Figure 11.2 presents the dimuon mass spectra after the selection. The remnant of the J/ψ peak is clearly seen in the bin $3.0 \div 3.3$ GeV. The part of the spectrum above 4 GeV is expected to consist of a smooth and wide distribution dominated by open $c\bar{c}$ and $b\bar{b}$ production with two muons in their decay products, the only peak-resonant structure coming from the decay of Υ(1S,2S,3S) states.

The background estimation has been performed with a straight line fit (1-st order polynomial) in the range $5 \div 15$ GeV, the signal region $9 \div 10.5$ GeV being excluded from the fit. Consequently the number of the events in the signal region above the background was assumed to come from the $\Upsilon \rightarrow \mu\mu$ decay channel, the statistical error was estimated as the square root of the number of events in the data histogram in the signal region, thus the number of Υ candidates is $N_{\Upsilon(1S,2S,3S)} = 31 \pm 7$ events. The bulk of the signal is distributed from 0.5 to 0.95 in z.

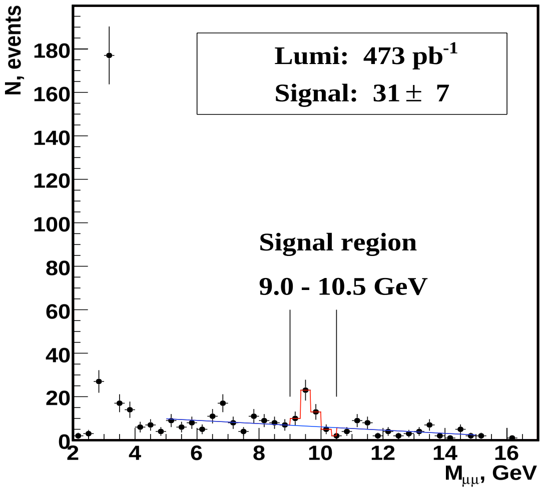

Figure 11.2: *The invariant dimuon mass distribution in the inelastic Υ meson production selection. The signal was estimated as the excess over the linear background.*

The cross section measurement as function of z can be anticipated with the first measured point at $z = 1$ coming from the elastic cross section (Chapter 10) and the second one covering the range $0.5 < z < 0.95$. The range $0.95 < z < 1$ formally not included into the inelastic production definition can be also considered for the measurement.

As it has been mentioned the cuts were not yet optimised for the cross section measurement, and in a subsequent analysis the cuts should be tuned according to the **Pythia** MC (see Appendix B). The cut on the transverse CAL energy suppresses both the elastic and proton dissociation production contributions. For the signal of marginal significance it makes sense to drop the CAL transverse energy cut and choose a strategy of a combined elastic/proton-dissociations/inelastic cross section measurement. The DIS contribution should be also included into the study by default.

Part IV

Concluding part

Chapter 12

Measurement summary and outlook

The elastic Υ production cross section measurement with the ZEUS detector and its dependence on the kinematic variables W, $|t|$ and Q^2 is presented in Chapter 10. The muon decay channel was considered in the thesis.

The results presented in this thesis are based on several tracking software versions not yet completely optimised for the HERA II data. The ZEUS HERA II calibration, allignment and reconstruction software were finalized only by the end of 2008 and the best results in terms of the tracking possibilities were achieved.

The Υ cross section measurements can be improved after the HERA II Grand Reprocessing has been completed. The HERA II data set then becomes uniform in terms of the tracking both in the data and in the MC. The improvements in the tracking resolution directly affect the mass peak resolution giving possibly a better signal to background ratio as well as the $|t|$ resolution and allow the t-slope measurement with well-determined systematic uncertainties.

Further benefits from the HERA II upgrade such as the STT impact and inclusion of the BAC trigger on the measurement are to be explored. Another possibility of an improved W and $|t|$ dependence measurement is opened in the combination of the PHP and DIS elastic production channels due to an increase in the statistics.

The Υ photoproduction electron decay channel has been studied on part of the ZEUS data in [169]. The PHP cross section measurement presented in this thesis is based on the muon triggers, which were diligently maintained throughout all HERA running periods. The electron based trigger slots were not equally well maintained and the profit of the extention of the measurement to the electron channel needs to be carefully estimated. The Q^2 dependence measurement is based on the DIS trigger slots, which have been given highest possible care during the ZEUS data taking. The benefit from the combination of the muon and the electron Υ decay channels for the production in DIS cross section measurement is anticipated.

The inelastic production of Υ meson and the cross section z dependence measurement was shown to be feasible (Chapter 11). The following recommendations for the cross section measurement can be given: the cuts are to be tuned according to the MC ($\Upsilon(1S)$, **Pythia** , Appendix B). For the signal of poor statistical significance one might prefer to loosen the CAL transverse energy cut and choose a strategy of a combined elastic/proton-dissociation/inelastic cross section measurement. The cross section measurement should be pursued. The combination with the inelastic DIS and with the electron decay channel should be considered.

Chapter 13

Measurement comparison to theory

In Chapters 10 the exclusive $\Upsilon(1S)$ production cross section measurement is presented as a function of W and Q^2. The feasibility of a measurement of the $|t|$ dependence of the cross section is discussed, as well as an extension of the measurement to inelastic Upsilon production (Ch. 11) as function of the event inelasticity z.

The W dependence of the exclusive vector meson production cross sections is an important source of information about the gluon GPDs, $f(x, \vec{k}_T^2)$, in the proton. A steep rise of the W-slope is observed in the transition from light to heavy vector meson photoproduction and equally in the transition from low to high values of Q^2 for light vector mesons (Ch. 1.3.4). The expected W-slope for $\Upsilon(1S)$ photoproduction can be estimated from the $\sigma(\gamma p)$ total cross section (Fig. 1.14) within an assumption of $\delta \approx 4\lambda$ according to Eq. 2.5 and value $\lambda \approx 0.27$ read from Fig. 1.14(right) at $\frac{Q^2+M^2_{\Upsilon(1S)}}{4} = Q^2_{eff} = 23\ GeV^2$, which gives: $\delta \approx 1.1$. The measured W-slope value $\delta_{\Upsilon(1S)} = 1.2 \pm 0.8$ agrees well with the expected value of the W-slope. Unfortunately the error on the measurement does not allow to say that it is inconsistent with a flat W dependence.

Fig 13.1 presents the combined $\delta = \delta(Q^2 + M_V^2)$ plot for exclusive vector meson production at HERA. The values of the W-slope δ obtained in various exclusive vector meson production reactions show that the δ value rises as the scale of the interaction increases. The measured δ dependence of the $\sigma(\gamma p \to \Upsilon(1S)p)$ agrees with the expectation based on the extrapolation from the lighter vector meson production.

A comparison with calculations from various perturbative QCD approaches has been performed. The calculations for the models IKS, MNRT, FMS, and RSS, discussed in Chapter 2, are plotted together with the measured cross sections on

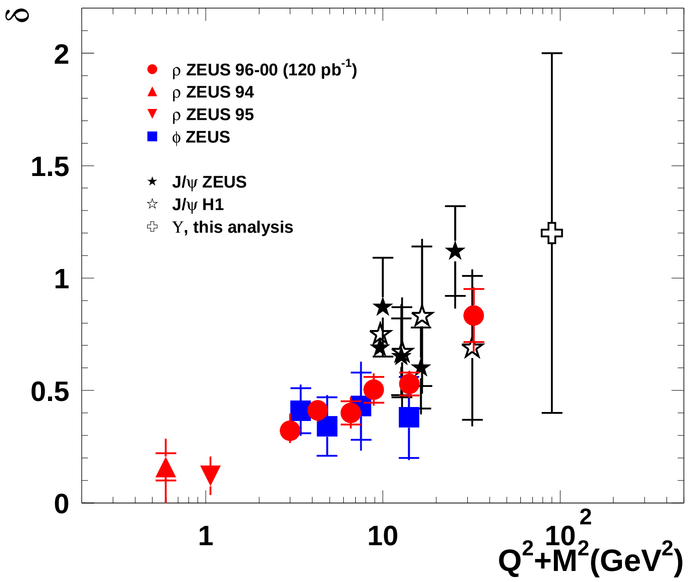

***Figure 13.1:** The combination of available δ values measured in vector meson exclusive production by H1 and ZEUS.*

Figures 13.2, 13.3, 13.4, 13.5.

The NRQCD NLO calculations (Fig. 13.2) by IKS (see Section 2.1.3, Fig. 10.7, 10.8) are based on a rigorous QCD scheme taking into account only colour singlet components of the produced $b\bar{b}$ pair. The GPDs used in the LO and NLO calculations are based on the CTEQ6 set of forward distributions.

The IKS calculations were performed with two values of the hard scale $\mu = 1.3$ GeV and $\mu = 7$ GeV. The comparison with the data suggests an intermediate value of the scale to be used in the IKS calculations. The W-slope of the measured cross section agrees with the slope predicted at both values of the scale.

Other calculations involved into the discussion are variations of the colour dipole approach and are different in the form of the vector meson wave function or in the way to perform the gluon GPD evolution. All calculations differ in the way the hard scale of the process is defined.

The MNRT (Fig. 13.3, Section 2.2.1) is based on the PDF evolution in $log(\frac{1}{x})$, the vector meson formation is based on a parton-hadron duality and does not involve any assumption on the structure of the wave function. The hard scale is set by Eq. 2.7. The calculations were performed to LO and NLO. The NLO shows a flatter W-dependence than LO. The data agrees well with the calculations.

In the FMS (Fig. 13.4, Section 2.2.2) the PDF evolution is performed in $logQ^2$ and the vector meson wave function is based on a non-relativistic potential and accounts for the Fermi motion of quarks in the vector meson. The hard scale is set by Eq. 2.10. The calculations were performed to LO. According to [75] taking into account the effect of the gluon skewness and real part of the amplitude introduces a normalisation correction factor ≈ 5. The predicted cross section W-dependence with the corrections mentioned above taken into account agrees well with the measurement.

The RSS (Fig. 13.5, Section 2.2.3) is a k_T-factorisation approach, which uses unintegrated gluon distributions, constrained by the inclusive DIS structure functions, and two forms of the vector meson wave functions. The hard scale is set by Eq. 2.17, 2.18. The vector meson wave functions of a Gauss and Coulomb type potential were used. The data prefers the oscillator (Gauss) type of the vector meson wave function. The Coulomb type of the wave function introduces long tails in the quark distribution, which are seemingly disfavoured. The calculations were performed to NLO.

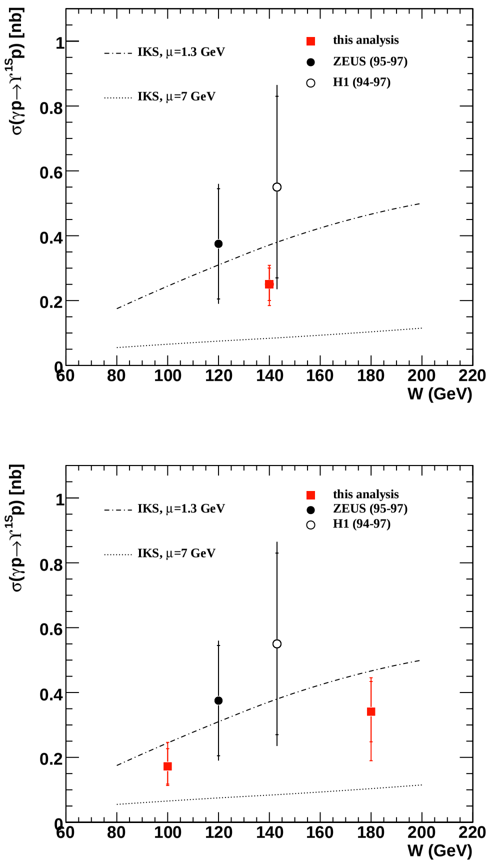

Figure 13.2: *The comparison with NRQCD NLO (IKS) predictions, two values of the hard scale considered.*

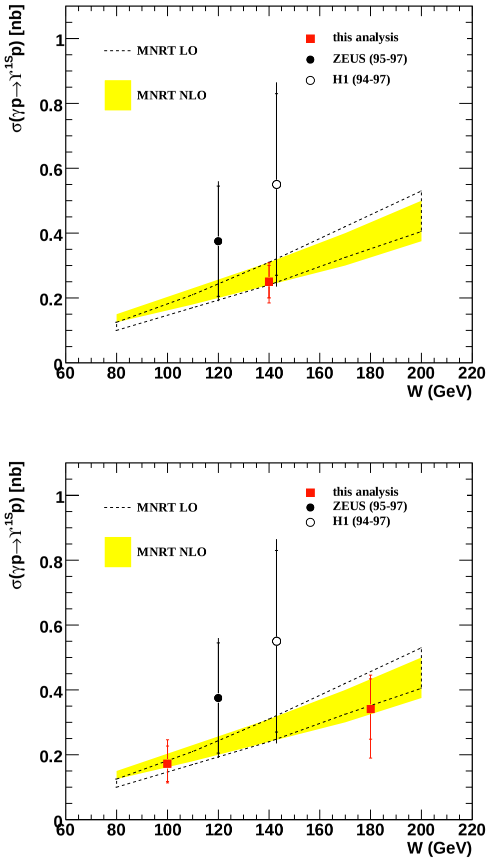

Figure 13.3: *The comparison with MNRT LO and NLO predictions.*

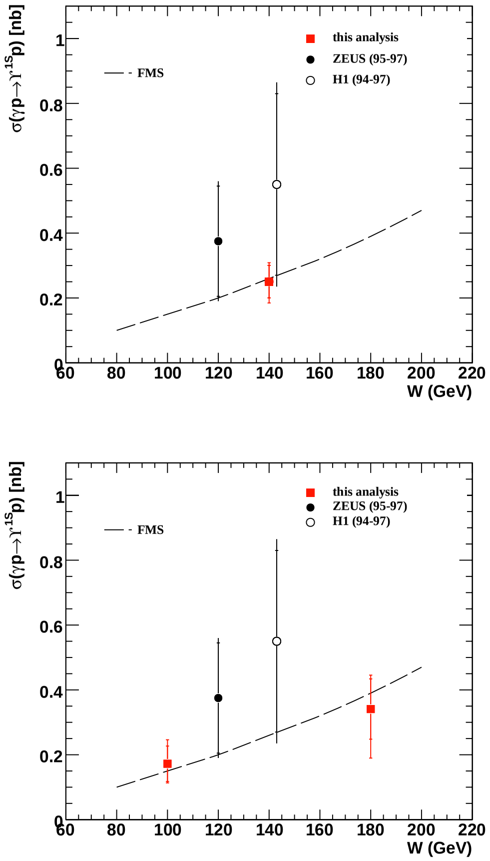

Figure 13.4: *The comparison with FMS.*

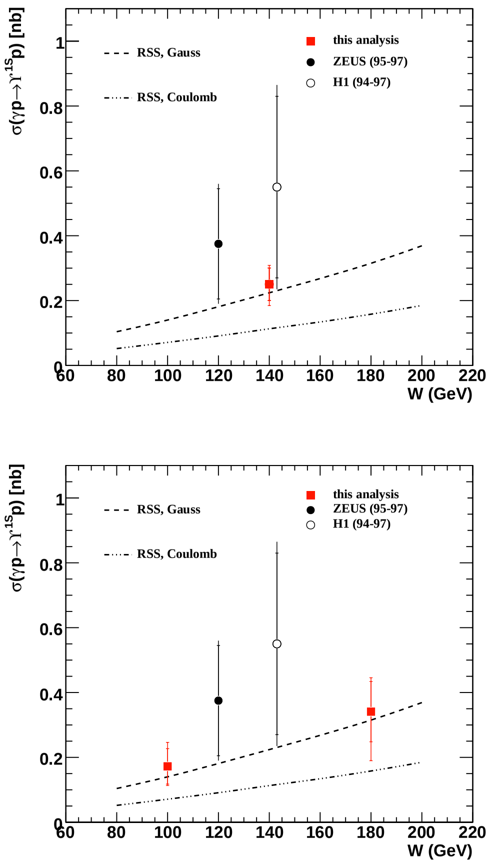

Figure 13.5: The comparison with RSS Gauss-like and Coulomb-like potentials for the vector meson wave functions.

The observed t-dependences of the vector meson processes are an important source of information on the shape of the proton in the low-x region [170]. The parameter b describes the area size of the interaction region and is obtained from a simple parameterisation of the differential cross section $d\sigma/dt \sim e^{-bt}$ at small values of $|t|$, usually $|t| < 1\ GeV^2$. The t-slope value measured for the exclusive Υ photoproduction (Chapter 10) is:

$$b = 4.7^{+1.7}_{-0.8}\ GeV^{-2}(stat.error\ only). \tag{13.1}$$

The Fig. 13.6 depicts the *t-slope* values extracted in different vector meson elastic production reactions and compared to the Υ *t-slope* presented in this thesis.

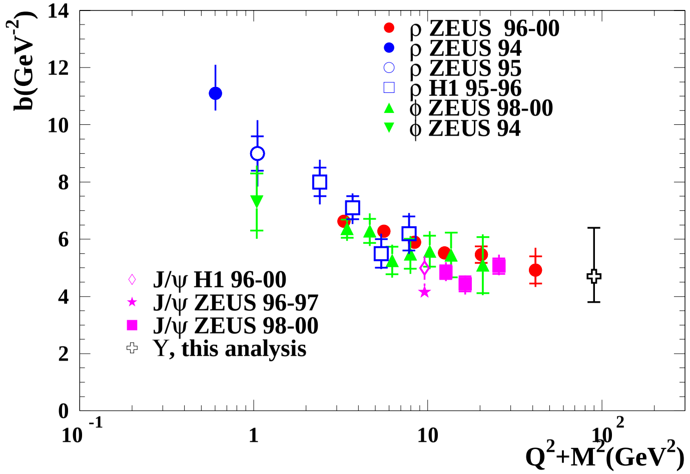

Figure 13.6: The combination of available b values measured in vector meson exclusive production by H1 and ZEUS.

The Q^2 dependence of the exclusive $\Upsilon(1S)$ production cross section has been measured at HERA for the first time. The cross section dependence is consistent with the hypothesis of the hard scale of the process introduced in Eq. 2.7, so that in the limit $Q^2 \ll M_V^2$ (for $\Upsilon(1S)$ it holds for $Q^2 \lesssim 20$ GeV^2, $|t|$ can be neglected), the $\sigma(\gamma p \rightarrow \Upsilon(1S)p)$ cross section does not depend on the Q^2 of the process in the region of measurement. In addition to the cross section dependence on the Q^2 of the process (Fig. 10.15) the dependence of the cross section on the assumed parameterisation of the hard scale $Q_{eff}^2 = Q^2 + M_V^2$ is presented on Fig. 13.7. The cross section values have been corrected for the corresponding charge factors ϵ_V given in Table 2.1. As it is seen from the plot the cross section of the process $\gamma^* p \rightarrow Vp$ can be parameterised with the function:

$$\frac{1}{\epsilon_V}\frac{d\sigma(\gamma^* p \rightarrow Vp)}{dQ_{eff}^2} = \frac{a_V}{(Q_{eff}^2)^n}, \tag{13.2}$$

where the effective scale is chosen to be $Q_{eff}^2 = Q^2 + M_V^2$, a_V is the normalisation parameter and $n = 1.7 + 0.13 \cdot ln(Q_{eff}^2)$ found from the fit to the ρ meson production points. The ratio of the normalisation parameters $a_\rho : a_\phi : a_{J/\psi} : a_\Upsilon = 1.0 : 1.11 \pm 0.02 : 1.55 \pm 0.01 : 4.9 \pm 0.9$ is expressed in ρ meson normalisation units a_ρ. The expected flavour symmetry restoration can be argued in a positive way for the light vector mesons. The J/ψ : ρ meson production ratio is known to be broken by $\lesssim 50\%$ [171]. This tendency is confirmed by the Υ meson measurement presented in this thesis. The ratio can be restored for all 4 vector mesons considered in this comparison with new effective scale:

$$Q_{eff}^2 = \frac{Q^2 + M_V^2}{ln(\frac{b^2 + M_V^2}{1\ GeV^2})}, \tag{13.3}$$

where $b^2 = 12\ GeV^2$ is a phenomenological parameter found in an iterative procedure.

In [172] by Frankfurt, Strikman, Weiss a form of the effective scale has been presented (see Fig. 13.8 (top-left)) which qualitatively agrees with Eq. 13.3 (see Fig. 13.8 (top-right)). As it is seen from Fig. 13.8 (bottom) the ratio of the cross sections $a_\rho : a_\phi : a_{J/\psi} : a_\Upsilon = 1.0 : 1.07 \pm 0.02 : 0.99 \pm 0.01 : 0.9 \pm 0.2$ is almost perfectly restored, if the ρ meson is taken as the reference. The only deviating value is the $\rho : \phi$ which has a 3.5 σ effect which can be considered as insignificant in this context and can be accounted for an approximate character of the exercise.

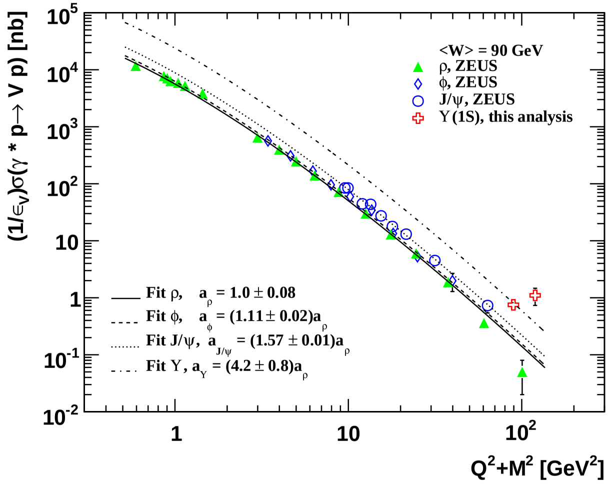

Figure 13.7: *The cross section dependence on $Q^2 + M^2$ presented for ρ, J/ψ, and $\Upsilon(1S)$ mesons. The cross sections are corrected for the constituent quark charges according to the ratio values ϵ_V given in Table 2.1. The ρ meson production fitted similar to Fig. 10.15. The fit of the ρ meson production giving $n = 2.2$ and of the J/ψ production giving $n = 2.5$ is extrapolated to higher values of the $Q^2 + M^2$ for comparison with the Υ meson measurement.*

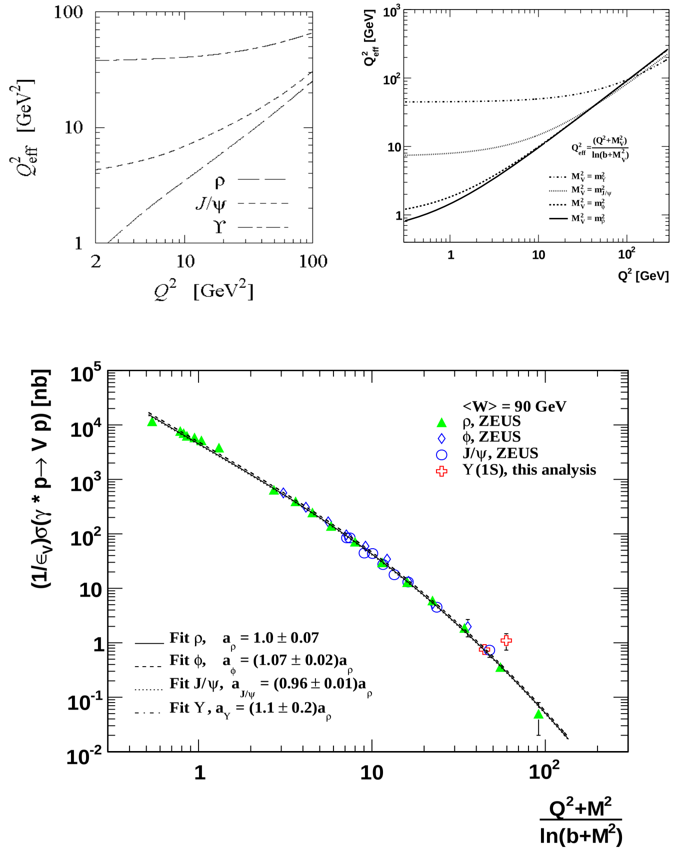

Figure 13.8: *(top-left) The effective scale Q^2_{eff} versus Q^2 dependence found in theory (see text), ρ, J/ψ, Υ mesons are considered, (top-right) The effective scale Q^2_{eff} versus Q^2 dependence found in this thesis, (bottom) the flavour symmetry restoration is seen with the new scale Q^2_{eff}. On the latter two plots ρ, ϕ, J/ψ, Υ mesons are considered. The data points presented in the bottom plot were fitted with a one parameter fit function of a kind in Eq. 13.2, where all parameters were defined from the fit of the ρ meson production points and only the normalisation factor a_V was considered to be the free parameter.*

Chapter 14

Conclusions

The measurement of bound beauty pair production in ep collisions via $\Upsilon^{1S,2S,3S}$ vector mesons observed in the muon decay channel have been presented using data from the ZEUS detector corresponding to an integrated luminosity of 468 pb^{-1} at a centre-of-mass energy of $\sqrt{s} = 318$ GeV.

The exclusive Υ photoproduction has been given most attention in the analysis (Chapter 2, 10). The cross section $\sigma(\gamma p \to \Upsilon(1S)p)$ has been measured in the kinematic region $Q^2 < 1$ GeV^2 and $60 < W < 220$ GeV, as well as in the W region split in two parts: $60 < W < 130$ GeV and $130 < W < 220$ GeV. The measured cross section behaviour agrees with the perturbative QCD predictions.

The measured $\sigma(\gamma p \to \Upsilon(1S)p)$:

- suggests a scale close to the centre of the considered range $1.3 < \mu < 7$ GeV^2 for the NRQCD NLO calculations (see Chapter 13),
- prefers the Gauss type of the wave function to the Coulomb type used in the RSS model based on k_T-factorisation,
- agrees with the FMS calculations, in which the gluon skewness and real part of the amplitude were taken into account, and disagrees if not,
- agrees with the MNRT calculations based on unintegrated gluon densities extracted from the exclusive J/ψ DIS cross section.

All models agree with the measurement and none of them can be considered as describing the data better than the others.

The b slope of the exponential $|t|$-dependence has been estimated for the $\Upsilon(1S)$ meson photoproduction. The b value was measured (Eq. 13.1):

$$b = 4.7^{+1.7}_{-0.8}\ GeV^{-2} (stat.error\ only),$$

where only the statistical error is given. The systematics can not be precisely evaluated due to the non-final tracking used in this analysis and, assuming that the systematic uncertainty will turn out to be small, therefore not quoted here.

The result can be quoted also in terms of the confidence level intervals, which makes it easier to interpret. If only the statistical errors are to be treated one can exclude at a 95% CL values $b < 3.4\ GeV^{-2}$ and $b > 7.2\ GeV^{-2}$, and at 99% CL values $b < 3.2\ GeV^{-2}$ and $b > 7.8\ GeV^{-2}$. Therefore, the measurement is consistent with the values obtained in exclusive J/ψ PHP and DIS measurements and allows to exclude high values of b like in ρ meson photoproduction and low b values like those observed in the production with proton dissociation. The results are consistent with the hard production mechanism, as expected.

The Q^2-dependence of the $\sigma(\gamma^* p \to \Upsilon(1S)p)$ has been measured in the kinematic region $15 < Q^2 < 100$ GeV^2 and W region identical to the full W region in PHP: $60 < W < 220$ GeV. The measured cross section behaviour is consistent with being flat in the region $Q^2 < 50$ GeV^2, and agrees with the perturbative QCD expectations. The Q^2-dependence can be measured with higher precision, if one considers also the electron decay channel. Potentially the statistical significance of the signal will improve by a factor $\approx \sqrt{2}$ raising the significance to the $4 \div 5\ \sigma$ significance level and will allow more definite conclusions.

The z-dependence measurement of the cross section has been shown to be feasible (Chapter 11). Due to the low statistical significance of the signal one should consider re-optimising the cuts with looser or even no rejection by the CAL transverse energy. The potential inelastic DIS contribution should be included into the measurement as well. The opportunities to measure the Υ cross section at $\approx 4\sigma$ are seen and an increase of the statistical significance can be anticipated due to the improved tracking in HERA II and signal to background optimisation.

The Straw Tube Tracker, to which the authors contribution was described in the technical part of this thesis (Chapters 4, 5), extends the kinematic coverage of the ZEUS tracking system by one pseudorapidity unit in the forward direction. The potential physics impact from the STT extention is yet to be carefully investigated. The physics tasks, which should be addressed in the context of STT in the analyses based on tracking:

- forward heavy flavour production: charm ($D^{*\pm}$) and beauty (B) mesons,
- strange hadron production: K^0, Λ^0,
- vector meson production at low W (both the electron and the muon decay channels), [also the Υ meson production discussed in this thesis],
- DVCS (in the forward part of the detector the DIS electron and the gamma quantum now can be distinguished by a track in the STT),

- lepton flavour violation ($\mu^+\mu^-/e\mu$),
- Charge Current at low hadronic system angles $\gamma_{had} < 0.4$ *radians* (Section 4.2),
- exotics state search: Penta- and Tetraquark states, leptoquarks in NC→ $e + jet$.

So far the STT has been applied successfully to the CC studies, both the trigger and the offline analysis 4, [124]. Other implementations are strongly dependent on the tracking issues, and will resume after the Grand Reprocessing of the HERA II data has been completed.

Part V

Supplementary material

Appendix A

Event selection via Trigger bits

A.1 Barrel/Rear Muon Chamber

At TLT level muon identification and reconstruction is performed via an online modification of the GLOMU algorithm. In a simple description the algorithm searches for a match between a CTD track and a track segment in the inner/outer Barrel/Rear muon chambers. There is a minor difference ($\approx 1-3\%$ in the reconstruction efficiency when one compares the online (TLT) and offline (Zephyr) GLOMU versions.

The described below TLT bits must be used in coincedence with the FLT and SLT bits based on the BRMuon information.

The full FLT-SLT-TLT BRMUON chain requires the following bits:

- 1996-2000
  - FLT 10,11,14,15
  - SLT MUO 1,2
  - TLT MUO 3, EXO 11,12
- 2003-2004
  - FLT 8,10,14,15
  - SLT MUO 1,2
  - TLT MUO 3, EXO 11,12, HFL 16
- 2005-2007
  - FLT 8,9,10,14,15

  - SLT MUO 2, GTT 5
  - TLT MUO 3, EXO 11,12, HFL 16

A.1.1 years 1996 to 2007

A.1.1.1 TLT MUO 3

Requires a GLOMU and MIP coincedence.

- one muon reconstructed by GLOMU finder
- good inner barrel/rear muon found on the second level trigger level
- hit in barrel or rear inner muon chambers
- muon-like CAL-island (requires a MIP coincedence)
- $n_{tracks-CTD} \geq 1$
- track going into barrel or rear CAL, with $p_T > 1\ GeV$
- second level trigger slot: SLT MUO 1 for 1996-2004 (replaced by SLT GTT 5 from 2005
- SLT MUO 1 includes - logical OR of the first level trigger slots FLT 8,9,10,11

NB : (for ≤2000, GLOMU does not perform the match if hit is only in the outer BRMUON chamber)

A.1.1.2 TLT EXO 11,12

Based on a version of GLOMU algorithm (GLOEXO), it does no require a coincidence with a MIP)

- one muon reconstructed by GLOMU finder
- cosmics rejection if:
  - $n_{tracks-CTD} \leq 3$
  - $E_{FCAL} < 1.0\ GeV$
  - two tracks with highest $p_T > 0.5$ and $cos(\theta_{tracks}) < -0.9998$
- CAL timing cut compatible with physics event

- includes a logical or of the first level trigger slots: FLT 14(barrel muon), FLT 15(rear muon)
- FLT 14,15 use not only the inner but also the outer muon chamber hits information
- implicit requirement of any SLT physics slot

A.1.2 years 2003 to 2007

A.1.2.1 TLT HFL 16

- a logical OR of SLT slots based on muon identification and SLT diffractive physics. In terms of internal logic this slot contains 4 branches:
  - a track segment in the Barrel/Rear muon chambers,
  - the logic is based on a version of GLOMU algorithm (GLOMU1),
  - SLT: HFL 3,4,9,10 or MUO 1,2,6,7 or GTT 2,5

A.2 FMUON

The described below TLT bits must be used in coincedence with the FLT and SLT bits based on the FMuon information.

The full FLT-SLT-TLT FMUON chain requires the following bits:

- 1996-2000
  - (FLT 4) and (SLT MUO 3) and (TLT MUO 4)
- 2004-2007, an OR of the following three chains:
  - (FLT 0 or FLT 18) and (SLT MUO 3) and (TLT MUO 4)
  - (FLT 0) and (SLT MUO 4) and (TLT MUO 1)
  - (FLT 6) and (SLT MUO 5) and (TLT MUO 2)

A.2.1 years 1996 to 2000

A.2.1.1 TLT MUO 4

- muon identified and reconstructed by MAMMA algorithm
  - logical OR of an FMUON$_{hit}$ with FCAL$_{mip}$ OR CTD$_{track}$

  - mass of the dimuon > 1.5 GeV
  - vertex z coordinate $Z_v tx$ >75 [cm]
- SLT MUO 3 must be required explicitely in addition
- FLT 4 must be required explicitely in addition

A.2.2 years 2003 to 2007

A.2.2.1 TLT MUO 1

- MUO 1: isolated muon in FMU
  - $\geq$ 1 FMU matched to MIP
  - No beam gas
  - Vertex
- SLT MUO 4 must be required explicitely in addition
- FLT 0 must be required explicitely in addition

A.2.2.2 TLT MUO 2

- high E_T in CAL and FMU
  - $\geq$ 1 Spline matched to MIP or CTD
  - E_T > 10 GeV
  - $E - P_z$ > 5
  - Vertex
- SLT MUO 5 must be required explicitely in addition
- FLT 6 must be required explicitely in addition

A.2.2.3 TLT MUO 4

- MUO 4: elastic J/ψ in FMU
  - SLT MUO3
  - MAMMA match
  - mass(ctd-ctd, spline-ctd or spline spline)¿1.5 GeV
- a logical OR of FLT 0 and 18 must be explicitely required in addition

A.2.2.4 TLT HFL 16

A general HFL selection (not used in this thesis):

- track segment in the forward muon chambers
- SLT: HFL 5,6,11,12 or MUO 3,4,5,19 or GTT 6

A.3 BAC

The described below TLT bits must be used in coincedence with the FLT and SLT bits based on the BAC information.

The full FLT-SLT-TLT FMUON chain requires the following bits:

- 2006-2007:
  - FLT 5, 12
  - SLT MUO 8, GTT 24
  - TLT MUO 10,11,12,13,14, HFL 16

A.3.1 years 2006 to 2007

A.3.1.1 TLT MUO 10,11,12,13,14

- track segment in BAC
- caution: no built-in requirement on FLT, SLT bits

A.3.1.2 TLT HFL 16

- track segment in BAC with coincedence on SLT bits,
- SLT MUO 8 or GTT 24

The BAC chain is not used in this thesis and is given here for completeness of the muon trigger selection.

A.4 DIS

The described below TLT bits must be used in coincedence with the FLT and SLT bits based on the CAL electron information.

The full FLT-SLT-TLT FMUON chain requires the following bits:

- 1996-2000:
  - FLT 23,28,30,40,41,43,44,46,47,50,
  - SLT not required,
  - TLT DIS 3,5,
- 2003-2005:
  - FLT 30,40,41,43,44,46,47,62,
  - SLT not required,
  - TLT SPP 2,5,
- 2006-2007:
  - FLT 30,40,41,43,44,46,47,62,
  - SLT not required,
  - TLT SPP 5,9, HFL 17,

A.4.1 years 1996 to 2000

A.4.1.1 TLT DIS 3: medum Q^2 electron

- good electron
- with $E_e > 4$ GeV and $30 < E - p_z < 100$ GeV
- box cut around beam pipe with $\sqrt{x^2+y^2} > 35$ cm

A.4.1.2 TLT DIS 5: Vector meson DIS

- good electron
- with $E_e > 7$ GeV and $30 < E - p_z <$ GeV
- box cut around beam pipe with $x, y = 12$x6

- vertex tracks ≥ 1
- other energy ($E_{tot} - FCAL_{bp} - E_{el}$) less then 30 GeV
- CTD tracks from 2 to 5
- FCAL beam pipe energy less then 5 GeV

A.4.1.3 TLT DIS 27: electron plus muon

- good electron
- $E_e > 7$ GeV and
- a good BRMuon segment match with a CTD track with selection:
  - $p > 1\ GeV$
  - track crossed more then 3 CTD superlayers
  - DCA (beamline-track) < 10 cm
  - DCA-vertex < 10 cm

A.4.2 years 2003 to 2007

A.4.2.1 TLT SPP05: Vector Meson DIS

- SLT SPP2
- 30 GeV $< E - p_z <$ 100 GeV
- $E_{el} > 7$ GeV
- Box cut 12x12 cm
- FCAL beam pipe energy less then 20 GeV
- other energy ($E_{tot} - FCAL_{bp} - E_{el}$) less then 30 GeV
- number of vertex tracks ≥ 1
- CTD tracks from 2 to 5

A.4.3 years 2003 to 2005

A.4.3.1 TLT SPP02: NC DIS

inclusive DIS slot, prescaled after 05.09.2005

- SLT SPP1
- FLT 28, 30, 40, 41, 42, 43, 44, 46 this already at SLT
- Sinistra or Emille electron finders
- 30$< E - p_z <$100
- $E_e >$4 GeV (from cards)
- box cut (from cards) 12x12 cm

A.4.4 years 2006 to 2007

A.4.4.1 TLT SPP09: NC DIS

- SLT SPP1
- FLT 28, 30, 40, 41, 42, 43, 44, 46 this already at SLT
- Only Sinistra electron finder
- 33$< E - p_z <$100 (from cards)
- $E_e >$4 GeV (from cards)
- box cut (from cards) 14x16 cm

A.4.4.2 TLT HFL17: NC DIS

- same as SPP02 + at least two tracks with $p_T > 0.35$ GeV
- in case a DIS electron has $\theta_e < 0.3$ it must have $p_T > 10$ GeV

Appendix B

MC samples - detailed list

B.1 Trigger periods

The ZEUS data taking periods include the trigger subperiods (see Table B.1), which are coded in the sequence of 6 alpha-numeric symbols (see also [173]).

year	MC version	trigger subperiod	data lumi, pb^{-1}
96p-97p	num97v5.2	psep97	38.62
98e-99e	num98v5.0	emar99	16.68
99p-00p	num98v5.0	paug00	65.87
03p-04p	num03t3.1	pnov03	8.61
		papr04	4.83
		pjun04	14.46
		phau04	5.28
		pgla04	7.45
05e	num05t0.2	egap05	27.02
		ehap05	76.27
		egoc05	8.05
		ehoc05	26.23
06e	num06t0.2	efma06	11.53
		efhm06	43.21
06p-07p	num07t1.0	pfde06	47.49
		pfhd06	51.79

Table B.1: *The ZEUS data taking periods with the trigger subperiods and the data luminosity corresponding to each subperiod.*

B.2 BH

The BH MC samples were generated with the recommended phase space sharing between ELA:QEL:DIS di-lepton production subprocesses. There were no explicit cuts imposed on the kinematic region of the produced sample. The di-muon samples were generated with each muon to have the transverse momentum of at least 0.5 GeV.

MC tape id	Number of the events in the sample
74p717.f8123.GRAPE_ELA_2PT_0_5_01_12	20000
...	...
74p717.f8123.GRAPE_ELA_2PT_0_5_12_12	20000
74p717.f10688.GRAPE_ELA_2PT_0_5_01_03	50000
74p717.f10688.GRAPE_ELA_2PT_0_5_02_03	50000
74p717.f10688.GRAPE_ELA_2PT_0_5_03_03	42000
74p717.f10688.GRAPE_ELA_2PT_0_5k01_03	50000
74p717.f10688.GRAPE_ELA_2PT_0_5k02_03	50000
74p717.f10688.GRAPE_ELA_2PT_0_5k03_03	50000
82e819.f8123.GRAPE_ELA_2PT_0_5_01_05	20000
...	...
82e819.f8123.GRAPE_ELA_2PT_0_5_05_05	20000
82e819.f10688.GRAPE_ELA_2PT_0_5_01_02	50000
82e819.f10688.GRAPE_ELA_2PT_0_5_02_02	50000
82e819.f10688.GRAPE_ELA_2PT_0_5k01_02	50000
82e819.f10688.GRAPE_ELA_2PT_0_5k02_02	50000
82p020.f8123.GRAPE_ELA_2PT_0_5_01_20	20000
...	...
82p020.f8123.GRAPE_ELA_2PT_0_5_20_20	20000
82p020.f10688.GRAPE_ELA_2PT_0_5_01_06	50000
...	...
82p020.f10688.GRAPE_ELA_2PT_0_5_06_06	50000
82p020.f10688.GRAPE_ELA_2PT_0_5k01_06	50000
...	...
82p020.f10688.GRAPE_ELA_2PT_0_5k06_06	50000
CVN324.F8123.GRAPE_ELA_2PT_0_5_05_12	20000
CVN324.F8123.GRAPE_ELA_2PT_0_5_06_12	20000
cvn324.f10688.GRAPE_ELA_2PT_0_5_01_01	45000
cvn324.f10688.GRAPE_ELA_2PT_0_5k01_01	45000
CVA424.F8123.GRAPE_ELA_2PT_0_5_11_12	20000
CVA424.F8123.GRAPE_ELA_2PT_0_5_12_12	20000
cva424.f10688.GRAPE_ELA_2PT_0_5_01_01	7000
cva424.f10688.GRAPE_ELA_2PT_0_5k01_01	7000
CVH424.F8123.GRAPE_ELA_2PT_0_5_09_12	20000
CVH424.F8123.GRAPE_ELA_2PT_0_5_10_12	20000
cvh424.f10688.GRAPE_ELA_2PT_0_5_01_01	12000
cvh424.f10688.GRAPE_ELA_2PT_0_5k01_01	12000

Table B.2: *Number of QED di-muon generated events in the Elastic mode of the* ***Grape*** *generator.*

MC tape id	Number of the events in the sample
CVK424.F8123.GRAPE_ELA_2PT_0_5_01_12	20000
CVK424.F8123.GRAPE_ELA_2PT_0_5_02_12	20000
CVK424.F8123.GRAPE_ELA_2PT_0_5_03_12	20000
CVK424.F8123.GRAPE_ELA_2PT_0_5_04_12	20000
cvk424.f10688.GRAPE_ELA_2PT_0_5_01_02	50000
cvk424.f10688.GRAPE_ELA_2PT_0_5_02_02	50000
cvk424.f10688.GRAPE_ELA_2PT_0_5k01_02	50000
cvk424.f10688.GRAPE_ELA_2PT_0_5k02_02	13000
cvgl24.f10688.GRAPE_ELA_2PT_0_5k01_01	34000
dwga25.f10688.GRAPE_ELA_2PT_0_5k01_06	50000
...	...
dwga25.f10688.GRAPE_ELA_2PT_0_5k06_06	17000
dwbe25.f10688.GRAPE_ELA_2PT_0_5_01_16	50000
...	...
dwbe25.f10688.GRAPE_ELA_2PT_0_5_16_16	50000
dwbe25.f10688.GRAPE_ELA_2PT_0_5k01_16	50000
...	...
dwbe25.f10688.GRAPE_ELA_2PT_0_5k16_16	50000
dwgo25.f10688.GRAPE_ELA_2PT_0_5k01_02	50000
dwgo25.f10688.GRAPE_ELA_2PT_0_5k02_02	29000
dwde25.f10688.GRAPE_ELA_2PT_0_5_01_06	50000
...	...
dwde25.f10688.GRAPE_ELA_2PT_0_5_06_06	50000
dwde25.f10688.GRAPE_ELA_2PT_0_5k01_06	50000
...	...
dwde25.f10688.GRAPE_ELA_2PT_0_5k06_06	50000
eyse26.f10688.GRAPE_ELA_2PT_0_5k01_09	50000
...	...
eyse26.f10688.GRAPE_ELA_2PT_0_5k09_09	50000
eyue26.f10688.GRAPE_ELA_2PT_0_5k01_03	50000
eyue26.f10688.GRAPE_ELA_2PT_0_5k02_03	50000
eyue26.f10688.GRAPE_ELA_2PT_0_5k03_03	50000
fzy627.f10688.GRAPE_ELA_2PT_0_5k01_15	50000
...	...
fzy627.f10688.GRAPE_ELA_2PT_0_5k15_15	50000
fzz627.f10688.GRAPE_ELA_2PT_0_5k01_10	50000
...	...
fzz627.f10688.GRAPE_ELA_2PT_0_5k10_10	50000

Table B.3: *Number of QED di-muon generated events in the Elastic mode of the* ***Grape*** *generator.*

MC tape id	Number of the events in the sample
$74p717.f8123.GRAPE\_QEL1\_2PT\_0\_5\_01\_03$	20000
$74p717.f8123.GRAPE\_QEL1\_2PT\_0\_5\_02\_03$	20000
$74p717.f8123.GRAPE\_QEL1\_2PT\_0\_5\_03\_03$	20000
$74p717.f10688.GRAPE\_QEL1\_2PT\_0\_5\_01\_01$	23000
$74p717.f10688.GRAPE\_QEL1\_2PT\_0\_5k01\_01$	23000
$82e819.f8123.GRAPE\_QEL1\_2PT\_0\_5\_01\_01$	20000
$82e819.f10688.GRAPE\_QEL1\_2PT\_0\_5\_01\_01$	15000
$82e819.f10688.GRAPE\_QEL1\_2PT\_0\_5k01\_01$	15000
$82p020.f8123.GRAPE\_QEL1\_2PT\_0\_5\_01\_04$	20000
$82p020.f8123.GRAPE\_QEL1\_2PT\_0\_5\_02\_04$	20000
$82p020.f8123.GRAPE\_QEL1\_2PT\_0\_5\_03\_04$	20000
$82p020.f8123.GRAPE\_QEL1\_2PT\_0\_5\_04\_04$	20000
$82p020.f10688.GRAPE\_QEL1\_2PT\_0\_5\_01\_02$	50000
$82p020.f10688.GRAPE\_QEL1\_2PT\_0\_5\_02\_02$	50000
$82p020.f10688.GRAPE\_QEL1\_2PT\_0\_5k01\_02$	50000
$82p020.f10688.GRAPE\_QEL1\_2PT\_0\_5k02\_02$	50000
$cva424.f10688.GRAPE\_QEL1\_2PT\_0\_5\_01\_01$	10000
$cva424.f10688.GRAPE\_QEL1\_2PT\_0\_5k01\_01$	10000
$CVK424.F8123.GRAPE\_QEL1\_2PT\_0\_5\_01\_03$	20000
$cvk424.f10688.GRAPE\_QEL1\_2PT\_0\_5\_01\_01$	11000
$cvk424.f10688.GRAPE\_QEL1\_2PT\_0\_5k01\_01$	11000
$cvh424.f10688.GRAPE\_QEL1\_2PT\_0\_5\_01\_01$	11000
$cvh424.f10688.GRAPE\_QEL1\_2PT\_0\_5k01\_01$	11000

Table B.4: *Number of QED di-muon generated events in the Quasi-Elastic(1) mode of the* ***GRAPE*** *generator.*

MC tape id	Number of the events in the sample
$dwga25.f10688.GRAPE\_QEL1\_2PT\_0\_5k01\_02$	50000
$dwga25.f10688.GRAPE\_QEL1\_2PT\_0\_5k02\_02$	8000
$dwbe25.f10688.GRAPE\_QEL1\_2PT\_0\_5\_01\_04$	50000
$dwbe25.f10688.GRAPE\_QEL1\_2PT\_0\_5\_02\_04$	50000
$dwbe25.f10688.GRAPE\_QEL1\_2PT\_0\_5\_03\_04$	50000
$dwbe25.f10688.GRAPE\_QEL1\_2PT\_0\_5\_04\_04$	50000
$dwbe25.f10688.GRAPE\_QEL1\_2PT\_0\_5k01\_04$	50000
$dwbe25.f10688.GRAPE\_QEL1\_2PT\_0\_5k02\_04$	50000
$dwbe25.f10688.GRAPE\_QEL1\_2PT\_0\_5k03\_04$	50000
$dwbe25.f10688.GRAPE\_QEL1\_2PT\_0\_5k04\_04$	50000
$dwgo25.f10688.GRAPE\_QEL1\_2PT\_0\_5k01\_01$	17000
$dwde25.f10688.GRAPE\_QEL1\_2PT\_0\_5\_01\_02$	50000
$dwde25.f10688.GRAPE\_QEL1\_2PT\_0\_5\_02\_02$	50000
$dwde25.f10688.GRAPE\_QEL1\_2PT\_0\_5k01\_02$	50000
$dwde25.f10688.GRAPE\_QEL1\_2PT\_0\_5k02\_02$	50000
$eyse26.f10688.GRAPE\_QEL1\_2PT\_0\_5k01\_02$	50000
$eyse26.f10688.GRAPE\_QEL1\_2PT\_0\_5k02\_02$	50000
$eyue26.f10688.GRAPE\_QEL1\_2PT\_0\_5k01\_01$	24000
$fzy627.f10688.GRAPE\_QEL1\_2PT\_0\_5k01\_04$	50000
$fzy627.f10688.GRAPE\_QEL1\_2PT\_0\_5k02\_04$	50000
$fzy627.f10688.GRAPE\_QEL1\_2PT\_0\_5k03\_04$	50000
$fzy627.f10688.GRAPE\_QEL1\_2PT\_0\_5k04\_04$	50000
$fzz627.f10688.GRAPE\_QEL1\_2PT\_0\_5k01\_03$	50000
$fzz627.f10688.GRAPE\_QEL1\_2PT\_0\_5k02\_03$	50000
$fzz627.f10688.GRAPE\_QEL1\_2PT\_0\_5k03\_03$	50000

Table B.5: *Number of QED di-muon generated events in the Quasi-Elastic(1) mode of the* ***GRAPE*** *generator.*

MC tape id	Number of the events in the sample
74p717.f8123.GRAPE_QEL2_2PT_0_5_01_01	20000
74p717.f10688.GRAPE_QEL2_2PT_0_5_01_01	5000
74p717.f10688.GRAPE_QEL2_2PT_0_5k01_01	5000
82e819.f8123.GRAPE_QEL2_2PT_0_5_01_01	4000
82e819.f10688.GRAPE_QEL2_2PT_0_5_01_01	2000
82e819.f10688.GRAPE_QEL2_2PT_0_5k01_01	2000
82p020.f8123.GRAPE_QEL2_2PT_0_5_01_01	20000
82p020.f10688.GRAPE_QEL2_2PT_0_5_01_01	6000
82p020.f10688.GRAPE_QEL2_2PT_0_5k01_01	6000
cvn324.f10688.GRAPE_QEL2_2PT_0_5_01_01	3000
cvn324.f10688.GRAPE_QEL2_2PT_0_5k01_01	3000
cva424.f10688.GRAPE_QEL2_2PT_0_5_01_01	1000
cva424.f10688.GRAPE_QEL2_2PT_0_5k01_01	1000
CVH424.F8123.GRAPE_QEL2_2PT_0_5_01_01	10000
cvk424.f10688.GRAPE_QEL2_2PT_0_5_01_01	5000
cvk424.f10688.GRAPE_QEL2_2PT_0_5k01_01	5000
cvgl24.f10688.GRAPE_QEL2_2PT_0_5k01_01	3000
dwga25.f10688.GRAPE_QEL2_2PT_0_5k01_01	10000
dwbe25.f10688.GRAPE_QEL2_2PT_0_5_01_01	30000
dwbe25.f10688.GRAPE_QEL2_2PT_0_5k01_01	30000
dwgo25.f10688.GRAPE_QEL2_2PT_0_5k01_01	3000
dwde25.f10688.GRAPE_QEL2_2PT_0_5_01_01	10000
dwde25.f10688.GRAPE_QEL2_2PT_0_5k01_01	10000
eyse26.f10688.GRAPE_QEL2_2PT_0_5k01_01	17000
eyue26.f10688.GRAPE_QEL2_2PT_0_5k01_01	4000
fzy627.f10688.GRAPE_QEL2_2PT_0_5k01_01	30000
fzz627.f10688.GRAPE_QEL2_2PT_0_5k01_01	20000

Table B.6: *Number of QED di-muon generated events in the Quasi-Elastic(2) mode of the **Grape** generator.*

MC tape id	Number of the events in the sample
74p717.f8123.GRAPE_DIS_2PT_0_5_01_01	10000
74p717.f10688.GRAPE_DIS_2PT_0_5_01_01	8000
74p717.f10688.GRAPE_DIS_2PT_0_5k01_01	8000
74p717.f10688.GRAPE_DIS_2PT_0_5k2_01_04	50000
...	...
74p717.f10688.GRAPE_DIS_2PT_0_5k2_04_04	50000
82e819.f8123.GRAPE_DIS_2PT_0_5_01_01	20000
82e819.f10688.GRAPE_DIS_2PT_0_5k2_01_02	50000
82e819.f10688.GRAPE_DIS_2PT_0_5k2_02_02	50000
82p020.f8123.GRAPE_DIS_2PT_0_5_01_03	20000
82p020.f8123.GRAPE_DIS_2PT_0_5_02_03	20000
82p020.f8123.GRAPE_DIS_2PT_0_5_03_03	20000
82p020.f10688.GRAPE_DIS_2PT_0_5k2_01_01	30000
cvn324.f10688.GRAPE_DIS_2PT_0_5_01_01	4000
cvn324.f10688.GRAPE_DIS_2PT_0_5k01_01	4000
cvn324.f10688.GRAPE_DIS_2PT_0_5k2_01_01	40000
CVA424.F8123.GRAPE_DIS_2PT_0_5_01_01	20000
cva424.f10688.GRAPE_DIS_2PT_0_5k2_01_01	20000
cvh424.f10688.GRAPE_DIS_2PT_0_5_01_01	2000
cvh424.f10688.GRAPE_DIS_2PT_0_5k01_01	2000
cvh424.f10688.GRAPE_DIS_2PT_0_5k2_01_01	20000
cvk424.f10688.GRAPE_DIS_2PT_0_5_01_01	6000
cvk424.f10688.GRAPE_DIS_2PT_0_5k01_01	6000
cvk424.f10688.GRAPE_DIS_2PT_0_5k2_01_02	50000
cvk424.f10688.GRAPE_DIS_2PT_0_5k2_02_02	50000
cvgl24.f10688.GRAPE_DIS_2PT_0_5k01_01	3000
cvgl24.f10688.GRAPE_DIS_2PT_0_5k2_01_01	30000

Table B.7: *Number of QED di-muon generated events in the DIS mode of the **Grape** generator.*

MC tape id	Number of the events in the sample
dwga25.f10688.GRAPE_DIS_2PT_0_5k01_01	12000
dwga25.f10688.GRAPE_DIS_2PT_0_5k2_01_03	50000
dwga25.f10688.GRAPE_DIS_2PT_0_5k2_02_03	50000
dwga25.f10688.GRAPE_DIS_2PT_0_5k2_03_03	50000
dwbe25.f10688.GRAPE_DIS_2PT_0_5_01_01	35000
dwbe25.f10688.GRAPE_DIS_2PT_0_5k01_01	35000
dwbe25.f10688.GRAPE_DIS_2PT_0_5k2_01_08	50000
...	...
dwbe25.f10688.GRAPE_DIS_2PT_0_5k2_08_08	50000
dwgo25.f10688.GRAPE_DIS_2PT_0_5k01_01	3000
dwgo25.f10688.GRAPE_DIS_2PT_0_5k2_01_01	30000
dwde25.f10688.GRAPE_DIS_2PT_0_5_01_01	12000
dwde25.f10688.GRAPE_DIS_2PT_0_5k01_01	12000
dwde25.f10688.GRAPE_DIS_2PT_0_5k2_01_03	50000
dwde25.f10688.GRAPE_DIS_2PT_0_5k2_02_03	50000
dwde25.f10688.GRAPE_DIS_2PT_0_5k2_03_03	50000
eyse26.f10688.GRAPE_DIS_2PT_0_5k01_01	20000
eyse26.f10688.GRAPE_DIS_2PT_0_5k2_01_05	50000
...	...
eyse26.f10688.GRAPE_DIS_2PT_0_5k2_05_05	50000
eyue26.f10688.GRAPE_DIS_2PT_0_5k01_01	5000
eyue26.f10688.GRAPE_DIS_2PT_0_5k2_01_02	50000
fzy627.f10688.GRAPE_DIS_2PT_0_5k01_01	35000
fzy627.f10688.GRAPE_DIS_2PT_0_5k2_01_08	50000
...	...
fzy627.f10688.GRAPE_DIS_2PT_0_5k2_08_08	50000
fzz627.f10688.GRAPE_DIS_2PT_0_5k01_01	23000
fzz627.f10688.GRAPE_DIS_2PT_0_5k2_01_05	50000
...	...
fzz627.f10688.GRAPE_DIS_2PT_0_5k2_05_05	50000

Table B.8: *Number of QED di-muon generated events in the DIS mode of the **Grape** generator.*

B.3 J/ψ

The J/ψ samples were generated with ***Diffvm*** in the Elastic and in the Proton Dissociation modes. The proton dissociation mode followed the Jetset simulation for the proton remnant kinematics.

MC tape id	Number of the events in the sample
74p717.f10688.DIFFVM.PSI1SMU.EL.b4.01_04	50000
...	...
74p717.f10688.DIFFVM.PSI1SMU.EL.b4.04_04	43000
82e819.f10688.DIFFVM.PSI1SMU.EL.b4.01_02	50000
82e819.f10688.DIFFVM.PSI1SMU.EL.b4.02_02	33000
82p020.f10688.DIFFVM.PSI1SMU.EL.b4.01_07	50000
...	...
82p020.f10688.DIFFVM.PSI1SMU.EL.b4.07_07	29000
cvn324.f10688.DIFFVM.PSI1SMU.EL.b4.01_01	-
cva424.f10688.DIFFVM.PSI1SMU.EL.b4.01_01	24150
cvgl24.f10688.DIFFVM.PSI1SMU.EL.b4.01_01	37250
cvh424.f10688.DIFFVM.PSI1SMU.EL.b4.01_01	26400
cvk424.f10688.DIFFVM.PSI1SMU.EL.b4.01_02	50000
cvk424.f10688.DIFFVM.PSI1SMU.EL.b4.02_02	22300
dwbe25.f10688.DIFFVM.PSI1SMU.EL.b4.01_08	50000
...	...
dwbe25.f10688.DIFFVM.PSI1SMU.EL.b4.08_08	-
dwde25.f10688.DIFFVM.PSI1SMU.EL.b4.01_03	50000
dwde25.f10688.DIFFVM.PSI1SMU.EL.b4.02_03	50000
dwde25.f10688.DIFFVM.PSI1SMU.EL.b4.03_03	-
dwga25.f10688.DIFFVM.PSI1SMU.EL.b4.01_03	50000
dwga25.f10688.DIFFVM.PSI1SMU.EL.b4.02_03	50000
dwga25.f10688.DIFFVM.PSI1SMU.EL.b4.03_03	35000
dwgo25.f10688.DIFFVM.PSI1SMU.EL.b4.01_01	40000
eyse26.f10688.DIFFVM.PSI1SMU.EL.b4.01_05	50000
...	...
eyse26.f10688.DIFFVM.PSI1SMU.EL.b4.05_05	16000
eyue26.f10688.DIFFVM.PSI1SMU.EL.b4.01_02	50000
eyue26.f10688.DIFFVM.PSI1SMU.EL.b4.02_02	7000
fzy627.f10688.DIFFVM.PSI1SMU.EL.b4.01_08	50000
...	...
fzy627.f10688.DIFFVM.PSI1SMU.EL.b4.08_08	27000
fzz627.f10688.DIFFVM.PSI1SMU.EL.b4.01_05	50000
...	...
fzz627.f10688.DIFFVM.PSI1SMU.EL.b4.05_05	46000

Table B.9: *Number of generated events in the* J/ψ *in the elastic mode of the* ***Diffvm*** *generator.*

MC tape id	Number of the events in the sample
74p717.f10688.DIFFVM.PSI1SMU.PD.b1.01_04	50000
...	...
74p717.f10688.DIFFVM.PSI1SMU.PD.b1.04_04	43000
82e819.f10688.DIFFVM.PSI1SMU.PD.b1.01_02	50000
82e819.f10688.DIFFVM.PSI1SMU.PD.b1.02_02	33000
82p020.f10688.DIFFVM.PSI1SMU.PD.b1.01_07	50000
...	...
82p020.f10688.DIFFVM.PSI1SMU.PD.b1.07_07	29000
cva424.f10688.DIFFVM.PSI1SMU.PD.b1.01_01	24150
cvgl24.f10688.DIFFVM.PSI1SMU.PD.b1.01_01	37250
cvh424.f10688.DIFFVM.PSI1SMU.PD.b1.01_01	26400
cvk424.f10688.DIFFVM.PSI1SMU.PD.b1.01_02	50000
cvk424.f10688.DIFFVM.PSI1SMU.PD.b1.02_02	22300
cvn324.f10688.DIFFVM.PSI1SMU.PD.b1.01_01	43050
dwbe25.f10688.DIFFVM.PSI1SMU.PD.b1.01_08	50000
...	...
dwbe25.f10688.DIFFVM.PSI1SMU.PD.b1.08_08	31000
dwde25.f10688.DIFFVM.PSI1SMU.PD.b1.01_03	50000
dwde25.f10688.DIFFVM.PSI1SMU.PD.b1.02_03	50000
dwde25.f10688.DIFFVM.PSI1SMU.PD.b1.03_03	31000
dwga25.f10688.DIFFVM.PSI1SMU.PD.b1.01_03	50000
dwga25.f10688.DIFFVM.PSI1SMU.PD.b1.02_03	50000
dwga25.f10688.DIFFVM.PSI1SMU.PD.b1.03_03	35000
dwgo25.f10688.DIFFVM.PSI1SMU.PD.b1.01_01	40000
eyse26.f10688.DIFFVM.PSI1SMU.PD.b1.01_05	50000
...	...
eyse26.f10688.DIFFVM.PSI1SMU.PD.b1.05_05	16000
eyue26.f10688.DIFFVM.PSI1SMU.PD.b1.01_02	50000
eyue26.f10688.DIFFVM.PSI1SMU.PD.b1.02_02	7000
fzy627.f10688.DIFFVM.PSI1SMU.PD.b1.01_08	50000
...	...
fzy627.f10688.DIFFVM.PSI1SMU.PD.b1.08_08	27000
fzz627.f10688.DIFFVM.PSI1SMU.PD.b1.01_05	50000
...	...
fzz627.f10688.DIFFVM.PSI1SMU.PD.b1.05_05	46000

Table B.10: *Number of generated events in the* J/ψ *in the proton dissociation mode of the* ***Diffvm*** *generator.*

B.4 Upsilon

The three states Υ 1S,2S,3S were simulated with ***Diffvm*** in the Elastic and Proton Dissociation modes. The proton dissociation mode follows Jetset simulation for the proton remnant kinematics. The decay channels $\Upsilon(1S) \to \mu\mu$, $\Upsilon(2S) \to \mu\mu$, $\Upsilon(3S) \to \mu\mu$ and cascade decays $\Upsilon(2S) \to \Upsilon(1S)\pi^+\pi^-$, $\Upsilon(3S) \to \Upsilon(1S)\pi^+\pi^-$ are included in the samples.

The inelastic production of the Υ 1S,2S,3S mesons with the subsequent decay into the di-electrons and di-muons was done with ***Pythia*** version 6.400 generator. The settings for 1S and 2S states are provided in the generator control cards. The generation of the Υ(3S) state was done via modification of the Υ(2S) mass in the particle types ASCI file, which accompanies the event generation process. According to the MC simulations with ***Pythia*** the predicted cross section of the inelastic Υ meson production is $\sigma(\gamma g \to \Upsilon(1S)g) =$ 1.5 pb (1.0 pb for 2S, 0.85 pb for 3S).

MC tape id	Events number in the sample
74p717.s10688.DIFFVM.UPS1SMU.EL.1	10000
82e819.s10688.DIFFVM.UPS1SMU.EL.2	5000
82p020.s10688.DIFFVM.UPS1SMU.EL.1	10000
cvn324.s10688.DIFFVM.UPS1SMU.EL.2	2155
cva424.s10688.DIFFVM.UPS1SMU.EL.2	1207
cvgl24.s10688.DIFFVM.UPS1SMU.EL.2	1885
cvh424.s10688.DIFFVM.UPS1SMU.EL.2	1319
cvk424.s10688.DIFFVM.UPS1SMU.EL.2	3629
dwbe25.s10688.DIFFVM.UPS1SMU.EL.2	19067
dwde25.s10688.DIFFVM.UPS1SMU.EL.2	6558
dwga25.s10688.DIFFVM.UPS1SMU.EL.2	6755
dwgo25.s10688.DIFFVM.UPS1SMU.EL.2	2001
eyse26.s10688.DIFFVM.UPS1SMU.EL.2	10803
eyue26.s10688.DIFFVM.UPS1SMU.EL.2	2883
fzy627.s10688.DIFFVM.UPS1SMU.EL.2	18850
fzz627.s10688.DIFFVM.UPS1SMU.EL.2	12340

Table B.11: *Number of generated events in the $\Upsilon(1S)$ in the elastic mode of the* ***Diffvm*** *generator.*

MC tape id	Events number in the sample
74p717.s10688.DIFFVM.UPS2SMU.EL.1	10000
82e819.s10688.DIFFVM.UPS2SMU.EL.2	5000
82p020.s10688.DIFFVM.UPS2SMU.EL.1	10000
cvn324.s10688.DIFFVM.UPS2SMU.EL.2	2155
cva424.s10688.DIFFVM.UPS2SMU.EL.2	1207
cvgl24.s10688.DIFFVM.UPS2SMU.EL.2	1885
cvh424.s10688.DIFFVM.UPS2SMU.EL.2	1319
cvk424.s10688.DIFFVM.UPS2SMU.EL.2	3629
dwbe25.s10688.DIFFVM.UPS2SMU.EL.2	19067
dwde25.s10688.DIFFVM.UPS2SMU.EL.2	6558
dwga25.s10688.DIFFVM.UPS2SMU.EL.2	6755
dwgo25.s10688.DIFFVM.UPS2SMU.EL.2	2001
eyse26.s10688.DIFFVM.UPS2SMU.EL.2	10803
eyue26.s10688.DIFFVM.UPS2SMU.EL.2	2883
fzy627.s10688.DIFFVM.UPS2SMU.EL.2	18850
fzz627.s10688.DIFFVM.UPS2SMU.EL.2	12340

Table B.12: *Number of generated events in the $\Upsilon(2S)$ in the elastic mode of the* ***Diffvm*** *generator.*

MC tape id	Events number in the sample
74p717.s10688.DIFFVM.UPS3SMU.EL.1	10000
82e819.s10688.DIFFVM.UPS3SMU.EL.2	5000
82p020.s10688.DIFFVM.UPS3SMU.EL.1	10000
cvn324.s10688.DIFFVM.UPS3SMU.EL.2	2155
cva424.s10688.DIFFVM.UPS3SMU.EL.2	1207
cvgl24.s10688.DIFFVM.UPS3SMU.EL.2	1885
cvh424.s10688.DIFFVM.UPS3SMU.EL.2	1319
cvk424.s10688.DIFFVM.UPS3SMU.EL.2	3629
dwbe25.s10688.DIFFVM.UPS3SMU.EL.2	19067
dwde25.s10688.DIFFVM.UPS3SMU.EL.2	6558
dwga25.s10688.DIFFVM.UPS3SMU.EL.2	6755
dwgo25.s10688.DIFFVM.UPS3SMU.EL.2	2001
eyse26.s10688.DIFFVM.UPS3SMU.EL.2	10803
eyue26.s10688.DIFFVM.UPS3SMU.EL.2	2883
fzy627.s10688.DIFFVM.UPS3SMU.EL.2	18850
fzz627.s10688.DIFFVM.UPS3SMU.EL.2	12340

Table B.13: *Number of generated events in the $\Upsilon(3S)$ in the elastic mode of the **DIFFVM** generator.*

MC tape id	Events number in the sample
74p717.f10688.DIFFVM.UPS1SMU.PD.2	9655
82e819.f10688.DIFFVM.UPS1SMU.PD.2	4170
82p020.f10688.DIFFVM.UPS1SMU.PD.2	16467
82p020.s10688.DIFFVM.UPS1SMU.PD.1	10000
cvn324.f10688.DIFFVM.UPS1SMU.PD.2	2155
cva424.f10688.DIFFVM.UPS1SMU.PD.2	1207
cvgl24.f10688.DIFFVM.UPS1SMU.PD.2	1885
cvh424.f10688.DIFFVM.UPS1SMU.PD.2	1319
cvk424.f10688.DIFFVM.UPS1SMU.PD.2	3629
dwbe25.f10688.DIFFVM.UPS1SMU.PD.2	19067
dwde25.f10688.DIFFVM.UPS1SMU.PD.2	6558
dwga25.f10688.DIFFVM.UPS1SMU.PD.2	6755
dwgo25.f10688.DIFFVM.UPS1SMU.PD.2	2001
eyse26.f10688.DIFFVM.UPS1SMU.PD.2	10803
eyue26.f10688.DIFFVM.UPS1SMU.PD.2	2883
fzy627.f10688.DIFFVM.UPS1SMU.PD.2	18850
fzz627.f10688.DIFFVM.UPS1SMU.PD.2	12340

Table B.14: *Number of generated events in the $\Upsilon(1S)$ in the proton dissociation mode of the **DIFFVM** generator.*

MC tape id	Events number in the sample
74p717.f10688.DIFFVM.UPS2SMU.PD.2	9655
82e819.f10688.DIFFVM.UPS2SMU.PD.2	4170
82p020.f10688.DIFFVM.UPS2SMU.PD.2	16467
cvn324.f10688.DIFFVM.UPS2SMU.PD.2	2155
cva424.f10688.DIFFVM.UPS2SMU.PD.2	1207
cvgl24.f10688.DIFFVM.UPS2SMU.PD.2	1885
cvh424.f10688.DIFFVM.UPS2SMU.PD.2	1319
cvk424.f10688.DIFFVM.UPS2SMU.PD.2	3629
dwbe25.f10688.DIFFVM.UPS2SMU.PD.2	19067
dwde25.f10688.DIFFVM.UPS2SMU.PD.2	6558
dwga25.f10688.DIFFVM.UPS2SMU.PD.2	6755
dwgo25.f10688.DIFFVM.UPS2SMU.PD.2	2001
eyse26.f10688.DIFFVM.UPS2SMU.PD.2	10803
eyue26.f10688.DIFFVM.UPS2SMU.PD.2	2883
fzy627.f10688.DIFFVM.UPS2SMU.PD.2	18850
fzz627.f10688.DIFFVM.UPS2SMU.PD.2	12340

Table B.15: *Number of generated events in the $\Upsilon(2S)$ in the proton dissociation mode of the **DIFFVM** generator.*

MC tape id	Events number in the sample
74p717.f10688.DIFFVM.UPS3SMU.PD.2	9655
82e819.f10688.DIFFVM.UPS3SMU.PD.2	4170
82p020.f10688.DIFFVM.UPS3SMU.PD.2	16467
cva424.f10688.DIFFVM.UPS3SMU.PD.2	1207
cvgl24.f10688.DIFFVM.UPS3SMU.PD.2	1885
cvh424.f10688.DIFFVM.UPS3SMU.PD.2	1319
cvk424.f10688.DIFFVM.UPS3SMU.PD.2	3629
cvn324.f10688.DIFFVM.UPS3SMU.PD.2	2155
dwbe25.f10688.DIFFVM.UPS3SMU.PD.2	19067
dwde25.f10688.DIFFVM.UPS3SMU.PD.2	6558
dwga25.f10688.DIFFVM.UPS3SMU.PD.2	6755
dwgo25.f10688.DIFFVM.UPS3SMU.PD.2	2001
eyse26.f10688.DIFFVM.UPS3SMU.PD.2	10803
eyue26.f10688.DIFFVM.UPS3SMU.PD.2	2883
fzy627.f10688.DIFFVM.UPS3SMU.PD.2	18850
fzz627.f10688.DIFFVM.UPS3SMU.PD.2	12340

Table B.16: *Number of generated events in the $\Upsilon(3S)$ in the proton dissociation mode of the **DIFFVM** generator.*

MC tape id	Events number in the sample
74p717.f10688.py6.UPS1S_E_MU	5940
82e819.f10688.py6.UPS1S_E_MU	2560
82p020.f10688.py6.UPS1S_E_MU	10140
bsa424.f10688.py6.UPS1S_E_MU	740
bsh424.f10688.py6.UPS1S_E_MU	810
bsk424.f10688.py6.UPS1S_E_MU	2230
bsl424.f10688.py6.UPS1S_E_MU	1160
bsn324.f10688.py6.UPS1S_E_MU	1320
dxae25.f10688.py6.UPS1S_E_MU	4160
dxbe25.f10688.py6.UPS1S_E_MU	11740
dxce25.f10688.py6.UPS1S_E_MU	1230
dxde25.f10688.py6.UPS1S_E_MU	4030
eyse26.f10688.py6.UPS1S_E_MU	6650
eyue26.f10688.py6.UPS1S_E_MU	1770
fzy627.f10688.py6.UPS1S_E_MU	11610
fzz627.f10688.py6.UPS1S_E_MU	7600

Table B.17: *Number of generated events in the Υ(1S) with **Pythia** , decays into di-electrons and di-muons are included.*

MC tape id	Events number in the sample
74p717.f10688.py6.UPS2S_E_MU	5940
82e819.f10688.py6.UPS2S_E_MU	2560
82p020.f10688.py6.UPS2S_E_MU	10140
bsa424.f10688.py6.UPS2S_E_MU	740
bsh424.f10688.py6.UPS2S_E_MU	810
bsk424.f10688.py6.UPS2S_E_MU	2230
bsl424.f10688.py6.UPS2S_E_MU	1160
bsn324.f10688.py6.UPS2S_E_MU	1320
dxae25.f10688.py6.UPS2S_E_MU	4160
dxbe25.f10688.py6.UPS2S_E_MU	11740
dxce25.f10688.py6.UPS2S_E_MU	1230
dxde25.f10688.py6.UPS2S_E_MU	4030
eyse26.f10688.py6.UPS2S_E_MU	6650
eyue26.f10688.py6.UPS2S_E_MU	1770
fzy627.f10688.py6.UPS2S_E_MU	11610
fzz627.f10688.py6.UPS2S_E_MU	7600

Table B.18: *Number of generated events in the Υ(2S) with **Pythia** , decays into di-electrons and di-muons are included.*

MC tape id	Events number in the sample
74p717.f10688.py6.UPS3S_E_MU	5940
82e819.f10688.py6.UPS3S_E_MU	2560
82p020.f10688.py6.UPS3S_E_MU	10140
bsa424.f10688.py6.UPS3S_E_MU	740
bsh424.f10688.py6.UPS3S_E_MU	810
bsk424.f10688.py6.UPS3S_E_MU	2230
bsl424.f10688.py6.UPS3S_E_MU	1160
bsn324.f10688.py6.UPS3S_E_MU	1320
dxae25.f10688.py6.UPS3S_E_MU	4160
dxbe25.f10688.py6.UPS3S_E_MU	11740
dxce25.f10688.py6.UPS3S_E_MU	1230
dxde25.f10688.py6.UPS3S_E_MU	4030
eyse26.f10688.py6.UPS3S_E_MU	6650
eyue26.f10688.py6.UPS3S_E_MU	1770
fzy627.f10688.py6.UPS3S_E_MU	11610
fzz627.f10688.py6.UPS3S_E_MU	7600

Table B.19: *Number of generated events in the Υ(3S) with **Pythia** , decays into di-electrons and di-muons are included.*

List of Figures

List of Tables

Bibliography

[1] A. Signer, *The Standard Model* (unpublished). University of Durham, Lectures presented at the School for Young High Energy Physicists, RAL, 2002.

[2] M. Gell-Mann, Phys. Lett. **8**, 214 (1964).

[3] J.D. Bjorken and S.L. Glashow, Phys.Lett. **11**, 255 (1964).

[4] S.L. Glashow, J. Iliopoulos and J. Maiani, Phys.Rev. **D 2**, 1285 (1970).

[5] F.J. Hasert et al., Phys.Lett. **46B**, 138 (1973).

[6] M.I. Perl et al., Phys.Rev.Lett **35**, 1489 (1975).

[7] DONUT Collaboration, available on `http://www.fnal.gov/pub/presspass/press_releases/donut.html`.

[8] K. Kodama, Physics Letters **B**, 218 (2001).

[9] Guang-jiong Ni Guo-hong Yang Rong-tang Fu Haibin Wang, *Running Coupling Constants of Fermions with Masses in Quantum Electro Dynamics and Quantum Chromo Dynamics*, available on `http://arxiv.org/abs/hep-ph/9906364v1`.

[10] A. Donnachie and P.V. Landshoff, Nucl. Phys. **B 231**, 189 (1984).

[11] A. Donnachie and P.V. Landshoff, Phys. Lett. **B 191** (1987).

[12] A. Donnachie and P.V. Landshoff, Phys. Lett. **B 296**, 227 (1992).

[13] A. Donnachie and P.V. Landshoff, Phys. Lett. **B 437**, 408 (1998).

[14] M.G. Ryskin, Z. Phys. **C 57**, 89 (1993).

[15] A.D. Martin, M.G. Ryskin and T. Teubner, Phys. Rev. **D 55**, 4329 (1997).

[16] A.D. Martin, M.G. Ryskin and T. Teubner, Phys. Rev. **D 62**, 14022 (2000).

[17] E.D. Bloom et al., Phys.Rev.Lett. **23**, 930 (1969).

[18] D.H. Perkins, *Introduction to High Energy Physics.* Addison-Wesley, 1982.

[19] H1,ZEUS Collaborations. H1-prelim-08-045, ZEUS-prel-08-003.

[20] R.P. Feynman, Phys.Rev.Lett. **23**, 1415 (1969).

[21] V. Elias, Physics Letters **B 68**, 335 (1977).

[22] M. Gell-Mann, Phys.Lett. **8**, 214 (1964).

[23] D. Kollar, ZEUS collaboration. Measurement of the longitudinal structure function FL, DIS 2008, XVI International Workshop on Deep Inelastic Scattering and Related Subjects, 7-11 April 2008.

[24] S. Glazov, H1 collaboration. Measurements of the longitudinal structure function FL, Conference New trends in HERA Physics 2008, 5 - 10 October 2008, Germany.

[25] G. Altarelli and G. Parisi, Nucl.Phys. **B 126**, 298 (1977).

[26] V.N. Gribov and L.N. Lipatov, Sov.J.Nucl.Phys. **15**, 438 (1972).

[27] Yu.L. Dokshitzer, Sov.Phys. JETP **46**, 641 (1977).

[28] E.A. Kuraev, L.N. Lipatov, V.S. Fadin, Sov.Phys.JETP **44**, 443 (1976).

[29] Y.Y. Balitskii, L.N. Lipatov, Sov.J.Nucl.Phys. **28**, 882 (1978).

[30] M. Ciafaloni, Nucl.Phys. **B 296**, 49 (1998).

[31] S. Catani, F. Fiorani and G. Marchesini, Nucl.Phys. **B 336**, 18 (1990).

[32] L.V. Gribov, E.M. Levin and M.G. Ryskin, Phys.Rep. **100**, 1 (1983).

[33] ZEUS Coll, S. Chekanov et al., Phys.Rev. **D 67** (2003).

[34] CTEQ Collaboration, available on `http://www.phys.psu.edu/~cteq/`.

[35] MRS/MRST/MSTW PARTON DISTRIBUTIONS, available on `http://durpdg.dur.ac.uk/hepdata/mrs.html`.

[36] M. Glück, E. Reya and A. Vogt, Z. Phys. **C 67**, 433 (1995).

[37] M. Glück, E. Reya and A. Vogt, Eur. Phys. J. **C 5**, 461 (1998).

[38] Parton Density Functions, available on `http://durpdg.dur.ac.uk/HEPDATA/PDF`.

[39] H1-ZEUS. B. Reisert (ZEUS): Measurement of F2 and PDF fits at HERA. 34th International Conference in High Energy Physics. 30 July - 5 August 2008, Philadelphia, USA: ICHEP 08.

[40] H1-ZEUS. C. Diaconu (H1): Structure functions and PDFs, 34th International Conference in High Energy Physics. 30 July - 5 August 2008, Philadelphia, USA: ICHEP 08.

[41] M. Diehl, *Generlized Parton Distributions*. Thesis, 2003, available on `http://arxiv.org/abs/hep-ph/0307382`. DESY-THESIS-2003-018.

[42] A.V. Radyushkin, Phys.Lett. **B 380**, 417 (1996).

[43] X. Ji, Phys. Rev. **D 55**, 7114 (1997).

[44] A.V. Radyushkin, Phys.Lett. **B 385**, 333 (1996).

[45] J.C. Collins, L. Frankfurt and M. Strikman, Phys. Rev. **D 56**, 2982 (1997).

[46] M. Burkardt, Phys. Rev. **D 62**, 071503 (2000). Erratum-ibid.D 66, 119903(2002).

[47] Small x Collaboration, B. Andersson et al., Eur. Phys. J. **C 25**, 77 (2002).

[48] A.D. Martin and M.G. Ryskin, Phys. Rev. **D 64**, 094017 (2001).

[49] B. List and A. Mastroberardino, *DIFFVM - A Monte Carlo Generator for Diffractive Processes in ep Scattering.*, October 16, 1998, available on `https://www.desy.de/~blist/diffvm.html`.

[50] P.D.B. Collins, *An Introduction to Regge Theory and High Energy Physics.* Cambridge University Press, England, 1997.

[51] T. Regge, J.A. Wheeler, Phys. Rev. **108**, 1063 (1957).

[52] V. Barone and E. Predazzi, *High-Energy Particle Diffraction.* Springer, 2002.

[53] Chew and S.C. Frautschi, Phys.Rev.Lett. **7**, 394 (1961).

[54] V.N. Gribov, Zh.Exp.Teor.Fiz. **41**, 667 (1962).

[55] V.N. Gribov, transl. Sov.Phys.JETP **14**, 478 (1962).

[56] R.G. Newton, *The Complex j-Plane.* Benjamin, New York, 1964.

[57] D.H. Perkins, *Introduction to High Energy Physics.* Addison-Wesley, 1982.

[58] F. Halzen and A.D. Martin, *Quarks and Leptons: An Introductory Course in Modern Particle Physics.* John Wiley & Sons, Inc, 1984.

[59] J.J. Sakurai, Phys.Rev.Lett **22**, 981 (1969).

[60] H. Kowalski and D. Teaney, Phys. Rev. **D 68**, 114005 (2003).

[61] CERN Yellow Report CERN-2005-005, 2005, available on `http://arxiv.org/abs/hep-ph/0412158v2`.

[62] D.Yu. Ivanov, G. Krasnikov, L. Szymanowski, Nucl. Phys. B Proc. Suppl. **146**, 134 (2005).

[63] G.T. Bodwin, E. Braaten and G.P. Lepage, Phys. Rev. **D 51**, 1125 (1995). Erratum in Phys. Rev. **D 55**, 5853 (1997).

[64] J.H. Kuehn, Phys.Lett **B 89**, 385 (1980).

[65] T.A. DeGrand and D. Toussaint, Phys.Lett. **B 89**, 256 (1980).

[66] J.H. Kuehn, S. Nussinov, R. Rueckl, Z.Phys. **C 5**, 117 (1980).

[67] M.B. Wise, Phys.Lett. **B 89**, 229 (1980).

[68] C.H. Chang, Nucl.Phys. **B 172**, 425 (1980).

[69] A. Martin, M. Ryskin and T. Teubner, Phys.Rev. **D 63**, 014022 (2000).

[70] M.G. Ryskin, Z. Phys. **C 57**, 89 (1993).

[71] M. Diehl, *Elastic meson production and Compton scattering*, available on `http://arxiv.org/abs/hep-ph/0109040`. DESY 01-126.

[72] N.N. Nikolaev, *Colour transparency: a novel test of QCD in nuclear interactions*, 1993, available on `http://arxiv.org/abs/nucl-th/9304015v1`.

[73] I. Rubinsky, *Study of color transparency effect with* $\pi \rightarrow 3\pi N$ *reaction at* $\sqrt{s} \approx 4$ *GeV.* (unpublished). Diploma thesis, MEPhI, Moscow, Russia, 1999.

[74] A. Martin, C. Nockles, M. Ryskin and T. Teubner, *Small x gluon from exclusive J/psi production*, available on `http://arxiv.org/abs/hep-ph/0709.4406v1`.

[75] L.L. Frankfurt, M.F. McDermott, M. Strikman, 1999, available on `http://arxiv.org/abs/hep-ph/9812316v3, DESY 98-196, MC/TH 98-18`.

[76] L. Frankfurt, W. Koepf and M. Strikman, Phys.Rev. **D 54**, 3194 (1996).

[77] A. Rybarska, W. Schäfer, A. Szczurek, available on `http://arxiv.org/abs/0805.0717v2`.

[78] A.G. Shuvaev, K.J. Golec-Biernat, A.D. Martin and M.G. Ryskin, Phys.Rev **D 60**, 014015 (1999).

[79] I.P. Ivanov, N.N. Nikolaev and A.A. Savin, Phys.Part.Nucl. **37**, 1 (2006).

[80] I. Ivanov, *Diffractive production of vector mesons in deep inelastic scattering within k(t)-factorisation approach.* Ph.D. Thesis, Bonn University, Bonn (Germany), 2003, available on `http://arxiv.org/abs/hep-ph/0303053v1`.

[81] 1981. HERA : A Proposal for a Large Electron Proton Colliding Beam Facility at DESY, DESY-HERA81/10, Hamburg.

[82] M. Seidel. The upgraded interaction regions of HERA. DESY-HERA-00-01.

[83] U. Schneekloth (ed.). The HERA luminosity upgrade. DESY-HERA-98-05.

[84] U. Schneekloth. Recent HERA results and future prospects (1998), hep-ex/9806010.

[85] I.Bloch, *Measurement of Beauty Production from Dimuon Events at HERA/ZEUS.* Ph.D. Thesis, Hamburg University, Hamburg (Germany), 2005. DESY-THESIS-05-034.

[86] A.A. Sokolov and I.M. Ternov, Sov. Phys. Dokl. **8**, 1203 (1964).

[87] M. Beckmann et al., *The Longitudinal Polarimeter at HERA*, available on `http://arxiv.org/abs/physics/0009047`.

[88] M. Beckmann et al., Nucl. Inst. Meth. **A 479**, 334 (2002).

[89] V.Gharibyan, K.P.Schuler, *HERA Transverse Polarimeter absolute scale and error by rise-time calibration*, available on `http://arxiv.org/abs/hep-ex/0310045`.

[90] D.P. Barber et al., Nucl. Inst. Meth. **A 329**, 79 (1993).

[91] ZEUS Collaboration, U. Holm (ed.), *The ZEUS Detector.* Status Report (unpublished), DESY (1993), available on `http://www-zeus.desy.de/bluebook/bluebook.html`.

[92] N. Harnew et al., Nucl. Inst. Meth. **A 279**, 290 (1989).

[93] B. Foster et al., Nucl. Phys. Proc. Suppl. **B 32**, 181 (1993).

[94] B. Foster et al., Nucl. Inst. Meth. **A 338**, 254 (1994).

[95] I.C. Brock, V. Bashkirov et al.for the ZEUS Collaboration. ZEUS Note 98-046, A Straw-Tube Tracker for ZEUS.

[96] V. Bashkirov for the FDET group. ZEUS Note 98-001, A Straw-Tube Transition Radiation Detector/Tracker for the ZEUS Experiment at HERA.

[97] V. Bashkirov, B. Dolgoshein, A. Stifutkin. ZEUS Note 95-003, Test-beam Performance of a Straw-Tube TRD Prototype for the ZEUS Experiment at HERA.

[98] T. Akesson et al., *Particle Identification Performance of a Straw Transition Radiation Tracker Prototype.* CERN-PPE/95-111, 19 June 1995.

[99] A. Polini et al., Nucl. Inst. Meth. **A 581**, 31 (2007).

[100] M. Derrick et al., Nucl. Inst. Meth. **A 309**, 77 (1991).

[101] A. Andresen et al., Nucl. Inst. Meth. **A 309**, 101 (1991).

[102] A. Caldwell et al., Nucl. Inst. Meth. **A 321**, 356 (1992).

[103] A. Bernstein et al., Nucl. Inst. Meth. **A 336**, 23 (1993).

[104] T. Jezinski et al., Proc. SPIE **5484**, 180 (2004).

[105] K. Pozniak et al., Proc. SPIE **5484**, 186 (2004).

[106] M. Herzog, *Experimentelle Untersuchungen an der planaren Driftkammer FTD2 des ZEUS-Vorwaertsdetektors.* Diploma Thesis, Universitaet Bonn, Bonn, Germany, Report BONN-IR-92-50, 1992.

[107] A. Bamberger, Nucl.Instr.Meth. **A 401**, 63 (1997).

[108] M.N. Rosenbluth, Nucl.Instr.Meth. **A 277**, 176 (1989).

[109] M. Bobrowski et al., Nucl. Inst. Meth. **A 323**, 309 (1992).

[110] P. Plucinski. Ph.D. Thesis, Institute for Nuclear Studies, Warsaw, Poland, (2008).

[111] G. Abbiendi et al., Nucl. Inst. Meth. **A 333**, 342 (1993).

[112] K.J. Gaemers, M. van der Horst, Nucl. Phys. **B 316**, 269 (1989).

[113] J. Andruszków et al., Acta Phys. Polon. **B 32**, 2025 (2001).

[114] H1 Collab., *Luminosity measurement in the H1 experiment at HERA*. Submitted to the 28th International Conference on the High-Energy Physics, ICHEP1996, Warsaw, Poland.

[115] M. Helbich et al., 2006. ZEUS Note 06-002. The Spectrometer System for Measuring ZEUS Luminosity at HERA.

[116] A. Caldwell, S. Paganis, R. Sacchi and F. Sciulli, *A Luminosity Spectrometer for ZEUS* (unpublished). HERA-ZEUS document Oct-22-1999, 1999.

[117] *The STT webpage*, available on `http://www-zeus.desy.de/components/fdet/stt.php3`.

[118] G. Aghuzumtsyan, *Charm production using Electron Taggers with the ZEUS Detector at HERA*. Ph.D. Thesis, Bonn University, Bonn (Germany), 2006. BONN-IR-2006-07.

[119] R. Renner, *Dijets in diffractive photoproduction measured with the ZEUS experiment*. Ph.D. Thesis, Bonn University, Bonn (Germany), 2006. BONN-IR-2006-13.

[120] A. Antonov, *Measurement of Inelastic J/psi Production in Deep Inelastic ep Scattering at HERA*. Ph.D. Thesis, Hamburg University, Hamburg (Germany), 2007. DESY-THESIS-07-030.

[121] D. Gladkov, *Charm quark pair correlations with D^*-muon tag at HERA*. Ph.D. Thesis, Hamburg University, Hamburg (Germany), 2007. DESY-THESIS-07-025.

[122] R. Shehzadi, *Internal alignment of the straw-tube tracker in the ZEUS detector*. Thesis, Bonn University, Bonn (Germany), 2006. BONN-HE-2006-01.

[123] Available on `http://adamo.web.cern.ch`.

[124] K. Oliver, available on `https://www-zeus.desy.de/zems/ZEUS_ONLY/display.php?p_active=10642`. Talk on 2008-09-24 at the High-Q2 weekly meeting.

[125] Available on `http://www.slac.stanford.edu/econf/C0303241/proc/papers/MOLT002.PDF`. Computing in High Energy and Nuclear Physics, 24-28 March 2003, La Jolla,California.

[126] Particle Data Group, S. Eidelman et al., Phys. Lett. **B 592**, 1 (2004).

[127] V. Kuzmin, Nucl. Instr. Meth. **A 453**, 336 (2000). Partially based on V. Kuzmin, The Muon Finder for FCAL, ZEUS note 96-134.

[128] G. Abbiendi. BREMAT, Global Tracking of muons in the Barrel and Rear region, ZEUS note 99-063.

[129] M. Corradi. MPMATCH algorithm, http://www-zeus.desy.de/ corradi/ZEUS ONLY/mpmatch/mpmatch2.html based on L. Bellagamba, MVMATCH: A package to match FMUON tracks with Central Detectors, ZEUS note 96-051.

[130] G. Bruni, available on `http://www-zeus.desy.de/˜bruni/ZEUS ONLY/muons.html`. MUFO algorithm.

[131] Available on `http://www-zeus.desy.de/˜robertc/ZEUS ONLY/mubac.html`. MUBAC algorithm.

[132] A. Geiser (ed.), DESY Hamburg. GMUON - a general ZEUS muon finder, ZEUS note 06-016.

[133] Available on `http://giroz.desy.de/bluebook/ch03/subsubsection2_5_1_6_4.html`.

[134] BRMUON, available on `http://www-zeus.desy.de/components/bmuon/`.

[135] R. Hall-Wilton et al.. The CTD Tracking Resolution (unpublished). ZEUS-note 99-024, 1999.

[136] E. Maddox, *Study of heavy quark production at HERA using the ZEUS microvertex detector*. Ph.D. Thesis, Univ. Amsterdam, Amsterdam (Netherlands), 2004.

[137] K. Goulianos, Phys.Rep. **101**, 169 (1983). (fig.25-p.198).

[138] T. Sjostrand and K. Goulianos, Comp.Phys.Comm. **82**, 74 (1994).

[139] A. Tetsuo, *GRAPE - Dilepton v1.1, A Generator for Dilepton Production in ep Collisions*, June 15, 2006, available on `http://arxiv.org/abs/hep-ph/0012029v2 5 Dec 2000`.

[140] F.W. Brasse et al., Nucl. Phys. **B 110**, 413 (1976).

[141] H. Abramowicz and A. Levy, Preprint DESY-97-251 (hep-ph/9712415), DESY, 1997.

[142] A. Mucke et al., Comp. Phys. Comm. **124**, 290 (2000).

[143] H. Plothow-Besch, Comp. Phys. Comm. **75**, 396 (1993).

[144] T. Sjöstrand et al., Comp. Phys. Comm. **135**, 238 (2001).

[145] I. Bloch, A. Geiser, O. Gutsche, I. Rubinsky and J. Ziemann. Muon Efficiency Correction for GMUON, ZEUS note 07-006.

[146] M. Corradi. Efficiency corrections for the Muon finders BREMAT and MPMATCH2, ZEUS note 04-006.

[147] A. Bertolin, R. Brugnera, M. Turcato. Study of the GLOMU and BREMAT Muon-Finders Efficiencies, ZEUS note 05-022.

[148] ZEUS Collaboration; S. Chekanov et al., Eur. Phys. J. **C44**, 13 (2005). DESY-05-071.

[149] O. Gutsche, *Measurement of beauty quark cross sections in photoproduction with the ZEUS experiment at the electron-proton collider HERA*. Ph.D. Thesis, Hamburg University, Hamburg (Germany), 2005. DESY-THESIS-2005-010.

[150] B. Kahle, *Measurement of Beauty-Production in Deep Inelastic Scattering at HERA II*, 2006. DESY-THESIS-06-011.

[151] BRMUON web page, available on `http://www-zeus.desy.de/components/bmuon/effic/bmeffic.html (FCLR, CTD FLT, CFLT)`.

[152] ZEUS Coll., J. Breitweg et al., Eur. Phys. J. **C 14**, 213 (2000).

[153] ZEUS Collaboration, S. Chekanov et al., Eur. Phys. J. **C 24**, 345 (2002).

[154] R. Ciesielski, *Exclusive J/ψ Production in Deep Inelastic ep Scattering in the ZEUS Experiment at HERA*. Ph.D. Thesis, Faculty of Physics of the Warsaw University, Institute of Experimental Physics, 2004. For the effective photon flux see formula 9.3.

[155] H.Abramowicz. Private communication.

[156] R. Barlow and C. Beeston, Comp. Phys. Comm. **77**, 219 (1993).

[157] ZEUS Collaboration, J. Breitweg et al., Phys. Lett. **B 437**, 432 (1998).

[158] D. Acosta et al., Phys. Rev. Lett. **88**, 161802 (2002).

[159] ZEUS Collaboration, *Exclusive photoproduction of Upsilon mesons at HERA*, 2009. DESY 09-036, to be published.

[160] ZEUS Collaboration, J. Breitweg et al., ZfP **C 75**, 421 (1997).

[161] ZEUS Collaboration, J. Breitweg et al., Eur. Phys. J. **C 14**, 213 (2000).

[162] BRMUON, http://www-zeus.desy.de/components/bmuon/effic/bmeffic.html.

[163] Available on `http://www-zeus/physics/lumi`.

[164] L.H. Lai et al., Phys. Rev. D **55**, 1280 (1997).

[165] W.K. Tung et al., JHEP **02**, 053 (2007).

[166] H1 Collaboration, C. Adloff et al., Phys. Lett. **B 483**, 23 (2000).

[167] L.L. Frankfurt, M.F. McDermott and M. Strikman, JHEP **02**, 002 (1999).

[168] ZEUS Collaboration, *Exclusive ρ^0 Production in Deep Inelastic Scattering at HERA*, 2007, available on `http://arxiv.org/abs/0708.1478`. DESY 07-118.

[169] B. Mellado, *Measurement of Diffractive Heavy Vector Meson Photoproduction at HERA with the ZEUS Detector*. Ph.D. Thesis, Columbia Univ., Columbia (USA), 2002. DESY-THESIS-2002-002.

[170] H. Kowalski, L. Motyka and G. Watt., Phys. Rev. **D 74**, 074016 (2006).

[171] A. Levy, *Energy Dependence of exclusive vector-meson production in ep interactions at HERA*, 2002. ICHEP02 proc.

[172] L. Frankfurt, M. Strikman, C. Weiss, *Small-x Physics: From HERA to LHC and beyond*, 2005, available on `http://arxiv.org/abs/hep-ph/0507286v1`.

[173] *The ZEUS trigger subperiods*, available on `http://www-zeus.desy.de/~rubinsky/zeus/mc/lumi_subperiods.php`.

Acknowledgements

When someone works in such a big international team like ZEUS, one understands rather quickly how important the people that one works with day-to-day are. The work presented in this thesis is largely based on the work and experience of other people. I would like to use this opportunity to thank at least those of whom I met and was lucky enough to work with during my years at DESY.

First of all I would like to thank Prof. R. Klanner for making this thesis possible and for all his help during these years.

I am deeply thankful to A.Geiser for his wise supervision of this thesis. The experience I obtained during the years of working with him will remain with me for my whole life. The current structure and the style of this thesis evolved during many discussions with Achim.

I thank R. Ciesielski for thoroughly reading this thesis and for his comments. I owe a thank you to M. Turcato for her experience in many aspects of the muon based analyses at ZEUS. I appreciate greatly her calm and reasoned approach.

I am indebted to H. Abramowicz, A. Levy, M. Arneodo and M. Ruspa for their experience in ZEUS diffractive physics. Their friendly support and vivid interest in my work can not be overstated.

I also thank J. Malka and Prof. J. Ciborowski for their effort in working on the journal publication. I would also like to thank everybody who helped us with their constructive criticism and attention at different stages of the ZEUS editorial process. I would like also to thank A. Bruni and M. Corradi for their extensive remarks to the paper draft contents.

I am indebted to Prof. B. Dolgoshein for making my participation in the ZEUS experiment possible and to the MEPhI group members: A. Stifoutkine, A. Antonov, D. Gladkov and S. Fourletov for introducing me into the STT project. Thanks to Y. Yamazaki, A. Polini, S. Fourletov and G. Hartner for their support during my work in the Trigger group.

It's my pleasure to mention here the Bonn University group members, R. Renner, G. Aghuzumtsyan, V. Schoenberg and M. Juengst as my co-STT-enthusiasts. I am grateful to Prof. I. Brock for leading the STT project and also for commenting on the thesis.

I would like to thank the ZEUS Event Display team R. Mankel, O. Gutsche, O. Kind, H. Studie, J. Ferrando and A. Montanari for introducing me to the world of the object-oriented visualisation software and teaching me to effectively hunt down the bugs in the code.

I also thank I. Bloch, O. Gutsche, B. Kahle and U. Samson for their fundamental contribution to the GMUON C++ software, on which I based my analysis.

The people who were not mentioned yet are by no means less important. I would like to thank, for very helpfull discussions on various topics, my multilangual colleagues in semialphabetical order from the West to the East, R. Hall-Wilton, J. Loizides, T. Namsoo, A. Tapper, M. Wing, I. Abt, O. Behnke, K. Borras, T. Haas, B. Kahle, U. Klein, B. Löhr, F. Roloff, T. S.-Schoerner, W. Zeuner, N. Coppola, A. Parenti, E. Gallo, P. Kulinski, V. Aushev, M. Borodin, S. Chekanov, L. Gladilin, J. Grebenyuk, I. Katkov, S. Proskurjakov, S. Savin, S. Spiridonov, N. Zotov, K. Nagano and Y. Yamazaki.

This thesis would not be possible without the love and support from my beloved wife, Tetyana, and my little daughter, Daria, to whom I devote this work.